A Thesis Submitted for the Degree of PhD at the University of Warwick

Permanent WRAP URL:

http://wrap.warwick.ac.uk/169259

Copyright and reuse:

This thesis is made available online and is protected by original copyright.
Please scroll down to view the document itself.
Please refer to the repository record for this item for information to help you to cite it.
Our policy information is available from the repository home page.

For more information, please contact the WRAP Team at: wrap@warwick.ac.uk

warwick.ac.uk/lib-publications

WARWICK
THE UNIVERSITY OF WARWICK

Computational Prediction of Core-Level Spectroscopy of Metal-Organic Interfaces to Reveal Chemical Interactions, Bonding and Behaviours

by

Samuel Joseph Hall

Thesis

Submitted to the University of Warwick

in partial fulfilment of the requirements

for admission to the degree of

Doctor of Philosophy in Analytical Science

Department of Chemistry

March 2022

Contents

List of Tables iv

List of Figures vi

Acknowledgments xii

Declarations xiii
- 1 Publications xiii
- 2 Sponsorships and Grants xiv

Abstract xv

Acronyms xvi

Chapter 1 Introduction 1

Chapter 2 Background 4
- 2.1 Principles of Core-Level Spectroscopy 5
  - 2.1.1 X-ray Photoemission Spectroscopy 5
  - 2.1.2 X-ray Absorption Spectroscopy 6
- 2.2 Principles of Density Functional Theory 8
  - 2.2.1 The Schrödinger Equation 9
  - 2.2.2 Hohenberg-Kohn Theorems 9
  - 2.2.3 Kohn-Sham Approach 10
- 2.3 Using DFT to Simulate Core-Level Spectroscopy 11
  - 2.3.1 Simulation of XPS 11
  - 2.3.2 Simulation of NEXAFS 13
  - 2.3.3 Other Methods in the Literature 16

Chapter 3 Practical Considerations 17
- 3.1 Software Used in this Work 17
  - 3.1.1 CASTEP Software 17
  - 3.1.2 FHI-aims Software 18
  - 3.1.3 ASE Package 19
- 3.2 Computational Workflow for XPS and NEXAFS Simulations 19

3.3 Computational Details 29
3.3.1 General Details for Core-Level Spectroscopy 29
3.3.2 Details for this Chapter 33
3.4 Performance of Core-Level Spectroscopy Simulations 33
3.4.1 Practical Considerations of Calculations in Atomic Orbital Basis 33
3.4.2 Practical Considerations of Calculations in Planewave Pseudopotential Basis 39
3.4.3 Analysis of Core-Level Spectra in Terms of Initial- and Final-state Contributions 44
3.4.4 Truncated Cluster vs Periodic Core-Level Simulations . . . 47
3.4.5 Influence of Charge in Periodic Core-Hole Simulations . . . 51
3.5 Conclusions 54

Chapter 4 Comparison Between Experimental and Simulated Core-Level Spectroscopy 55
4.1 Introduction 56
4.2 Azulene and Naphthalene 57
4.2.1 Core-level Spectroscopy 59
4.3 Computational Details 61
4.4 Comparison of Simulated Core-Level Spectroscopy 62
4.4.1 XPS 63
4.4.2 NEXAFS 64
4.5 Spurious Charge Transfer in XPS Simulations 66
4.5.1 The Missing XPS Shoulder for Azulene on Ag(111) 67
4.5.2 Molecular Orbital Based Self-Interaction Correction: DFT+U (MO) 70
4.5.3 Implications of Charge Transfer Artefacts for NEXAFS Predictions 74
4.6 Pyrene and Azupyrene 75
4.7 Conclusions 77

Chapter 5 Influence of the Interaction Strength at the Metal-Organic Interface on Core-Level Spectroscopy 79
5.1 Introduction 79
5.2 Computational Details 81
5.3 Results 81
5.3.1 Effect of Molecular Topology on XPS and NEXAFS Signatures 81
5.3.2 Properties of the Molecule-metal Interfaces 84
5.3.3 Physisorption Regime 86
5.3.4 Weak Chemisorption Regime 89
5.3.5 Strong Chemisorption Regime 92

5.4 Discussion 95
5.5 Conclusion 98

Chapter 6 Simulation of X-ray Core-Level Spectroscopy of Two-Dimensional Self-Assembled Molecular Networks 99
6.1 Introduction 99
6.1.1 Experimental Data 100
6.2 Computational Details 105
6.2.1 Geometry Optimisation 105
6.2.2 XPS and NEXAFS Calculations 106
6.3 Results 106
6.3.1 DFT Structure Optimisation 106
6.3.2 XPS and NEXAFS Spectroscopy 109
6.4 Discussion 112
6.5 Conclusions 114

Chapter 7 Characterisation of Oxygen-Terminated Diamond via Measurements and Simulations of XPS 115
7.1 Introduction 115
7.2 Computational Details 117
7.3 Results 118
7.3.1 Convergence 118
7.3.2 XPS results 120
7.4 Discussion 121
7.5 Conclusion 122

Chapter 8 Conclusion 124

Appendix A Code 128

Appendix B Additional Results 150

List of Tables

3.1 Relative shifts of the carbon 1s binding energies of the azupyrene molecule in dependence of the XC functional. 38

3.2 Absolute XPS binding energies for azupyrene calcualted with FHI-aims and CASTEP. 41

4.1 Experimentally recorded adsorption heights with NIXSW and adsorption energies with TPD for azulene and naphthalene adsorbed on Ag(111) and Cu(111) metal surfaces. 59

4.2 Comparison of the experimentally recorded adsorption heights D^{H} by NIXSW of naphthalene and azulene on Ag(111) and Cu(111) metal surfaces 62

4.3 DFT calculated gap between the HOMO and LUMO of an azulene molecule in a 20 Å periodic vacuum cube performed with different exchange correlation functionals. 72

5.1 Relative intensities of the first three peaks seen in the NEXAFS spectra of azulene on Ag(111) and Cu(111) with respect to the corresponding peaks of azulene gas-phase spectrum. 90

5.2 Summary of features to look out for and how they change depending on the interaction strength between molecule and metal. 96

6.1 Experimentally recorded values of the unit cells of the three phases of HTA on Au(111) surfaces from STM. 102

6.2 Unit cell values of both the experimentally observed unit cell and the DFT geometry optimised unit cell where cell angles were allowed to relax. 109

6.3 N1s XPS binding energy difference between aminic and pyridylic nitrogen atoms in HTA molecule for different experimental and DFT simulated phases. 110

7.1 C1s XPS BE each layer in two systems of bulk diamond consisting of either 7- or 9-layers. 120

7.2 Comparison of C1s BE shifts for the Keto-Ether$_5$ phases with respect to the diamond bulk signal (ΔBE) for simulation, experiment, and literature. 120
7.3 Comparison of the O1s BE difference (ΔBE) for the Keto-Ether$_5$ phases between simulation, experiment and literature. 121

B.1 Comparison of the absolute carbon 1s binding energies of ETFA calculated with various XC functional with the experimental values. 151
B.2 Comparison of the relative shifts in the carbon 1s binding energies of ETFA calculated with various XC functional with the experimental values. 151
B.3 Comparison of the absolute carbon 1s binding energies of azupyrene calculated with various XC functionals. 151
B.4 Comparison of the relative shifts of the carbon 1s binding energies of azupyrene calculated with various XC functionals. 151
B.5 Mulliken and Hirshfeld charges and dipole moments calculated for gas-phase azulene. 153
B.6 Molecular orbital energy levels of the HOMO, LUMO and LUMO+1 for different functionals including the differences between the HOMO-LUMO and LUMO-LUMO+1 on azulene. 154
B.7 Calculated net charge transfer of all metal adsorbed systems investigated using various charge analysis methods and electronic structure codes. 156
B.8 Table showing the convergence data of the C1s and O1s absolute BEs for supercells and clusters of various sizes of the $p(1 \times 1)$Peroxide phase. 161
B.9 Table showing the convergence data of the C1s BEs with respect to the diamond bulk and O1s absolute BEs for supercells and clusters of various sizes of the $p(2 \times 1)$Keto-Ether$_5$ and $p(2 \times 2)$Keto-Ether$_5$ phases. 161

List of Figures

2.1 An illustration of the process of the creation of core-holes in (a) x-ray photoelectron spectroscopy (XPS) and (b) x-ray adsorption spectroscopy (XAS). 4

2.2 Visual representation describing the angular dependence seen in NEXAFS spectroscopy for π^* and σ^* orbitals. 8

2.3 Principles of ΔSCF and ΔIP-TP methods with representation of the core-hole occupation used in the calculations. 12

2.4 Schematic showing the orientation of the electric field vector described by the polar ϑ and azimuthal φ angles. 15

3.1 Tree diagram of how the working directory will look with all subdirectories and location of the scripts. 23

3.2 Computational workflow to generate a K-shell NEXAFS spectrum with the ΔIP-TP approach for a example molecule of azupyrene. . . 30

3.3 A NEXAFS spectrum showing the three broadening ranges applied across the spectrum. 32

3.4 Examples of core-hole localisation problems in FHI-aims demonstrated on azupyrene. 34

3.5 Comparison of the C1s XP spectra of ETFA and azupyrene calculated with different XC functionals. 37

3.6 Comparison of the XPS and NEXAFS spectra of gas-phase azupyrene with different pseudopotentials. 40

3.7 Graphs comparing the influence of the vacuum box size on the XPS binding energies of gas-phase molecules in periodic calculations of ETFA and azupyrene. 42

3.8 Convergence of the NEXAFS spectrum of azupyrene with respect to increasing box size and cut-off energy of the planewave basis. . . . 43

3.9 Comparison of XPS and NEXAFS spectra calculated with three different GGA XC functionals. 44

3.10 Initial- and final-state decomposition of the simulated NEXAFS spectrum of azupyrene. 45

3.11 MO=projected NEXAFS spectra of gas-phase azulene using either a ground-state or final-state reference. 46

3.12 K-grid convergence series for the molecular azulene crystal for XPS and NEXAFS. 47
3.13 Convergence series for azulene adsorbed on Cu(111) with respect to k-grid, planewave cut-off and vacuum layer. 48
3.14 XPS calculations of azulene, as a free molecule, in the molecular crystal, and when adsorbed on Cu(111). 49
3.15 NEXAFS simulations of azulene in periodic systems with CASTEP. 51
3.16 Core-level spectra calculated with and without background charge compensation for azulene molecule in the gas-phase and adsorbed on the Cu(111) surface. 52
3.17 Comparison of the core-level spectra calculated with and without forced charge compensation for azulene molecule in the gas-phase with experimental data. 53

4.1 Lewis structures of naphthalene, azulene, pyrene and azupyrene. . . 57
4.2 Experimentally recorded C1s XP spectra of azulene and naphthalene in a multilayer structure and adsorbed on three metal(111) surfaces. 60
4.3 Experimentally recorded carbon K-edge NEXAFS spectra of azulene and naphthalene in a multilayer structure and adsorbed on three metal(111) surfaces. 61
4.4 Comparison between the experimentally recorded and DFT simulated C1s XP spectra of azulene and naphthalene in a multilayer structure and adsorbed on three metal(111) surfaces. 64
4.5 Comparison between the experimentally recorded and DFT simulated carbon K-edge NEXAFS spectra of azulene and naphthalene in a multilayer structure and adsorbed on three metal(111) surfaces. . . . 65
4.6 DFT simulated XP spectra of azulene in different configurations. . . 66
4.7 Simulated XPS, calculated using the ΔSCF method, of Az/Ag(111) using an aperiodic cluster structure. 67
4.8 Visualisations of the highest occupied molecular orbital (HOMO) and lowest unoccupied molecular orbital (LUMO) for azulene. 68
4.9 DFT simulated XPS of neutral and anionic gas-phase azulene. . . . 69
4.10 Total density of states and MO-DOS of structures of azulene adsorbed on a Ag(111) surface and with the azulene molecule 12 Å away from the metal surface. 71
4.11 DFT simulated XP spectra of azulene 12 Å away from the metal surface and in the equilibrium adsorbed geometry calculated with the +U(MO) correction. 73
4.12 Comparison of the experimentally measured and simulated NEXAFS data for azulene/Ag(111). 75

4.13 Comparison between experimental and DFT simulated C1s XPS spectra of pyrene and azupyrene in a multilayer structure and adsorbed on a Cu(111) surface. 76
4.14 Comparison between experimental and DFT simulated C K-edge NEXAFS spectra of pyrene and azupyrene in a multilayer structure and adsorbed on a Cu(111) surface. 77

5.1 Comparison of the simulated core-electron spectra for the gas-phase molecules naphthalene and azulene. 82
5.2 Initial-state decomposition of the XP spectra and final-state decomposition for the NEXAFS for gas-phase azulene on the left and naphthalene on the right. 83
5.3 Schematic depiction of six metal organic interfaces arranged according to increasing interaction strength. 84
5.4 Comparison of XPS spectra for naphthalene and azulene in the gas-phase, and adsorbed on three metal surfaces, Ag(111), Cu(111), and Pt(111). 86
5.5 Electronic structure of the systems in the physisorbed regime DFT calculated NEXAFS spectra of naphthalene gas-phase adsorbed on Ag(111) adsorbed on Cu(111) and the density of states. 87
5.6 DFT calculated NEXAFS spectra of azulene in two different systems. Gas-phase and the type I system, adsorbed on a Ag(111) surface, along with the density if states. 88
5.7 Comparison of the physisorbed Az/Ag(111) and weakly chemisorbed Az/Cu(111) for XPS, NEXAFS and density of states. 89
5.8 MO-projected NEXAFS of azulene on Ag(111) and Cu(111) using the simulated 25° spectra. 91
5.9 Simulated NEXAFS spectra, at 25° incidence angle, for naphthalene and azulene in different configurations. 93
5.10 MO decomposition of 25° NEXAFS of the type III systems of naphthalene, and azulene, adsorbed on Pt(111). 94
5.11 Simulated NEXAFS spectra of naphthalene and azulene at three different incidence angles, 25°, 53°, and 90°, for the free gas-phase molecule, the Pt(111) surface deformed molecule without the metal, and molecule adsorbed on a Pt(111) surface. 95

6.1 Skeletal structure of the HTA molecule, with molecular formula $C_{42}H_{36}N_4$ along with a ball-and-stick representation of HTA. 100
6.2 STM of the three phases (α, β and γ) of HTA formed on an Au(111) surface. 101

6.3 N1s and C1s experimentally recorded XPS spectra for three found coverages. 103
6.4 N K-edge and C K-edge experimentally recorded NEXAFS spectra for three found coverages. 104
6.5 Relaxed unit cell geometries of HTA in the α-phase, β-phase, and in the γ-phase with and without the presence of a gold adatom. 106
6.6 Unit cell geometries of optimised structures of HTA on a 2-layer Au(111) surface in the α-phase, with two molecule adsorption site where the central aminic nitrogen was in a top site or a hollow site. . 107
6.7 Unit cell geometries of optimised structures of HTA on a 2-layer Au(111) surface in the γ-phase with adatoms, with two molecule adsorption site where the central aminic nitrogen was in a top site or a hollow site. 108
6.8 The structure of HTA shown in along with two breakdowns of the atoms in terms of symmetry equivalent carbon atoms by colour and chemically in-equivalent carbon atoms by number. 111
6.9 Comparison between the experimental carbon and nitrogen K-edge spectra and the DFT simulated spectra of the α-phase. 112

7.1 Experimental x-ray photoelectron carbon 1s and oxygen 1s spectra of diamond sample taken at normal emission after annealing to 500 °C. 117
7.2 Structure visualisation of the $p(1 \times 1)$Peroxide and $p(2 \times 1)$Keto-Ether$_5$ and $p(2 \times 2)$Keto-Ether$_5$ structures shown from three different perspectives. 118
7.3 Graphs showing the convergence behaviour of XPS BEs calculations of the $p(1 \times 1)$Peroxide phase and the $p(2 \times 1)$Keto–Ether$_5$ phase for with respect to either unit cell and cluster size. 119

B.1 Overview of the various core-hole constraining approaches in a schematic diagram to visualise each approach utilises its core hole. 150
B.2 Graphs showing the convergence of the XPS BEs of azupyrene with respect to the planewave cut-off energy for different types of PP and for ultrasoft, and for two ultrasfot and and for norm conserving PPs. 152
B.3 DFT simulated XPS spectra of azulene on Ag(111) recorded with the molecule move upwards at different distances away from the metal surface, starting at the equilibrium adsorbed structure to 12 Å away. 153
B.4 DFT Simulated XP spectra of Np/Ag(111) performed in periodic boundary conditions using the CASTEP code using the ΔSCF method and with the PBE+U(MO) to shift specific orbitals. 155
B.5 Absolute carbon shifts for each individual carbon atom in azulene and naphthalene adsorbed onto an Ag(111) surface. 156

B.6 MO-projected NEXAFS using the calculated 25° spectra for azulene in the gas-phase and adsorbed on a Ag(111) and Cu(111) surface, either with the ground-state as the reference or the final-state. 157
B.7 DFT density of states (DOS) for naphthalene and azulene on a Pt(111) surface. 157
B.8 Unit cell geometries of optimised structures of HTA on a 2-layer Au(111) surface in the γ-phase, with two molecule adsorption site where the central aminic nitrogen was in a top site or a hollow site. . 158
B.9 DFT simulation of C1s XPS for structures of the α-phase. 158
B.10 Visualisations of the cluster models of $p(2\times1)$Keto-Ether$_5$ with different cluster radii. 159
B.11 Visualisations of the cluster models of $p(1\times1)$Peroxide with different cluster radii. 160

Listings

3.1 Main input settings for autoscript.py. 22
3.2 Calculation settings for autoscript.py. 23
3.3 Example .deltascf file for Az/Ag(111). 24
3.4 Settings to be changed at the top of castep_get_xps_energies.py. . 25
3.5 Designation of the broadening parameters for pseudo-Voigt broadening and selection of element in plot_xps.py. 26
3.6 Example .molpdos file used for Az/Ag(111). 28
A.1 autoscript.py 128
A.2 core_excitation.py 132
A.3 castep_get_XPS_energies.py 134
A.4 plot_xps.py 137
A.5 execute_molpdos.sh 140
A.6 plot_nexafs.py 141
A.7 plot_mo.py 145

Acknowledgments

The work presented in this thesis would not have been possible without the opportunity presented to me by the Molecular Analytical Science Centre of Doctoral Training at the University of Warwick. I thank the members involved in accepting me onto the course and the work and support through my PhD.

My gratitude goes to my supervisor Dr. Reinhard J. Maurer for granting me this project and the continued support and the expertise he provided throughout. The patience and acceptance I have received throughout my PhD have been invaluable along with the relaxed group environment he has created.

I would like to thank Dr. Benedikt Klein, for always willing to lend a helpful hand and for all the advice, feedback and answers he has provided during this work. Thanks go to Georg Michelitsch for his initial help and guidance in creating the first tools that would grow to become what they are now. I also thank members of the Maurer Group both new and old for their help provided with engaging discussions and comments about science and various other, not so work, related topics. Thanks go to other members of the larger computational chemistry group at Warwick for help given. Support from the Warwick Scientific Computing Research Technology Platform (SCRTP) in relation to IT issues has been greatly appreciated.

This work would not have been possible without the amazing support and encouragement from Kelsey Cremin. She has been a true friend and has always been there and has immensely helped me through the hard times that have arisen, and would not of made it through without her friendship. Further thanks to my friends and family for their support and understanding given to help push me forward and at times distract me from the toils of work.

Declarations

This thesis is submitted to the University of Warwick in support for the degree of Doctor of Philosophy. It has been composed by myself and has not been submitted in any previous application for any degree. The work presented was carried out by the author except in cases by collaborators which have been explicitly stated at the beginning of each chapter and referenced in the main text.

1 Publications

Parts of this thesis have been previously published by the author in the following:

Molecule-Metal Bond of Alternant versus Nonalternant Aromatic Systems on Coinage Metal Surfaces: Naphthalene versus Azulene on Ag(111) and Cu(111)
Benedikt P. Klein, Juliana M. Morbec, Markus Franke, Katharina K. Greulich, Malte Sachs, Shayan Parhizkar, François C. Bocquet, Martin Schmid, Samuel J. Hall, Reinhard J. Maurer, Bernd Meyer, Ralf Tonner, Christian Kumpf, Peter Kratzer and J. Michael Gottfried
The Journal of Physical Chemistry C **123**, 29219-29230 (2019)
https://doi.org/10.1021/acs.jpcc.9b08824

Enhanced Bonding of Pentagon–Heptagon Defects in Graphene to Metal Surfaces: Insights from the Adsorption of Azulene and Naphthalene to Pt (111)
Benedikt P. Klein, S. Elizabeth Harman, Lukas Ruppenthal, Griffin M. Ruehl, Samuel J. Hall, Spencer J. Carey, Jan Herritsch, Martin Schmid, Reinhard J. Maurer, Ralf Tonner, Charles T Campbell and J. Michael Gottfried
Chemistry of Material **32**, 1041-1053 (2020)
https://doi.org/10.1021/acs.chemmater.9b03744

The nuts and bolts of core-hole constrained ab initio simulation for K-shell x-ray photoemission and absorption spectra
Benedikt P. Klein, Samuel J. Hall and Reinhard J. Maurer
Journal of Physics: Condensed Matter **33**, 154005 (2021)
https://doi.org/10.1088/1361-648X/abdf00

Topology Effects in Molecular Organic Electronic Materials: Pyrene and Azupyrene
Benedikt P. Klein, Lukas Ruppenthal, Samuel J. Hall, Lars E. Sattler, Sebastian M. Weber, Jan Herritsch, Andrea Jaegermann, Reinhard J. Maurer, Gerhard Hilt and J. Michael Gottfried
ChemPhysChem **22**, 1065-1073 (2021)
https://doi.org/10.1002/cphc.202100222

Coexistence of carbonyl and ether groups on oxygen-terminated (110)-oriented diamond surfaces
Shayantan Chaudhuri, Samuel J. Hall, Benedikt P. Klein, Marc Walker, Andrew J. Logsdail, Julie V. Macpherson and Reinhard J. Maurer
Communications Materials **3**, 6 (2022)
https://doi.org/10.1038/s43246-022-00228-4

2 Sponsorships and Grants

This research was funded by EPSRC through the EPSRC Centre for Doctoral Training in Molecular Analytical Science, grant number EP/L015307/1.

Abstract

Molecules adsorbed onto metal surfaces, especially carbon-based aromatic molecules, can provide systems that offer tunable properties and can be used in organic light-emitting diodes (OLEDs). It is important to understand the behaviour of these systems at a molecular level in order to rationally engineer interfaces with specific properties. Core-level spectroscopy can provide a beneficial method to probe aspects of molecule-metal interfaces such as geometrical structure, stability, chemical bonding and electronic structure. X-ray photoelectron spectroscopy (XPS) and near-edge absorption fine structure (NEXAFS) spectroscopy can be used in tandem to gain significant insight into the studied system. However, the resulting spectra from these techniques can often prove hard to fully analyse as they contain multiple close-lying features and loss of clarity from broadening. This is where simulations of spectra can come in to help to disentangle and interpret spectra. This thesis establishes practical simulation workflows to predict XPS and NEXAFS spectra of metal-organic interfaces based on Density Functional Theory (DFT). These methods are applied to study the adsorption of aromatic adsorbates on metal surfaces, two-dimensional networks, and an oxidised diamond surface. As part of this work, the assessment of the performance and accuracy of simulations against experiment was carried out. Core-level simulations on various systems were performed to rationalise experimental findings on structure, stability, and surface chemical bonding.

Acronyms

ΔIP-TP Delta Ionisation Potential-Transition Potential.

ΔSCF Delta Self-Consistent Field.

AES Auger Electron Spectroscopy.

AFM Atomic Force Microscopy.

ASE Atomic Simulations Environment.

Az Azulene.

BDD Boron-Doped Diamond.

BE Binding Energy.

BSE Bethe-Salpeter Equation.

CC Coupled Cluster.

CVD Chemical Vapour Deposition.

DCD Dewar-Chatt-Duncanson.

DFT Density Functional Theory.

DOS Density of States.

EOM-CC Equation of Motion Coupled Cluster.

ESCA Electron Spectroscopy for Chemical Analysis.

ETFA Ethyl Trifluoroacetate.

EXAFS Extended X-ray Absorption Fine Structure.

FCH Full Core-Hole.

FOB Force Occupation Basis.

FOP Force Occupation Projector.

FSO Free Standing Overlayer.

FWHM Full Width at Half Maximum.

G/L Gaussian-Lorentzian.

GGA Generalised Gradient Approximation.

GTP Generalised Transition Potential.

GTS Generalised Transition State.

GUI Graphical User Interface.

HK Hohenberg-Kohn.

HMO Hückel Molecular Orbital.

HOMO Highest Occupied Molecular Orbital.

HTA 4,4,8,8,12,12-hexamethyl-2,6,10-tripyridin-4-yl-4H,8H, 12H-benzo[1,9] quinolizino[3,4,5,6,7-defg]acridine.

IMFP Inelastic Mean Free Path.

KS Kohn-Sham.

LDA Local Density Approximation.

LEED Low-Energy Electron Diffraction.

LUMO Lowest Unoccupied Molecular Orbital.

MO Molecular Orbital.

MO-DOS Molecular Orbital Density of States.

MOM Maximum Overlap Method.

NEXAFS Near-Edge X-ray Adsorption Fine Structure.

NIXSW Normal Incidence X-ray Standing Wave.

Np Naphthalene.

OLED Organic Light-Emitting Diode.

PBC Periodic Boundary Conditions.

PP Pseudopotential.

PW Planewave.

Ref. Reference.

SCAC Single-Crystal Adsorption Calorimetry.

SCF Self-Consistent-Field.

SEXAFS Surface extended X-ray Absorption Structure.

SGM Square Gradient Minimisation.

STEX Static Exchange.

STM Scanning Tunneling Microscopy.

TDDFT Time-Dependent Density Functional Theory.

TP Transition Potential.

TPD Temperature Programmed Desorption.

TS Transition State.

XAFS X-ray Absorption Fine Structure.

XANES X-ray Absorption Near-Edge Structure.

XAS X-ray Absorption Spectroscopy.

XC Exchange-Correlation.

XCH Excited Electron and Core-Hole.

XES X-ray Emission Spectroscopy.

XGTP Excited Generalised Transition Potential.

XPS X-ray Photoelectron Spectroscopy.

XTP Excited Transition Potential.

Chapter 1

Introduction

Atoms and molecules adsorbed onto metal surfaces represent an almost endless number of possible systems to create and use for a wide range of applications. This is down to each system possessing different behaviours and properties brought about from the interaction between the atom or molecule with the surface. Adsorbing a molecule onto a surface can affect the electronic structure based on the nature of the surface chemical bond. This can range from instances of weak interaction, where little change is seen between the free molecule and adsorbed structure, to substantially stronger chemical bonds where the electronic structure of the valence region can be greatly altered. Therefore, appropriate tools that can help probe and outline the electronic structure is of great importance.

Hybrid organic-inorganic thin films containing carbon aromatic π-electron structures from conjugated molecular solids, [1, 2] polymers, [3, 4] and graphene derivatives [5] have found practical uses as organic light-emitting diode (OLED) displays [3, 6]. Being able to control and tune the properties, such as the charge carrier rate, [7] has become a focus for many studies to improve the performance of such devices.

Core-level spectroscopy techniques have become essential methods to study molecular adsorbate systems due to the possibility of determining a wide range of information on the chemical state, structural geometries, chemical bonding, and electronic structure of either core or valence electrons whilst also being surface sensitive techniques. This provides a great tool to examine molecule adsorbed systems as a wealth of information can be gleamed from these experiments, especially electronic structure information as depending on the level of interaction and chemical bonding between the adsorbate and surface, the electronic structure can change forming new electronic states through hybridisation.

The two main forms of core-level spectroscopy that will be focused on in this thesis are x-ray photoelectron spectroscopy (XPS) and near-edge x-ray absorption fine structure (NEXAFS) spectroscopy. By combining these two techniques this allows for a detailed picture of electronic structure. These techniques allow for the electronic structure to be studied by irradiating a sample with x-rays which are adsorbed by core-electrons and either ejecting an electron (XPS) from the sample or exciting to an unoccupied state (NEXAFS).

When probing information from single atoms or simple diatomic molecules, the interpretation of the spectra can be relatively straightforward. Problems can occur when systems feature a large number of core-levels with similar binding energies such as molecules with conjugated π-bonds and similar chemical environments. On top of that, when such molecules are adsorbed onto a surface, interactions and chemical bonding with the surface can create new electronic states that complicate spectra even more. These can all cause interpretation and peak assignment to be much more difficult to achieve as specific features can possess similar chemical shifts. Furthermore, broadening of resonances will lead to overlapping features and washing out of specific peaks.

Historically, interpretation of experimental spectra was performed through the use of previously performed spectra of reference compounds, which help to identify local environments of specific elements [8]. This meant that an obvious downside to this approach was the size and scope of the reference database. For accurate interpretation, relevant reference spectra were required and as time progressed, suitable reference spectra became much harder to find due to larger and more complex molecules with more diverse functional groups being studied and systems on new, previously unreported surfaces and interfaces. To overcome this limitation theoretical methods provided a source of spectroscopic data which could take over the role of reference spectra [8].

Computational simulations based on first principles electronic structure theory can provide an indispensable tool to help with the interpretation of various core-level spectra. Various methods have been established to calculate both XPS and NEXAFS spectra, such as density functional theory (DFT) and its extension time-dependent density functional theory (TDDFT), [9, 10] many-body perturbation theory methods such as GW and Bethe-Salpeter equation (BSE), [11, 12] coupled cluster (CC) calculations and multiconfigurational wave function methods [13–15]. A problem with these methods can be the high computational effort required to perform such calculations. One of the most cost-effective methods remains DFT in its various semi-local and hybrid approximations.

This thesis will detail and describe a methodology and workflow created to perform simulations of both XPS and NEXAFS spectra through the use of DFT. This method is then tested on a range of various molecules on metal surfaces and other systems. It seeks to determine how DFT simulated spectra can be used to interpret structure, stability, and chemistry at metal surfaces. To begin with, an introduction into the principles of core-level spectroscopy, DFT and how the latter can be used to simulate XPS and NEXAFS is presented in Chapter 2. Chapter 3 will present the methodology to calculate XPS and NEXAFS spectra for molecules adsorbed onto a metal surface as well as tools developed. It also includes a comprehensive study into the numerical settings and practical details of the calculations. The accuracy of core-level spectroscopy simulations are tested against experimental spectra in Chapter 4 and shortcomings in prediction accuracy are analysed. Chapter 5 will show how these core-level simulations are used to gain significant insight into the interaction between the molecule and metal surface. Chapter 6 presents how core-level spectroscopy can be used to aid in the investigation into the structure of self-assembled molecular networks adsorbed on a metal surface. In Chapter 7, the core-level simulations are applied to characterise an insulator surface, namely an oxygen-terminated diamond (110). Finally, Chapter 8 presents the conclusions and outlook of the next steps and future progress of the work presented in this thesis.

Chapter 2

Background

In general core-level spectroscopy techniques involve probing the electronic structure of various types of samples such as molecules, solids, surfaces, and adsorbates. Techniques can be categorised into two distinct groups based on either the creation or decay of a core-hole. Experiments revolving around the creation of a core-hole are known as x-ray photoelectron spectroscopy (XPS) and x-ray absorption spectroscopy (XAS), which are the techniques that are the main focus in this work. The decay of a core-hole forms the basis of such techniques as auger electron spectroscopy (AES) and x-ray emission spectroscopy (XES) [16].

The formation of these core-holes occurs through the irradiation of the sample with an x-ray beam inducing the adsorption of a photon by a core-electron. The core-electron is then either ejected above the vacuum level (XPS) or be excited into a valence state (XAS). A simple single-particle representation of this process is shown in figure 2.1.

XPS and XAS have both been extensively used to characterise various materials and surfaces [17–19]. XPS can be used to provide information on the chemical composition and oxidation state of elements in oxides [20] and metal-organic interfaces, [16, 21–23] which will be the focus of this work. XAS can provide more detailed

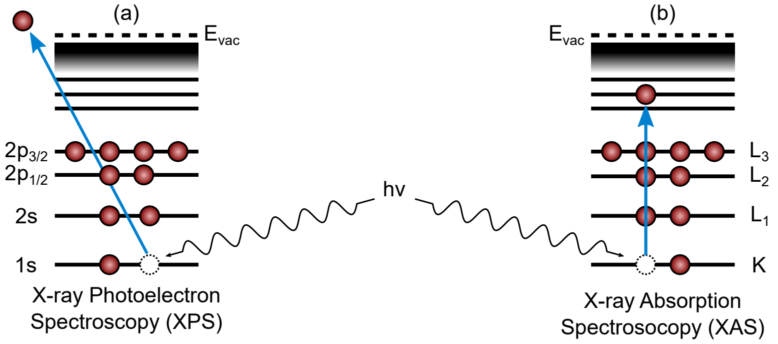
(a)
E_vac
2p3/2
2p1/2
2s
1s
X-ray Photoelectron Spectroscopy (XPS)
hv
(b)
E_vac
L3
L2
L1
K
X-ray Absorption Spectroscopy (XAS)

Figure 2.1: An illustration of the process of the creation of core-holes in (a) x-ray photoelectron spectroscopy (XPS) and (b) x-ray adsorption spectroscopy (XAS). Spectra are labelled based on the origin of the excited electron with labels for each shown.

information into the electronic structure and orientation of thin films, [24] surfaces and adsorbates, [25] and even liquids [26].

2.1 Principles of Core-Level Spectroscopy

In this thesis the focus will be on two different methods, XPS and near-edge absorption fine structure (NEXAFS) spectroscopy. The following section will review details about each of the spectroscopy techniques.

2.1.1 X-ray Photoemission Spectroscopy

The beginning of XPS is traced back to the discovery of the photoelectric effect which was first observed by Hertz and Hallwachs, [27, 28] discovering that interaction between light and solids led to the emission of electrons. Albert Einstein later described in more detail the concept with the introduction of light quanta $h\nu$ [29]. Development of XPS into an analytical technique was developed by Steinhardt et al. [30] and Siegbahn et al. [31] and was initially referred to as electron spectroscopy for chemical analysis (ESCA) [32]. However, since the early days of photoemission spectroscopy experiments to modern-day experiments, the fundamental process of performing these experiments has changed very little [33]. XPS essentially works by bombarding a sample with x-rays and measuring the kinetic energy of the emitted electrons. Information on the elemental composition and chemical state of each element in the sample can be found. It is also a surface sensitive technique as only electrons generated near the surface can escape and be detected due to the inelastic mean free path (IMFP), which is the average distance that an electron can travel between successive inelastic collisions. The IMFP for a typical photoemission experiment is in the order of a few nm, therefore making the technique surface sensitive [34].

In more detailed terms, XPS works through irradiating a sample with x-rays with enough energy to excite an electron with enough energy to be ejected as depicted in figure 2.1 (a). The kinetic energy of this electron E_{kin} is related to the energy of the photons $h\nu$, the electron binding energy (BE) E_{B} and the work function of the spectrometer Φ, which is the minimum energy needed to remove an electron.

$$E_{\mathrm{kin}} = h\nu - E_{\mathrm{B}} - \Phi \tag{2.1}$$

XPS spectra are labelled by the element and orbital in which the electron was ejected from as for example C1s describes a spectra where a 1s electron from a carbon has been emitted, which is the main type of XPS that is focused on in the following work. The resulting spectra can be interpreted through three key observables; line position, line intensity and line width/shape [35]. These three factors can help determine the chemical environment of the core-atom. The chemical environment is influenced by various factors such as oxidation state, nearest neighbours and substrate influences. A typical XPS spectrum will consist of the intensity of the detector signal in counts per second (y-axis) against the BE in electronvolt, eV, (x-axis) with decreasing energy from left to right. The binding energies can be characterised in terms of element with each element having a specific energy range (carbon $\approx$285 eV) and more information on the local chemical environment, electronic structure and band structure based on the chemical shift within the elemental range. Higher binding energies correlates to more energy needed to remove the core-electron from the atom. The intensity and shapes can be used to determine the number of atoms present in the environment as the relative peak area is proportional to this value.

The measured intensity of the photoelectron I in an experiment is related to the photoelectric cross-section $\sigma_{i\rightarrow f}$ (i and f referring to the initial and final state of the excited electron respectively) [35]

$$I(h\nu) \sim n\sigma_{i\rightarrow f}\lambda_{\text{in}}AJ_{h\nu} \tag{2.2}$$

with n being the number of atoms per volume, λ_{in} the IMFP, A the surface area of the radiation, and $J_{h\nu}$ the flux density of incoming photons with an energy of $h\nu$. In most cases when performing XPS experiments on molecule-metal structures the IMFP can be neglected [36, 37] because the electrons from the monolayer only pass through a vacuum on their way to the detector, and therefore there is no attenuation.

The cross-section $\sigma_{i\rightarrow f}$ itself can be related to the spectral function $A_{ii}(E_{\text{kin}} - h\nu)$ of photoemission of an electron with momentum $\mathbf{k}$ from core-state i via Fermi's golden rule and the sudden approximation:

$$\sigma_{\mathbf{k}}(h\nu) = \sum_i |\langle\psi_{\mathbf{k}}|\mathbf{p}\cdot\mathbf{A}(\mathbf{r})|\psi_i\rangle|^2 A_{ii}(E_{\text{kin},\mathbf{k}} - h\nu) \tag{2.3}$$

where $\mathbf{A}(\mathbf{r})$ is the vector potential of the incident electromagnetic field and $\mathbf{p}$ is the momentum operator. This is calculated through the use of Fermi's golden rule, which provides the rate of atomic or electronic transitions between two states after applying time-dependent perturbation theory and is first-order stating that the transition rate is dependent on the square of the matrix element of the operator.

2.1.2 X-ray Absorption Spectroscopy

The term x-ray absorption structure is an all encompassing term that can refer to many different techniques: extended x-ray absorption spectra (EXAFS), x-ray absorption near-edge structure (XANES), near-edge absorption spectra (NEXAFS) and surface extended x-ray absorption spectra (SEXAFS). Both XANES and NEXAFS refer to the same experiment but usually are used in conjunction with the type of sample investigated, with the former saved for solids and inorganic complexes and the latter for surfaces and adsorbed molecules [17]. In an x-ray absorption fine structure (XAFS) experiment, while both the NEXAFS and EXAFS are recorded, in practise different experimental parameters are needed to record each. In an XAFS experiment the first 30-50 eV from the adsorption edge corresponding to the NEXAFS and the rest of the spectrum called the EXAFS [8].

XAFS was first presented in theory by Kossel [38, 39] and Kronig [40–42], with the fine structure near the absorption edge initially called the Kossel structure and extending past the edge called the Kronig structure. Nowadays these are defined by the terms presented above. The first use of XAFS as a structural tool was developed during the 1970s, initially the near-edge structure was discarded as too complicated and only the EXAFS spectrum being the studied aspect. The near-edge structure was ultimately used for only low atomic number molecules with photon energies below 750 eV (C, N, O and F). But since then has developed to encompass a wider range of systems [17, 43].

In principle, NEXAFS works in a similar way to XPS and retrieves information about the electronic structure. Whilst XPS probe only the occupied states in the core-region, NEXAFS probes the unoccupied states but can also provide information on the core-electrons but the two techniques are often seen as complimentary techniques. In an experiment where a sample is exposed to x-ray radiation, the measured x-ray absorption coefficient $\mu(E)$ describes how strongly the x-rays are absorbed as a function of energy E [44]. When the energy of the x-ray photons have enough energy to excite an electron to a higher state as depicted in figure 2.1 (b), a sudden increase called x-ray absorption edge can be seen. The position of the edges in the spectrum is characteristic to the atoms in the sample. These edges correspond to the core-electron levels the electron was excited from and are labelled as K-, L- and M-edge referring to the principle quantum number with $n = 1(\mathrm{K}), 2(\mathrm{L}), 3(\mathrm{M})$ as shown in figure 2.1 (b). Therefore spectra are described as the element and edge in which they correspond to such as for example carbon 1s spectra are referred to as C K-edge NEXAFS.

The x-ray absorption coefficient $\mu(E)$, or the photoabsorption cross-section $\sigma(h\nu)$ can be described using Fermi's golden rule

$$\mu(E) \propto \sigma(h\nu) \propto \sum_f |\langle\psi_f|e^{i\mathbf{kr}} \cdot \mathbf{e} \cdot \mathbf{P}|\psi_i\rangle|^2 \, \delta(h\nu + E_i - E_f) \tag{2.4}$$

where ψ_i and ψ_f are the wavefunctions of the initial and final state respectively, and E_i and E_f the corresponding energies of each state. $h\nu$ is the energy of the x-ray photon whilst $\mathbf{k}$ and $\mathbf{e}$ are the wavenumber vector and the unit vector for the polarisation direction and $\mathbf{P}$ is the sum of the linear momentum operators of the electrons. The above equation can be simplified in XAS experiments due to the dipole approximation, where $e^{i\mathbf{kr}} \approx 1$ then

$$\sigma(h\nu) \propto \sum_f |\langle\psi_f|\mathbf{e} \cdot \mathbf{r}|\psi_i\rangle|^2 \, \delta(h\nu + E_i - E_f) \tag{2.5}$$

where $\mathbf{r}$ is the position operator. Along with acquiring information about the electronic

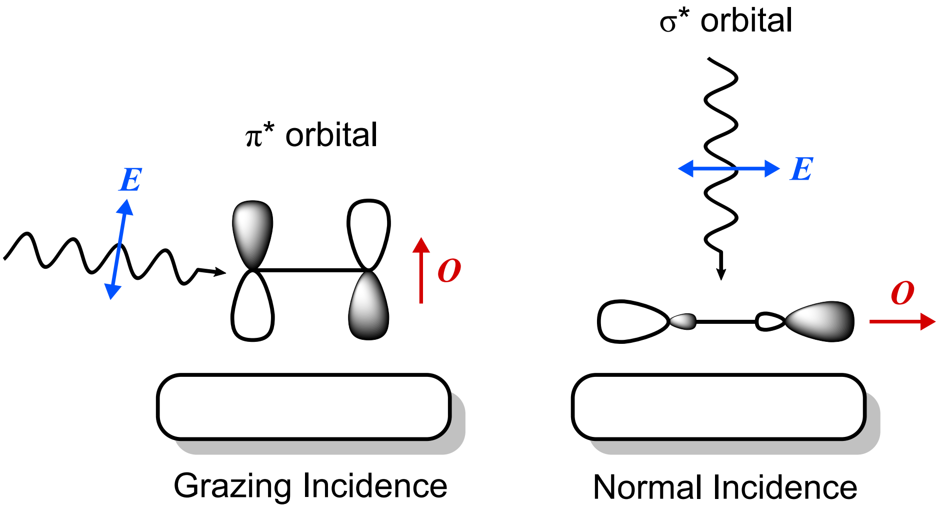

Figure 2.2: Visual representation describing the angular dependence seen in NEXAFS spectroscopy for π^* and σ^* orbitals. The left shows the behaviour between the electric field vector **E** and the dipole of the final state orbital **O** at grazing incidence where the intensity is at its greatest for the π^* and on the right for the normal incidence where intensity is greatest for the σ^*.

structure, NEXAFS can give information about the orientation of molecules on metal surfaces. This can be done by recording measurements at multiple incidence angles at the sample and taking advantage of the polarisation of the x-ray radiation. For a molecule laying flat on the surface of a metal substrate as illustrated in figure 2.2 the π^*-orbitals are orientated above and below the plane of the molecule. They have a maximum orbital amplitude perpendicular to the molecular plane. For the σ^*-orbitals this amplitude is along the molecular plane. When using linearly polarised light, the angular dependence of the matrix is $\mid \langle \psi_f \mid \mathbf{e}.\mathbf{r} \mid \psi_i \rangle \mid^2 = \mid \mathbf{e} \langle \psi_f \mid \mathbf{r} \mid \psi_i \rangle \mid^2$, the dipole of the final-state orbital **O** aligns with the matrix element and the transition intensity I becomes [43]

$$I \propto \mid \mathbf{e} \langle \psi_f \mid \mathbf{r} \mid \psi_i \rangle \mid^2 \propto \mid \mathbf{E} \cdot \mathbf{O} \mid^2 \propto cos^2 \delta \tag{2.6}$$

with δ corresponding to the angle between the electric field vector, **E** and the direction of the final state orbital **O**. This is shown visually in figure 2.2 where for the case where grazing incidence (left) is used the electric field vector **E** is along the same direction as the π^*-orbitals and so the intensity will be maximised and will altogether disappear with normal incidence, with the opposite seen for the σ^*-orbitals.

2.2 Principles of Density Functional Theory

This section will present an overview of the main computational method used throughout this work namely density functional theory (DFT). The information in this section follows the details laid out int textbooks by Koch and Holthausen, [45] Engel and

Dreizler, [46] and Parr and Yang [47]. The reader is referred to these works for a more detailed description of the theory.

2.2.1 The Schrödinger Equation

In quantum mechanics, the Schrödinger equation [48] can be used to predict the many-body behaviour of a system. For stationary states, the equation can be simplified to arrive at a time-independent, non-relativistic form. By further applying the Born-Oppenheimer approximation [49] it more simply becomes

$$\hat{H}\Psi(\mathbf{r}_1, \mathbf{r}_2, ..., \mathbf{r}_N) = E\Psi(\mathbf{r}_1, \mathbf{r}_2, ..., \mathbf{r}_N) \tag{2.7}$$

Using the Born-Oppenheimer approximation, the Hamiltonian operator $\hat{H}$ can be reduced by neglecting the kinetic energy of the nuclei and describing the energy from the nucleus-nucleus repulsion as a mere constant, the so-called electronic Hamiltonian can be described by three terms which include the kinetic energy ($\hat{T}$), electron-electron repulsion ($\hat{V}_{\mathrm{ee}}$), and the external potential ($\hat{V}_{\mathrm{ext}}$)

$$\hat{H} = \underbrace{-\frac{1}{2}\sum_{i=1}^{N}\nabla_{\mathrm{i}}^{2}}_{\text{kinetic energy}} + \underbrace{\sum_{i=1}^{N}\sum_{j>i}^{N}\frac{1}{rj}}_{\text{e-e repulsion}} - \underbrace{\sum_{i=1}^{N}\sum_{A=1}^{M}\frac{Z_A}{r_{iA}}}_{\text{external potential}} = \hat{T} + \hat{V}_{\mathrm{ee}} + \hat{V}_{\mathrm{ext}} \tag{2.8}$$

for a system with N electrons and M nuclei and with the nuclear charge being Z_A. The variational principle states that an approximate wavefunction Ψ_0 must yield an energy eigenvalue E_0 that is higher (or at best equal) to the true ground-state energy. The problem with using this approach is that one must calculate the many-body wave function which is not a reliable method.

2.2.2 Hohenberg-Kohn Theorems

The many-body problem was circumvented by Hohenberg and Kohn who described two theorems [50]. They first stated that the external potential ($\hat{V}_{ext}$) can be described as a functional of the electron density $\rho(\mathbf{r})$. With this, the electron density can be used to determine the Hamiltonian operator (2.8) and thus the total energy can be written as

$$\hat{E}_{\mathrm{HK}}[\rho(\mathbf{r})] = \underbrace{\hat{T}[\rho(\mathbf{r})] + \hat{V}_{\mathrm{ee}}[\rho(\mathbf{r})]}_{\text{independent}} + \underbrace{\hat{V}_{\mathrm{ext}}[\rho(\mathbf{r})]}_{\text{dependent}} \tag{2.9}$$

Both the kinetic energy and electron-electron repulsion terms are actually system independent and do not rely on the number of electrons N, the radius of the nucleus R_A or the nuclear charge Z_A and are collected together as the Hohenberg-Kohn (HK) functional F_{HK}. Whilst the nuclei-electron attraction is dependent on the system or the potential energy from the nuclei-electron attraction. The above equation can be written as

$$\hat{E}_{\mathrm{HK}}[\rho(\mathbf{r})] = F_{\mathrm{HK}}[\rho(\mathbf{r})] + \int \rho(\mathbf{r}) v_{\mathrm{ext}}(\mathbf{r}) d\mathbf{r} \tag{2.10}$$

The second theorem proposed by Hohenberg and Kohn utilises the variational principle, stating that the ground-state energy can be calculated using the HK functional given that the ground-state density is given ρ_0

$$E_0 = E[\rho_0(\mathbf{r})] \leq E[\rho(\mathbf{r})] \tag{2.11}$$

Taking into consideration these two theorems, then a variational constraint that the density must integrate to N electrons can be defined

$$\delta \left\{ E[\rho] - \mu \left[\int \rho(\mathbf{r}) d\mathbf{r} - N \right] \right\} = 0 \tag{2.12}$$

where μ is the chemical potential. This leads to the fact that the ground-state energy can be defined as a universal density functional $E[\rho]$. If the exact form of this functional would be known, then the exact ground-state density and energy could be calculated.

2.2.3 Kohn-Sham Approach

The next challenge was to find a method of calculating both the kinetic energy $\hat{T}$ and the electron-electron repulsion $\hat{V}_{\mathrm{ee}}$ of the HK functional. The latter could be represented by separating out the classical Hartree contribution.

$$V_{\mathrm{H}}[\rho] = \frac{1}{2} \int \frac{\rho(\mathbf{r}_1)\rho(\mathbf{r}_2)}{\mid \mathbf{r}_1 - \mathbf{r}_2 \mid} d\mathbf{r}_1 \mathbf{r}_2 \tag{2.13}$$

For the kinetic energy, Kohn and Sham [51] proposed that this could be represented by a system of N non-interacting electrons which reproduce the true ground state density expressed in terms of the Kohn-Sham (KS) orbitals ϕ_i

$$\rho(\mathbf{r}) = \sum_{i}^{N} \mid \phi_i \mid^2 \tag{2.14}$$

This non-interacting kinetic energy was not a direct calculation of the total kinetic energy ($T_{\mathrm{S}} \neq T$) and so the exchange-correlation (XC) functional was introduced

$$T_{\mathrm{S}}[\rho] = -\frac{1}{2} \sum_{i}^{N} \langle \phi_{\mathrm{i}} \mid \nabla^2 \mid \phi_{\mathrm{i}} \rangle \tag{2.15}$$

$$E_{\mathrm{XC}}[\rho] = (T[\rho] - T_{\mathrm{S}}[\rho]) + (V_{\mathrm{ee}}[\rho] - V_{\mathrm{H}}[\rho]) \tag{2.16}$$

which describes the sum of the error made by using the non-interacting electron kinetic energy and the error from treating the electron-electron repulsion classically through the Coulomb interaction. With this the energy functional can be expressed as

$$E[\rho(\mathbf{r})] = T_\mathrm{S} + V_\mathrm{ext}[\rho(\mathbf{r})] + V_\mathrm{H}[\rho(\mathbf{r})] + E_\mathrm{XC}[\rho(\mathbf{r})] \tag{2.17}$$

This leaves only the XC functional which contains all the non-solvable parts in (2.17). The accuracy of DFT relies solely on the chosen XC functional and as the magnitude of the functional is rather small in comparison to the other terms the error is minimal. A wide range of functionals have been developed and can be set into a hierarchical fashion on their "chemical accuracy" from lowest to highest, local density approximation (LDA), generalised gradient approximation (GGA) meta-generalised gradient approximation (meta-GGA) and exact XC which incorporates Hartree-Fock theory and know as hybrid functionals [52].

GGAs functionals have proven to be very popular in condensed matter physics as they provide a great performance balance for most bulk materials including metals. GGAs allow for the exchange and correlation energies to be dependant on the density but also on the gradient of the density and take the form of

$$E_\mathrm{XC}^\mathrm{GGA}[\rho] = \int \rho(\mathbf{r})\varepsilon_\mathrm{XC}^\mathrm{GGA}(\rho, \nabla\rho)d\mathbf{r} \tag{2.18}$$

where ε_XC represents the exchange and correlation energy density for a given density of ρ. One example of a GGA functional is the PBE functional [53] which has found popular use in the community and is the main functional used throughout this work.

2.3 Using DFT to Simulate Core-Level Spectroscopy

The simulation of core-level spectroscopy can provide significant insight into the interpretation of spectroscopy. Therefore, sustainable and accurate predictions of spectra have been developed throughout history through theoretical modelling. In the case of core-level spectroscopy, these simulations are able to provide much detail about XP and NEXAFS spectra not easily interpreted by experimental methods alone.

2.3.1 Simulation of XPS

In the prediction of XP spectra, the simplest approach to the calculation of the binding energies is through the use of Koopmans' theorem [54]

$$E_\mathrm{B} = -\varepsilon_{i,\mathrm{HF/KS}} \tag{2.19}$$

This states that the ionisation potential of an electronic state can be related to the negative of the Hartree-Fock eigenstate. In DFT this is only true for the highest occupied KS-state, [55, 56] with the binding energies estimated using the KS energies of the core-levels from the calculation which is typically referred to as only capturing initial state effects as the core-hole is not explicitly modelled [57–59].

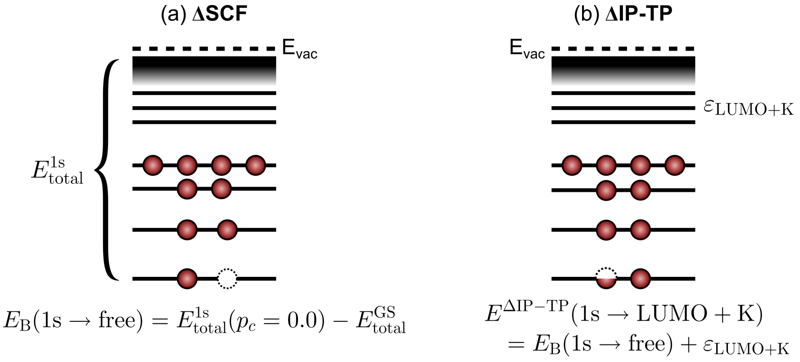
(a) ΔSCF
E_{vac}
E^{1s}_{total}
$E_{\text{B}}(1\text{s} \rightarrow \text{free}) = E^{1s}_{\text{total}}(p_c = 0.0) - E^{\text{GS}}_{\text{total}}$
(b) ΔIP-TP
E_{vac}
$\varepsilon_{\text{LUMO+K}}$
$E^{\Delta\text{IP}-\text{TP}}(1\text{s} \rightarrow \text{LUMO}+\text{K})$
$= E_{\text{B}}(1\text{s} \rightarrow \text{free}) + \varepsilon_{\text{LUMO+K}}$

Figure 2.3: Principles of (a) ΔSCF and (b) ΔIP-TP methods with representation of the core-hole occupation used in the calculations.

For more accurate and reliable BE predictions the effects of the core-hole need to be included which are termed final-state effects. The Delta-self-consistent-field (ΔSCF) [60–62] method is one of the most widely used approaches to simulate core-level binding energies [58, 63–66]. ΔSCF works by performing two self-consistent KS DFT calculations, one in the ground-state and another in a core-hole excited state (with an electron population p_c constrained to remove an electron) as shown in figure 2.3 (a). These constraints can be implemented in various ways depending on the DFT software used and descriptions of the implementation for two methods are described in Chapter 3. The BE is then calculated as the total energy difference between these two calculations

$$E_{\text{B}}(1\text{s} \rightarrow \text{free}) = E^{1\text{s}}_{\text{total}}(p_c = 0.0) - E^{\text{GS}}_{\text{total}} \tag{2.20}$$

Various other core-hole constraining approaches have been proposed with various different types of occupation constraints from the Slater transition state (TS) [60] which includes a half core-hole to methods with a third of a core-hole [67]. A summary of the different types of core-hole constraining approaches is shown in the appendix in figure B.1.

When simulating XPS using the single particle approach of DFT the absorption cross-section is approximated by a set of single particle transitions between the KS states. Equation (2.3) can be simplified by assuming independent electrons $A_{\text{ij}} = \delta_{\text{ij}}\delta(h\nu - \varepsilon_{\text{i}})$ in Fermi's golden rule

$$\sigma_{\mathbf{k}}(h\nu) = \sum_i |\langle \psi_{\mathbf{k}} | \mathbf{e} \cdot \mathbf{P} | \psi_i \rangle|^2 \, \delta(E_{\text{kin}} - h\nu - \varepsilon_i) \tag{2.21}$$

Disregarding the selection rules from any angular dependence, the matrix elements in (2.21) are often neglected as all final-states are assumed to be extended planewave (PW) sates. This amounts to associating each excitation that originates from an atom-centred core-state i with the same intensity i.e. eliminating all but n and $\sigma_{\mathbf{k}}(h\nu)$ from (2.2). This means that the spectrum calculated is in the form of infinitely narrow

δ-peaks located at the binding energies of the N atoms calculated and all with the same intensity.

This means that the results neglect any lifetime broadening from many-body effects such as electron-electron correlation and do not accurately represent the experimentally recorded spectra. This is accounted for by applying an empirical line broadening onto the δ-peaks and summing up all contributions into a total spectrum. Usually Gaussian, Lorentzian or convoluted Gaussian-Lorentzian (Voigt) functions are chosen to best match the experimental broadening effects.

2.3.2 Simulation of NEXAFS

Unlike in the case for XPS simulations where only one BE per core-state is needed to be calculated, for NEXAFS there are multiple transition energies ΔE_{fi} that are required. ΔSCF can be used to calculate this by constraining the occupation of the core-level state p_c to include a core-hole and by placing the electron into the relevant unoccupied state p_u [68, 69]. The transition energy is calculated from the difference between the core-excited and ground state calculations

$$\Delta E^{\Delta\mathrm{SCF}} = E(p_c = 0.0, p_u = 1.0) - E(p_c = 1.0, p_u = 0.0) \tag{2.22}$$

By employing the Slater-Janak theorem [55] $\frac{\partial E}{\partial q_i} = \varepsilon_i$ and using the midpoint integration rule the transition energies can be found by substituting in a half core-hole instead of a full core-hole TS method [60]. A consequence of using this method is that a calculation is required for every valence state that is chosen. Add this with the need to run this for all symmetry inequivalent atoms N in the system then the total number of calculations needed can reach high numbers: $(N \cdot M) + 1$ (extra calculation for ground-state).

A way to overcome this calculation burden is to use the transition potential (TP) method [70, 71]. The need to perform a calculation for every unoccupied state using the TS method is overcome by using the difference between KS energies of the unoccupied ε_u and core-states ε_c to define the transition energy. This is carried out by placing a half core-hole in the core-state but not adding anything to the valence state (as shown in figure 2.3), so the energy is

$$\Delta E^{\mathrm{TP}} = \varepsilon_u(p_c = 0.5, p_u = 0.0) - \varepsilon_c(p_c = 0.5, p_u = 0.0) \tag{2.23}$$

by doing so a single DFT calculation can be used to provide all the KS states and therefore all possible energy transitions needed for a full NEXAFS spectrum. Multiple variations of these methods have been proposed and are laid out in detail in figure B.1. A summary of these methods has been presented by Michelitsch and Reuter [69] where the methods were tested for the carbon and nitrogen K-edge spectra for gas-phase molecules. They found that the excited electron core-hole (XCH), (2.24) [72–75] and excited transition potential (XTP) (2.25) [69] performed the best when looking at the performance of both the intensities and energies of NEXAFS spectra. These two methods apply the same philosophy as ΔSCF by exciting a full electron from the core-state to an unoccupied state but the excited electron is constrained into the lowest unoccupied molecular orbital (LUMO) p_l

$$\Delta E^{\mathrm{XCH}} = \varepsilon_u(p_c = 0.0, p_l = 1.0) - \varepsilon_c(p_c = 0.0, p_l = 1.0) \tag{2.24}$$

$$\Delta E^{\mathrm{XTP}} = \varepsilon_u(p_c = 0.5, p_l = 0.5) - \varepsilon_c(p_c = 0.5, p_l = 0.5) \tag{2.25}$$

In general, on the performance of the ΔSCF and TP methods (or similar versions of XCH and XTP) it is seen that methods that include a half core-hole (TP and XTP) perform well for the relative peak positions and intensities of NEXAFS spectra [69]. The absolute energies are better described with the full core-hole methods (ΔSCF and XCH) [76]. This poses the question of which method is better to use overall as there is not a clear winner for all factors. Triguero et al. noticed this problem and proposed a hybrid approach to bridge the deficiencies of each method [76]. This was carried out by using the ionisation potential of the full core-hole state to correct the relative energies provided by the half core-hole TP calculation. This method has been called Delta-ionisation potential-transition potential (ΔIP-TP) [77] with the transition energies calculated as following

$$\Delta E^{\Delta\mathrm{IP-TP}} = \varepsilon_u(p_c = 0.5, p_u = 0.0) + E_{\mathrm{B}}(1\mathrm{s} \rightarrow \mathrm{free}) \tag{2.26}$$

This method performs well in the calculation of NEXAFS spectra, achieving good agreement with experiment [78–81] by using the accurate description of relative transition energies and shifting to more reliable absolute energies. However, there is also the fact of the angular dependence of the spectra as described in figure 2.4 where the polarisation of the incident x-ray can be used to probe the orientation [82]. As described in section 2.1.2 the intensity of the spectrum depends on the polarisation of the incoming light **e** with respect to the dipole moment of the orbital **O**. Equation (2.6) can be rewritten as

$$I \propto |\, \mathbf{e} \cdot \mathbf{O}\, |^2 = \left(\sum_{r=x,y,z} e_r \cdot \mathbf{O}_{fi,r} \right)^2 \tag{2.27}$$

Not all samples measured in NEXAFS experiments are heavily reliant on the angular dependence, with such samples in the gas-phase, liquid or amorphous/disordered polycrystalline solids, this will be averaged out. To account for this, the orientational dependence can be neglected

$$\mu_{fi}^{\mathrm{total}} = \mathbf{O}_{fi,x}^2 + \mathbf{O}_{fi,y}^2 + \mathbf{O}_{fi,z}^2 \tag{2.28}$$

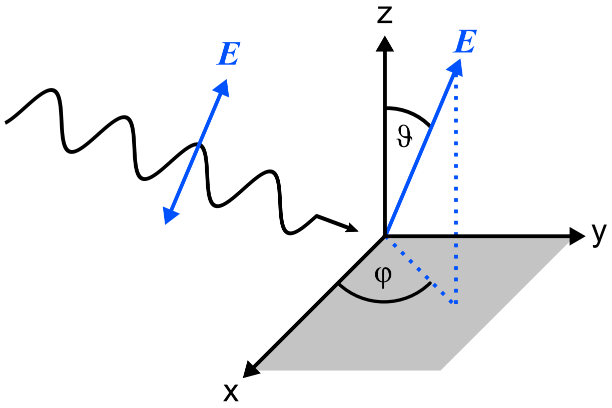

Figure 2.4: Schematic showing the orientation of the electric field vector described by the polar ϑ and azimuthal φ angles.

For molecules adsorbed on a metal surface there is a significant influence on the spectra related to the polarisation of the light (dichroism) which is used to help elicit structural information [24]. To achieve this the polarisation of the light can be defined as a vector $\mathbf{e} = (e_x, e_y, e_z)$ in terms of two angles, the polar ϑ and azimuthal φ angles which are shown in figure 2.4.

$$\mathbf{e} = (e_x, e_y, e_z) = (sin\vartheta \cdot cos\varphi, sin\vartheta \cdot sin\varphi, cos\vartheta) \tag{2.29}$$

The resulting intensity for a transition between state i and state f excited by polarised light defined by the angles ϑ and φ would be

$$\mu_{fi}^{\mathrm{p}}(\vartheta, \varphi) = (\mathbf{O}_{fi,x} \cdot e_x + \mathbf{O}_{fi,y} \cdot e_y + \mathbf{O}_{fi,z} \cdot e_z)^2 \tag{2.30}$$

For some systems the variation of the azimuthal orientation φ of the incident radiation relative to the substrate can also be used to extract structural information [83]. Most systems, however, and this includes most metal–organic interfaces, possess a random azimuthal orientation, or many rotational domains which cancel out the φ-dependence due to the symmetry of the underlying substrate [17]. For such systems, it is therefore best practice to average over the azimuthal φ-dependence of the signal (in the x, y plane) for the corresponding simulations, while fully describing the ϑ-dependence, yielding

$$\mu_{fi}^{\mathrm{p,av}}(\vartheta) = (\mathbf{O}_{fi,x}^2 + \mathbf{O}_{fi,y}^2) \cdot sin^2\vartheta + \mathbf{O}_{fi,z}^2 \cdot cos^2\vartheta \tag{2.31}$$

A final important factor to take into consideration for such calculations are any scalar relativistic effects. This is usually done by solving the Dirac equation; however this can be tricky and long winded process to calculate. The process can be made a lot easier by removing any spin-orbit coupling effects and leaving only other relativistic effects such as mass-velocity and Darwin. This greatly simplifies and speeds up the calculation times. Two different relativistic treatments have been used in this and details of this are given in section 3.1 for each code.

2.3.3 Other Methods in the Literature

Many other methods of calculating core-level spectroscopy exist in the literature that use different approaches and methods in order to obtain accurate spectra. Early adoptions in DFT to calculate spectra involved the direct static exchange (STEX) method [84–86]. Where calculations were performed of the core-hole with the valence orbitals frozen and vice versa (optimisation of valence with core-hole frozen), however a disadvantage of this method was it neglected any electron correlation effects. More recent methods in DFT that haven been proposed is the square gradient minimisation (SGM) approach [87, 88] which aims to prevent variational collapse of the target excited state.

Time-dependent density functional theory (TD-DFT), an extension of DFT with a time-dependent external potential, is mainly used to study the excited state properties of molecular systems, [89] and has been effectively utilised in core-level spectroscopy simulations [90–93] which succeeds in effects of electron screening. However, it is still restricted in accuracy by the choice of XC functional used. Other methods such as coupled cluster (CC) [94, 95] and EOM-CC [96–98] have been used for accurate simulations of XAS but are limited to calculations on free molecules.

Full many-body calculations for core-level spectroscopy such as GW [11, 12] and BSE [99, 100] can provide very accurate spectra. These quasiparticle methods are based on Hedin's equations [101]. The GW method is used for simulations of XPS and BSE for XAS. These work through the use of the single particle Green's function G and the screened Coulomb interaction W. The GW method builds the spectral function from the single particle Green's function that describes the removal or addition of particles to the system [12] and describes the frequency-dependent probability of photoemission and the associated lineshape. An advantage of this method is that many interaction processes such as collective screening, electron-electron scattering and relaxation effects due to the core-hole are accounted for, which are neglected in simple ΔSCF-type approaches. However, the applicability of these methods are limited as they are only suitable for small molecular systems and require a high amount of computational throughput.

Whilst these methods can provide alternative and sometime more accurate methods for core-level spectroscopy, this usually comes with added computational cost and limited system ranges. This is where DFT and the ΔSCF and ΔIP-TP methods are such a useful tool that can be applied to a variety of systems including metal surfaces. They offer a reliable balance between accuracy and computational efficiency as long as effort is taken to limit any possible factors that can affect the results.

Chapter 3

Practical Considerations

This chapter discussed work that has been previously published in the below mentioned publication and is detailed in section 3.4. The presented work in section 3.4.1 and work involving molecular crystals in section 3.4.4 were performed by Dr. Benedikt P. Klein. and included for completeness.

The nuts and bolts of core-hole constrained ab initio simulation for K-shell x-ray photoemission and absorption spectra
Benedikt P. Klein, Samuel J. Hall and Reinhard J. Maurer
Journal of Physics: Condensed Matter **33**, 154005 (2021)
`https://doi.org/10.1088/1361-648X/abdf00`

3.1 Software Used in this Work

As described in the previous chapter there are many different approaches and methods to simulate core-level spectra. Even within one method, such as ΔSCF, there are many different possible ways to perform the calculations in practise due to the vast amount of electronic software packages available to use. In this chapter, presented is a reliable methodology and readily available tools to help in the process of calculating spectra for metal-organic interfaces using the CASTEP software package. A brief description of the software and packages used are detailed below.

3.1.1 CASTEP Software

CASTEP [102] is an electronic structure software package that utilises a planewave (PW) basis set and pseudopotentials (PPs). The wavefunctions are expanded in the PW basis set through Bloch's theorem and requires structures to be set in periodic boundary conditions (PBCs), which is a unit cell of any given size that will be infinitely repeated in all directions. CASTEP makes uses of both a real space grid and a reciprocal space grid transformed via Fast Fourier Transform, and splitting into parts to solve the Hamiltonian in each space it is easy to do so. When using reciprocal space, efficient k-space sampling is required and was implemented through a Monkhorst-Pack grid to sample the first Brillouin zone. To adequately simulate gas-phase calculations in PBCs, a molecule was placed in a large vacuum box with sufficient space on all sides to limit any interaction with repeating images. For metal slab calculations the repeating images created a continuous metal slab in the x and y directions with a vacuum layer in the z direction.

The KS wavefunctions used in the code are expanded in PW basis set and based on Bloch's theorem, with the potential between the core-electrons and nuclei being described by PPs. These PPs match the wave function given in all-electron systems distances far away from the nucleus to include the valence orbitals. The core-states much closer to the nucleus are simplified and described as *frozen* as these are seen as unimportant in chemical bonding and impractical to represent with a PW approach as the number of basis sets would be extremely high. To counter this, the core-electrons and the strong Coulomb potential of the nucleus are replaced with a small set of pseudo wavefunctions. Using this method, the potential can now be represented with a significantly smaller basis set. Optimisation of these PPs are carried out to ensure a smooth and simple wavefunction within the defined core-region and match with the all-electron wavefunction in the valence region. PPs can be described by their *hardness*, which corresponds to the number of Fourier components needed for accurate representation of the wavefunction (*soft* for small amount, *hard* for large).

Calculations using CASTEP utilised the Koelling-Harmon scalar relativistic treatment [103].

MolPDOS

MolPDOS [104] is a tool that is included in the CASTEP package. The program can be used to calculate the density of states (DOS) and DOS projected onto molecular states as a post-processing tool for the CASTEP software. The contribution from a reference orbital ϕ_j can be projected out from the KS states of the main system ψ_i through

$$\rho_i^{MO}(E) = \sum_i |\langle\phi_j|\psi_i\rangle|^2 \, \delta(E - \varepsilon_i) \tag{3.1}$$

The reference orbital ϕ_i used can be used from many different sources and in this work is taken to be molecular orbitals (MOs) of a gas-phase molecule or from the free standing overlayer (FSO) of a molecule-metal system (system with metal surface deleted leaving only the molecule). The MolPDOS tool has been used in the simulation of angle-dependant NEXAFS spectra and for MO projections.

3.1.2 FHI-aims Software

FHI-aims [105] is an all-electron electronic structure code based on numeric atom-centred orbitals. These basis functions allow for correct descriptions of the nuclear potential close to the nucleus and also at large distances. These are local basis sets which result in quick convergence with respect to the number of basis functions. FHI-aims offers four default levels to control the numerical settings of the chosen element and are set as *light*, *intermediate*, *tight* and *really tight*, or can be manually set to a required preference. Along with this, the basis set are set up from a minimal basis and increase therefrom up in 'tiers'. These 'tiers' are a closed shell of basis functions. FHI-aims can make use of both PBCs and also aperiodic (cluster) models where no repeating images are included. A zeroth-order expansion of the Koelling-Harmon equation [103] is used for the scalar relativistic treatment for FHI-aims calculations known as the zero-order regular approximation (ZORA) [106–108].

3.1.3 ASE Package

The Atomic Simulation Environment (ASE) [109] is a Python based tool that can be used to create, manipulate and analyse atomistic simulations. The tool provides both a graphical user interface (GUI) as well as scripting capabilities for various tasks. ASE can also perform calculations of energy, forces, stresses and other quantities along with structure optimisations, molecular dynamics, and nudged elastic band calculations [109]. ASE has been developed to work with a wide range of electronic structure packages and enables input and output of many different file formats needed for different codes. The GUI has been used extensively throughout this work to help build and visualise structural models to be used for calculations whilst implemented in the tools described in section 3.2 to help write the necessary input files for calculations.

3.2 Computational Workflow for XPS and NEXAFS Simulations

Several tools have been created as part of this thesis to facilitate and automate workflows of the calculations necessary and to enable post processing to simulate both XPS and NEXAFS spectra with the CASTEP software package. Here a detailed description of these tools will be presented. The code is provided in full in the appendix. In this section the font style will be used to represent various things with **bold** font indicating a directory, sans serif font to indicate a file and `text` font to represent code or text inside a file or script.

- autoscript.py - Python script which will generate all XPS and NEXAFS input files needed for CASTEP.
- core_excitation.py - Python code use by autoscript.py to search structure for chosen element and change to a new X:exc element.
- castep_get_XPS_energies.py - Python script to calculate XPS binding energies.

- `plot_xps.py` - Python script to apply broadening to XPS binding energies and sum up all peaks for a full spectra.
- `execute_modos.sh` - Bash script to run MODOS analysis for all specified incidence angles and atoms.
- `plot_nexafs.py` - Python script to process MODOS output data into broadened NEXAFS spectra.
- `plot_mo.py` - Python script to process MODOS output data into MO orbital NEXAFS contributions.

Initial Setup

The first step before using any of the tools is to familiarise and adopt the naming convention that will be used throughout the work process. In CASTEP, the input and output files all have the same name prefix and only differ by the extension name with an example of input files being called `castep.cell` and `castep.param` and example output files called `castep.castep` or `castep.bands`. With this in mind and for use of metal-organic interfaces the name will follow a *molecule_metal* configuration. The *molecule* is simply just the investigated molecule, e.g. azulene, benzene, pyridine, and the *metal* is the metal substrate, e.g. Cu, Au, or simply gas if no metal surface is present. In the example followed through in this work, the system of azulene (Az) on a Ag(111) surface will be used so the name for the files would use *azulene_Ag*, which would result in input files called `azulene_Ag.cell` and `azulene_Ag.param`.

The next step would be to organise the filing system that will be used to contain all of the calculation data into easily labelled and ordered directories, and should contain:

- Input files for the ground-state calculation in parent directory
- **freestand** directory (sub-directory containing files from calculation of free standing overlayer, only needed when including metal surface)
- **XPS** directory (sub-directory generated by `autoscript.py`)
- **NEXAFS** directory (sub-directory generated by `autoscript.py`)

The first calculation to be performed is the initial DFT ground-state calculation of your chosen system. There are two uses for this calculation, firstly is to calculate the total ground-state energy of the system which will later be used to calculate the XPS binding energy (BE). Secondly to generate all the on-the-fly PPs in CASTEP with a string of parameters for each element, that will be used throughout, if these are not already known. These PPs are described by a list of numeric parameters that define the settings of the element and can be found in their corresponding `.usp` files. For the example carbon the default settings and the specific string that needs to be copied is `2|1.4|10|12|13|20:21(qc=7)`. These numbers define various parameters of the pseudopotential, the first number is the angular quantum number (l) of the local channel followed by the core radius. The next three numbers relate the levels of convergence for the pseudopotential. The `20:21` are the n and l quantum numbers of the valence states. It is important to have to hand all of the PP strings for all elements being used and to keep them the same throughout the whole process.

When coming to calculate the NEXAFS spectra, a restart file is needed as a reference in order to project the MO contributions onto the spectra. For a gas-phase calculation this is simply the azulene_gas.check file from the initial ground-state calculation. However, for a molecule-metal structure, this reference needs to be of the FSO. The FSO is the system of interest with the metal surface removed. In order to generate this for a molecule-metal system both the azulene_Ag.cell and azulene_Ag.param ground state files should be copied into the **freestand** sub-directory and the name should be changed to azulene_free. Only the azulene_free.cell file should be edited and should only be changed by deleting the atoms and coordinates for all of the metal atoms. Once this calculation is completed the azulene_free.check file will need to be saved for future use.

Generation of the XPS and NEXAFS Inputs Using autoscript.py

To generate the XPS and NEXAFS directories with all the input files needed for each individual carbon atom a separate directory is set up with:

- autoscript.py
- core_excitation.py
- Geometry file of the system

These two python scripts are used to read in the chosen geometry of the system and to create input files for all the calculations needed for XPS and NEXAFS in a clear and ordered manner. These codes make use of the CASTEP calculator found in ASE [109]. The core_excitation.py script can be left alone and unchanged and is used to locate all atoms that will be needed and systematically change them one by one to a new core-excited element defined as for example for `C` to `C:exc`. All settings for this script are set in the autoscript.py code. Settings that should be changed are all shown in listing 3.1. Firstly, the `input_name` and `output_name` should be changed to the required corresponding names. Through the use of the ASE calculator which supports many various file formats the input file can be any supported file format, but the full file name and extension needs to be written out for the `input_name`. The output file will always be a CASTEP .cell file so only the name of the molecule-metal system needs to be written down for the `output_name`. Secondly, all the PP strings of the elements involved that were saved earlier can be included, which for this case are for

```
#Full name of the geometry input file for script to read and create files for
input_name = 'hta.cell'
#Seedname of the CASTEP files that the script will output
output_name = 'azulene_Ag'

#Add all atom pseudopotentials you want
Cpseudo = 'C 2|1.4|10|12|13|20:21(qc=7)'
Hpseudo = 'H 1|0.6|13|15|17|10(qc=8)'
#Npseudo = 'N 2|1.1|14|16|18|20:21(qc=7)'
Agpseudo = 'Ag 3|1.5|1.5|0.8|15|17|19|40U:50:41:42(qc=7)'

#If a MO analysis is needed as the list of MOs to be projected and
#checkfile name to be used as the reference for the MODOS calculation
MO = list(map(str, range(17,29)))
check = 'azulene_free.check'
```

Listing 3.1: Main input settings for autoscript.py.

carbon, hydrogen and silver. The settings for the MO projection are next and include a range of orbital numbers. As many states as needed can be given but a general adequate amount are several above and below the lowest unoccupied molecular orbital (LUMO) and highest molecular orbital (HOMO) respectively. The script has two options when running the part that handles writing the settings needed for the MO projection as the way these are set in the code change between versions. For versions of CASTEP 20 and above the settings can be given in the .param file and what needs to be given are the range of numbers of the MOs for the projection and the name of the restart check file under `MO` and `check` respectively. At the end of the script, you can chose which version you are using and if 20 and above will print out these settings if not then a separate file will need to be created and explained later.

These are reliant on the version of CASTEP. The setting keywords to run MODOS changed between versions, and it is possible to pick the correct keywords depending on the version of CASTEP, with the older keywords for CASTEP 19 and below and newer keywords for CASTEP 20 and later.

Next are the calculation settings, which are all listed under `QM1` and `QM2`, which are shown in listing 3.2. `QM1` settings relate to settings for the XPS calculations and `QM2` relate to the NEXAFS calculations. The majority of these settings are located in the `QM1` part and should be kept the same to the settings used for the ground-state calculation. Certain settings may need to be changed between XPS and NEXAFS calculations and mainly include `nextra_bands` and `elnes_nextra_bands`, with the latter not needed in XPS calculations. It might be beneficial to choose a lower number of `nextra_bands` for the XPS calculation as only a small amount is needed whilst for a NEXAFS calculation a much greater number is needed to obtain a full spectrum. A key point at this stage to point out is that for the NEXAFS calculation the number of `nextra_bands` and `elnes_nextra_bands` need to be the same value.

```
#Using core_excition.py read the input file and run XPS and NEXAFS to generate the folder
#and files
cell = read(input_name);
xce = XPS(atoms=cell, element=’C’, pspots=’2|1.4|10|12|13|20:21{1s1,2s2,2p3}(qc=7)’, calc=QM1)
xce.move_hole()

QM1.merge_param(QM2.param) #Merge QM2 with QM1 to overwrite any changes needed in the NEXAFS files
cell = read(input_name);
nce = NEXAFS(atoms=cell, element=’C’, pspots=’2|1.4|10|12|13|20:21{1s1.5,2s2,2p2.5}(qc=7)’, calc=QM1)
nce.move_hole()
```

Listing 3.2: Calculation settings for autoscript.py.

Next is to define the chosen element to include the core-hole. In the `xce` and `nce` variables, the element can be changed to perform different element calculations and `pspot` should correspond to the PP string with either the full core-hole for `xce`, or half core-hole, `nce`, by including the electron configuration in the string with a core-electron moved to a valence state for example in carbon case, `2|1.4|10|12|13|20:21{1s1,2s2,2p3}(qc=7)` for `xce` and for `nce` the same PP string but the electron configuration is `{1s1.5,2s2,2p2.5}`. This valence state electron will then be removed by CASTEP during the calculation through the charge setting laid out in the .param file by applying a total charge on the system of $+1.0\,\mathrm{e}$ or $+0.5\,\mathrm{e}$, for the respective core-hole to fulfil the ΔSCF and TP core-hole constraints.

Once all of the settings have been changed, the code can run to generate two directories named XPS and NEXAFS which will contain a folder for each atom of

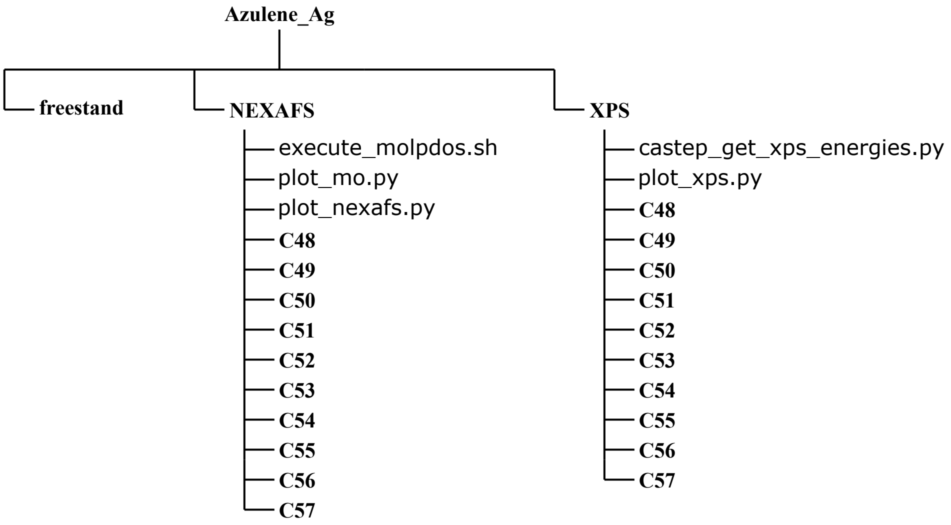
Azulene_Ag
freestand
NEXAFS
execute_molpdos.sh
plot_mo.py
plot_nexafs.py
C48
C49
C50
C51
C52
C53
C54
C55
C56
C57
XPS
castep_get_xps_energies.py
plot_xps.py
C48
C49
C50
C51
C52
C53
C54
C55
C56
C57

Figure 3.1: Tree diagram of how the working directory will look with all sub-directories and location of the scripts. All CASTEP input files are not shown, font style meanings are the same as in the text.

the chosen element labelled by the number it appears in the geometry file and in each will contain both a .cell and .param file, which can then be copied over to the main working directory. Your final working directory should follow the outline shown in figure 3.1

MO Decomposition Files and Running Jobs

As mentioned previously if running versions of CASTEP 19 or below then the settings for the MO decomposition are given in a separate .deltascf file. In the newer versions of CASTEP 20 and above these settings where included in the .param file and written by the autoscript.py script.

The settings that need to be included are shown in listing 3.3 and consist of `deltascf_mode` and `deltascf_iprint` both set to `1` selecting a deltascf calculation. `deltascf_file` which is the reference .check file and this file needs to be copied over into all individual atom directory in **NEXAFS**. Finally, a list of all the MO states to be used for the MO projection given with `modods_state` with the first number the state and the second the spin of the electron. Once all that is done the calculations for each atom in the XPS and NEXAFS directories can be performed.

XPS Processing and Plotting

Once all XPS and NEXAFS calculations are performed, before any post-processing can be done, the XPS binding energies for each individual atom need to be calculated. The two tools used for this are:

- castep_get_xps_energies.py - Calculates the BE shift for each atom using the ΔSCF method
- plot_xps.py - Takes XPS BEs and applies broadening to generate a spectrum

```
deltascf_mode         :  1
deltascf_iprint       :  1
deltascf_file         :  azulene_free.check
# MOLPDOS projection states      <state> <spin>
modos_state         :  17      1
modos_state         :  18      1
modos_state         :  19      1
modos_state         :  20      1
modos_state         :  21      1
modos_state         :  22      1
modos_state         :  23      1
modos_state         :  24      1
modos_state         :  25      1
modos_state         :  26      1
modos_state         :  27      1
modos_state         :  28      1
```

Listing 3.3: Example .deltascf file for Az/Ag(111).

Using the ΔSCF method, the XPS BE is calculated as the total energy difference of two single-point calculations: a ground-state and an excited-state calculation. However, due to the use of a PP method where the core-electrons are frozen out and only the valence electrons are included in the total energy, this is not sufficient enough as the difference between the excited- and ground-states, $\Delta E_{\text{total(valence)}}$ does not fully represent the full picture, as the core electrons are not explicitly modelled. A consequence of this is an error in the BE shifts but as this affects all BEs calculated the relative shifts between each BE remain a valid comparison. A correction term, $\Delta E_{\text{core(atom)}}$, is then needed as a consequence of using a PP method and to calculate the theoretical BE, E_{BE} [110].

$$E_{\text{BE}} = \Delta E_{\text{total(valence)}} + \Delta E_{\text{core(atom)}} \tag{3.2}$$

The correction term, $\Delta E_{\text{core(atom)}}$, only needs to be calculated for the specific element which has the core-hole once for all atoms in the system and is generated solely from the isolated atom calculation when the PPs are created and is calculated by:

$$\Delta E_{\text{core(atom)}} = \Delta E_{\text{All orbitals(atom)}} - \Delta E_{\text{valence(atom)}} \tag{3.3}$$

$\Delta E_{\text{core(atom)}}$ is the energy difference between the total atomic energy of the excited-state and ground-state of the chosen atom with $\Delta E_{\text{valence(atom)}}$ the valence energy contributions to the total atomic energy of each atom. The valence energy contribution is subtracted here because they have already been included in the previous equation 3.2, in $\Delta E_{\text{total(valence)}}$ and are not required again. The XPS binding energies for each individual atom can be calculated by using (3.2) and (3.3). First, the correction term can be calculated once to be used for all other atoms and then used in (3.2) for the BEs of each atom.

The settings need to be set in the castep_get_xps_energies.py script and are in listing 3.4. These are `element`, which is the chosen element which the core-hole is located on, carbon in this case so is `C`. The two settings of `num_start` and `num_end` are used to give the range of the atoms files as shown in figure 3.1, with the first and lowest number given in `num_start` and last and largest in `num_end`. Finally,

```
#Set the element, the numbers of the XPS directories and the seedname of
#the castep calculations
element = ’C’
num_start = 48
num_end = 57
filename = ’azulene_Ag.castep’
#Set the range of atom numbers
```

Listing 3.4: Settings to be changed at the top of castep_get_xps_energies.py.

```
###################################
xstart = 285.
xstop = 305.
broad1 = 0.7
broad2 = 0.7
firstpeak = 285.0
ewid1 = firstpeak+1.0
ewid2 = firstpeak+2.0
mix1 = 0.3
mix2 = 0.3
########################################

#Set what element you have calculated XPS for
element = 'C'
```

Listing 3.5: Designation of the broadening parameters for pseudo-Voigt broadening and selection of element in plot_xps.py.

`filename` corresponds to the name that all the output files are called and is given in the *molecule_metal* convention.

The next step is to run the castep_get_xps_energies.py script to read all the data needed and calculate the BEs. The script first reads the data needed to calculate the correction term once using the first atom in the list. Then it will read the total energies of the ground-state and individual atom excited states and generate a text file called C_XPS_peaks.txt with all the XPS BEs for each carbon atom.

Once carried out, to obtain a broadened XPS spectrum, the plot_xps.py script is used to summed up all of the contributions and apply a pseudo-Voigt function [111, 112] described in section 3.3.1. The section where the broadening parameters are given in shown in listing 3.5. The energy range to apply the broadening to is given by `xstart` and `xstop`. Multiple broadening ranges can be given but for an XPS simulation these are kept the same with `broad1` and `broad2` corresponding to the full width at half maximum (FWHM) value. The `ewid` value specifies when the broadening ranges start in relation to the `firstpeak` value and are redundant in this case and the `mix` values are the Gaussian/Lorentzian (G/L) ratio. Finally, the `element` setting should be set to the correct element.

NEXAFS Post-Processing and MolPDOS

Once all the calculations are finished, the post processing using the MolPDOS binary that is packaged as part of CASTEP tools can be used. For this a .molpdos file will be used as an input for all the settings with the example used shown in listing 3.6. This file again should follow the same naming convention and be called the same as all the other CASTEP input files. In the file, a variety of settings are defined to allow for NEXAFS and MO projection processing to be performed, these are:

- `nexafs_theta` - Settings to simulate the theoretical x-ray incidence angle you want to calculate for, as shown in figure 2.4. Will be set by the execute_molpdos.sh script.

- `nexafs_phi` - Settings to simulate the theoretical x-ray incidence angle you want to calculate for, as shown in figure 2.4.
- `nexafs_xshift` - The XPS BE of the individual atom to be used to align the energy transitions. Set by the execute_molpdos.sh script.
- `nexafs_state` - Which atomic species you want to calculate for, you will only need to change the first number. The four numbers correspond to:
  1. *element* - The index value of the element where the core-hole is included (as you create a new species for this `C:exc`, this will always be the last element)
  2. *ion* - The index value in the list of the above chosen element (only ever 1 core-hole species so will be 1).
  3. *n* - The principle quantum number of the core-hole.
  4. l_m - The angular momentum quantum number of the core-hole (will start from 1).
- `modos_state` - Setting the corresponding states to the same orbitals range selected previously.
- `axis_energy_start` & `axis_energy_stop` - Energy range for the outputted density of states.

To use the `execute_molpdos.sh` script the MolPDOS binary from the CASTEP tools needs to be compiled and the executable needs to be located somewhere else but stored into the $PATH. The script will run the MolPDOS binary for all atoms in the **NEXAFS** directory. The settings for the atom numbers and the chosen ϑ and φ values should be placed as arrays at the top, followed by the `molecule`, `metal` and `element`. The script works by first locating the C_XPS_peaks.txt file of the BEs and automatically changes the `nexafs_xshift` value to the first BE and run the MolPDOS binary for all the selected angles changing the value in-between. It will create a directory in the corresponding atom file (first BE will be **C48** in this example), for each angle given. For an angle of 25° the directory will be **t25** and will place all the outputted files in the correct directory. The script works through each atom, changing the `nexafs_shift` value for each corresponding atom and will print out the progress as it goes along.

Summation and Broadening of the NEXAFS Spectra

The final step is to take all of the data produced from the MolPDOS post-processing and to sum all the data from each individual atom contribution and apply an over-

```
d#o_#fermi_shift
#d#o_lorentzian
molpdos_bin_width    :  0.01
molpdos_smearing     :  0.1
modos_state        :  28     1
modos_state        :  27     1
modos_state        :  26     1
modos_state        :  25     1
modos_state        :  24     1
modos_state        :  23     1
modos_state        :  22     1
modos_state        :  21     1
modos_state        :  20     1
modos_state        :  19     1
modos_state        :  18     1
modos_state        :  17     1
#m#olpdos_scaling      :  0.50
axis_energy_start    :  -10.00
axis_energy_stop     :   20.00
nexafs_smear2        :  0.20
nexafs_ewid          :  5.0         15.0
nexafs_theta         :   90.0
nexafs_phi           :   60.0
nexafs_xshift        :  290.3961461999743
#n#exafs_yscale        :  100.0
nexafs_state         :  4   1     1     1
calculate_deltas
sh#ow#_all_states
```

Listing 3.6: Example .molpdos file used for Az/Ag(111).

all broadening to create the final NEXAFS spectra and project out the MO state contributions of the NEXAFS. In order to perform this, two scripts are needed:

- plot_nexafs.py
- plot_mo.py

These scripts are placed in the NEXAFS directory and various settings are changed to match the system calculated. These are summed up into the broadening parameters and system parameters. The broadening parameters to state are the same as the ones for the XPS but make use of the `ewid` settings to create two broadening ranges and connecting the two with a linear scale. `firstpeak` is set to the position of the leading edge on the spectra, the `ewid1` defines the end of the first broadening range by taking the `firstpeak` value and adding a value on, usually 5 and `ewid2` defines the start of the third broadening range referenced from the `firstpeak` again. The G/L ratio for the ranges are given as a decimal in `mix1` and `mix2`.

For the system parameters these start with the types of NEXAFS spectra to be calculated. These were described in section 2.3.2 with there being four total options. `1` is for a total NEXAFS spectra where the spectra for all angles are summed up together (2.28) (will produce the same spectra no matter which data you give). 2 for angular resolved spectra with no polarisation, `3` gives a polarised spectra according to the two angles provided (2.30) and `4` gives and averages the contribution with respect to the φ angle and only depends on ϑ (2.31). Next is `angles` in the form of the names of the directories where each angle data is kept so in this case is `'t25','t53','t90'`. `molecule`, `metal`, `elem`, `num_start` and `num_end` are the same as been previously given in other scripts and the final setting of `atom` is the element number in the whole calculation, which is the first number in the `nexafs_state` setting in the .molpdos file. These settings are both present in plot_nexafs.py and plot_mo.py with only two extra settings in the latter, `MO_start` and `MO_end` for the first and last numbers of the MO orbital range.

Running the plot_nexafs.py script will result in two files for each angle. These will be a deltas.txt file with the energy transitions as points with an energy shift value and an intensity. The second file will be the spectra after applying the pseudo-Voigt broadening parameters that were given. If `atom_contribute` is set to `True` then the script will generate the two files for each individual atoms contribution to the total NEXAFS spectrum. The same two types of files will be created using `plot_mo.py` and these will be for each MO orbitals at each angle given.

A summary of the whole process outlining the steps taken in order to simulate XPS and NEXAFS spectra is detailed in figure 3.2. An initial ground-state calculation (3.2 (a)) is carried out followed by N ΔSCF calculations (3.2 (b)) which can by used to obtain an XP spectrum. The NEXAFS transitions can be calculated with a TP calculation (3.2 (c)). The calculated BEs are then used to align the TP-eigenvalue spectra from the different atomic species onto a single energy axis, followed up by summing all contributions into a NEXAFS spectrum 3.2.

3.3 Computational Details

3.3.1 General Details for Core-Level Spectroscopy

DFT calculations have been performed with two different electronic software codes. These two were the PP PW code CASTEP [102] and the all-electron atomic orbital code FHI-aims [105]. XPS and NEXAFS spectra were simulated using the ΔSCF [60–62, 113] and ΔIP-TP [76, 77] methods and with CASTEP calculations following the methodology laid out in section 3.2 and depicted in figure 3.2.

ΔSCF calculations preformed with the FHI-aims code were carried out utilising two different approaches to localise the core-hole onto a chosen atom with either the *force_occupation_basis* (FOB) or *force_occupation_projector* (FOP) keywords that have been implemented by Matthias Gramzow (Fritz-Haber-Institute of the Max Plank Society, Berlin). Each keyword can enforce a constraint onto with a specific basis set for FOB or onto a particular KS state for FOP. For example, the settings would be written as `force_occupation_basis 1 1 atomic 1 0 0 0.0 10` and

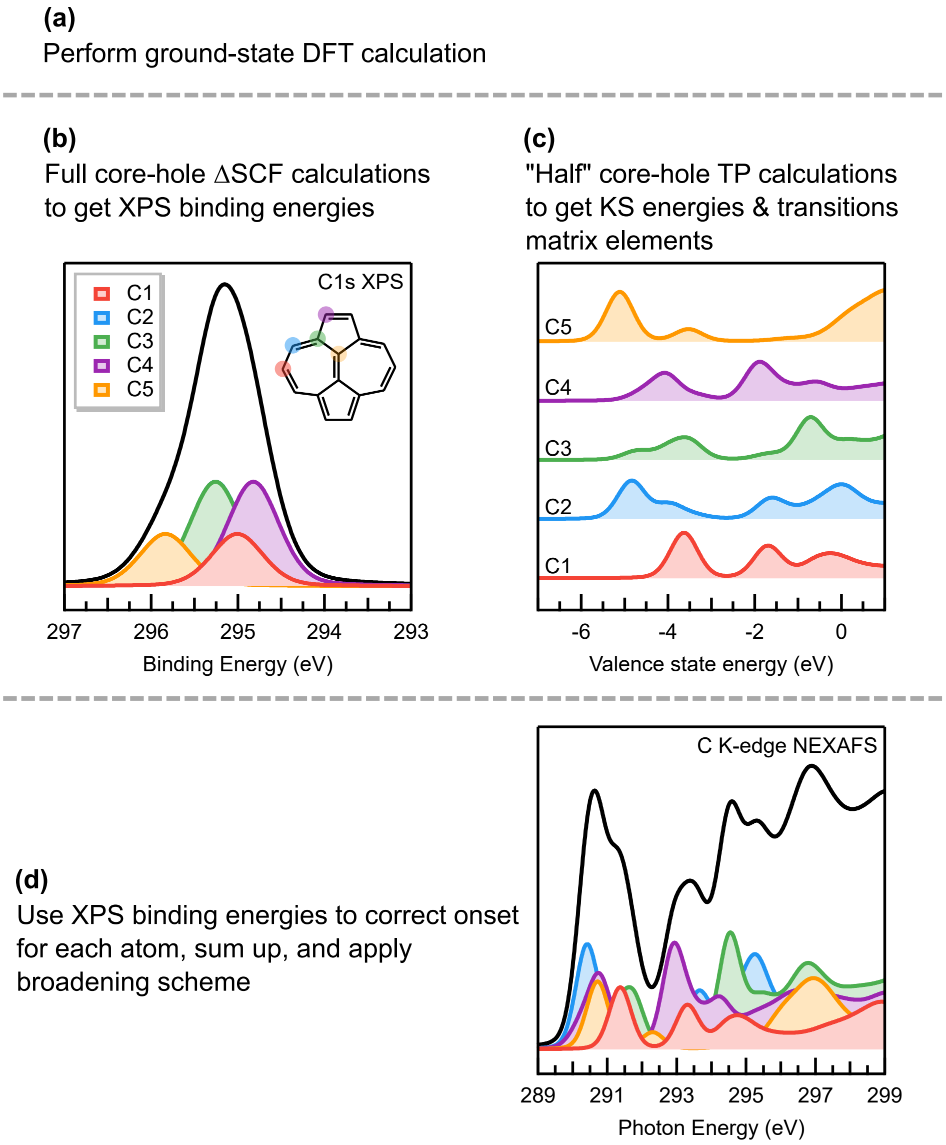

Figure 3.2: Computational workflow to generate a K-shell NEXAFS spectrum with the ΔIP-TP approach for a example molecule of azupyrene. (a) Ground state DFT calculation. (b) N full core-hole ΔSCF calculations to establish the chemical shifts of each atomic species. (c) N half core-hole TP calculations to obtain the absorption spectra for each species. (d) Each atomic species is shifted according to its ΔSCF BE and finally all atomic contributions are summed up and a broadening scheme is applied.

`force_occupation_projector 1 1 0.0 1 10`. For the basis keyword, the values given represent the *atom* number, *spin*, *basis type*, *principle quantum number*, *angular momentum*, *magnetic*, *occupation* and *maximum KS state to be included*. The settings for the projector case are *KS state to constrain*, *spin*, *occupation*, *lowest KS state* and *highest KS state* for the MOM (maximum overlap method) to check whether it has moved during the SCF cycle.

These two methods can be used to apply an occupation constraint on KS eigenstates and use variants of the MOM to keep the constraint satisfied [65] and yield numerically identical results if successful. The MOM method prevents variational collapse by maintaining the occupancy of the constrained core-orbital throughout the self-consistent-field (SCF) cycle by identifying the overlap between the old (previous step) orbitals and the new (current step) orbitals and keeps the constraint with the orbital with the most *span* of the old orbital [65].

The FOP keyword works by defining the occupation constraint directly onto the KS eigenstate. The core-hole can move with the eigenstate if the order changes throughout the SCF steps and follows the maximum overlap of the constrained state in the previous SCF step. The FOB keyword applies the constraint differently with the core-hole constrained in terms of a localised atomic orbital basis function, enforcing the constraint on the KS eigenstate of the highest contribution from the core-atomic orbital. This constraint will follow the highest contribution from the atomic orbital through the SCF steps to ensure the correct atom and population is constrained. Additional core-augmentation basis functions were added onto the core-excited atom to better represent the core-hole as set out by Kahk and Lischner [114]. These approaches fair well for cases with localised core-states but can become troublesome when dealing with more delocalised core-states. FOP calculations were implemented using the method proposed by Kahk and Lischner [114], which involves breaking the symmetry of the molecule with an initial calculation where an additional 0.1 electron charge is added onto the chosen atom. This helps separate the selected atom from equivalent atoms by changing the energy level and helping the constraint localise onto the correct choice. The calculation is then only allowed to run for one SCF step and the core-hole calculation is then restarted but with the extra core-charge removed and the full core-hole constrained.

Calculations in CASTEP were performed using the ΔSCF and ΔIP-TP methods used in the simulations of XPS and NEXAFS respectively and described in section 3.2 and in figure 3.2. CASTEP versions 18.1 and 19.11 were used throughout with the same PP definitions employed in both software version. Calculations were performed in PBCs with on-the-fly generated PPs.

For XPS calculations the core-electron BE was calculated from the difference in total energy of two singlepoint calculations, one being the ground-state configuration and the second a core-hole excited configuration, by removing one electron from the 1s orbital. This was carried by modifying the PP definition of the chosen excited atom to include a full core-hole [110, 115]. To correct for the use of PPs which do not fully model the core-electrons a correction term is added to the difference in total energies [110]. This was performed for each atom in the molecule for a full XPS spectrum.

Simulations of the NEXAFS spectra were performed with the ΔIP-TP method. The TP approach was used to calculate all the transition energies from the 1s state to all possible unoccupied states in one single calculation. The PP was modified to include a half core-hole on the chosen excited atom. The ELNES module [110,

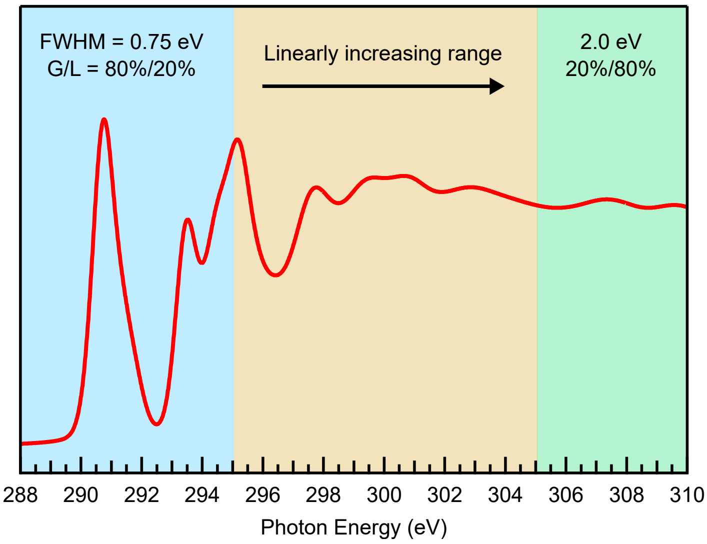

Figure 3.3: A NEXAFS spectrum showing the three broadening ranges applied across the spectrum. The first and last ranges are given specific values for the full width at half maximum (FWHM) and a Gaussian/Lorentzian (G/L) ratio with the middle range connecting these two values through a linear scale.

116, 117] in CASTEP was used to simulate NEXAFS energies and transition dipole moments. This module performs a total energy SCF calculation followed by a band structure calculation in order to converge the unoccupied states. The ionisation potential correction aligns all individual core-level spectra to the same energy frame by using the corresponding BE for each atom.

Finally, a pseudo-Voigt broadening scheme [111, 112] was used in order to resemble experimental spectra. Spectra were broadened with parameters chosen that were a typical reflection of experimental resolutions. XPS consisted of a full width at half maximum (FWHM) of 0.7 eV and a G/L ratio of 70 %/30 %. NEXAFS spectra were generated using the same pseudo-Voigt scheme but due to the different life-times of excited states below and above the ionisation potential the spectra is divided into three separate ranges. The first range of 5 eV from the leading edge, has a FWHM of 0.75 eV and a 80 %/20 % G/L ratio. At 15 eV above the leading edge the third range consists of FHWM of 2.0 eV and 20 %/80 %. In-between connecting these two ranges is an intermediate range where the FWHM and G/L ratio linearly increases from the first to the third. Figure 3.3 breaks down the typical broadening ranges for NEXAFS spectrum.

The resulting energies of the simulated spectra can often disagree with the experimentally recorded spectra. This can be due to various different inherent aspects of the calculations. These can range from the use of pseudopotentials, the type of basis set, PBCs, relativistic effects and well-known errors of DFT such as the self-interaction error. Comparison between simulated spectra can be carried out by shifting the spectra to a zero value by subtracting the mean average weight across the whole spectra. For comparison with experimental results the whole spectrum is shifted by a single value to align it to the experiment as best as possible.

3.3.2 Details for this Chapter

XPS calculations in this chapter were performed using FHI-aims and CASTEP. Calculations in FHI-aims were performed with a range of XC functionals including PBE, [53] PW91, [118] TPSS, [119] SCAN, [120] PBE0, [121] B3LYP, [122] HSE06, [123] and xDH-PBE0 [124]. Electronic convergence settings were set to 1×10^{-4} e/Å^3 for the electron density, 1×10^{-2} eV for the KS eigenvalues and 1×10^{-6} eV for the total energy. Relativistic effects were taken into account by employing the atomic ZORA functionality [105]. Higher order relativistic effects such as spin-orbit coupling could be neglected for the K-shell excitations and binding energies.

CASTEP calculations were performed with the PBE functional, [53] PW91, [118] and BLYP [125, 126]. The total energy per atom convergence of at least 1×10^{-6} eV/atom was used. All gas-phase calculation were performed with a $1 \times 1 \times 1$ k-grid in a cubic supercell with dimensions of 20 Å in all directions. The input and output files for the data presented in section 3.4 have been previously deposited in the NOMAD repository and are freely available online (DOI: https://dx.doi.org/10.17172/NOMAD/2020.10.15-1).

3.4 Performance of Core-Level Spectroscopy Simulations

The following section will discuss calculations carried out on a small set of typical systems to exemplify the technical and numerical aspects of x-ray photoelectron and absorption spectra. The test set of systems include gas-phase molecules of azupyrene and ethyl trifluoroacetate (ETFA). These were chosen as the represent the two extreme ends of chemical behaviours. The ETFA molecule shows strong chemical shifts in its carbon 1s binding energies and has been an important reference system since the dawn of photoelectron spectroscopy [127–129]. Azupyrene on the other hand is a polycyclic aromatic hydrocarbon, represents a system with a large number of equivalent carbon atoms due to its high symmetry. These different systems are chosen to test the versatility of the method to calculate core-level spectra. Further systems of azulene adsorbed onto a Cu(111) surface and azulene in the gas-phase, bulk crystal and adsorbed onto a Cu(111) surface [79] were tested.

3.4.1 Practical Considerations of Calculations in Atomic Orbital Basis

Core-Hole Localisation

XPS binding energies can be simply extracted from ground-state DFT calculations by use of Koopmans' theorem (2.19) by using the negative KS orbital energy values for each orbital. However, this method carries problems as it neglects relaxation effects due to core-hole screening but also creates errors due to delocalised KS-states. This problem is most prevalent when dealing with highly symmetric molecules e.g azupyrene with symmetry point group D_{2h}. For symmetrically equivalent atoms in such molecules, the KS-states are linear combinations of the atomic core-states shown in figure 3.4. This can cause issues when equivalent atoms are energetically close together and causes appreciable overlap where the energy of the bonding contribution of the core-states is lowered while the energy of the anti-bonding combination is raised. This leads to two different binding energies between the two equivalent atoms depicted in figure 3.4 (a).

The problem with delocalised KS-states as present in FHI-aims can also extend to ΔSCF calculations where core-hole screening effects are taken into account. This can happen when the occupation of a core-level is changed to include the core-hole needed for the ΔSCF calculation. This is done when using the FOP keyword by removing an electron from a KS-state. The core-hole may become unphysical by distributing

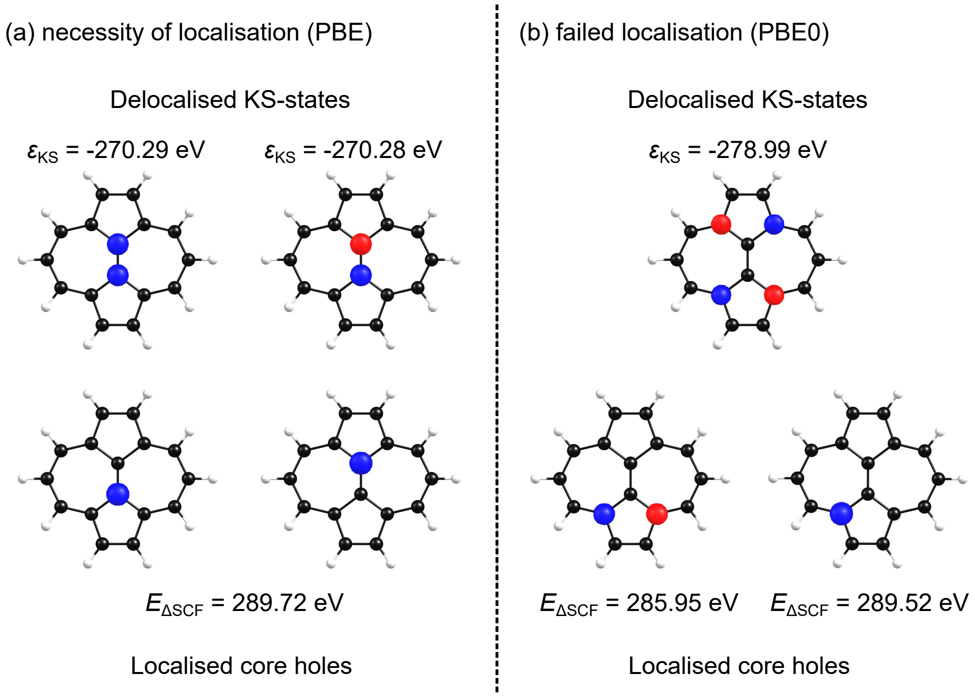
(a) necessity of localisation (PBE)
Delocalised KS-states
ε_{KS} = -270.29 eV
ε_{KS} = -270.28 eV
$E_{\Delta SCF}$ = 289.72 eV
Localised core holes
(b) failed localisation (PBE0)
Delocalised KS-states
ε_{KS} = -278.99 eV
$E_{\Delta SCF}$ = 285.95 eV
$E_{\Delta SCF}$ = 289.52 eV
Localised core holes

Figure 3.4: Examples of core-hole localisation problems in FHI-aims demonstrated on azupyrene. (a) The KS states for the C1s orbitals in the centre of the molecule are delocalised, resulting in two KS energies both spread across both atoms (upper part). When correctly localised, the orbital is located on a single atom and both carbon atoms yield the same energy (lower part). (b) For hybrid functionals (PBE0) the core-hole localisation, if not strictly enforced, often fails. In this example, the localisation work for one case resulting in a properly localised on on atom with BE of 289.52 eV, yet failed for the second case with the core-sate still delocalised over the two carbon atoms with unusually low BE of 285.95 eV. The iso-values for all states shown is 0.1.

over multiple atoms and the corresponding BE valued between the KS-states and the properly localised core-holes shown in figure 3.4 (b).

There are methods to ensure proper localisation of the core-hole in calculations of the ionised states for the ΔSCF approach. This includes breaking the symmetry of the electronic wave function of the system. When dealing with PP codes, this is done automatically as the chosen atom has a PP with a built-in core-hole and instantly breaks the symmetry and localises the core-hole [115]. This is also the case with with frozen-core calculations, where the ionic occupation for the core-orbitals is frozen out with a core-hole localised at the desired atom [59].

All-electron codes can prove to be more difficult in this respect to solve. Kahk and Lischner [114, 130] have proposed an approach to break the symmetry of the wave function by introducing an intermediary step where a slightly increased nuclear charge is added onto the chosen atom. This breaks the symmetry of the wave function and is used as a starting point for the core-hole calculation, which is all implemented in the FHI-aims code with the core-hole constraint carried out with the FOP keyword [114, 130]. Alternatively, localisation can be achieved by using the FOB keyword, here the occupation constraint on the KS-state is defined by its overlap with a 1s atomic orbital basis function localised at the relevant atom. Using this approach, the symmetry is automatically broken in most cases during the self-consistent core-hole calculation.

These two approaches were carried out on the systems used in this work and both methods were found to yield numerically identical results as long as the core-hole localisation was successful. Out of the two approaches the FOB approach tended to be more stable with regard to the electronic convergence and preferred due to not requiring an extra symmetry breaking initialisation step. However, the FOB approach did not work for azupyrene when used with hybrid functionals where problems with localising the core-hole remained (figure 3.4 (b)). This problem was able to be overcome by using the Boys localisation [131] as proposed in the literature [69] to first break the symmetry, which proved to be successful for all molecules and XC functionals.

It appears that hybrid functionals, contrary to GGA and meta-GGA functionals, suffer much more from variational collapse during ΔSCF calculations and require a constraint that explicitly breaks symmetry to ensure core-hole localisation. An additional way for solving this problem would be the use of a modified version of the ΔSCF method, such as the local SCF method [132, 133] or the linear-expansion ΔSCF [104] approach. Additionally, one of the tested meta-GGA functionals (SCAN) showed unphysical behaviour with great differences in the valence spin channels caused by the core-hole. For all other functionals the overall spin density is determined by the core-hole, showing a localised difference in the core-state spin channels on the excited atom, while the valence spin states only show minute differences yielding a vanishing spin density at the other atoms. But for SCAN the wave functions of the valence spin channels differ by a lot, leading to a larger difference in the up and down electron densities and therefore the spin-density distributed over the whole molecule. This finding is consistent with the known "over-magnetisation" of SCAN reported in the literature [134]. For the unsymmetrical molecule ETFA (symmetry point group C_1 in the chosen rotational conformation), the localisation poses less of a problem. Here, both tested meta-GGA functionals (SCAN and TPSS) failed when using the FOB approach for some atoms, but results could be obtained using the FOP approach.

Exchange Correlation Functional

An investigation into the influence of the XC functional on the C1s XPS binding energies was performed using two gas-phase molecules of ETFA and azupyrene. These molecules were chosen as they represent two opposing ends of challenges when calculating XPS binding energies. For ETFA (figure 3.5 (a)), this is the calculation of carbon atoms with extreme chemical shifts thanks to the various environments across the four carbon atoms. This has lead to this molecule becoming a commonly used molecule for XPS measurements [127–129]. On the other end is azupyrene (figure 3.2 (b)), which posses carbon atoms with similar environments and such differences between chemical shifts will be smaller but still noticeable. Both the absolute and relative C1s XPS binding energies of these two molecules will be tested against a range of eight functionals of different types. These include the GGAs PBE and PW91, meta-GGAs SCAN and TPSS, hybrid functionals PBE0, B3LYP and HSE06 and finally a double hybrid functional of xDH-PBE0. These functionals were tested using the all-electron FHI-aims code and performed with a "tight-tier2" core-augmented basis set.

The C1s XPS binding energies of the ETFA molecule span a chemical shift range of 8 eV which produce four clearly separated peaks seen in typical XPS experiments with high quality experimental reference data on the gas-phase ETFA molecule available in the literature [128, 129]. The simulated XPS spectra for ETFA with the various XC functionals is compared to experimental data in figure 3.5 (a) where the spectra have been plotted on an absolute BE axis. The values of all the binding energies shown are compiled in the appendix in table B.1.

Assessing the performance of the XC functionals in comparison with the absolute binding energies is not straightforward to extract. This can be helped by plotting the relative shifts of the four peaks with respect to the C4, the lowest BE peak seen in figure 3.5 (b), and tabulated in table B.2. Using this the performance of the functionals from three different groups: (1) PBE, PW91, and TPSS where the average deviation to the experimental data is 0.74, 0.72, 0.73 eV, respectively; (2) SCAN with 0.53 eV; and (3) PBE0, HSE06, B3LYP and xDH-PBE0 with deviations of 0.45, 0.46, 0.46, 0.45 eV, respectively. This data shows that the best performing functionals are the hybrid functionals, next is the meta-GGA of SCAN and worst are the meta-GGA TPSS and the GGA functionals.

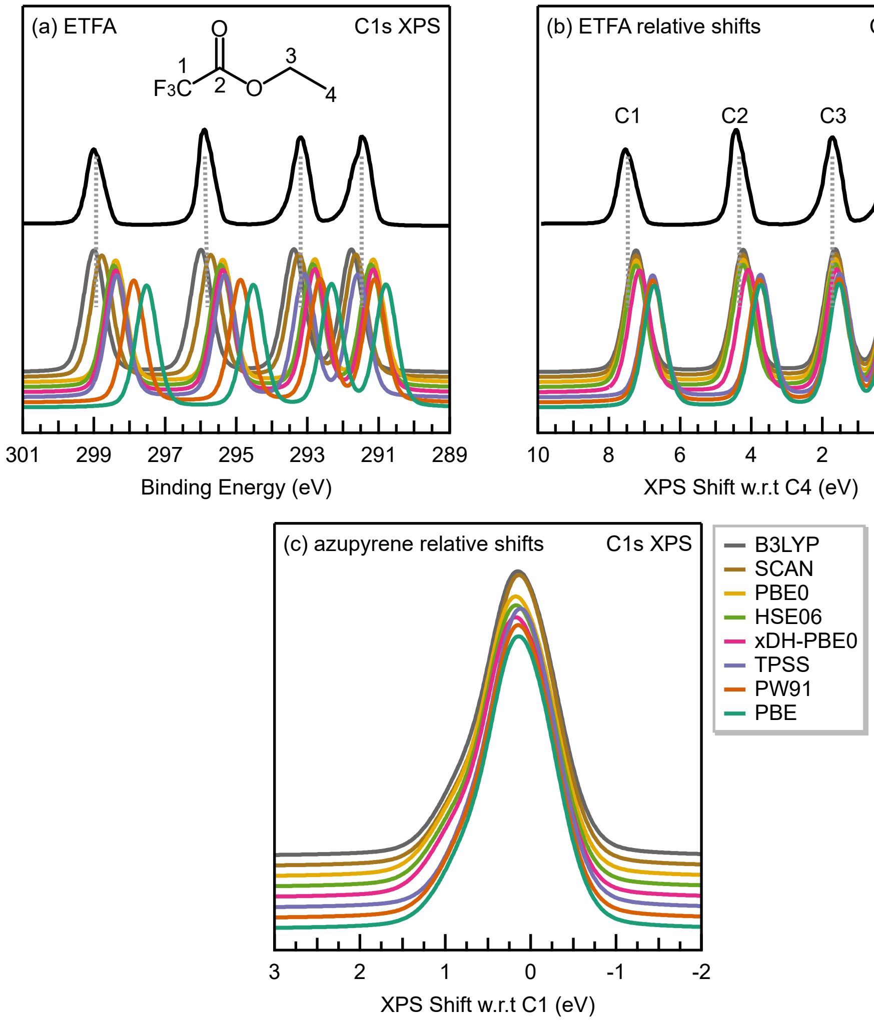

Figure 3.5: Comparison of the C1s XP spectra of ETFA and azupyrene calculated with different XC functionals. (a) shows the spectrum of ETFA on the absolute BE scale with respect to the vacuum level whilst (b) is presented relative scale with atom C4 placed at 0 eV. The upper part of the spectrum shows the experimental data from [129] with lower part showing the various calculated spectra along with lines to help align the peaks between. (c) XP spectrum of azupyrene on a relative binding scale with respect to the mean weighted average for all XC functionals. Legend is valid for all panels in the figure.

When discussing the performance on the absolute BE scale, things are more complex. Due to an additional global displacement of all calculated energies, the average deviation in the absolute binding energies would seem to be smallest for B3LYP and SCAN. But according to the relative shifts, the case can be made that all functionals have similar problems describing the binding energies of the carbon atoms with extreme BE shifts. In fact, the functionals PW91, PBE0, HSE06 and xD-PBE0 have an excellent agreement with the absolute BE of carbon C4, which possesses the lowest BE. Following this argument, the best performance for the absolute binding energies is provided by the hybrid functionals PBE0, HSE06 and xD-PBE0 with an

Table 3.1: Relative shifts of the carbon 1s binding energies of the azupyrene molecule in dependence of the XC functional, calculated using the ΔSCF approach in FHI-aims. All shifts are in eV and with respect to the BE of C1.

Carbon	PBE	PW91	TPSS	SCAN	HSE06	PBE0	B3LYP	xDH-PBE0
C1	0.00	0.00	0.00	0.00	0.00	0.00	0.00	0.00
C2	0.25	0.25	0.25	0.26	0.31	0.32	0.31	0.32
C3	0.25	0.25	0.19	0.23	0.26	0.26	0.22	0.26
C4	−0.18	−0.19	−0.18	−0.19	−0.19	−0.19	−0.20	−0.19
C5	0.82	0.82	0.77	0.86	0.90	0.91	0.85	0.91

average deviation of 0.50, 0.46, 0.50 eV and the GGA PW91 with the deviation of 0.81 eV.

By comparing absolute and relative deviations, it is obvious that the main error in these calculations is not only in the absolute energies, but already in the relative energies. Generally, the hybrid functionals perform slightly better than the meta-GGAs and GGAs but their results are still quite poor compared to experimental data. Apparently all functionals have problems calculating high binding energies in cases where the core-state is extremely descreened, e.g. for the carbon atom C1 in the CF_3 group of ETFA. For carbon atoms in more common chemical environments, e.g. C4 in ETFA, all functionals perform satisfactorily, i.e. yielding a deviation below or around 0.5 eV. It should also be noted that the use of the double hybrid functional xD-PBE0 brings no improvement relative to the regular hybrids. The better performance of hybrid functionals for K-shell XPS energies was also reported in the literature, [135] while other studies found a better performance of regular GGAs [136]. However, many test sets to judge the performance of BE calculations include only molecules with more moderate shifts [76, 135–137].

To further test the performance of the XC functionals for less extreme chemical shifts, we turn to the molecule azupyrene, which is an aromatic hydrocarbon without any hetero-atoms. The chemical shifts exhibited by its carbon atoms are therefore more subtle and only caused by its non-alternant topology, similar to the azulene molecule already discussed in the literature [79]. To compare the performance of the functionals with regard to these more subtle shifts, only relative differences in the binding energies are analysed. These relative shifts with respect to carbon C1 (figure 3.2) are compared in table 3.1 for the different XC functionals. For reference, the absolute binding energies can be found in table B.3.

Within each class of functional used, GGA, meta-GGA and hybrid, the values obtained for the relative XPS shifts are similar with maximal deviations of 0.06 eV within the hybrids and 0.09 eV in the meta-GGAs. As a caveat, the meta-GGA SCAN showed problems with the response of the valence electron states to the core-holes and produced an unphysical spin density. However, the C1s shifts are still in line with the other functionals. It should be noted that the simple approach using Koopmans' theorem (2.19) also gives similar relative shifts in the binding energies (table B.4 in the appendix). This indicates that for the azupyrene molecule the shifts are mainly determined by the chemical environment of the initial-state. The relaxation of the core-hole is very similar for all chemical species.

Figure 3.5 (c) shows the XPS spectrum of azupyrene obtained by applying the same pseudo-Voigt broadening as used in figure 3.5 (a) to all relative binding energies in table 3.1. When the results obtained with the different functionals are thereby compared against the backdrop of a typical experimental resolution, they provide almost indistinguishable results. For this reason, we chose the functional PBE for all subsequent calculations as this suitable balances the computational cost of calculations, which greatly increases when moving from GGAs to meta-GGAs to hybrid functionals, with reliable accuracy.

3.4.2 Practical Considerations of Calculations in Planewave Pseudopotential Basis

An important numerical choice to take into consideration when carrying out XPS and NEXAFS simulations is the type and size of basis set that is used for the calculations. For atomic orbital basis sets, the importance of core-augmented functions has been extensively discussed in literature [65, 114, 138, 139]. In such codes as the all-electron code FHI-aims, convergence has been shown to be very fast and detailed in the appendix, where the standard 'tight' settings definitions offer already converged results. The benefit of using a PP PW formalism is that the issues of core-hole localisation seen in all-electron methods as described in section 3.4.1, is eliminated as the core-hole excited PP accounts for the core-excitation only on the chosen atom. However, this introduces other challenges. For example, the frozen-core described by the PP does not relax and therefore absolute binding energies are typically much worse than all-electron descriptions. Similarly, as the core-states are not explicitly treated, the core-level wavefunctions needs to be rebuilt to enable the calculation of transition dipole moments between core and valence states in NEXAFS [115].

Different types of PPs exist varying in their degree of "hardness", i.e. the number of states that are pseudoised and the constraints that are placed on the core-region [140]. Examples include non-local norm-conserving PPs [141] and ultra-soft PPs [142]. The latter require much lower energy cut-offs and fewer PWs to accurately represent observables which they achieve by lifting the constraint of charge conservation in the core-region such that the wave functions satisfy the generalised orthonormality condition. XPS and NEXAFS spectra were calculated with three different PPs for the example molecule azupyrene. Those three are based on the default settings of on-the-fly generated PPs in CASTEP and only differ in the type of projector, namely they use (for each angular momentum channel): (1) a norm-conserving projector, (2) a single ultra-soft projector, or (3) two ultra-soft projectors. All other parameters

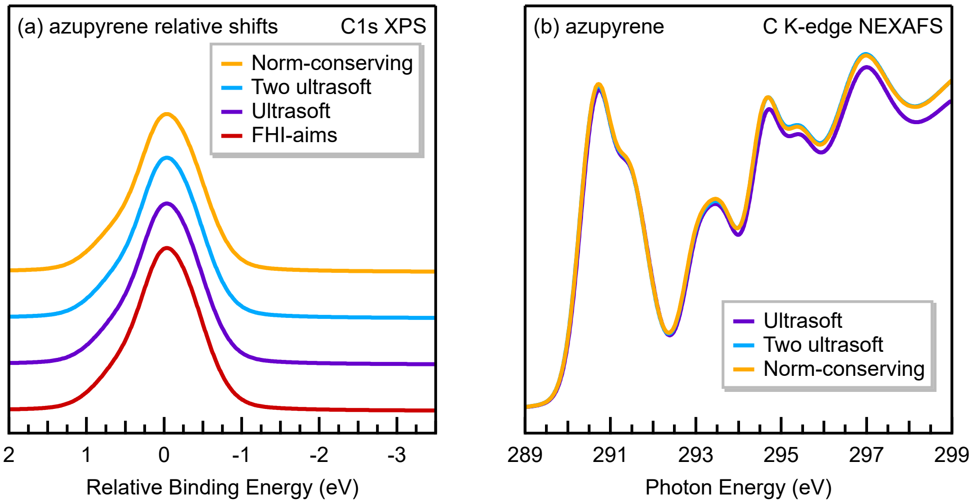

Figure 3.6: Comparison of the XPS spectra of gas-phase azupyrene (a), plotted as the weighted average, obtained when using three different on-the-fly generated pseudopotential projectors: purple, ultra-soft projectors; blue, two ultra-soft projectors per angular momentum channel; orange, norm-conserving projectors and FHI-aims FOB spectra in red. (b) shows total NEXAFS spectra of all three different pseudopotentials.

that define the PP were left unchanged from the defaults. This is implemented by altering a small portion of the PP string by adding for the case of carbon 20N:21N for norm-conserving and for ultra-soft changing the Ns for ultra-soft and 2 ultra-soft to U and UU, respectively.

XPS converged spectra of all three PP definitions were obtained. Convergence behaviour of all three definitions are shown in the appendix in figure B.2, where it can be seen that even though the absolute XPS BEs have not reached a fully converged value the relative shifts between the chemically in-equivalent carbon atoms show little change from a cut-off value of 450 eV upwards. The broadened XPS spectra are visualised in figure 3.6 (a) along with the spectra calculated using the all-electron code FHI-aims with the relative peak positions of the chemically in-equivalent species presented in table 3.2. The peak shape in all spectra are almost identical between the different types of projector and all-electron method.

The NEXAFS spectra were also simulated using the three different PP projectors and are plotted in figure 3.6 (b). For all three spectra the same XPS shift offset for each case was implemented to highlight only changes with the NEXAFS simulations themselves. As with the XPS spectra, there is little to distinguish between the three projectors, providing almost identical spectra in the lower excitation energies with only easily visible difference seen in higher energies. This shows that the main features of core-level spectra are robust with respect to the type of PP projection functions used. Moving forward from this point on-wards all calculations utilise the ultra-soft PP with two projectors per angular momentum as is the default setting in CASTEP.

Table 3.2: Absolute XPS binding energies for azupyrene calculated in FHI-aims with the FOB approach and with CASTEP utilising three different pseudopotential projectors. All calculations were performed with the PBE functional, [53] all energies are in eV.

Carbon	FHI-aims	Ultra-soft	Two Ultra-soft	Norm-conserving
C1	288.90	295.02	294.97	294.94
C2	289.14	295.28	295.22	295.19
C3	289.15	295.30	295.24	295.24
C4	288.71	294.84	294.78	294.76
C5	289.72	295.87	295.81	295.82

Periodic Boundary Conditions and Box Size Convergence

For calculations using a PW PP basis set, it is required for the calculations to be performed in PBCs. This introduces problems for core-hole simulations that can lead to possible errors in calculating XPS BEs. These errors are a consequence of finite size effects. These arise from when the unit cell is too small and core-holes in repeating periodic images are close enough to start interacting with one another. Another problem can be the addition of the core-hole introducing a positive charge onto the unit cell. ΔSCF calculations introduce a net charge of $+1$ e whilst TP calculations involve a half core-hole and charge of $+0.5$ e. These charges need to be compensated due to the need for the unit cell to be charge neutral otherwise the electrostatic potential would diverge. To prevent this problem a uniform negative background charge is applied over the whole unit cell. This is a fail-safe mechanism of an Ewald summation rather than an artefact, although it does introduce erroneous physics, such as a strong dependence of the total energy on the size of the unit cell.

To simulate the XPS for a gas-phase structure, the molecule is placed in a large cubic vacuum box. The convergence of the XPS BEs of both ETFA and azupyrene as a function of the size of this box is shown in figure 3.7. Several vacuum cubes of increasing size from 10 to 40 Å in all directions were used to investigate this influence. In the top two graphs (a) and (b) in figure 3.7, the absolute BE values for both molecules are shown, where the core-level BEs vary from 2-3 eV as the size of the unit cell is increased and does not reach a fully converged value at the largest size. This behaviour is due to the change in core-hole density and electrostatic interaction with the background charge as has been studied by Taucher et al. [143]. However, not unlike in the case of the cut-off energies for the PPs, when looking at the relative chemical shifts between the individual carbon atoms in the molecule, this behaviour is not seen as shown in figure 3.7 (c) and (d). Here the relative shifts of the other atoms with respect to the labelled carbon 1 is shown as the box size increases. Also compared in the graphs are the relative shifts calculated using the all-electron FHI-aims code (black lines). The size of the box has little effect on the relative shifts with only a slight

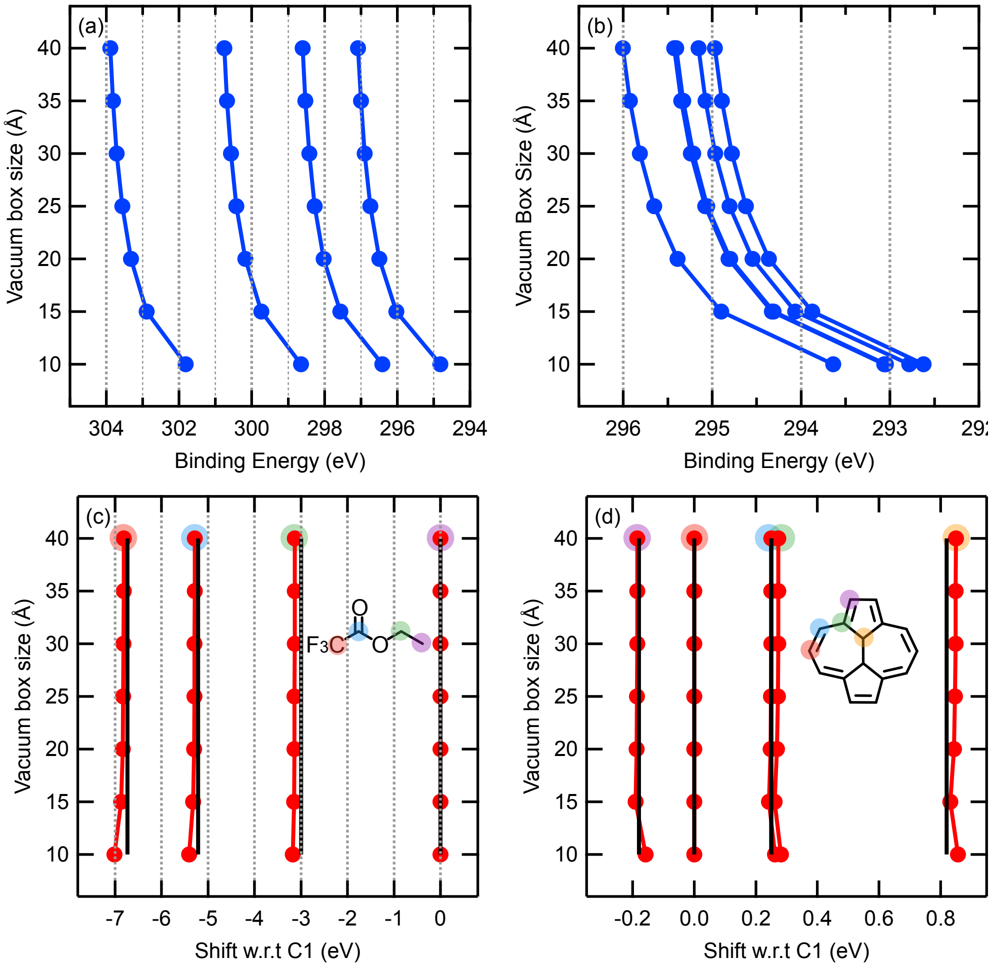

Figure 3.7: Graphs comparing the influence of the vacuum box size on the XPS binding energies of gas-phase molecules in periodic calculations. ETFA on the left and azupyrene on right. (a) and (b) show the changes in the absolute BE of C1s electrons. (c) and (d) show the relative shifts in C1s BE with respect to C1. Lines in black represent the relative shifts obtained from the all-electron FHI-aims calculations without PBCs and the grey gridlines highlight 1 eV energy steps. All calculations were performed with the PBE functional [53].

deviation seen in the smaller unit cells and values reached a convergence at about 20 Å box size. Comparing the results for the psuedopotential method with that of the all-electron calculations, with an average deviation of 0.1 eV and 0.01 eV for the ETFA and azupyrene molecules respectively. With this, it can be concluded that whilst the absolute binding energies are greatly affected by the homogeneous background compensation charge, the effect is not as severe for relative shifts and reliable results to all-electron values can be acquired.

Convergence of the NEXAFS spectra for azupyrene with respect to the box size was investigated. As before the same XPS shifts were used between all spectra to ensure only the difference in the unit cell size is studied, along with a constant cut-off energy of 400 eV. Increasing both the unit cell an PW basis increases the

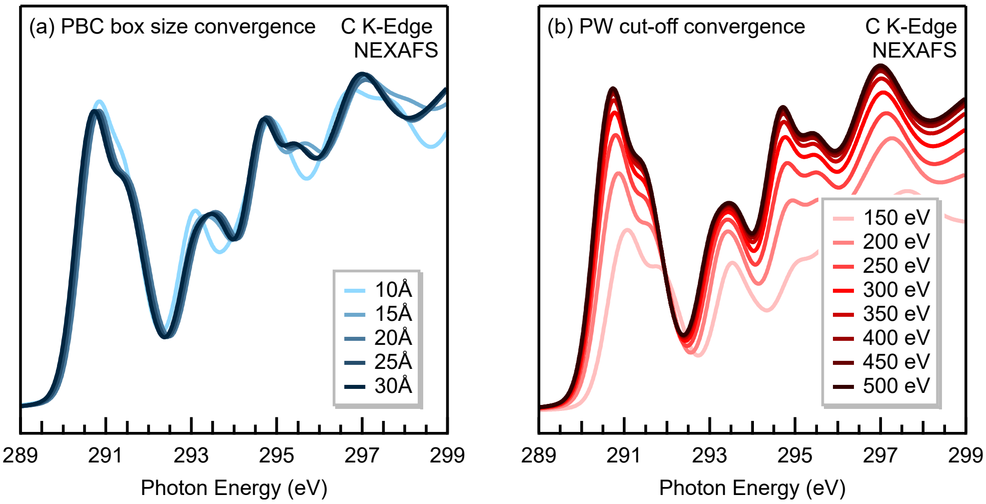

Figure 3.8: Convergence of the NEXAFS spectrum of azupyrene with respect to increasing box size (a) and cut-off energy of the planewave basis (b). A constant cut-off energy of 400 eV was used in the box size convergence and a 30 Å box size used for cut-off convergence. All spectra were calculated with ultrasoft pseudopotentials. Spectra in (a) have been shifted to align leading edges to the same energy.

computational cost of the calculation so it is advantageous to find the minimal value of each that can provide accuracy the required accuracy without unnecessary extra cost. The scaling of such calculations increases N^3, with N being a measure of system size, number of atoms, bands, or basis set so, it is important to find converged values. Total NEXAFS spectra for a unit cell box size ranging from 10 to 30 Å in 5 Å increments are shown in figure 3.8 (a). As seen with the relative XPS binding energies, the spectra converged quickly at a box size of 20 Å, where little to no change is seen afterwards. The basis set convergence was also carried out looking at the NEXAFS spectra in a 30 Å box size and increasing the cut-off energy in 50 eV increments between 150-500 eV. As the cut-off energy increases, little change is seen in the overall shape of the spectra, but the overall intensity increases and reaches convergence at 450 eV. This cut-off energy is similar to what is typically required for intermolecular interaction energies or adsorption energies with the employed default ultrasoft PPs.

Finally, a look at the effect of using different XC functionals with three different GGAs: PBE, BLYP, and PW91. Both the XPS and NEXAFS spectra were calculated and are shown in figure 3.9 (a) and (b), respectively. For the XPS spectra, the peaks for the three functionals produce near indistinguishable spectra whilst for the NEXAFS there are some more noticeable differences. These are mostly located at higher energy transitions after the leading peaks which offer little variation between the three cases.

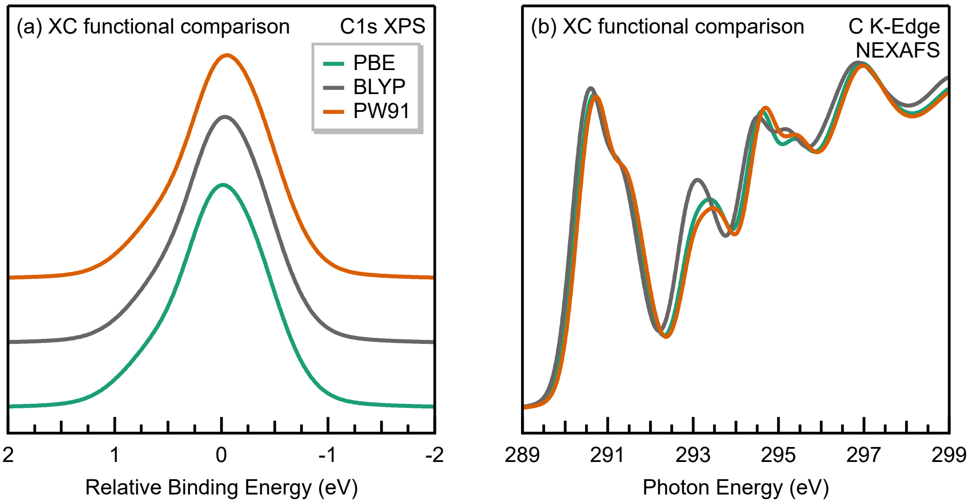

Figure 3.9: Comparison of XPS and NEXAFS spectra calculated with three different GGA XC functionals: PBE (green), [53] BLYP (orange) [125, 126] and PW91 (purple) [118]. XPS have been shifted to the weighted mean for comparison.

3.4.3 Analysis of Core-Level Spectra in Terms of Initial- and Final-state Contributions

Core-level spectra can be used to gain insight into the electronic structure of the system investigated. However, sometimes these details can be hard to reveal due to overlapping features. It can be beneficial to breakdown spectra into various initial- and final-state contributions. The DFT calculations performed allow for this to be done where the initial-state decomposition can be achieved by summing up the transitions which originate from the 1s orbital localised at a specific atom as shown in figure 3.10 (a) for the azupyrene molecule.

An analysis in terms of final-states in NEXAFS simulations requires further consideration but can be particularly appealing for organic molecules adsorbed at surfaces and in thin-films, as spectra are often interpreted in terms of the symmetry of these states (π^*, σ^*). The final unoccupied state decomposition for azupyrene presented in figure 3.10 (b), is carried out through the calculation of the NEXAFS spectrum:

$$\sigma_i(h\nu) \propto \sum_f \underbrace{|\langle\psi_f|\mathbf{e}\cdot\mathbf{p}|\psi_i\rangle|^2}_{\mu_{if}^2}\delta(h\nu-\Delta E_{fi}) \tag{3.4}$$

where μ_{if}^2 is the dipole matrix element between core-state i and valence state f. The KS states are normalised, it can be rewritten as:

$$\sigma_i(h\nu) \propto \sum_f \langle\psi_f|\psi_f\rangle\cdot\mu_{if}^2\cdot\delta(h\nu-\Delta E_{fi}) \tag{3.5}$$

By taking the MOs ϕ_m from the reference system as a complete orthonormal basis and

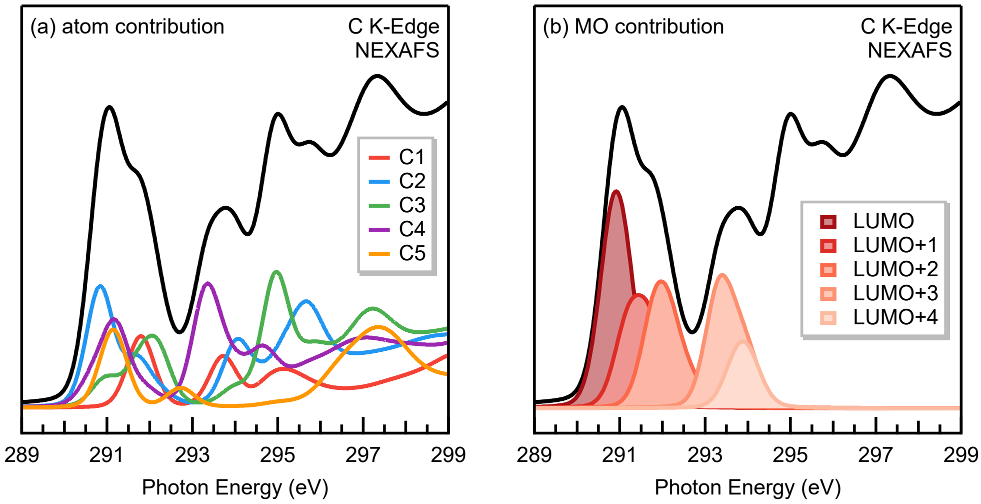

Figure 3.10: Different decomposition schemes for the simulated NEXAFS spectrum of azupyrene. (a) The initial-state decomposition reveals which part of the spectrum is related to which carbon 1s orbital. For the presented case of the highly symmetric azupyrene molecule, groups of symmetry equivalent atoms were summed up to improve visibility. (b) The final-state decomposition shows the contributions of the transitions to each unoccupied molecular orbital up to LUMO+4.

making sure that all the settings used are the same it is seen that

$$1 = \sum_m |\phi_m\rangle \langle\phi_m| \tag{3.6}$$

Equation (3.6) can be inserted into (3.5) to yield:

$$\sigma_i(h\nu) \propto \sum_f \langle\psi_f| \left(\sum_m |\phi_m\rangle \langle\phi_m| \right) |\psi_f\rangle \cdot \mu_{if}^2 \cdot \delta(h\nu - \Delta E_{fi}) \tag{3.7}$$

After rearrangement:

$$\sigma_i(h\nu) \propto \sum_m \sum_f |\langle\psi_f|\phi_m\rangle|^2 \cdot \mu_{if}^2 \cdot \delta(h\nu - \Delta E_{fi}) = \sum_m \sigma_i^{MO,m}(h\nu) \tag{3.8}$$

This allows for a full decomposition of the total NEXAFS spectrum as a sum of the MO projected states. To achieve this then $\sum_m |\langle\psi_f|\phi_m\rangle|^2 = 1$ which is the case when applying this to a gas-phase molecule as the reference MO states are the ground-state MOs so $|\psi_f\rangle \approx |\phi_m\rangle$ if $f = m$ as the only difference is the inclusion of a core-hole on one atom. By doing this, this allows for the same reference to be used for all atoms in the molecule. For a more accurate projection, the core-hole excited state of the gas-phase reference orbital should be used as the reference. The result of this in comparison to the ground-state projection is seen in figure 3.11 (a) and (b) for a gas-phase azulene system and very little difference is seen between the two projections with the only change in the higher MOs. These higher MOs show the limit of such a projection technique as these MOs are unbound and do not fully represent

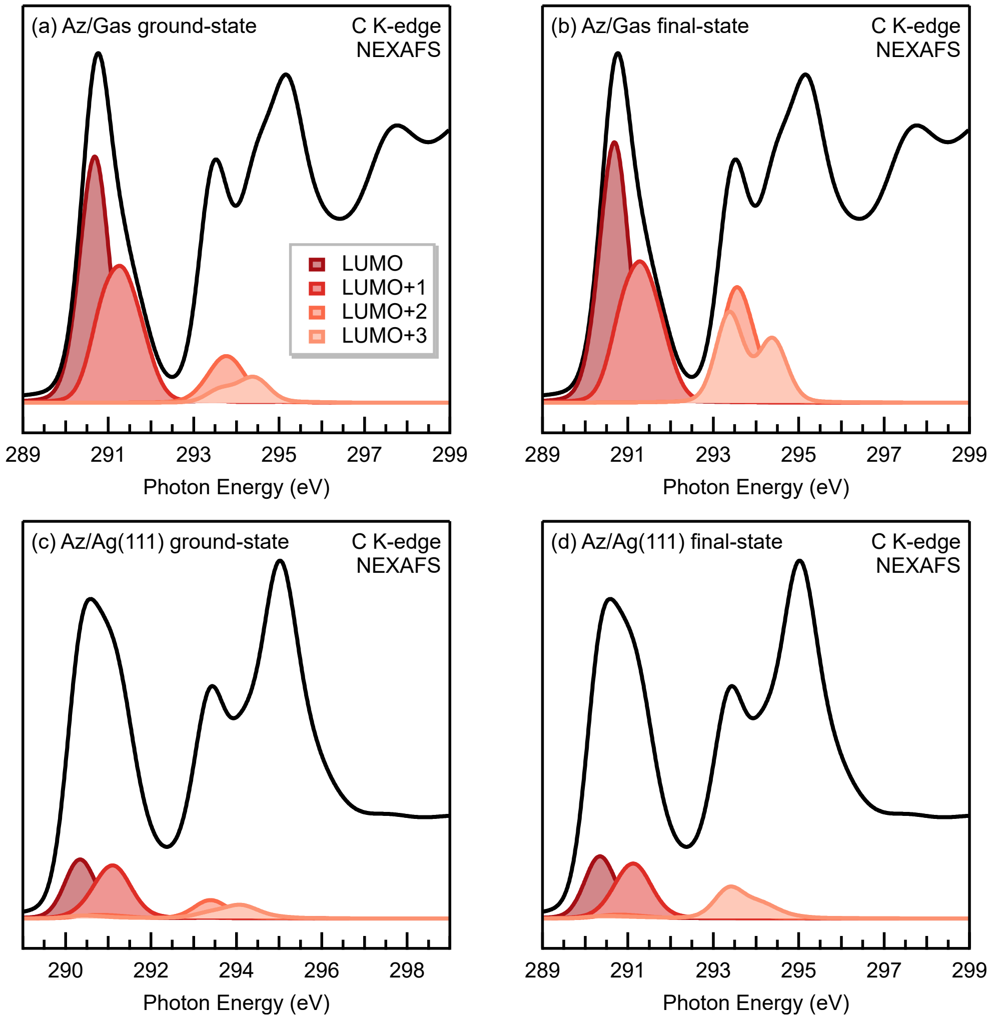

Figure 3.11: MO-projected NEXAFS spectra of azulene in the gas-phase (a) and (b) with the reference used for the MO-projection using either ground-state orbital reference or the corresponding final-state reference, respectively. The same for Az/Ag(111) in (c) and (d) for ground-state and final-state.

the physical orbitals present in the molecule and thus explain the broad nature or presence of a doublet structure seen in the LUMO+3s in figure 3.11. The downside for the excited-state projection is that a separate reference for each individual core-excited atom is needed where for the ground-state the same can be used.

For an organic molecule on a metal surface, the reference used is the freestanding overlayer (metal surface removed). Using this, the set of KS-sates $|\psi_f\rangle$ are not well represented by the set of the reference states $|\phi_m\rangle$ and the intensity of the MO-projection is not described well. In the system of azulene/Ag(111) where there is little interaction between the metal and molecule, the MO-projection should yield a similar result to the gas-phase, with the sum of the orbitals close to equalling the total NEXAFS spectrum. However, in figure 3.11 (c) and (d) for both the ground- and final-state reference the intensity is much lower than expected. It can also be seen again, that the change between the ground- and final-state reference is minimal.

To fix this issue in the MO-projection for molecules on a metal surface then in the future the aim will be to use a different spectral decomposition that also includes the contribution of the dipole matrix elements. When inserting the identity terms of ϕ_m into the dipole matrix, the following expressions can decompose the μ_{if}

$$\mu_{if} = \mid \langle \psi_f \mid \left(\sum_m \mid \phi_m \rangle \langle \phi_m \mid \right) \mathbf{e} \cdot \mathbf{p} \mid \phi_i \rangle \mid^2 \tag{3.9}$$

$$\mu_{if} = \sum_m \mid \langle \psi_f \mid \phi_m \rangle \langle \phi_m \mid \mathbf{e} \cdot \mathbf{p} \cdot \mid \psi_i \rangle \mid^2 = \sum_m \mu_{if}^m \tag{3.10}$$

In the future, this decomposition scheme will be implemented and assessed. For the remainder of this thesis, the decomposition in (3.8) is used being aware of its limitations.

3.4.4 Truncated Cluster vs Periodic Core-Level Simulations

All previous core-level simulations have dealt with isolated molecules and have both been performed with aperiodic structures (FHI-aims) and periodic structures (CASTEP). A look into the performance between these two methods was carried out. To test this, three different systems involving the azulene molecule are used. The three exemplar systems chosen are: azulene in the gas-phase, the molecular crystal of azulene and azulene adsorbed onto the Cu(111) surface.

A difference between condensed phase systems when compared to gas-phase calculations in PBCs is that you must be aware of sampling the electronic states across the periodic crystal via Brillouin zone integration (k-space sampling). There-

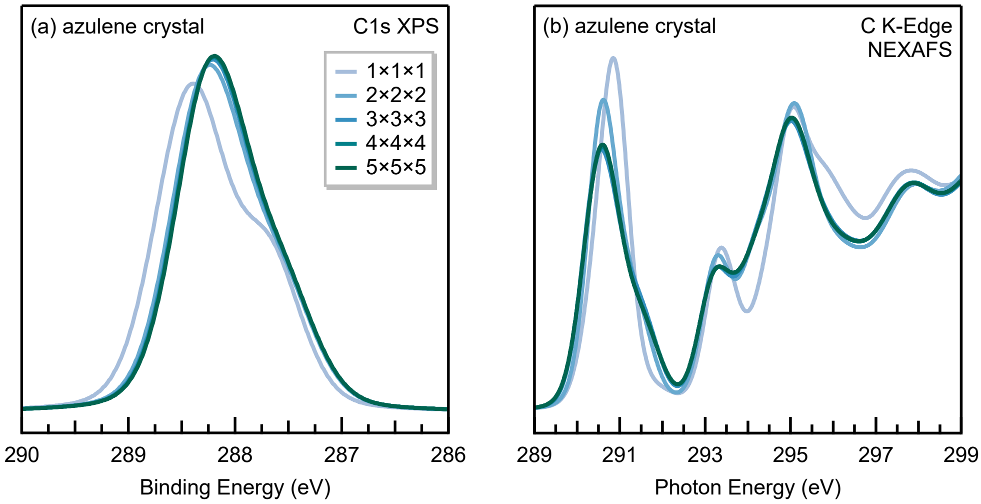

Figure 3.12: K-grid convergence series for the molecular azulene crystal. (a) XPS spectra, (b) NEXAFS spectra. The system is a molecular crystal with four molecules per unit cell.

fore, the convergence must be ensured with respect to the number of k-points included. Figure 3.12 shows the convergence behaviour of both the XPS and NEXAFS spectra of the azulene molecular crystal with respect to the density of the employed Monkhorst-Pack k-grid [144]. Lattice parameters for the structure used are $a = 8.563, b = 4.922, c = 7.810, \alpha = 90, \beta = 101.350, \gamma = 90$. Here it can be seen that both spectra converge rapidly, with a k-grid of $3 \times 3 \times 3$ with a k-point sampling density of 0.0434 Å^{-3} providing a converged result.

In the case of Az/Cu(111), along with the k-space sampling, the convergence with respect to the cut-off energy was repeated due to the presence of the copper metal surface and an additional factor of the vacuum slab that separates the surface model from its periodic image perpendicular to the surface was tested. As with the molecule crystal, rapid convergence with respect to the employed k-grid was found (figure 3.13 (a)) and similar behaviour with the gas-phase molecule (figure 3.8) for the PW cut-off energy was observed (figure 3.13 (b)). For the case with the vacuum slab, it was found that this parameter shows virtually no influence on the spectra (figure 3.13 (c)) in the studied range of 10 Å to 35 Å.

The comparison between gas-phase azulene, the azulene molecular crystal and azulene adsorbed on Cu(111) can be used to show that all three systems can be treated with approximate core-hole simulation methods such as ΔSCF and ΔIP-TP but also allows us to compare aperiodic simulations within FHI-aims and calculations under PBCs with CASTEP. First, XP spectra were calculated with the ΔSCF approach in both FHI-aims and CASTEP. FHI-aims employed the aperiodic (cluster) approach where we correctly account for the positive charge in all three systems after photoionisation. On the other hand, the PW nature of CASTEP made a 3D periodic cell necessary, even for those systems showing a lower periodicity.

The cluster approach in FHI-aims can easily simulate the isolated molecule, while

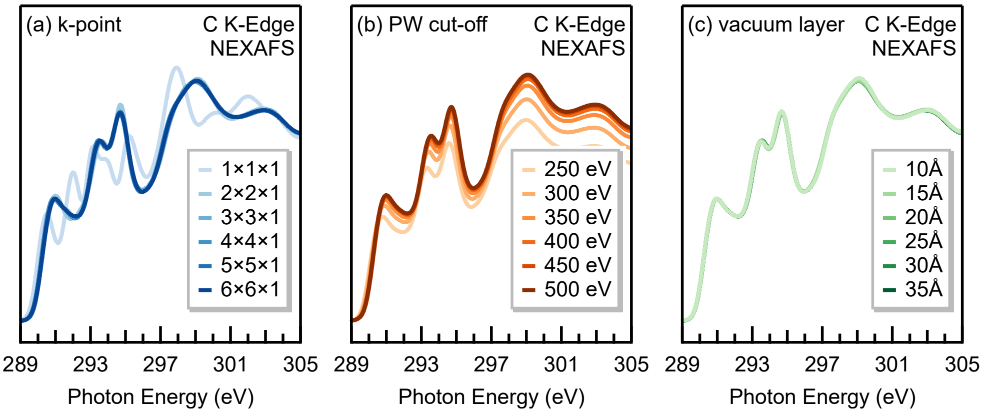

Figure 3.13: Convergence series for azulene adsorbed on Cu(111). (a) k-space convergence with 450 eV cut-off energy, (b) planewave cut-off convergence with a constant k-grid of $8 \times 8 \times 1$, (c) vacuum slab convergence with a 450 eV cut-off energy and a $6 \times 6 \times 1$ k-grid.

the inherently 3D periodic PW approach has to simulate the molecule in a large periodic vacuum box at significant computational overhead. For the molecular crystal and the molecule adsorbed on the surface, the PW code is more suitable, because it already includes the 3D/2D periodicity. In the cluster approach for the all-electron calculation of the crystal and the metal-organic interface, the choice of the cluster is not straightforward. For the molecular crystal, the 16 molecules surrounding a central molecule were cut out of the periodic crystal structure and the XPS shifts of the central molecule were calculated. For the surface-adsorbed molecule, a cluster was cut-out of the 2D periodic slab. The choice of the cluster was guided by the desire to preserve the hexagonal symmetry of the surface while simultaneously providing a sufficient surface area for adsorption. To reduce the number of subsurface atoms, the cluster was truncated into a conical shape, which becomes narrower in lower-lying layers. In the literature, no strong dependence of the XPS calculations on the specific cluster termination was found [114]. Still, the choice of both cluster models for the molecular crystal and the surface system is somewhat arbitrary, forming a draw-back of this method.

Figure 3.14 (a) shows a comparison of the XPS calculation results for both approaches and all three systems. The overall spectra were shifted (to account for the difference in absolute binding energies due to the charge background issue within the PBCs) and a broadening scheme was applied to simulate experimental resolution. Both methods agree very well for all systems, be it the free molecule, the molecular crystal or the molecule adsorbed on the metal surface. This agreement is a very important

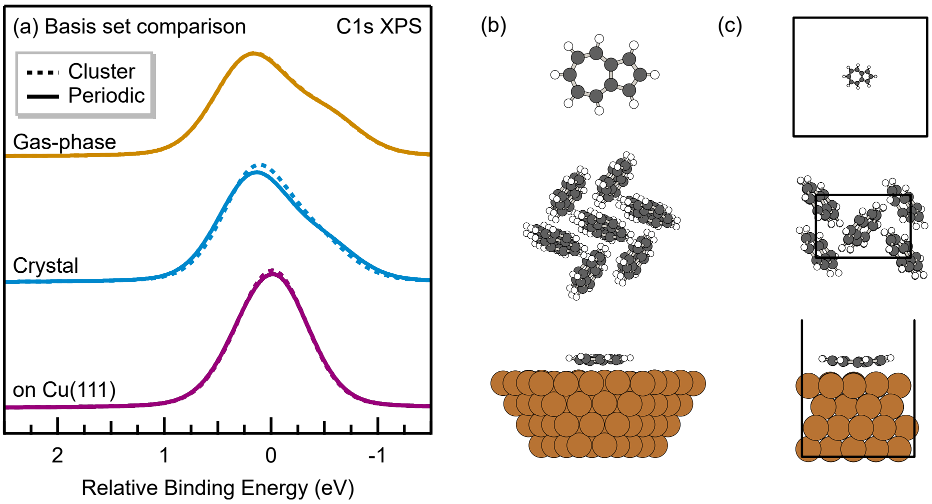

Figure 3.14: XPS calculations of azulene, as a free molecule, in the molecular crystal, and when adsorbed on Cu(111). (a) comparison of the XP spectra, calculated both with cluster approach with all-electron code FHI-aims (dashed line) and in a periodic system with the planewave code CASTEP (full line). XP spectra have been aligned by the weighted mean. Right side: structures of the used clusters (b) and periodic unit cells (c).

result, because it proves that cluster and periodic approaches can yield compatible results, despite their respective challenges. For the systems investigated here, both approaches appear to provide excellent agreement for the obtained relative binding energies. It should be noted, however, that the cluster calculations performed with FHI-aims, both for the molecular crystal and the molecule adsorbed on the surface were much more computationally demanding than the periodic calculations. The all-electron calculations required vastly more computational resources and proved to be less stable with regards to electronic convergence than the periodic calculations, which are straightforward as implemented in CASTEP.

The calculated spectra also provide insight into the interactions present in each system. It is apparent that the interaction between the azulene molecules in the molecular crystal exerts only a minor influence on the XPS peak, which retains its gas-phase shape. The interaction between the molecule and the Cu(111) surface, on the other hand, changes the peak shape a lot, which is an indication of the increased molecule-metal interaction and was already discussed in connection to the experimental data elsewhere [79, 80]. For the adsorbed azulene, the coverage as modelled within PBCs is different to the low-coverage situation captured by the cluster. However, the coverage only exerts a minor influence on the XPS binding energies for this system, as was also observed in experiment.

The NEXAFS spectra of all three systems, calculated with the ΔIP-TP approach in the PW code CASTEP, are compared in figure 3.15. The spectra were not shifted with respect to each other. The good agreement, despite the presence of the space-charge effect, is due to the ionisation potential correction (ΔIP) of the NEXAFS transitions according to the C1s BE of each carbon. In figure 3.15 (a) it can be seen that the spectra of free molecule and molecular crystal are very similar. For the NEXAFS spectrum of the adsorbed molecule (figure 3.15 (b)), the angular dependence of the NEXAFS transitions with regard to the polarisation vector is important. For this, three different polar angles ϑ were chosen to simulate the polarisation direction. Two of those correspond to the polarisation direction parallel (90°) and orthogonal to the surface (0°), while the third is the so-called *magic angle* (53°). The *magic angle* is the polarisation angle, at which the orientation of the transition dipole moment μ_{fi} relative to the substrate does not influence the transition intensity. It should be noted that the ideal magic angle (for a threefold-symmetric substrate) is in fact 54.7° [17]. However, the actual magic angle encountered in an experiment is dependent on the degree of polarisation of the used radiation [17, 24].

The value for the degree of polarisation of 0.9 used in the corresponding experiments [79] leads to a magic angle of 53°. For all polar angles, the spectra are averaged over the azimuthal angle, due to the symmetry of the substrate. The comparison between NEXAFS of gas-phase and adsorbed molecule reveals stark differences in the spectra, giving insight into the mechanism of the molecule-surface interaction. While the overall dichroism reveals that the molecule is approximately flat on the Cu(111)

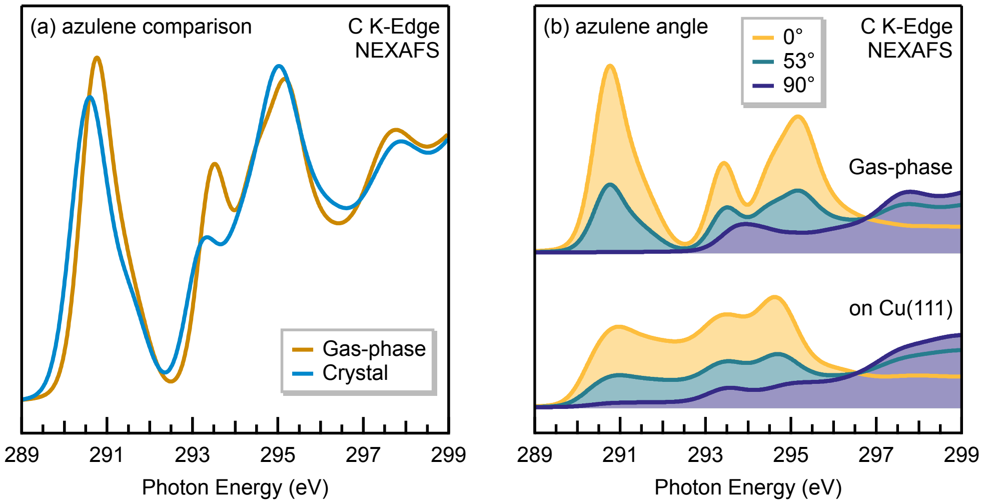

Figure 3.15: NEXAFS simulations of azulene in periodic systems with CASTEP. (a) Comparison of the spectra of the gas-phase molecule and the molecular crystal. (b) Comparison of the spectra of the gas-phase molecule and the molecule adsorbed on Cu(111) for three incidence angles of 25° (yellow), 53° (green), and 90° (blue).

surface, there is another telling detail in the spectra. The non-vanishing intensity of the C1s to LUMO transition (291 eV) for the 90° polar angle shows that the clear separation of σ^* and π^* states (as present for the free molecule) is now broken due to the hybridisation between the electronic states of adsorbed molecule and metal surface [78, 145]. The simulated data show good agreement with the corresponding experimental spectra comparison with the experiment will be discussed in Chapter 4 and interpretation of simulated data in Chapter 5.

3.4.5 Influence of Charge in Periodic Core-Hole Simulations

As previously discussed, calculations with PBCs require a uniform background counter charge to maintain a net-neutral unit cell and can significantly influence electrostatic properties [143]. However, there is the XTP method, [69] which does not require this background charge to be imposed for ΔSCF and ΔIP-TP calculations. The array of calculations making up a ΔIP-XTP simulation differs only in the third step (as shown in figure 3.2 (c)) from the ΔIP-TP method: where N half core-hole (but zero charge) XTP calculations are performed with the introduction of half an electron into the lowest unoccupied state to compensate for the core-hole (schematic of the electron occupations cane be seen in figure B.1).

The results of the ΔIP-TP and ΔIP-XTP simulations are compared for the azulene molecule in the gas phase and adsorbed on the copper surface in figure 3.16. In this figure, all spectra were rigidly shifted to compensate for the global shift due to the different charge state of the systems and therefore enable a better inspection of their spectral shape. Both methods produce virtually indistinguishable XPS peak shapes for the molecule adsorbed on the metal surface, while stark differences are

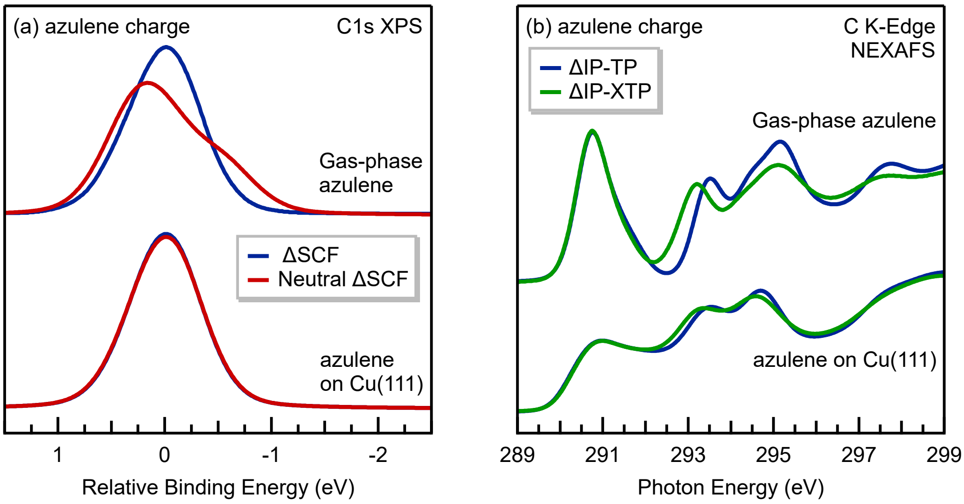

Figure 3.16: Core-level spectra calculated with and without background charge compensation for azulene molecule in the gas-phase and adsorbed on the Cu(111) surface. (a) Comparison of ΔSCF XP spectra calculations with a homogeneous compensation charge (blue) and with a compensation charge introduced in the lowest unoccupied state (red). XP spectra are averaged to the weighted mean. (b) Comparison of the ΔTP-IP (blue) and ΔIP-XTP (green) NEXAFS spectra. Both spectra share a 0.5 e core-hole. The TP calculation includes −0.5 e background charge (blue) while the XTP calculations compensate charge by adding half and electron into the lowest unoccupied state (green).

present for the gas-phase molecule (figure 3.16 (a)). This fact is unsurprising, as the peculiar peak shape of the gas-phase azulene molecule is due to the localised charge distribution onto the metal surface, as already discussed in the literature on the backdrop of experimental XPS data for thin multicrystalline films of azulene [79].

The neutral ΔSCF calculations do not remove the electron taken from the core-state, but instead promote it into the lowest unoccupied state. The occupation of the former LUMO has massive consequences for the electronic structure of the gas-phase molecule and therefore the resulting spectra are negatively influenced. On the other hand, in the case of azulene adsorbed on Cu(111), the continuous density of states of the metal surface around the Fermi level has the effect that the additional electron does not present a significant change in the electronic structure and the resulting spectra remain similar.

For the proper simulation of the NEXAFS spectra in figure 3.16 (b), the obvious error in the neutralised ΔSCF calculations for the free molecule made it necessary to perform the ΔIP shift both for the TP and XTP simulation on the basis of the charged ΔSCF calculations. The results show that again the spectra for the molecule adsorbed on the metal surface are almost identical for ΔIP-TP and ΔIP-XTP, while there are some differences for the gas-phase molecule.

Michelitsch and Reuter have previously compared various core-hole constraining methods. They reported that the XTP method (note that no ΔIP correction is applied) on balance provides the best agreement with experiment for absolute energies and intensities of first and second transition energies of NEXAFS spectra for a range of isolated organic molecules [69]. Compared are the ΔIP-TP and ΔIP-XTP spectra with the experimental data for the multicrystalline azulene films from reference [81] shown in figure 3.17, where the broadening parameters of the two simulated spectra have been changed to fit the resulting spectra with the experimental result. The quantitative comparison extracted from these spectra yields an average deviation of 0.13 eV for ΔIP-TP and 0.05 eV for ΔIP-XTP, when the relative shifts between the four lowest-energy peaks are compared to the experiment. The relative peak intensities for those four peaks deviate by average factors of 1.8 and 1.5 for ΔIP-TP and ΔIP-XTP, respectively. Therefore, it is found that both ΔIP-TP and ΔIP-XTP are in good agreement with the experiment, with ΔIP-XTP providing slightly smaller deviations both in transition energies and intensities. As can be seen by this quantitative comparison, the approximate treatment with the ΔIP-TP and ΔIP-XTP methods based on transitions with infinite lifetime and empirical lifetime broadening already provides a reasonable agreement with experiment in the near-edge region, even as many-body effects such as inelastic scattering, Auger effects, and vibronic coupling are neglected.

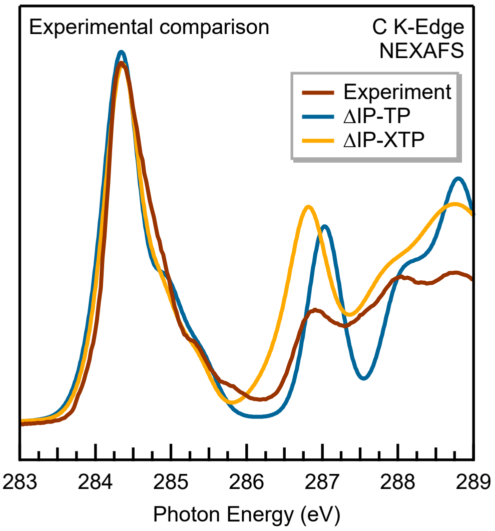

Figure 3.17: Comparison of the core-level spectra calculated with and without forced charge compensation for azulene molecule in the gas-phase with experimental data from [81]. The simulated spectra were shifted by −8.25 eV (XTP) and −6.4 eV (TP) for better comparison of the spectral features. Both XTP and TP simulations included broadening to resemble the experimental resolution. The broadening applied here was directly adjusted according to this specific experimental data and uses slightly different parameters that the “best guess” values mentioned previously. The simulated spectra shown here were obtained by using a FWHM of 0.5 eV combined with an 85 %/25 % G/L ratio in the low energy range and a 2.0 eV FWHM with a 20 %/80 % G/L ratio in the high energy range.

3.5 Conclusions

In this chapter a full breakdown of the methodology and workflow, along with description of the tools developed have been described showing how XPS and NEXAFS spectra can be simulated. The numerical and technical details of DFT based core-hole simulations for 1s XPS and K-edge NEXAFS for a variety of systems involving organic molecules, organic molecular crystals, and metal-organic interfaces have been detailed. These calculations were performed utilising the ΔSCF and ΔIP-TP methods. Simulations have been analysed with respect to various computational parameters involving the choice of XC-functional, basis set and if the model is represented as aperiodic or with PBCs. It is found that for systems with not too extreme chemical shifts, the effect of the XC-functional is minimal and little difference can be seen between XC functionals. However, for cases with more extreme chemical shifts, as represented by the ETFA molecule, hybrid functionals perform better when compared to GGAs and meta-GGAs.

Calculations have been performed using both an aperiodic structure through FHI-aims and in PBCs with CASTEP. Both of these two methods pose various challenges. Whilst aperiodic calculations have the benefit of being able to provide absolute XPS binding energies, such calculations can encounter problems with proper localisation of the core-hole. Care must be taken especially when dealing with symmetrically equivalent atoms, even more so when located close together to achieve proper localisation of the core-hole onto the correct atom and avoiding unphysical delocalised states. For PBCs, where absolute binding energies are more difficult to obtain, care must be taken in regard to the core-hole density and electrostatic interaction of the background charge and ensuring a large enough unit cell to minimise these effects. When comparing the results of these two methods by looking at the relative XPS shifts, it can be seen that both methods yield comparable results when simulated correctly.

It has been shown that the core-level spectra calculated through the ΔSCF and ΔIP-TP methods implemented in CASTEP can provide a versatile and reliable method and in agreement with an all-electron DFT approach. The method is versatile and can work for organic molecules in multiple environments which can be valuable to support the interpretation and assignment of experimental spectra measured in gas-phase, on molecular monolayers or multilayer thin films.

Chapter 4

Comparison Between Experimental and Simulated Core-Level Spectroscopy

This chapter presents work published in the below listed papers that was part of a collaboration with various authors. Work of the authors are included in this chapter to provide a full overview and background to the work carried out for this thesis and include experimental results laid out in section 4.2 and the creation of structural models in section 4.4.

Molecule-Metal Bond of Alternant versus Nonalternant Aromatic Systems on Coinage Metal Surfaces: Naphthalene versus Azulene on Ag(111) and Cu(111)
Benedikt P. Klein, Juliana M. Morbec, Markus Franke, Katharina K. Greulich, Malte Sachs, Shayan Parhizkar, François C. Bocquet, Martin Schmid, Samuel J. Hall, Reinhard J. Maurer, Bernd Meyer, Ralf Tonner, Christian Kumpf, Peter Kratzer and J. Michael Gottfried
The Journal of Physical Chemistry C **123**, 29219-29230 (2019)
https://doi.org/10.1021/acs.jpcc.9b08824

Enhanced Bonding of Pentagon–Heptagon Defects in Graphene to Metal Surfaces: Insights from the Adsorption of Azulene and Naphthalene to Pt (111)
Benedikt P. Klein, S. Elizabeth Harman, Lukas Ruppenthal, Griffin M. Ruehl, Samuel J. Hall, Spencer J. Carey, Jan Herritsch, Martin Schmid, Reinhard J. Maurer, Ralf Tonner, Charles T Campbell and J. Michael Gottfried
Chemistry of Material **32**, 1041-1053 (2020)
https://doi.org/10.1021/acs.chemmater.9b03744

Topology Effects in Molecular Organic Electronic Materials: Pyrene and Azupyrene
Benedikt P. Klein, Lukas Ruppenthal, Samuel J. Hall, Lars E. Sattler, Sebastian M. Weber, Jan Herritsch, Andrea Jaegermann, Reinhard J. Maurer, Gerhard Hilt and J. Michael Gottfried
ChemPhysChem **22**, 1065-1073 (2021)

https://doi.org/10.1002/cphc.202100222

Topological Stone-Wales Defects Enhance Bonding and Electronic Coupling at the Graphene/Metal Interface
Benedikt P. Klein, Alexander Ihle, Stefan R. Kachel, Lukas Ruppenthal, Samuel J. Hall, Lars E. Sattler, Sebastian M. Weber, Jan Herritsch, Andrea Jaegermann, Daniel Ebeling, Reinhard J. Maurer, Gerhard Hilt, Ralf Tonner-Zech, Andre Schrimeisen and J. Michael Gottfried
ACS Nano "*in review*" (2022)

4.1 Introduction

Structures of graphene can usually exhibit topological defects in the form of pentagons, heptagons and pentagon-heptagon pairs. These defect can cause a change in various chemical and physical properties of the graphene sheet resulting in changes in chemical reactivity, [146, 147] mechanical strength, [148–151] electron transport, [152, 153] and magnetism [154]. By controlling the concentration of these defects, the properties of graphene can be tailored [155].

The characterisation of these defects can be tricky, and they remain largely unexplored due to low concentrations of these defects in experimental structures. However, a molecular model system can be used to study these defects and compare them with systems representing a regular graphene structure. The group of Prof. J. Michael Gottfried at the Philipps-Universität Marburg have been extensively looking into these defects and identified 4 model molecules to study these defects. They consist of naphthalene (Np), azulene (Az), pyrene and azupyrene which are shown in figure 4.1 and have been been studied in great detail [79–81, 156, 157]. Naphthalene and pyrene consist of 6-6 ring structures whilst azulene and azupyrene are formed from the 5-7 ring defects. The four molecules contain two isomer pairs, azulene/naphthalene and pyrene/azupyrene. The isomers only differ by their topology; therefore a comparison reveals the influence of the topology on the studied properties.

This change in topology can affect the properties of the π-electron system. The molecules can be classed as alternant (naphthalene and pyrene) or non-alternant (azulene and azupyrene). These terms are based on Hückel molecular orbital (HMO) theory, where the atoms are split into two group (red and green dots in figure 4.1). Where throughout the molecule the atoms of the same group are separate from each other, the molecule is alternant structure. Where this is not possible, the molecule is non-alternant. The non-alternant structure leads to the violation of the Coulson-Rushbrooke pairing theorem causing a lifting of some of the symmetries in the electronic structure of alternant molecules [158].

This chapter aims to collate and discuss the spectroscopy simulations produced during this thesis, which have been published in the following papers [79–81, 157]. A

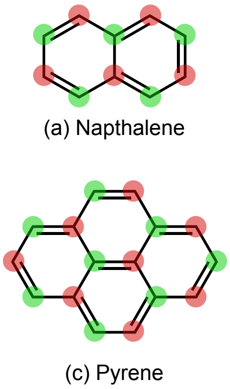

Figure 4.1: Lewis structures of (a) naphthalene, (b) azulene, (c) pyrene and (d) azupyrene. Green and red dots show the connection of atoms to determine if the structure is alternant or non-alternant

brief summary overview of the experimental data will be given in section 4.2 for the findings found on the behaviour of azulene and naphthalene on three metal surfaces Ag(111), Cu(111), and Pt(111) through various experimental techniques. This work was carried out by Klein et al. [79–81, 156]. Using structural models created and optimised by Dr. Benedikt P. Klein, XPS and NEXAFS simulations were performed and section 4.4 reports a comparison between experimental and simulation to assess the accuracy of the calculations. From the comparison between experiment and simulation, a self-interaction error was identified to affect the results and addressed which is detailed in section 4.5. Finally, section 4.6 reports the performance of the calculations for larger analogue molecules pyrene and azupyrene in a multilayer structure and adsorbed on a Cu(111) surface.

4.2 Azulene and Naphthalene

The results reported in this section are experiments performed by Klein et al. for azulene (Az) and naphthalene (Np) adsorbed on three different metal surfaces Ag(111), Cu(111) and Pt(111), whilst also including in a multilayer structure [79–81, 156].

The experimentally characterised samples were created through deposition of azulene and naphthalene on metal surfaces in ultrahigh vacuum conditions. Various experiments were performed on the structures to gain information on aspects such as the adsorption height of the molecule on the metal surface through normal incidence x-ray standing wave (NIXSW) [159, 160] and the adsorbate-substrate bond energies measured with temperature programmed desorption (TPD) [161].

Measuring the distance between an adsorbed molecule from the surface can give structural information on the adsorbate-substrate bond. NIXSW was used to calculate the adsorption heights of the monolayer systems. NIXSW utilises the Bragg diffraction of the standing x-ray wave field that is generated by a crystalline substrate.

At various heights the x-ray intensity has a characteristic energy dependant profile. In a photoemission experiment, photoelectron emission intensity follows this same profile and can be extracted for each XPS signal using a fit-model from dynamical diffraction theory with correction from non-dipolar effects [159, 160, 162–164].

Fitting the results of NIXSW measurements yields two values, the coherent fraction F^{H}, which reports the difference between the heights between all the atoms with similar XPS BE in the molecule and the adsorption height D^{H}. The recorded average adsorption heights for all carbon atoms in the monolayer coverage (1 ML) were found to be 3.13 ± 0.02 Å for Np/Ag(111) and 3.03 ± 0.04 Å for Cu(111). For azulene the heights were 3.06 ± 0.02 Å on Ag(111) and 2.30 ± 0.03 Å on the Cu(111) surface [80].

It can be seen from the adsorption heights that azulene features a shorter adsorbate-substrate bond for both metals than naphthalene, this is a typical indication that azulene forms a stronger bond with the metal surface [165]. For both azulene and Np/Ag(111) surface, the molecules are closer to the surface than the sum of their tabulated van der Waals radii (3.42 Å) [166] the distance agrees well with values of physisorbed planar organic molecules that have been previously reported [167, 168]. For Cu(111), naphthalene is close to the sum of the van der Waals radii (3.10 Å), [166, 169] whilst for azulene the adsorption height is much more akin to an organometallic carbon-copper bond (2.2 Å) [169].

Along with the adsorption height, another quantity that can be measured to highlight the strength of the adsorbate-substrate interaction is the activation energy of desorption. This is possible to record through temperature-programmed desorption (TPD) data [161, 170, 171]. The principle of TPD is increasing the temperature until there is enough energy to overcome the attraction between the molecule and substrate and measuring the desorption rate. The bond energies of azulene and naphthalene adsorbed on Ag(111) and Cu(111) surfaces were investigated. The desorption maxima for naphthalene occurred at 350 K and 370 K for Ag and Cu respectively, and azulene was at 400 K and 550 K for Ag and Cu [156]. Here we can see a large difference between the temperatures of the two molecules on both surfaces with higher temperatures for azulene, indicating significant difference in interaction strength between molecule and surface. Using the TPD data the desorption activation energy E_{d} can be extracted. The resulting adsorption energies are given as $-97\,\mathrm{kJ/mol}$ for Np/Ag(111) and $-100\,\mathrm{kJ/mol}$ for Cu and Az/Ag a value of $-111\,\mathrm{kJ/mol}$ and $-153\,\mathrm{kJ/mol}$ for Cu for a monolayer coverage [156]. These show that azulene possess a stronger bond with the metal surface than naphthalene. All the adsorption heights and adsorption energies of mentioned above are shown in table 4.1.

Experiments looking into the adsorption energy of azulene and Np/Pt(111) were performed from the lab of C. T. Campbell at the University of Washington and are from the references by Klein et al. and Gottfried et al. [81, 172]. The energy was fitted with respect to a second-order polynomial fit across different coverages [81].

Table 4.1: Experimentally recorded adsorption heights with NIXSW and adsorption energies with TPD for azulene and naphthalene adsorbed on Ag(111) and Cu(111) metal surfaces [80, 156].

	Np/Ag	Np/Cu	Az/Ag	Az/Cu
Adsorption Height (Å)	3.13	3.03	3.06	2.30
Adsorption Energy (kJ/mol)	-97	-100	-111	-153

The adsorption energy for azulene and naphthalene at a monolayer coverage were measured as $-329\,\mathrm{kJ/mol}$ and $-243\,\mathrm{kJ/mol}$, respectively. These values show a much greater adsorption energy than for the Ag(111) and Cu(111) metal surfaces indicating a far greater interaction strength between the molecule and the metal surface.

The adsorbate-substrate interactions can cause a change in the electronic structure. Core-level spectra can be used to probe the electronic structure of the molecule on metal surfaces. Both XPS and NEXAFS can provide information on both the core and valence electronic structure, respectively. To see how adsorption of these two molecules, azulene and naphthalene, can change the electronic structure, the behaviour without the influence of the metal surface needs to be studied first. This is achieved by absorbing molecules as a thick multilayer on the surface, enough so that any effect on the metal becomes negligible.

4.2.1 Core-level Spectroscopy

A collection of all the experimental XP spectra measured by Klein et al. are compiled into figure 4.2 with the multilayer spectra shown in figure 4.2 (a), and the molecule adsorbed metal structures for all three metals of Ag(111), Cu(111) and Pt(111) shown in figure 4.2 (b), (c) and (d) respectively. Comparing between the multilayer spectra, it can be seen that there is a difference in the XPS peaks. Azulene has a broader peak shape caused by a shoulder at lower BEs whereas naphthalene retains a more symmetric peak shape. Looking at the XP spectra for the metal adsorbed structures, there is not much change in the peak shape for naphthalene but for azulene the same broad peak shape is present for the Ag(111) structure but becomes much more narrow and loses the shoulder for both the Cu(111) and Pt(111) structures.

Along with the XPS, the NEXAFS spectra were recorded for all the azulene and naphthalene structures and are shown in full in figure 4.3. Spectra were recorded with three different x-ray incidence angles of 25°, 53° and 90°. Once again, it can be seen how the difference in topology causes a change in the electronic structure, from the multilayer spectra in figure 4.3 (a) and how the adsorption and subsequent interaction with the surface can affect the spectra. Both multilayer spectra have clear and identifiable features that can be used to distinguish them from each other. The azulene multilayer spectrum feature a broad single leading feature whilst naphthalene shows two distinct peaks in the leading feature. Once again, by looking at the NEXAFS

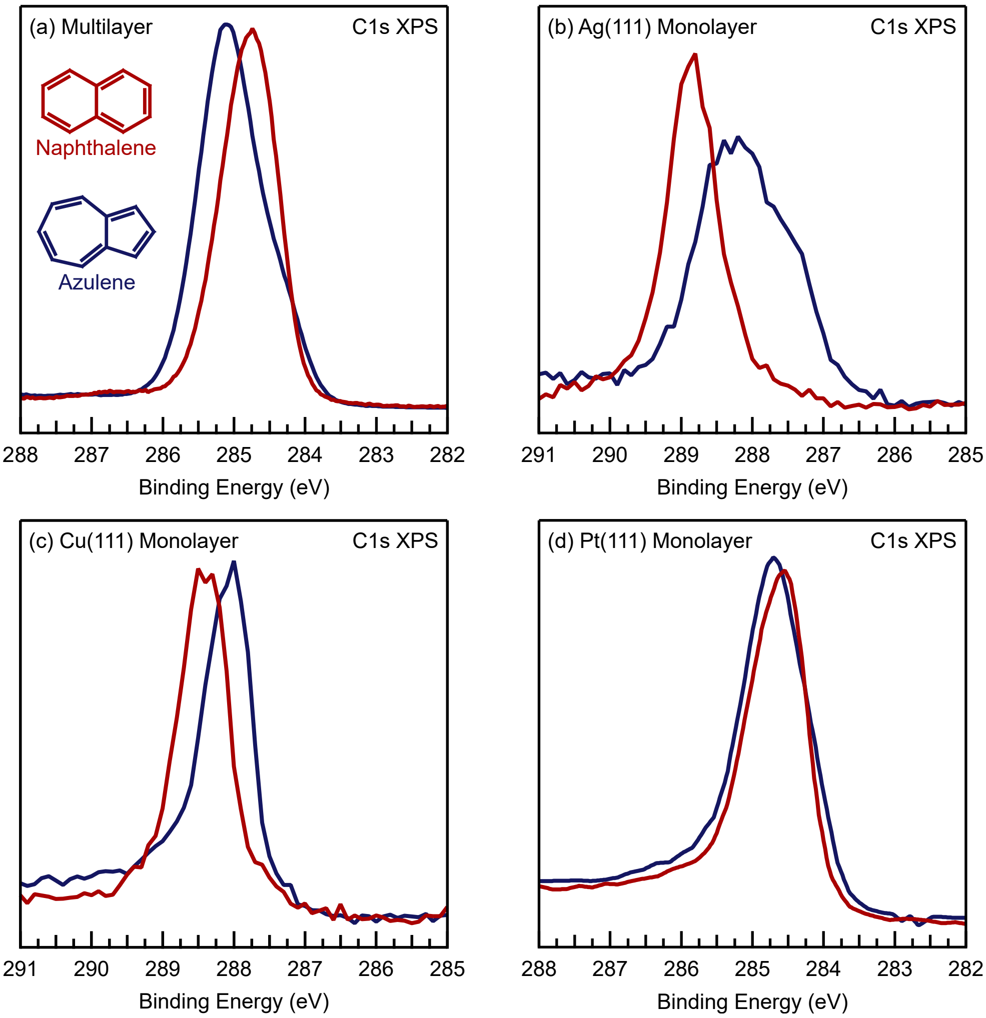

Figure 4.2: Experimentally recorded C1s XP spectra of azulene (blue) and naphthalene (red). (a) Spectra recorded from a multilayer structure of molecules to limit the surface interaction. (b), (c) and (d) show spectra recorded of molecules adsorbed onto a Ag(111), Cu(111) and Pt(111) surface respectively [79–81].

spectra for the metal adsorbed structures, a similar pattern that was seen in the XPS appears. For both molecules on Ag(111) and Np/Cu(111), where little change was seen in the XPS, there is also minimal change with distinct features still present in the NEXAFS spectra with only some broadening present. For Az/Cu(111) and both molecules on Pt(111) the spectra change, with the most drastic change seen in the Pt(111) cases. Here the spectra are significantly broadened and the leading peak has diminished in intensity, and all together vanishing for the Pt(111) spectra, where the spectra have lost all noticeable features. This can be seen as a direct consequence of the strong interaction between the molecule and metal surface that has been identified through the previously described experiments.

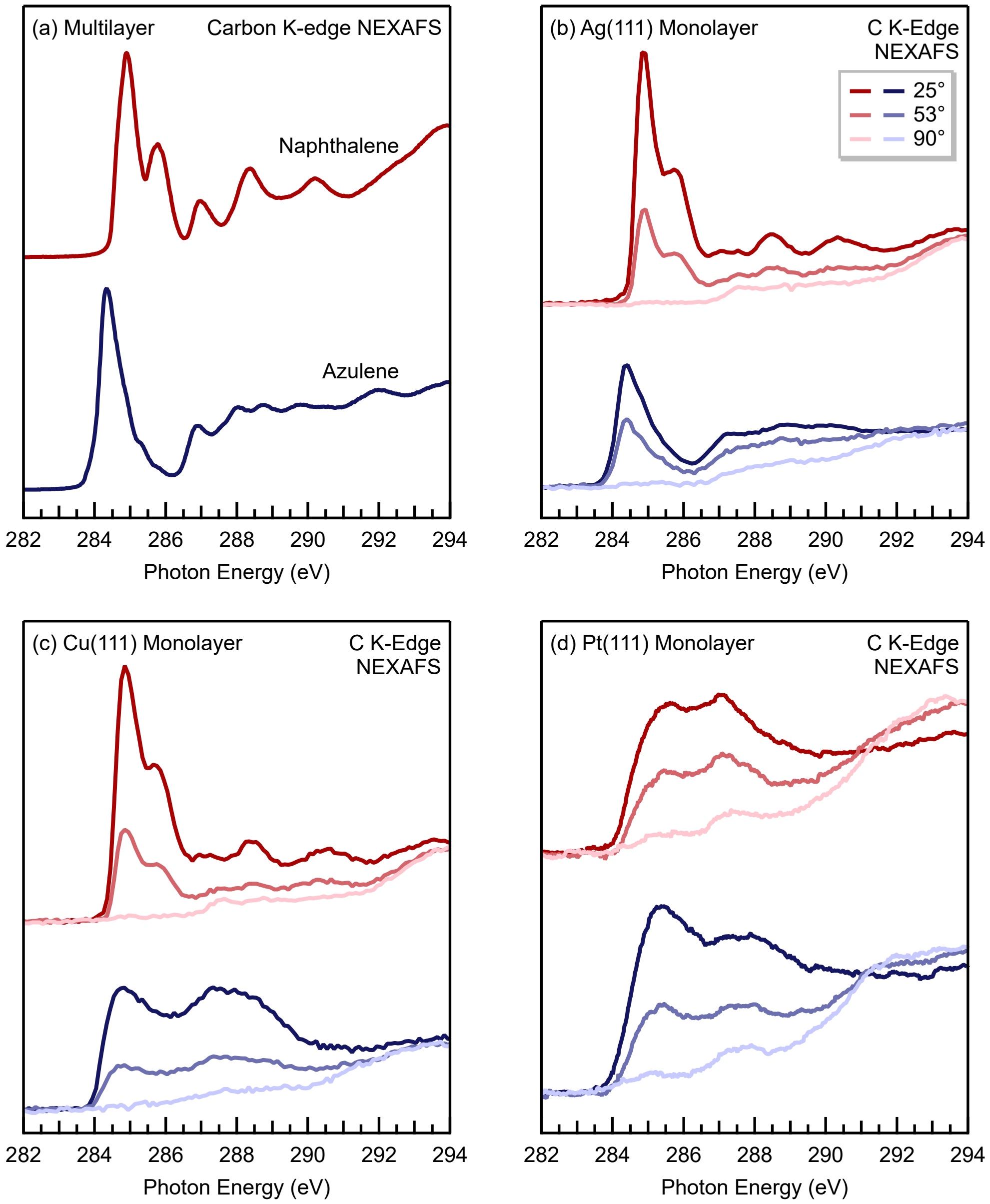

Figure 4.3: Experimentally recorded carbon K-edge NEXAFS spectra of azulene (blue) and naphthalene (red). (a) Spectra recorded from a multilayer structure of molecules to limit the surface interaction. (b), (c) and (d) show spectra recorded of molecules adsorbed onto a Ag(111), Cu(111) and Pt(111) surface, respectively [79–81]. Spectra in (b)-(d) show spectra for three different incidence angles 25°, 53° and 90° in lighter shades.

4.3 Computational Details

Geometry optimisations of the structures of azulene, naphthalene, pyrene and azupyrene adsorbed on metal surfaces were carried out by Dr. Benedikt P. Klein and full details of the methods and settings used are presented in the following references [80, 81, 157]. The optimisations were carried out using the PBE functional [53] in combination with the D3 van-der Waals correction scheme with Becke-Johnson damping [173, 174]. During relaxation the bottom two layers of the metal slab fixed into the bulk geometry whilst the rest was allowed to relax and a 30 Å vacuum layer included.

Core-level calculations were performed using the general method as describe in section 3.3.1. Calculations with CASTEP were performed with the PBE functional, [53] a PW cut-off energy of 450 eV and a k-grid of $6 \times 6 \times 1$ ($1 \times 1 \times 1$ for gas-phase calculations) for each metal surface. An electronic convergence criterion of the total density of at least 1×10^{-6} eV/atom were chosen.

Cluster calculations were performed with the all-electron numeric atomic orbital code FHI-aims [105]. Cluster cut-outs were created by repeating the periodic structure and cutting out a metal cluster for one single molecule. No further optimisation was carried out on the cluster. Calculations made use of either the FOP or FOB keywords to constrain a core-hole onto a specific atom. A 'tight-tier2' basis set was used for the molecule and first metal layer of the cluster with all lower metal layers utilising a 'light-tier1' basis set. In addition to the PBE functional, [53] XPS BEs were also calculated using the meta-GGAs SCAN, [120] and TPSS [119]. The hybrid functional HSE06 was used [123] with an ω value of 0.11 bohr^{-1} where a 'intermediate-tier1' basis set was used for the metal surface in this case. All calculations were performed to an electronic convergence setting of 1×10^{-4} e/Å^3 for the electron density, 1×10^{-2} eV for the KS-eigenvalues and 1×10^{-6} eV for the total energy. All spectra were broadened using the pseudo-Voigt scheme [111, 112] as detailed in section 3.3.1

4.4 Comparison of Simulated Core-Level Spectroscopy

Structural models were created and optimised by Dr. Benedikt P. Klein for both azulene and naphthalene on the three metal surfaces and were found to agree well with experimental results. The adsorption heights of the structures were compared with the available NIXSW data. The adsorption heights of the optimised structures were calculated with respect to the bulk-truncated surface layer [79, 80]. Table 4.2 shows the comparison of the adsorption heights of the experimental and DFT structures of azulene and naphthalene on Ag(111) and Cu(111) surfaces. The DFT structures show agreement with the experimental adsorption heights and show that Np/Ag(111) adsorbs at the highest height whilst Az/Cu(111) has the lowest. The adsorption energies for the

Table 4.2: Comparison of the experimentally recorded adsorption heights D^{H} by NIXSW of naphthalene (Np) and azulene (Az) on Ag(111) and Cu(111) metal surfaces with DFT-D3 calculated results [79, 80].

D^{H} in Å	Np/Ag	Az/Ag	Np/Cu	Az/Cu
Experiment	3.13	3.06	3.03	2.30
DFT-D3	3.10	2.94	2.96	2.33

Pt(111) calculated with DFT were compared with the experimental results described in section 4.2 where the DFT adsorption energy E_{ads} for azulene was $-335\,\text{kJ/mol}$ (exp. $-329\,\text{kJ/mol}$) and naphthalene was $-298\,\text{kJ/mol}$ (exp. $-243\,\text{kJ/mol}$). These show a greater adsorption energy that the values seen on Ag(111) and Cu(111) in table 4.1, indicating a much greater interaction to the metal surface. Whilst the agreement with azulene is good, for naphthalene is overestimated, which is not unexpected for the D3 dispersion correction that was used [81].

Using the structures that were optimised and shown to compare well with experimental results, both the XP and NEXAFS spectra were simulated using the ΔSCF and ΔIP-TP methods. In this section a full comparison between the simulated results with their experimental counterpart will be carried out for all the azulene and naphthalene systems.

4.4.1 XPS

In total, between azulene and naphthalene multilayer structure and adsorbed onto various metals, eight XP spectra were simulated. For each structure the comparison between the experimental reference and the simulated spectra are shown in figure 4.4. Here the experimental spectra are placed above and in the darker shade whilst the simulated spectra are beneath and in the lighter shade. To compare with the experimental spectra, the simulated spectra had to be empirically rigidly shifted to align them with the experiment, with the shifts reported in the figure captions. The shift for each molecule metal system is different due to different properties of each system with the biggest factor stemming from the metal surface as with each system the number of states increases, and a requirement of larger shifts needed. In figure 4.4 (a), a comparison between the multilayer structures was carried out with calculations of the isolated molecule. An excellent agreement is seen between the experiment and simulation even though the simulation is of a greatly simplified structure. This shows that the interactions between molecules in the multilayer are minimal and do not affect the electronic energies and transitions.

Figure 4.4 (b), (c) and (d) show the comparison of the spectra of the molecules adsorbed on the three metal surfaces of Ag(111), Cu(111) and Pt(111) respectively. The simulated spectra agree well with the experimental results, with importantly the loss of the shoulder in the azulene that was seen for the Cu(111) and Pt(111) structures being correctly modelled. However, there is one discrepancy with the azulene/Ag(111) case in figure 4.4 (b). The simulated spectra show a loss of the shoulder as seen with the other azulene/metal systems but in the experiment this is not the case with a similar peak shape to the multilayer present with a shoulder at lower energy. The cause for this error in the calculation is investigated and presented in section 4.5.

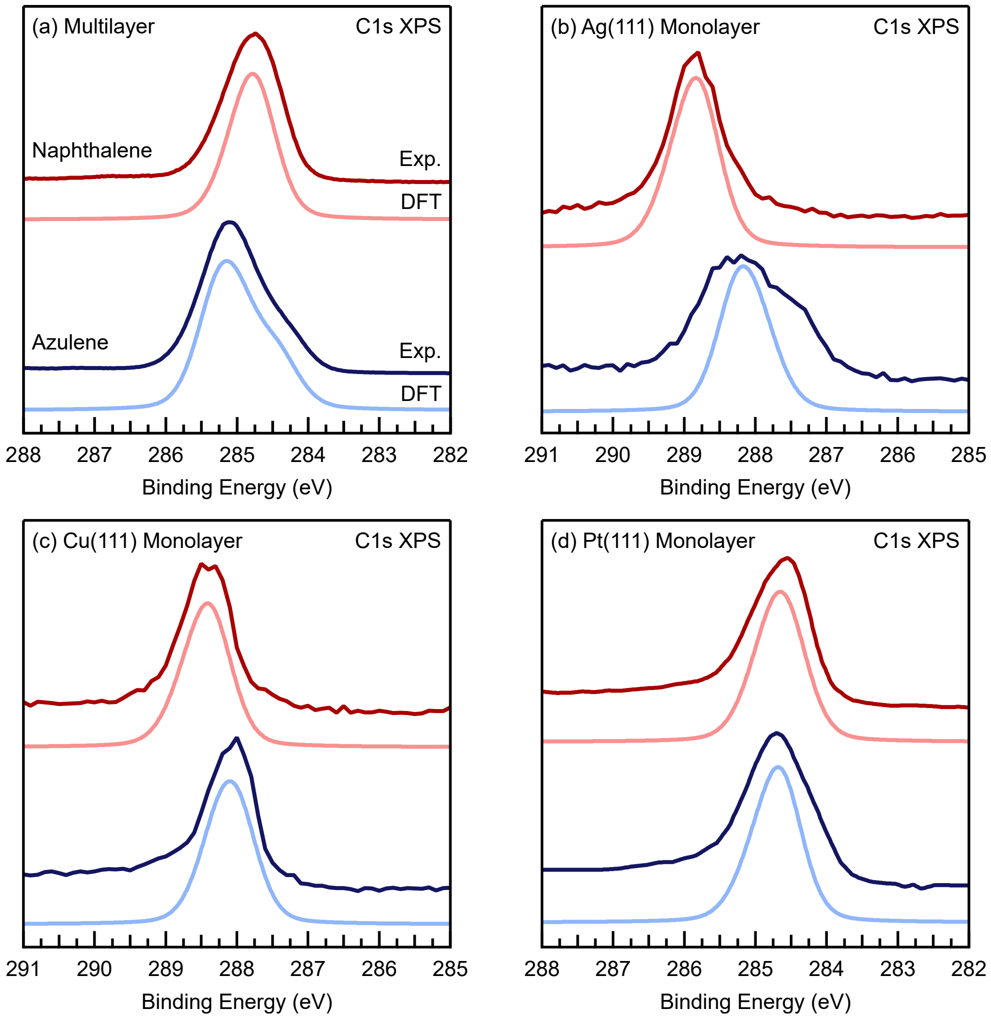

Figure 4.4: Comparison between the experimentally [79–81] recorded and DFT simulated C1s XP spectra of azulene (blue) and naphthalene (red) in a multilayer structure (a) and adsorbed on a Ag(111) surface in (b), on Cu(111) in (c) and on Pt(111) in (d). Experimental spectra shown on top and in darker shade whilst below and in lighter shades are the simulated results. The shifts applied to the DFT spectra (all in eV) are −10.3 (Np/Gas), −10.0 (Az/Gas), −1.95 (Np/Ag), −2.4 (Az/Ag), −4.95 (Np/Cu), −5.2 (Az/Cu), 8.0 (Np/Pt) and −8.1 (Az/Pt).

4.4.2 NEXAFS

Figure 4.5 compares the experimentally recorded NEXAFS spectra with the DFT simulated spectra for all examples. On the top are the experiments and below, shown as shaded spectra are the calculated results. Quantitative comparison between the experiment and simulated spectra can only be carried out once broadening has been applied and so the agreement between the two can heavily depend on the parameters used. In figure 4.5 (a) are the spectra recorded of the multilayer structures and the corresponding isolated molecule simulation performed with a 25° incidence angle. Once again, we can see great agreement between the two, all features present are well reproduced highlighting that again the isolated molecule provides a good approxim-

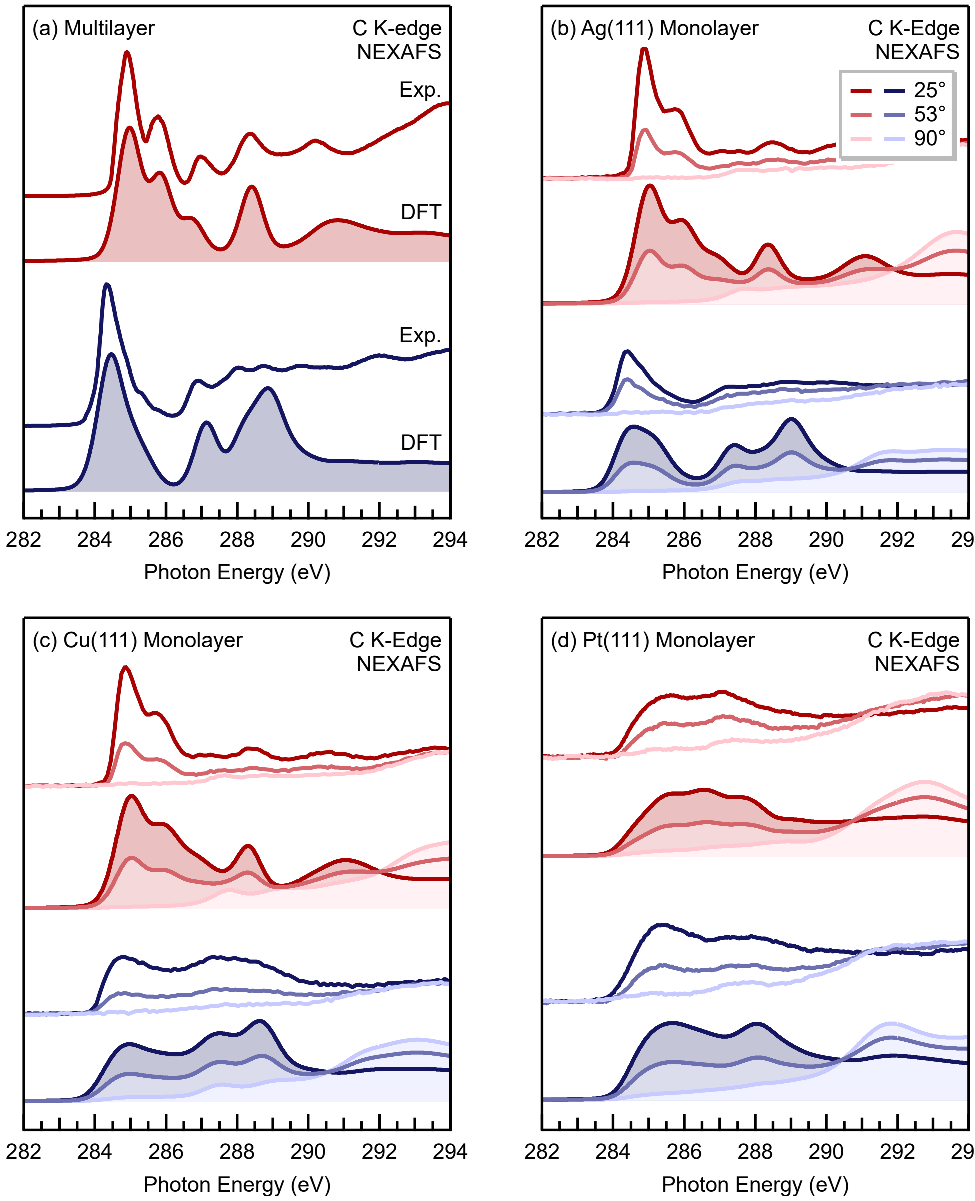

Figure 4.5: Comparison between the experimentally [79–81] and DFT simulated carbon K-edge NEXAFS spectra of azulene (blue) and naphthalene (red). (a) shows the spectra of the thick multilayer recorded at a 25° incidence angle. (b) are spectra for the molecule adsorbed on a Ag(111) surface, (b) for Cu(111) and (d) for Pt(111). Spectra for three different incidence angles of 25°, 53° and 90° are shown from darker to lighter shades. Experimental spectra are shown above with simulated spectra shown as shaded spectra below. The shifts for each spectra (in eV) are multilayer spectra −6.3, Ag(111) and Cu(111) −6.0 and Pt(111) −6.2.

ation for the multilayer system. For the metal adsorbed structures, three different incidence angles are shown in changing shades from dark to light for 25°, 53° and 90°. All spectra show good agreement with a slight discrepancy in the shape of the leading peak for the azulene/Ag(111) case. The simulated peak is much broader with the shoulder occurring at lower energy than in the experiment. This is likely a consequence of the error in the calculated XPS BEs used. As in the ΔIP-TP method the XPS BEs are used to shift the atoms to their relative positions to then sum up to achieve the full spectrum. So, any error that is present in the BEs will show up in the NEXAFS spectrum, this is addressed in section 4.5.3.

4.5 Spurious Charge Transfer in XPS Simulations

This section will focus on investigating the error in the simulated XP spectra that was found for the azulene/Ag(111) case when compared to the experimental spectra that are shown in figure 4.4 (b). A clear disagreement between the experimental and simulated spectra is seen, with the experiment possessing a lower energy shoulder consistent with the multilayer spectra which is not seen in the DFT calculated spectra. This is in contrast with the agreement between the adsorption structure, which could be a cause of the error, but this is not thought to be the reason as good agreement in the adsorption heights is seen in table 4.2. In the following an investigation into the origin of this disagreement is carried out.

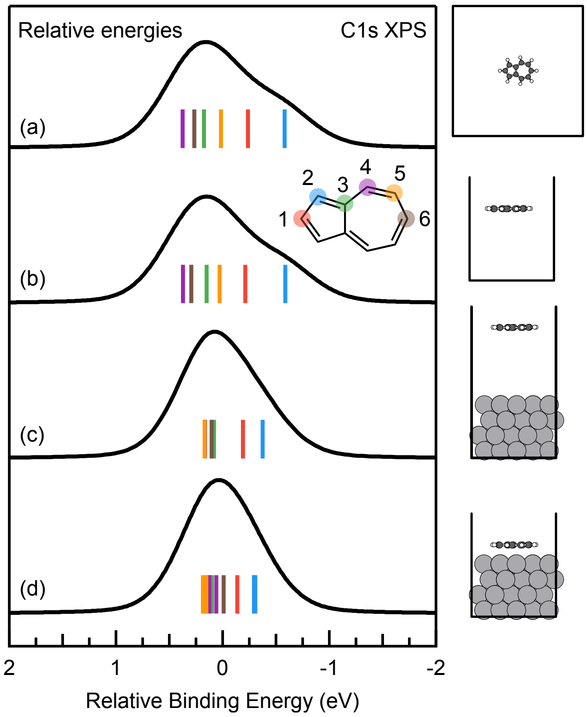

Figure 4.6: DFT simulated XP spectra of azulene in different configurations with individual atom shifts shown as coloured lines. (a) gas-phase, (b) the Az/Ag(111) FSO, (c) Az 12 Å away from the metal surface and (d) the adsorbed geometry. All spectra have been shifted to align their respective centres of gravity.

4.5.1 The Missing XPS Shoulder for Azulene on Ag(111)

Figure 4.6 (a) shows the XP spectrum of gas-phase azulene and figure 4.6(d) the spectrum for the equilibrium structure of azulene adsorbed on Ag(111), both including the contributions of all atomic species. The simulated spectra shown are shifted so that their respective centres of gravity align for comparison. All shifts in the adsorbed species are much more closely spaced than in the gas-phase and the summed XPS spectrum more closely resemble the case of gas-phase naphthalene rather than azulene. It appears that carbon atom 1 (red), which is located at the apex of the 5-membered ring of azulene is least affected by the changes whereas all atoms with higher BEs located at the 7-membered ring are shifted to smaller BEs and lie closer together in the adsorbed case. Simultaneously, carbon atom 2 (blue) on the 5-membered ring is shifted to higher BEs. The result is that all BEs lie within a range of less than 1 eV and the resultant XP spectral envelope constitutes a narrow peak. It is clear that the Az/Ag(111) slab model predicts a strong change in chemical environment on some carbon atoms, which is not present in the experimental data.

Possible causes for the discrepancy with experiment can lie in model errors related to structure, electrostatics, or electronic structure. It has been shown in section 4.4 that the lateral and vertical adsorption geometry of the molecule is in excellent agreement with experimental evidence from low-energy electron diffraction (LEED), scanning tunneling microscopy (STM), atomic force microscopy (AFM), and NIXSW measurements [79, 80]. Therefore, any errors from the misrepresentation

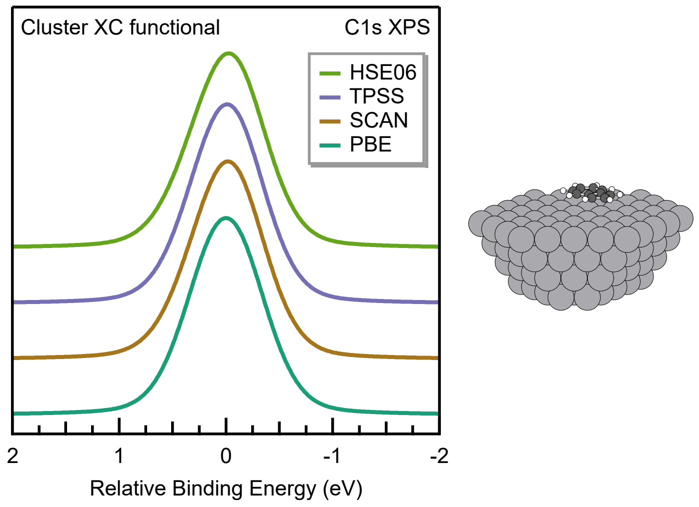

Figure 4.7: Simulated XPS, calculated using the ΔSCF method, of Az/Ag(111) using an aperiodic cluster structure shown alongside. Calculations were performed using FHI-aims for three different XC functionals, HSE06 [123] shown in green, TPSS [119] in purple, SCAN [120] in brown, and PBE [53] in turqouise. HSE06 was calculated using the FOB keyword to constrain the core-hole whilst SCAN, TPSS and PBE utilised the FOP keyword. All spectra are aligned to the average shift of the individual atoms.

of the adsorption structure can be excluded.

DFT core-hole calculations based on ΔSCF of periodic structures risk errors from known electrostatic artefacts that can arise from finite size effects [143]. Core-holes are introduced in all periodic repeats of the unit cell and if unit cells are not sufficiently large, core-holes can electrostatically interact with each other, which leads to shifts in the BEs. These artefacts typically converge relatively quickly with unit cell size and should not be significant in this case [77]. Unfortunately, the introduction of a homogeneous background charge in periodic core-hole calculations, leads to electrostatic interactions that introduce absolute BE shifts that converge slowly with unit cell size [143, 175]. This effect arises due to the presence of a dipole in the unit cell which causes a step in the electrostatic energy when in a periodic arrangement [143]. However, it has been shown that this typically does not affect relative BE shifts between different species once reasonable unit cell dimensions are established [77]. Kahk et al. have recently proposed an approach that remedies these electrostatic effects and enables the prediction of absolute BEs for periodic structures [176].

Figure 4.6 (b) shows the simulated spectrum of the FSO of azulene in the periodicity of the surface slab model. The resulting XP spectrum is virtually unchanged compared to the gas-phase and correctly exhibits a shoulder at low BE. The fact that electrostatics are not the cause of the discrepancy with experiment is further corroborated by our XPS calculations on cluster cut-outs of the Az/Ag(111) structure presented in figure 4.7. Seen here, even without the use of PBCs, the C1s XPS of adsorbed azulene lacks a shoulder at low energy.

Having excluded the effects of structure and electrostatics, the attention can turn to the electronic structure. It is reasonable to assume that the misrepresentation of the XP spectrum could arise from a misrepresentation of charge transfer between molecule and surface. In figure 4.8, the HOMO and LUMO frontier orbitals of azulene are depicted. It can be seen that the HOMO has more probability amplitude located at the 5-membered ring, while the LUMO has more probability amplitude located on the 7-membered ring. Because the HOMO is occupied and the LUMO is not, the net charge on the carbon atoms in the 5-membered ring is negative whereas the 7-membered ring is partially positively charged, giving rise to the substantial dipole moment of the molecule (see table B.7 for net atomic charge and dipole calculations in the appendix).

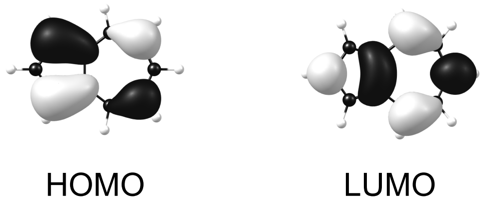

Figure 4.8: Visualisations of the highest occupied molecular orbital (HOMO) and lowest unoccupied molecular orbital (LUMO) for azulene.

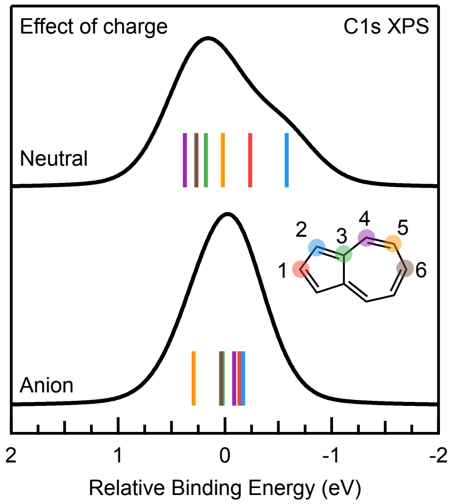

Figure 4.9: DFT simulated XPS of azulene in a gas-phase aperiodic structure, performed with the all-electron software package FHI-aims with the individual atom shifts shown as coloured lines according to the labelled structure. Spectra are calculated using the ΔSCF method with (a) keeping the molecule overall charge neutral or (b) with the molecule left in an anionic state. Spectra have been aligned to the average shift of the individual atom shifts.

Due to this inhomogeneous charge distribution pattern, charge transfer into the LUMO will lead to more charge being located at the 7-ring and a more homogeneous charge distribution in the anion with a smaller total dipole moment (seen in the calculated dipole moments in table B.7), which will affect the BE differences of the carbon atoms. Gas-phase calculations have been performed of the XP spectra of neutral and anionic azulene, which are presented in figure 4.9. As can be seen, the consequence of adding an electron to azulene is that the carbon BEs become more closely spaced, leading to a narrow XPS signature and to the removal of the shoulder in the spectrum. We suspect that the shift of the carbon atoms 1, 3, 4, and 6, (figure 4.6 where the LUMO is localised, is most responsible for the change in peak shape. The occupation of the LUMO is likely also the cause for the removal of the XPS shoulder in the case of azulene adsorbed on Cu(111) where significant surface-molecule charge transfer could be proved [79, 80].

However, known from previous works is that the charge transfer between molecule and surface for Az/Ag(111) as predicted by DFT is small and only amounts to 0.01 e as predicted by Bader charge analysis [80]. Evidence for this is provided by the molecular orbital density of states (MO-DOS) for the adsorbed molecule presented in figure 4.10 (a). All occupied gas-phase MOs are located clearly below the Fermi level; LUMO and LUMO+1 are fully located above the Fermi level. Yet, the simulated XP spectrum is consistent with what we find for a charged gas-phase azulene molecule.

The MO-DOS in figure 4.10 also shows that the molecule is only weakly hybridised with the surface as all MO features are energetically well localised. However, if the issue is due to overly strong chemical interaction and hybridisation rather than charge transfer, then a thought experiment where we lift the molecule from the metal surface should be able to fully restore the XPS spectrum as predicted by the FSO shown in figure 4.6 (b). The result for a calculation where the molecule is 12 Å away from the surface is shown in figure 4.6 (c) and it is puzzling: The XP shoulder at low BE is not restored. While there are some differential shifts between the equilibrium structure in figure 4.6(d), the overall spacing of the peaks increases resulting in a slightly broader XPS peak, this is not sufficient enough to restore the expected peak shape observed in experiment or in the simulated gas-phase or FSO spectra.

The simulation error is then established to be related to the presence of the surface and consistent with charge transfer into the molecule, yet no evidence for such transfer exists in the ground-state DFT calculation for the adsorbed or lifted molecule (see figure 4.10 (a) and (b)). Therefore, attention is turned to the core-hole calculations that are used to simulate the BE shifts. To simulate a spectrum for N number of carbon atoms, N independent DFT calculations are performed, where a 1s core-hole is introduced for each carbon atom in the molecule. The presence of the core-hole leads to orbital relaxation effects and screening of the effective potential that are captured in the total energy that are used to calculate the BE shift. Core-hole relaxation effects can lead to the lifting of orbital degeneracies and orbital realignment that contribute to screening or descreening of the relevant carbon atom. Figure 4.10 (c) and (d) visualises the calculated MODOS for Az/Ag(111) in the presence of the core-hole. The core-hole relaxation effects on the MODOS of this system are substantial. Most importantly, the LUMO is shifted to lower energies to the point that it becomes Fermi level pinned. This is the case for the adsorbed molecule and the molecule at 12 Å distance, where charge transfer is physically impossible due to the lack of orbital overlap.

In summary, the root cause of the discrepancy between experiment and simulation is therefore an artificial charge transfer between surface and molecule that arises during the core-hole calculations. The changes in effective potential as described by the underlying approximate XC functional lead to Fermi level pinning even at a large distance from the surface. This is in contradiction to experimentally measured XP spectra, which are not consistent with a significant charge transfer into azulene upon adsorption. In the following, a correction is applied to the calculations that will demonstrate that this is actually an artefact of the self-interaction error in the XC description within our DFT calculations.

4.5.2 Molecular Orbital Based Self-Interaction Correction: DFT+U (MO)

As can be seen in figure 4.10 (c) and (d), by removing a core-electron from the C1s orbital, the effective potential on the carbon atom becomes more attractive, which reduces the energy of electronic states with probability on this carbon atom. This

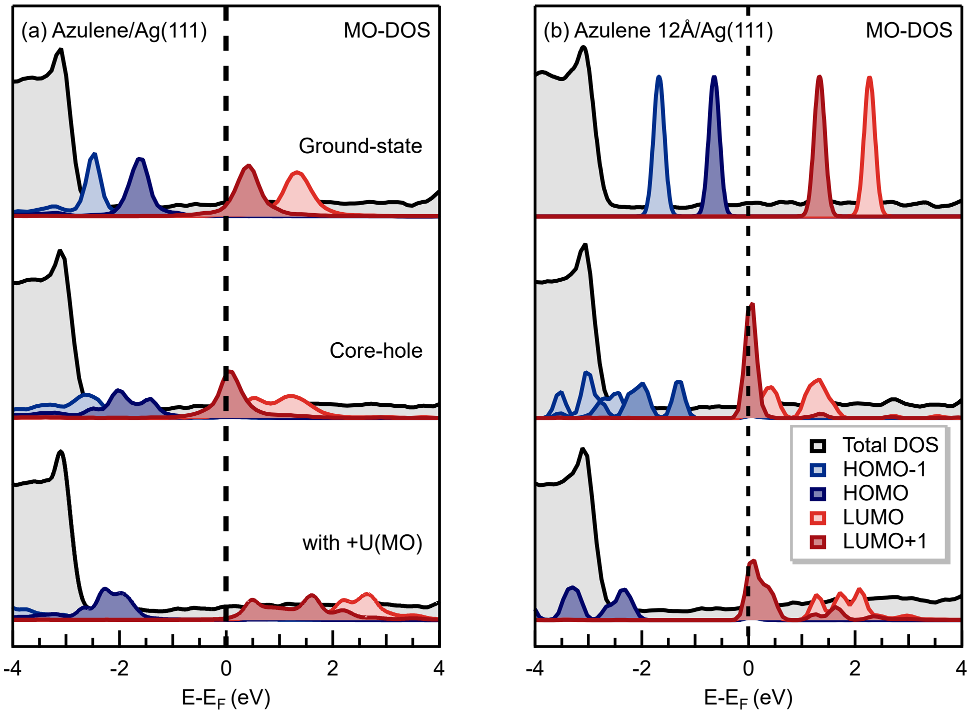

Figure 4.10: Total density of states and MO-DOS of structures of azulene adsorbed on a Ag(111) surface (a) and with the azulene molecule 12 Å away from the metal surface (b). From top to bottom, the DOS for the ground-state system, core-hole excited state and the core-hole excited state with +U(MO). For the core-hole excited DOS, all possible core-hole excited carbon species have been calculated and summed up. Total DOS is shown by the black line with grey shading. MO contributions have been scaled for ease of viewing.

includes most electronic states. Therefore, the fact that the LUMO orbital of azulene becomes Fermi-level-pinned in the core-hole excited state, is likely related to the error in the electron affinity and ionisation potential, i.e. the underestimation of the HOMO-LUMO gap. This underestimation arises from the many-electron self-interaction error of semi-local XC functionals, such as the here employed PBE functional. To explore this point, the gap between the HOMO and LUMO state of the azulene molecule is adjusted artificially with a penalty functional that is added to PBE. This approach is called PBE+U(MO) as it is similar to the use of atomic-orbital-based self-interaction corrections in +U methods, [177–180] but the projector states target gas-phase MOs. This approach has previously been implemented in the CASTEP code [181, 182].

The DFT+U(MO) energy functional [181] is augmented with an additional penalty term that leads to an orbital-dependent potential that increases or reduces the energy of the MO under consideration:

$$\hat{V}_c = \frac{U_c}{2} \left|\phi_c\right\rangle \left\langle\phi_c\right| \tag{4.1}$$

In (4.1), ϕ_c refers to the wave function of the reference MO that is to be constrained.

Table 4.3: DFT calculated gap between the HOMO and LUMO of an azulene molecule in a 20 Å periodic vacuum cube performed with three exchange correlation functionals, PBE, PBE0 and HSE06. PBE+U(MO) value is from a calculation where the positions of the HOMO and LUMO and LUMO+1 were shifted by 2.00, 5.25 and 5.30 eV, respectively

XC functional	HOMO-LUMO gap (eV)
PBE0	3.60
HSE06	2.84
PBE	2.07
PBE+U(MO)	3.60

The potential is applied in each step of the SCF algorithm and leads to the variational optimisation of the KS-orbitals under this constraint. The choice of U values for each constrained MO, c, is *ad hoc* and needs to be manually provided. In the calculations, a constraint is applied to the HOMO, the LUMO, and LUMO+1 orbitals. The values of U that are identified and used by searching for optimal values that give a HOMO-LUMO gap matching the value predicted by the PBE0 functional [121] for the gas-phase azulene molecule in a supercell box. As shown in table 4.3, the HOMO-LUMO gap of the PBE0 functional is matched with the PBE approach with a choice of $U_{\mathrm{HOMO}} = +2.00$ eV, $U_{\mathrm{LUMO}} = +5.25$ eV, and $U_{\mathrm{LUMO+1}} = +5.30$ eV. Several combinations of parameters have been explored including choices with and without application of a constraint to the LUMO+1 orbital. In cases where no constraint is applied to the LUMO+1, the orbital ordering is affected and the LUMO+1 becomes Fermi level pinned. Full details of the range of +U values tested and their performance on shifting the energy levels of each MO are shown in table B.6, the values chosen recreated the orbital gaps found for PBE0 whilst also shifting the MO values higher up in energy than the standard DFT PBE case. The same was applied for the gas-phase naphthalene molecule for the data presented in figure B.4 where the values were $U_{\mathrm{HOMO}} = +2.00$ eV, $U_{\mathrm{LUMO}} = +5.50$ eV, and $U_{\mathrm{LUMO+1}} = +5.55$ eV.

The validity of the PBE+U(MO) approach is tested by first applying it to the molecule at 12 Å distance from the metal surface shown in figure 4.6. The method indeed predicts the correct shape of the XPS in agreement with experiment. The individual carbon BEs and their relative shifts are in fair agreement with what is found for the case of the FSO shown in figure 4.6b. Some of the shifts deviate, particularly the relative BE shift between carbon 1 and 2 in the 5-membered ring. This may be related to the fact that the +U(MO) correction does not fully remove the artificial charge transfer into the molecule for this geometry, as can be seen in the MODOS for the core-hole excited state calculated with PBE+U(MO) shown in figure 4.10(f). This goes to show that even orbital energies equivalent to the hybrid functional level with PBE0 may not be fully sufficient to remove all artefacts.

In figure 4.11, the PBE+U(MO) XP spectrum for the metal-adsorbed geometry is

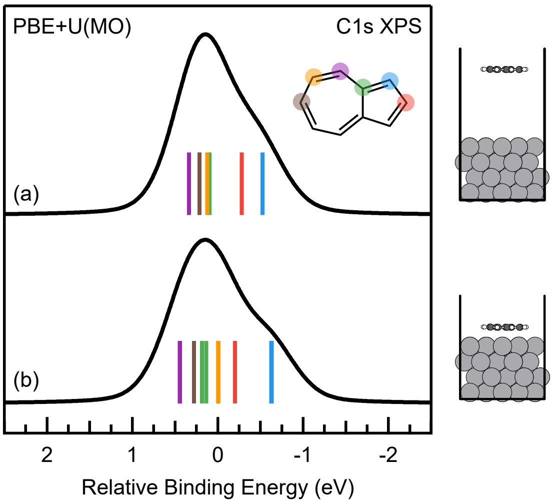

Figure 4.11: DFT simulated XP spectra of azulene 12 Å away from the metal surface (a) and in the equilibrium adsorbed geometry (b) calculated with the +U(MO) correction. Atom shifts shown as coloured lines and all spectra have been shifted to align their respective centres of gravity for comparison.

shown, which is in good agreement with the experimentally measured spectra for the monolayer of azulene adsorbed at Ag(111). Particularly noteworthy is the fact that the individual ordering of the carbon atoms in terms of their BE is fully preserved upon adsorption of the molecule. This is not unexpected as the molecule is only weakly hybridised and adsorbs in a physisorbed state at about 3.1 Å from the metal surface [80].

This is the same scenario as for Np/Ag(111), where the multilayer, monolayer, and gas-phase XP spectra of the molecule are virtually identical. It should be noted that the spectral prediction for Np/Ag(111) may also suffer from errors associated with the XC approximation, but similarity between the BEs of all the carbon atoms makes it impossible to use the experiment as meaningful benchmark reference. In fact, Np/Ag(111) suffers from the same artificial charge transfer issue as azulene as can be seen in figure B.4. But this issue does not measurably materialise, because due to the homogeneous electronic structure of naphthalene, the charge transfer shifts the contributions of all atoms equally and does not introduce a relative shift as can be seen in figure B.5 in the appendix. In figure B.4 the results of the PBE+U(MO) approach for the Np/Ag(111) are compared. The XP spectrum with the regular PBE result is virtually indistinguishable from the +U(MO) result. In contrast, the artificial charge transfer into azulene predominantly affects the shifts of the carbon where the LUMO has significant probability amplitude (figure B.5), which changes the shape of the spectrum.

It should be noted that this approach is not a universal solution to charge transfer artefacts that can arise from self-interaction error, but rather an *ad hoc* correction to exemplify the problem. The penalty potential applied to MO gas-phase reference orbitals is also only reasonable in cases where the MO gas-phase orbitals remain meaningful representations of the electronic structure, so where the molecule is only weakly hybridised with the surface.

Lasting solutions to this artefact require either the use of better exchange correlation functionals with non-local exchange and correlation description or the use of excited-state methodology beyond simple ΔSCF-based core-hole constraints. Note that even the use of range-separated hybrids such as HSE06 [123] does not remedy the shoulder problem for the cluster cut-out we studied in figure 4.7, however, the HOMO-LUMO gap predicted by HSE06 is also considerably lower than that of PBE0 [121]. Unfortunately, bare hybrid XC functionals such as PBE0 cannot simply be applied to the study of metals as they do not provide a reliable prediction of the metal electronic structure, but optimally tuned range-separated hybrid functionals with custom optimised parameters for individual systems may be able to address the problem [183, 184].

4.5.3 Implications of Charge Transfer Artefacts for NEXAFS Predictions

The role of XC errors and the resultant charge transfer artefacts in XPS simulation of metal-organic interfaces is a cautionary tale as this can lead to the misinterpretation of spectra and wrong conclusions on the surface chemistry. However, this error can also further affect the simulation of K-edge NEXAFS spectra at metal-organic interfaces, which are highly valuable for the interpretation of the surface-adsorption-induced changes in electronic structure and also the molecular orientation at the surface [17, 24].

While the most common approach to XPS simulations at the DFT level is the use of ΔSCF in combination with the MOM, [65] x-ray absorption is commonly simulated with the TP method [76] based on the TS approach [60]. In its realisation in periodic plane wave codes, the core-hole relaxation effects on the valence electronic states are simulated via the introduction of a half core-hole and a single TP calculation of the KS eigenvalues. As the atomic nucleus is represented by a PP in this approach, the ionisation potential associated with the removal of an electron from the 1s state is then corrected by shifting the spectrum with respect to the BE of the 1s state of the relevant carbon atom calculated with the ΔSCF method, this approach is called ΔIP-TP [77, 110]. Therefore, prediction errors in the XPS propagate into errors in the NEXAFS predictions as changes in relative BE shifts will lead to the misalignment of excitations that arise from different core-states into the same valence states.

In figure 4.12 we show the experimentally measured K-edge NEXAFS spectrum of azulene adsorbed on Ag(111) [80] against the ΔIP-TP prediction corrected by PBE XPS onsets (in figure 4.12 (b)) and PBE+U(MO) onsets (in figure 4.12 (c)). Here the first resonance of the NEXAFS spectrum based on the U-corrected XPS energies

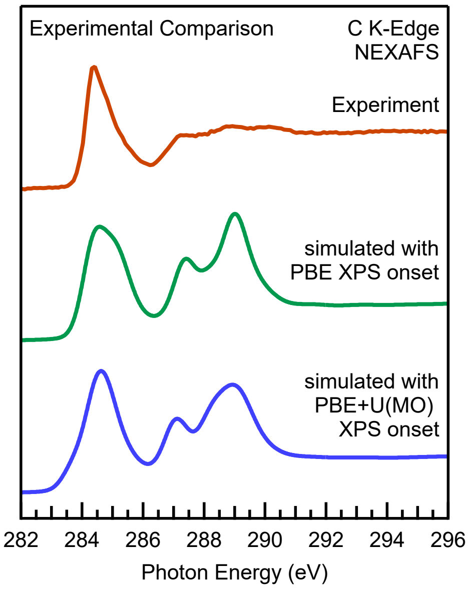

Figure 4.12: Comparison of the experimentally measured and simulated NEXAFS data for azulene/Ag(111). (a) experimental NEXAFS spectrum, (b) and (c) show NEXAFS simulations using the ΔIP-TP method with two different onset corrections to sum up the spectra. (b) uses the XPS binding energies obtained from a ΔSCF calculation with PBE and (c) from a ΔSCF calculation with PBE+U(MO). The simulated spectra have been shifted to align with the experimental energy scale. For both experimental and simulated data, a 25° incidence angle was chosen. Experimental data taken from Ref. [80].

becomes narrower and the broad shoulder present at about 285 eV in the PBE-only prediction is reduced. Note that only the conventional PBE functional for the TP calculations of the valence state relaxation and not the +U(MO) approach, because the orbital ordering and spacing of the unoccupied states will likely be affected by the +U(MO) correction. This is due to the fact that we have only selected U values under the criterion to reproduce the PBE0 HOMO-LUMO gap, but not to correctly capture the optical 1s→LUMO+X excitations of the system.

4.6 Pyrene and Azupyrene

It can be seen that excellent agreement of experimental core-level spectra with simulations can be obtained for the systems involving azulene and naphthalene adsorbed on various surfaces. These molecules presented an initial benchmark to test the accuracy of the calculations, and now the method is tested further by looking at slightly larger molecules of pyrene and azupyrene.

XPS and NEXAFS experiments were performed by Klein et al. [157] and carried out on multilayer structures of pyrene and azupyrene (to reduce the influence of a metal surface) and monolayer structures of the molecule adsorbed onto a Cu(111) surface. The XP spectra for these systems are shown in figure 4.13. To compare with the

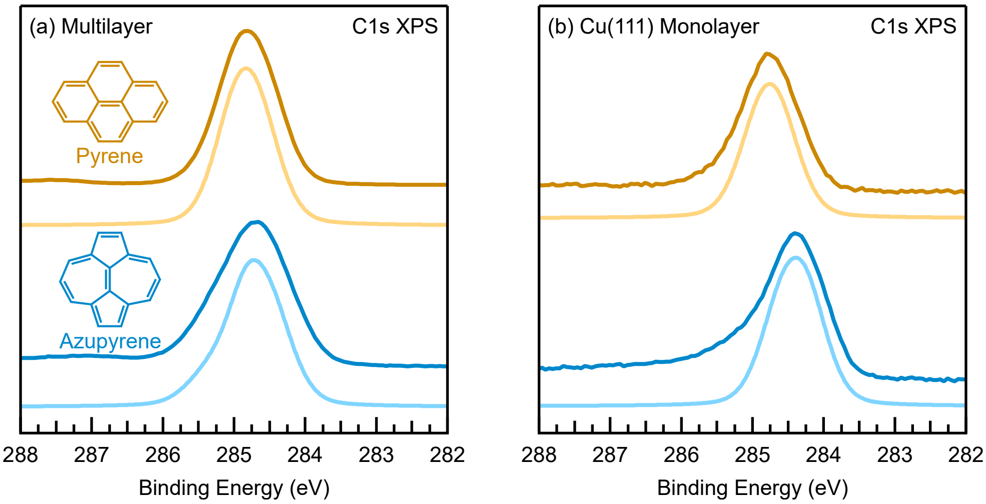

Figure 4.13: Comparison between experimental [157] and DFT simulated C1s XPS spectra of pyrene (orange) and azupyrene (blue) in a multilayer structure (a) and adsorbed on a Cu(111) surface (b). Experimental spectra are shown above in darker shades whilst simulated spectra are shown below in lighter shades. The DFT spectra are shifted (in eV) by −10.44 for the multilayer spectra and for the Cu monolayer, −8.7 for pyrene and −8.17 for azupyrene.

multilayer structure, the isolated molecule was simulated in a large vacuum box with this approach resulting in agreement with the experiment as seen in figure 4.13 (a). Pyrene (orange) shows a symmetric peak shape whereas azupyrene has a slightly broader peak with a tail at high energy which is well represented in the simulation. When both molecules are adsorbed onto the metal surface the spectra in figure 4.13 (b) show little change to the multilayer spectra. For azupyrene, the same behaviour as seen with azulene would be expected and this is seen with the loss of the tail when compared to the multilayer spectra. This is seen more clearly in the simulated spectra as in the experiment a the asymmetry in the spectra is from the strong interaction (an energy loss effect).

The NEXAFS spectra for both the multilayer and Cu(111) monolayer are presented in figure 4.14 alongside the simulated spectra for comparison. The isolated molecule in a large vacuum box once again can model the multilayer spectra well. Excellent agreement with the first feature in the pyrene spectrum is seen as it accurately models the first two peaks. For azupyrene the same two maxima are seen in the simulated but the second maxima is not as well defined in the experiment, but is present in the shoulder of the peak. The spectra for the molecule adsorbed on the Cu(111) surface shows the interaction between the molecule and metal surface is presented in figure 4.14 (b). Three different incidence angles are shown for each molecule at 25°, 53° and 90°. Compared with the multilayer spectra, the features in the pyrene spectra are broadened but not to the extent seen for azupyrene where the features seen in the spectra have significantly smeared out. This is representative of an increased

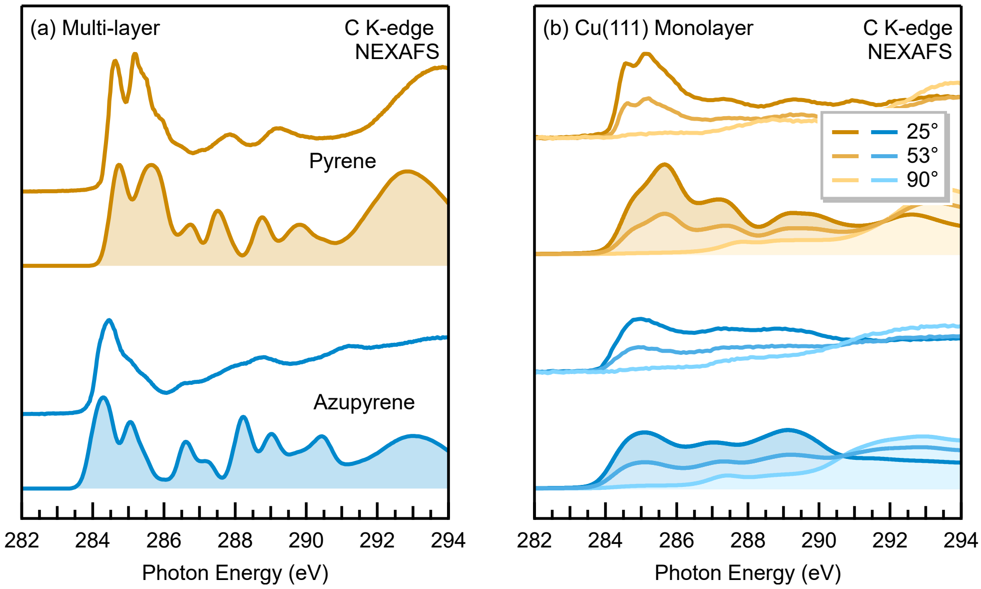

Figure 4.14: Comparison between experimental [157, 185] and DFT simulated C K-edge NEXAFS spectra of pyrene (orange) and azupyrene (blue) in a multilayer structure (a) and adsorbed on a Cu(111) surface (b). Experimental spectra are shown above in darker shades whilst simulated spectra shown below as shaded spectra. Multilayer spectra are recorded with an incidence angle of 25° whist the monolayer Cu(111) spectra are shown at three incidence angles of 25°, 53° and 90° in increasingly lighter shades. DFT spectra are shifted by -6.3 eV for the multilayer spectra and -6.0 eV for the Cu monolayer.

interaction between the molecule and the metal surface and was previously also seen for Az/Cu(111).

4.7 Conclusions

Following on from detailed analysis into the behaviour of the effect of topology in molecule-metal interactions that had previously been carried out, [79–81, 157, 185] core-level spectra were simulated with DFT using accurate adsorption geometries and compared to the experiments. Both the XPS and NEXAFS spectra were compared with simulations using the ΔSCF and ΔIP-TP methods, respectively. For azulene and naphthalene, across of multilayer and monolayer structures adsorbed onto Ag(111), Cu(111) and Pt(111), a total of eight different systems were recorded. Agreement between both the XPS and NEXAFS spectra was observed from the weakest interaction to the strongest. However, it was found that in the case of Az/Ag(111), spurious charge transfer caused a disagreement in the XP spectra which also follows through into the NEXAFS simulation. This effect arises from a self-interaction error and was reduced through the use of the +U(MO) method where a penalty functional is applied onto chosen reference orbitals to shift them either higher or lower in energy. By shifting the HOMO, LUMO and LUMO+1, the erroneous Fermi level pinning of the LUMO that was the cause of the charge transfer was able to be stopped and the resulting XPS spectra agreed with the experimental result. By applying this correct XPS BEs in the offset of the NEXAFS spectrum for Az/Ag(111) a better agreement in the leading peak is found. Further work in the future into identifying the types of systems where this is most prevalent should be carried out.

The simulations were then tested on a larger set of molecules, pyrene and azupyrene. Agreement with the experiment was once again achieved for both XP and NEXAFS spectra. Once again, the level of interaction can between the molecule and the metal surface can be seen in the spectra. Comparing the multilayer and Cu(111) monolayer, the interaction for pyrene is minimal and this is present in the spectra with minor changes seen across the two structure. Whereas for azupyrene, the interaction is much greater, and this substantially effects the spectra with clear and noticeable changes.

Chapter 5

Influence of the Interaction Strength at the Metal-Organic Interface on Core-Level Spectroscopy

Work presented in this chapter has been written up into a paper which will be submitted in the future.

5.1 Introduction

The strength and nature of interactions at a hybrid organic-inorganic interface crucially influence the performance of organic electronic devices, e.g. organic light emitting diodes [3, 6] or organic field effect transistors [186, 187]. To gain insight into the fundamental mechanisms of the interaction at the interface, model systems consisting of organic molecules adsorbed on single-crystal metal surfaces are often studied using surface science techniques [188]. Here, X-ray core-level spectroscopies such as X-ray photoelectron spectroscopy (XPS) and near edge X-ray absorption fine structure (NEXAFS) spectroscopy represent effective tools to characterise the electronic structure of the investigated model systems [17, 44].

However, the interpretation of the experimental spectra can be highly challenging in many cases. Often a large number of unoccupied states contribute to the spectra and overlap significantly. This complicates both initial-state decomposition according to the involved core-levels (XPS and NEXAFS), as well as the characterisation of final conduction band states (NEXAFS). Furthermore, without any further atomic-level information on the adsorption structure and electronic properties of the interface, the spectra cannot be connected to important conceptual quantities that relate to the nature of the molecule-surface bond, such as the adsorption energy and height, the magnitude of charge transfer, and the hybridisation between the electronic states originating from surface and molecule, respectively.

First-principles core-level spectroscopy simulations support the interpretation of experimental spectra and are able to disentangle the spectra according to the present initial- and final-state effects. The methodology taken in this work has been performed and studied before and shown to be a robust method for core-level spectroscopy [77, 78]. Advantages of using this approach are that more detailed understanding of the adsorption geometry, chemical bonding and electronic structure can be gained [189–191].

The interaction between a molecule and a metal surface is dependent on the electronic and geometric structure of both participants. On the side of the metal, the reactivity of the substrate can be modified by varying elements while maintaining the same crystal structure and surface orientation. Noble metal surfaces with (111) surface orientation are commonly used model surfaces in this regard. As can be directly inferred from the d-band model of surface chemical bonding, [192, 193] the reactivity of the surface increases from Ag(111) to Cu(111) to Pt(111).

On the side of the organic molecule, a wide range of options to tune reactivity exist. The structural variety of organic molecules is almost infinite and minor structural changes can lead to large changes in reactivity. Take two simple examples of aromatic hydrocarbons, azulene and naphthalene. These two molecules are an isomeric pair of bicyclic aromatic hydrocarbons and only differ by the topology of their aromatic system. Naphthalene consists of an alternant 6-6 ring structure and azulene of a non-alternant 5-7 ring structure (see insets in figure 5.1 (a)) [194]. This topological difference between azulene and naphthalene has a large influence on the molecular properties. Solutions of azulene show a brilliant blue colour and azulene has a substantial dipole moment while naphthalene is colourless and possesses no dipole moment [157, 169]. The ability of the two molecules to interact with metal surfaces is also strongly influenced by the different topologies.

A series of recent publications have produced a comprehensive picture of the surface bond of naphthalene and azulene adsorbed onto Cu, Ag and Pt (111) surfaces [79–81, 156]. The thorough characterisation in the literature includes the elucidation of the adsorption geometry, energetics and electronic properties by means of various experimental techniques such as NIXSW, [79, 80] LEED, [79] XPS, [79–81] NEXAFS, [79–81] TPD, [79, 156] and single-crystal adsorption calorimetry (SCAC), [81] all combined with DFT simulations. The two molecules and three surfaces represent six interface models that are comprehensively characterised in terms of their structure and electronic properties, which makes them ideally suited for the investigation of how the nature of the respective molecule-metal interaction is reflected in core-level spectroscopic signatures.

This chapter will build on the work detailed in the previous chapter and focus on the six molecule-metal interface models of azulene and naphthalene adsorbed on Ag(111), Cu(111) and Pt(111). Presented will be a comprehensive study of the C1s XPS and C-K edge NEXAFS simulations employed through ΔSCF [60, 61, 113] and ΔIP-TP [70, 71, 76] methods respectively. These were chosen to characterise and analyse the XP and NEXAFS spectra of these large periodic systems. It is found that the three different bonding regimes lead to characteristic signatures and changes in the respective spectra compared to pristine gas-phase spectra. It is possible to distinguish between three different molecule-metal surface bonding regimes being physisorption, weak chemisorption (one-way charge transfer) and strong chemisorption (two-way charge transfer leading to molecular rehybridisation). This could prove useful to interpret experimental spectral changes for complex hybrid organic-inorganic thin films.

5.2 Computational Details

The methods used to calculate the XP and NEXAFS spectra shown in this chapter are the same as previously presented in the previous Chapter 4 and full details of the core-level spectroscopy simualtions can be found in section 4.3. Additional details for this chapter are on the post-processing of the data, which was carried out through the use of a post-processing tool, MolPDOS, [104] which is part of the CASTEP source code. The molecular orbital (MO) projection scheme contained in this tool was used to estimate, what part of the spectrum can be attributed to the electronic structure of a reference system. When applying this method for gas-phase molecules, the same structure is chosen as reference, allowing for a full decomposition of the NEXAFS spectrum in terms of the individual MO states of the molecule. For molecules adsorbed on surfaces, the FSO was chosen as reference and a MO projection was performed to determine the overlap of its electronic states with the final-states of each transition in the total system. With this it is possible to identify which part of the core-level excitations can be attributed to the reference MO states of the molecule but unlike for gas-phase molecules the exact contribution to the spectra is not achievable as described in section 3.4.3. Previous work has shown this approach to work consistently well to identify molecular contributions to adsorbate spectra [77, 157].

5.3 Results

5.3.1 Effect of Molecular Topology on XPS and NEXAFS Signatures

The first aspect to look at is how the difference in topology between azulene and naphthalene changes their gas-phase XP and NEXAFS spectra (see figure 5.1). In the previous chapter, in order to achieve a direct comparison between simulated and experimental spectra, a global rigid energy shift was applied to simulated spectra to match the experimental energy scale. This correction is necessary due to the frozen-core approximation in the pseudopotential plane-wave calculation used [77]. For this chapter, the focus will solely be on the simulated spectra with no comparison to experimental data. Therefore, all spectra will be shown with the original energy scale obtained by the calculations.

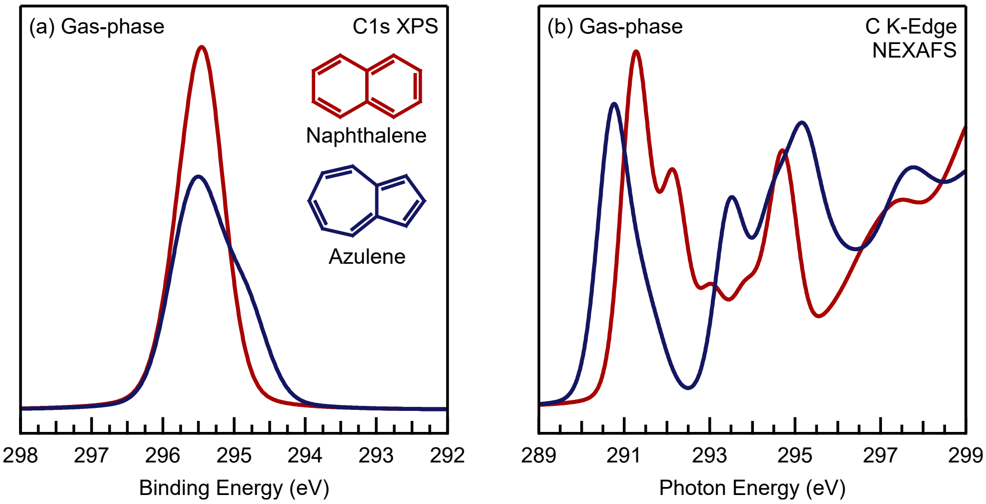

Figure 5.1: Comparison of the simulated core-electron spectra for the gas-phase molecules naphthalene (red) and azulene (blue). (a) C1s XP spectra. (b) C K-edge NEXAFS spectra.

The topological difference between naphthalene (alternant 6-6 structure) and azulene (nonalternant 5-7 structure) has a strong influence on both the XPS and NEXAFS data. In the XP spectra (figure 5.1 (a)) a much broader peak is observed for azulene, with a pronounced shoulder visible at lower BEs. In the NEXAFS spectra (figure 5.1 (b)) azulene shows the leading edge at lower photon energy and the first peak has a shoulder at higher energy, while naphthalene has its leading edge at higher photon energy and two maxima within the first spectral feature.

The XP and NEXAFS spectra can be analysed by disentangling the initial-state and final-state contributions to the overall spectrum, as shown in figure 5.2. The individual contributions of each carbon atom to the total XP spectrum are shown for naphthalene (figure 5.2 (a)) and azulene (figure 5.2 (b)). The shoulder of the peak in the azulene spectrum can be attributed to the carbon atoms in the 5-membered ring possessing a lower C1s BE than those in the 7-membered ring. For naphthalene, the C1s BEs are similar for all carbon atoms, with only slightly larger values for the bridging carbon atoms, yielding an almost symmetric peak shape.

In contrast to the shown initial-state decomposition of the XP spectra, the decomposition of the NEXAFS spectra (figure 5.2 (c), (d)) is performed according to the final-state contributions to the transitions, i.e. the contribution to the spectrum that arises from all 1s transitions into the LUMO, the LUMO+1 etc. Each coloured peak represents all transitions into the same molecular orbital as final-state, no matter what the initial-state, i.e. C1s orbital, is involved. For naphthalene (figure 5.2 (c)) the first three peaks in the spectra can clearly be seen to originate from transitions into the three lowest unoccupied molecular orbitals (LUMO, LUMO+1, LUMO+2). For azulene (figure 5.2 (d)) the first peak consists of transitions into the first two unoccupied orbitals, with the transition into the LUMO forming the leading edge and

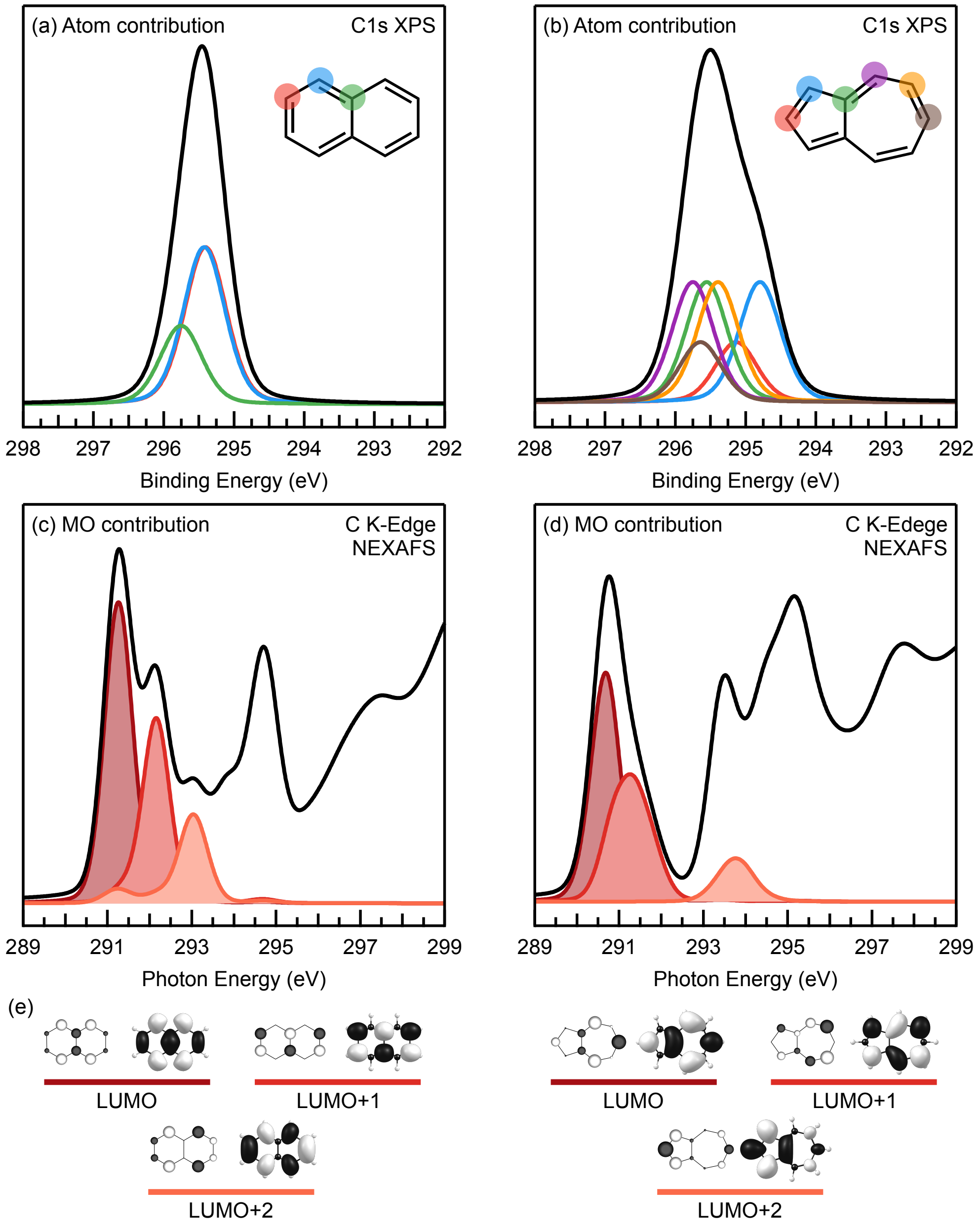

Figure 5.2: Initial-state decomposition of the XP spectra (top) and final-state decomposition for the NEXAFS (bottom) for gas-phase azulene on the left and naphthalene on the right. (a) and (b) show the contributions of each C1s atomic orbital to the XP spectrum, with coloured lines showing the corresponding atoms in the structure. (b) and (c) show the molecular orbital decomposition of the NEXAFS spectra. Red shaded peaks show the contribution of the respective orbital to the spectrum from LUMO to LUMO+2, increasing in lighter shades. The corresponding MOs are visualised in (e).

the transition into the LUMO+1 forming the shoulder at higher photon energy.

The simulations show that the topology of the molecular backbone has a pronounced influence on the shapes of the spectral features both in XPS and NEXAFS. The overall shape of the simulated spectra is also in good agreement with experimental data for multilayers of the molecules [79, 81]. However, the topology of the molecules also affects the adsorption of the molecules on metal surfaces, discussed in the next section.

5.3.2 Properties of the Molecule-metal Interfaces

To sample a wide range of different molecule-metal interactions, the two molecules naphthalene and azulene were combined with three different metal (111) surfaces of increasing reactivity, namely Ag(111), Cu(111), and Pt(111). Comprehensive experimental investigations into these systems are available in the literature and provide a thorough characterisation of the molecule-metal interaction based on a wide variety of experimental and theoretical techniques [79–81, 156]. Figure 5.3 summarises this information regarding all the metal-organic systems involved, arranged in order of increasing interaction between the molecule and the metal surface as given by the adsorption energy. The top row of figure 5.3 shows the structures of naphthalene and azulene, while the second row contains the side-on view of the adsorbed structure to highlight the change in adsorption height and molecule deformation. Below is a table containing a range of parameters that can be used to describe the level of

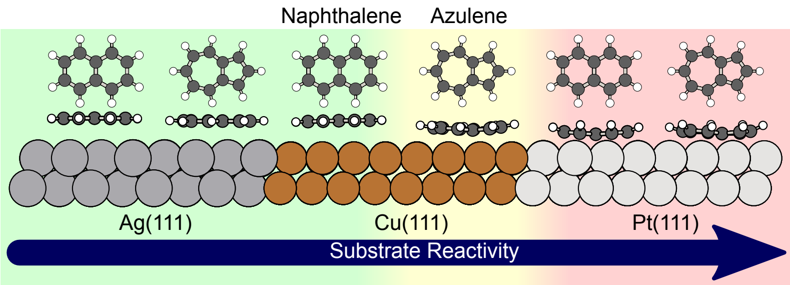

Adsorption Energy (kJ/mol)	118	128	135	173	298	335
Adsorption Height (Å)	3.10	2.94	2.96	2.33	2.09	2.10
Net Charge Transfer (e)	0.06	0.01	0.06	-0.49	0.03	0.02
Structural Deformation	None	None	None	Weak	Strong	Strong
Molecule-Metal Hybridisation	Weak	Weak	Weak	Intermediate	Strong	Strong
Regime	Physisorption			Weak Chemisorption	Strong Chemisorption	

Figure 5.3: Schematic depiction of six metal organic interfaces arranged according to increasing interaction strength. Background colour represents the classification of the interaction type: green, physisorption regime; yellow, weak chemisorption regime; red, strong chemisorption. The table shows adsorption energies and adsorption heights calculated using DFT-D3 calculations and charge transfer, as well as two qualitative criteria for the interaction strength. The presented data is compiled from Refs. [80, 81, 156]. The values for the charge transfer are results of the Bader atoms-in-molecules method. Further results of additional charge transfer analysis methods are shown in table B.7.

interaction between the molecule and metal surface. Moving across from left to right, the reactivity of the metal increases from Ag to Cu and Pt. Accordingly, the adsorption energy increases, and the adsorption height decreases, showing the strengthening of the bond between the molecule and surface. Furthermore, when comparing different molecules adsorbed at the same metal surface, a stronger interaction is observed for azulene than for naphthalene. The 5-7 nonalternant topology of azulene therefore leads to an increased reactivity at the metal-organic interface [79].

In contrast to the clear trends in adsorption energy and height, the charge transfer between the molecule and surface paints a more complicated picture. For the first three systems, both molecules on Ag(111) and Np/Cu(111), little to no charge transfer between the molecule and the metal can be observed. For Az/Cu(111) a substantial amount of charge transfer, -0.49 e from the surface to the molecule, shows a strong interaction between the electronic states of the molecule and metal. But for both molecules adsorbed on Pt(111), the overall net charge transfer is of vanishing magnitude. This finding seems to indicate a weak electronic interaction with the Pt(111) surface, even though the values of the adsorption height and energy show a very strong bond and the molecule is strongly deformed upon adsorption. This contradiction can be explained by a strong electronic interaction based on donation and backdonation of electrons between the metal and the surface. In the case of Az/Cu(111), with an adsorption height of 2.33 Å, only the diffuse unoccupied orbitals of the molecule overlap with the electronic states of the metal surface, resulting in unidirectional electron transfer from the surface to the molecule. Because both molecules are much closer to the Pt(111) surface, the more compact occupied electronic states of the molecule are now also available for electron backdonation into the unoccupied states of the metal surface. The resulting situation is a two-way charge transfer with donation and backdonation comparable to the situation in many organic transition metal complexes as described by the Dewar-Chat-Duncanson (DCD) model [81, 195, 196].

Finally, the six systems can be compared by the qualitative parameters of structural deformation and hybridisation of the electronic states of molecule and metal. The deformation describes how much the molecule and the surface are changed in the adsorbed structure compared to their relaxed structures. Again, the first three systems show only weak disturbance, with a planar molecule and all molecular C-C bond lengths unchanged [79, 80]. For Az/Cu(111), the deformation can be classified as weak, because a slight buckling is now present in the molecule and bond lengths have started to change noticeably [79, 80]. The structure of both molecules changes much more when adsorbed on Pt(111). Here, the molecules are strongly buckled, with the hydrogen atoms pointing upwards away from the surface. For all carbons, the bond angles and bond lengths are more in agreement with aliphatic sp^3 geometry than the aromatic sp^2 geometry of the free molecules [81]. The pattern observed for the deformation is repeated in the hybridisation between electronic states of the molecule and metal surface, which can be assessed by analysis of the projected density-of-states

(DOS) of the system. Only weak hybridisation is present for the first three systems with the MO signatures only weakly broadened [79, 80]. For Az/Cu(111) projected MO signatures in the DOS are further broadened and exhibit some level of splitting [79, 80]. For both molecules on Pt(111) molecular resonances are strongly hybridised with the metal covering a wide range of energies across the DOS [81]. The topic of hybridisation will be discussed in detail in the context of the core-level spectra.

All the information laid out above is supported by the experimental data in shown in Chapter 4 and leads us to identify three different regimes of interaction strength between the molecules and the metal surface. Type I (shaded in green in figure 5.3), which includes naphthalene on Ag(111) and Cu(111) and Az/Ag(111), is the weakest level of interaction, and can be described as physisorption. Type II (yellow) contains solely Az/Cu(111), and is best described as "weak chemisorption". The main indicator of this regime is the presence of a one-way charge transfer between metal and molecule that arises from Fermi level pinning of the azulene LUMO. Finally, Type III (red) encompasses naphthalene and azulene on Pt(111), which is designated as "strongly chemisorbed" systems that exhibit strong molecular deformation, large adsorption energies and adsorption heights consistent with atomic covalent radii. In the following sections the characteristic spectral features in XP and NEXAFS spectroscopy associated with the three regimes of molecule-metal interaction strength are discussed.

5.3.3 Physisorption Regime

The physisorption regime describes the weakest level of interaction between the molecule and metal surface and includes azulene and naphthalene on the Ag(111)

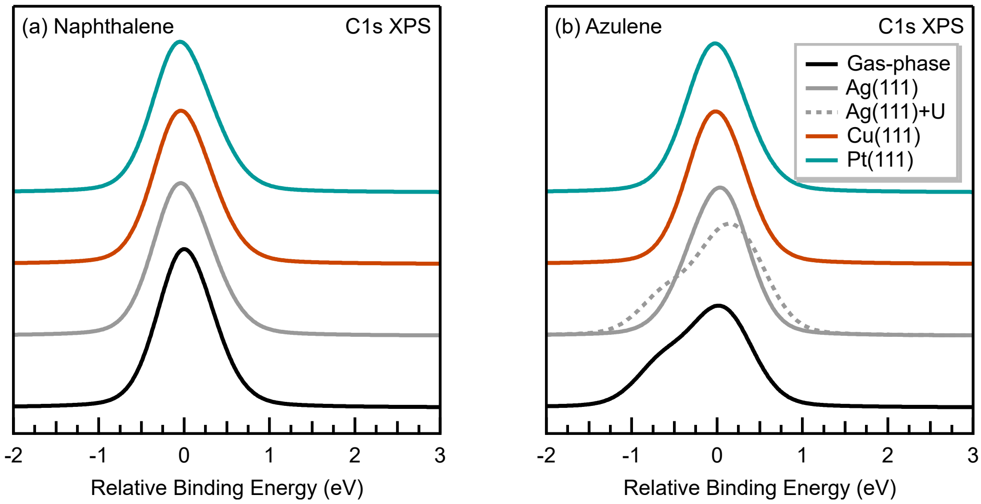

Figure 5.4: Comparison of XPS spectra for naphthalene (a) and azulene (b) in the gas-phase (black), and adsorbed on three metal surfaces, Ag(111) (grey), Cu(111) (orange), and Pt(111) (green). Dashed grey line for Az/Ag(111) is the +U(MO) corrected XPS. Spectra of the metal adsorbed systems have been aligned to the centre of mass.

surface and Np/Cu(111). The XPS spectrum of naphthalene in the gas-phase and adsorbed onto Ag(111) and Cu(111) are virtually identical as can be seen in figure 5.4. In the case of Az/Ag(111) it would seem that there is a noticeable change seen in the XPS spectra when compared to gas-phase azulene. However, this behaviour has been found to be the cause of a self-interaction error which causes spurious charge transfer between the molecule and metal and has been discussed in greater detail in in the previous chapter in section 4.5. Where it was discussed how this error can be addressed with an *ad hoc* correction and when done so the XP spectra (shown in figure 5.4 (b)) align much more with the gas-phase spectra.

Figure 5.5 (a) compares the simulated NEXAFS spectra of naphthalene in the gas-phase and adsorbed on Ag(111) and Cu(111). For each system, three different polarisation angles between the incident radiation and the molecular plane or surface normal are shown. Alike in the XPS, it is apparent that the adsorption of the molecule on the metal surface does not introduce major differences in the NEXAFS spectrum

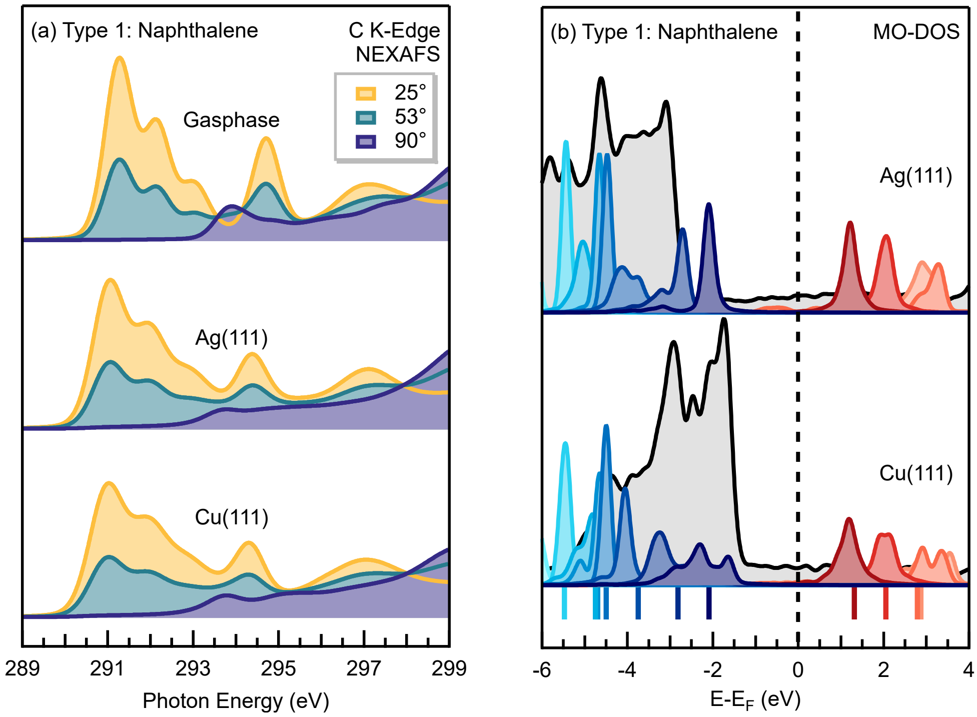

Figure 5.5: Electronic structure of the systems in the physisorbed regime (a) DFT calculated NEXAFS spectra of naphthalene: top, gas-phase; middle, adsorbed on Ag(111); bottom, adsorbed on Cu(111). For each system three different incidence angles are shown (25°, yellow; 53° green; 90°, blue). (b) DFT density of states (DOS), with scaled MO projections: top, Np/Ag(111); bottom, and Np/Cu(111). The total DOS is shown in black and the Fermi level as a dashed line, contributions from orbitals scaled for ease of viewing. Contributions shaded in blue represent projection onto occupied states, while contributions shaded in red represent unoccupied states. Lighter shades of these colours show states lower or higher in energy respectively. Coloured lines are bottom of graph represent position of the gas-phase orbitals.

when compared to the gas-phase. In this case, the only difference observed is a weak additional broadening, whereas peak positions and intensities are not strongly affected. The inspection of the spectra with different polarisation angles also shows that the dichroism from the gas-phase spectra is retained, i.e. the dependence of the signal with respect to the incident light polarisation. In all cases, the signals from the first two peaks diminish almost completely to zero for the normal incidence case. The fact that these peaks vanish at normal incidence is due to the orientation of the unoccupied states with respect to the incident radiation as described in section 2.1 (figure 2.4). As the LUMO, LUMO+1, and LUMO+2 are π^* orbitals, for which the molecular plane contains a nodal plane, they can only interact with light that has a polarisation contribution perpendicular to the molecular plane. As the light polarisation vector is perpendicular to the propagation direction, near-grazing incidence light shows the highest intensity for these resonances.

To show the reason for the lack of change in the NEXAFS spectra, the molecular orbital projected density-of-states (MO-DOS) is shown in figure 5.5 (b). Here, a present and clear gap between occupied molecular states (in shades of blue) and unoccupied states (in shades of red) is observed for both systems. The occupied states remain below the Fermi level (dashed line) and all unoccupied states stay above it, which indicates negligible charge transfer between molecule and surface. A small

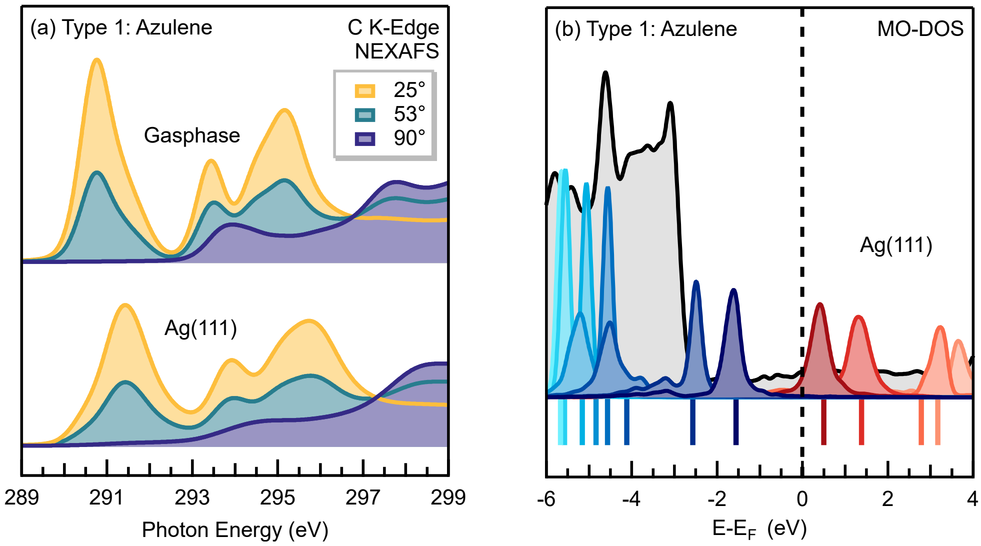

Figure 5.6: DFT calculated NEXAFS spectra of azulene in two different systems. Gas-phase (top) and the type I system, adsorbed on a Ag(111) surface (bottom). Three different incidence angles are shown of 25° (yellow), 53° (green) and 90° (blue). (b) shows DFT density of states (DOS) of the metal adsorbed system. Total DOS is shown in black and Fermi level shown with dashed line, contributions from orbitals scaled for ease of viewing. Orbitals labelled in blue represent the HOMOs and red the LUMOs with the lighter shade moving lower or higher in energy respectively. Coloured lines at the bottom of the graph represent the position of the gas-phase orbitals.

contribution of a higher LUMO state is seen below the Fermi level, however, this is a consequence of an unbound state and not fully representing a MO. The same observations can also be made for azulene adsorbed on Ag(111), for which the graphs are presented in figure 5.6. The coloured lines at the bottom of the figure 5.5 (b) are the molecular states of the gas-phase molecule. It can be seen that there is little shift in the positioning of the orbitals however some differences can be seen between the two metal surfaces. For copper, the orbitals are more broadened due to the higher reactivity of the metal which has been previously identified through the slightly higher adsorption energy and smaller adsorption height (see figure 5.3). The findings of both the unchanged NEXAFS spectra and DOS are in accordance with the previously discussed lack of charge transfer and electronic hybridisation.

5.3.4 Weak Chemisorption Regime

The weak chemisorption regime in the list of six systems only includes Az/Cu(111). Here, a noticeable interaction between the molecule and metal surface is present as previously identified in section 5.3.2. The increased interaction impacts both the XP and the NEXAFS spectra, as apparent in the direct comparison between physisorbed Az/Ag(111) and weakly chemisorbed Az/Cu(111) (figure 5.7).

When discussing the XP spectra (figure 5.7 (a)), a special point has to be mentioned. For Az/Ag(111), the self interaction error of DFT leads to a spurious charge transfer,

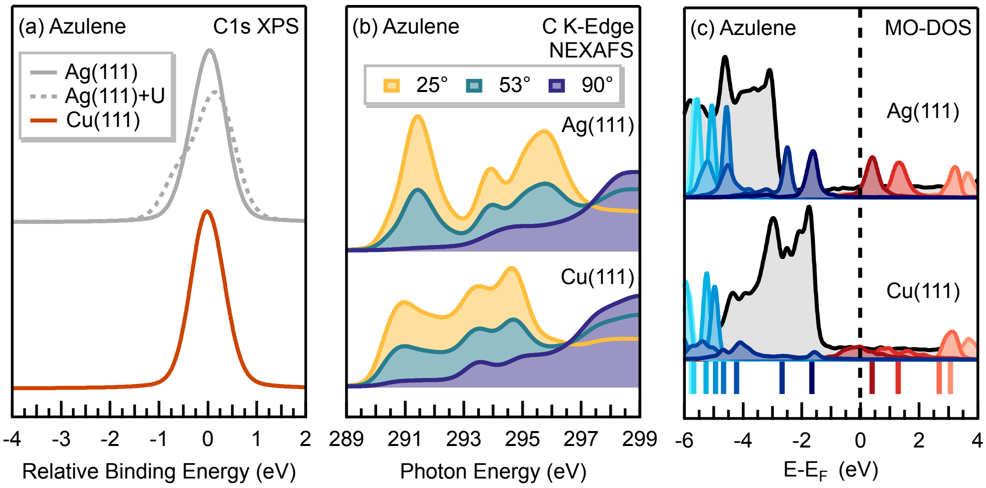

Figure 5.7: Comparison between the physisorbed Az/Ag(111) and the weakly chemisorbed Az/Cu(111) (a) XPS simulations, with an additional +U(MO) corrected spectrum for Az/Ag(111), aligned to centre of mass, to account for spurious charge transfer. (b) NEXAFS simulations at three different incidence angles. (c) DFT density of states (DOS), with scaled MO projections, with the total DOS shown in black and the Fermi level shown as a dashed line. Contributions in blue represent projected occupied states, while contributions in red represent unoccupied states. Lighter shades of these colours show states lower or higher in energy respectively. Coloured lines at the bottom of the graph represent the position of the gas-phase orbitals.

which has to be taken into account. The spectrum simulated with the regular ΔSCF approach (light grey in figure 5.7 (a)) shows a symmetric peak with a loss of the shoulder present in the gas-phase spectrum (figure 5.1). This change in peak shape disagrees with the experimental data, where the shoulder is still present for Az/Ag(111) [80]. It was pinpointed that this discrepancy between the experimental and simulation was caused by a spurious charge transfer, which in turn is the result of a self-interaction error in DFT. By using an *ad hoc* correction through a DFT+U(MO) approach this short coming was able to be fixed. The resulting spectrum is shown as a dashed grey line in figure 5.7.

Comparison of the corrected XPS spectrum for Az/Ag(111) and the one for Az/Cu(111) shows that the increased interaction from physisorption to weak chemisorption has a noticeable effect. The interaction with the Cu(111) surface results in charge transfer into the LUMO of the molecule which is the main driving force behind the reduced relative shifts between the individual carbon atoms. As a consequence, the contributions from the atoms in the 5- and 7-membered rings are no longer distinguishable, and a single, symmetric peak is present.

The polarisation dependent NEXAFS spectra (figure 5.7 (b)) also show a significant difference for azulene adsorbed on the Ag(111) or the Cu(111) surface. The spectra were calculated using the XPS BEs obtained with with regular ΔSCF method and with the use of the DFT+U(MO) correction. A discussion into the effect using the BEs of the correction as the offset in the ΔIP-TP NEXAFS calculation was given in section 4.5.3. The clear change when going from Ag(111) to Cu(111) is expressed by a significant diminishing of intensity and a shift in position to higher photon energy for the first peak along with an increase in overall broadening. When compared to the peak values from the gas-phase spectra (table 5.1), the first peak lowers to 65 % on silver and to only 44 % overall intensity on copper. However, the intensities of the 2nd and 3rd peaks remain relatively unaffected by the adsorption on the metal surfaces. In literature, the diminishing of the first peak is often attributed to charge transfer between the electronic states of the molecule to the metal but through experimental techniques this proves hard to quantify.

Comparing between the different incidence angles in figure 5.7 (a), a reduction

Table 5.1: Relative intensities of the first three peaks seen in the NEXAFS spectra of azulene on Ag(111) and Cu(111) with respect to the corresponding peaks of azulene gas-phase spectrum.

Peak	Relative Intensity	
	Az/Ag	Az/Cu
1	0.65	0.44
2	0.93	1.04
3	0.96	0.82

in dichroism on the copper surface is seen, with a larger amount of residual intensity remaining for the first peak at 90° incidence angle. This intensity should be vanishing, because the symmetry selection rules forbid an excitation into the corresponding π* states with this angle. The presence of residual intensity proves that the selection rules are not valid anymore, because the molecule is slightly deformed, and the electronic states of the molecule are already hybridised with metallic states and lose their symmetry.

In the MO-DOS for azulene on the two metal surfaces a clear difference can be seen between the two levels of interaction (figure 5.7 (c)). When azulene is adsorbed on Ag(111), the band gap between the HOMO and LUMO is preserved with the HOMO being below the Fermi level (black dashed line) and LUMO still above. This changes when azulene is adsorbed on Cu(111), where both the HOMO and LUMO have drastically changed shape, they have broadened and smeared out over a wide range and the LUMO is now partly below the Fermi level and therefore partially occupied. This is a clear indication of hybridisation and substantial interaction between the molecule and the metal for the copper compared to the silver surface.

The MO-decomposed NEXAFS spectra (figure 5.8) show the relative contribution of the ground-state MOs projected onto the NEXAFS spectrum. The intensities of the orbitals with respect to the overall NEXAFS spectra cannot be described quantitatively. The intensity of the MOs is much lower than expected. For Az/Ag(111) (top), where the system in physisorbed, one would expect to see a similar behaviour to the gas-phase projection in figure 5.2 with the sum of the MOs equalling the total NEXAFS spectra. The reason for this problem in the projection have been discussed in section 3.4.3. Figure 5.8 (b) shows the MOs scaled to what one would assume the contribution would

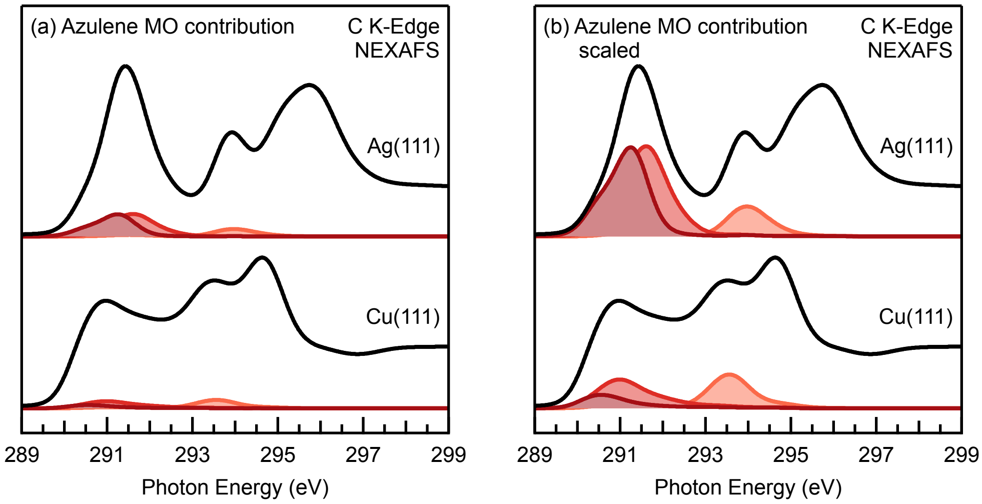

Figure 5.8: MO-projected NEXAFS of azulene on Ag(111) (top) and Cu(111) (bottom) using the simulated 25° spectra. (a) presents the MO-decomposition as calculated and (b) scaled contributions for both Ag(111) and Cu(111) by the same amount for ease of viewing.

be and to better compare the differences. The energies and relative change between the two interaction types can offer some qualitative insight. It is clear that the main difference between the physisorption and weak chemisorption examples is visible for the transitions into the first two unoccupied orbitals (LUMO and LUMO+1), with the transition into the LUMO diminishing more and now possessing a lower intensity than the transition into the LUMO+1. The higher energy LUMO, however, does not show any significant change between the physisorption and weak chemisorption regimes. The relative reduction between the silver and copper surfaces in the first two LUMOs indicate that some interaction must be happening. This can be explained through charge transfer, the orbitals are undergoing hybridisation with the metal surface and so their contribution to the spectra is lowered. This observation is also observed in the MODOS. Figure 5.7 (b) shows the change from clear and defined orbitals to drastically broadened orbitals with the LUMO now partially below the Fermi level where it is now pinned.

Along with the projection of the ground-state orbitals the results where also checked against the final-state relaxed orbitals. Here, instead of using the ground-state FSO as a reference, the same final-state molecule FSO was used. Shown in the figure B.6 is a comparison between the MO-projected NEXAFS for azulene gas-phase and on Ag(111) and Cu(111) for both reference examples. No discernible change can be seen in each case with the only exception being the unbound orbital, LUMO+2, in the gas-phase. This shows that the ground-state projection is a suitable method and does not neglect any effects that could be caused by the final-state orbitals.

5.3.5 Strong Chemisorption Regime

The third and final interaction type is the strong chemisorption observed for both molecules adsorbed on the Pt(111) surface. The XP spectrum for Az/Pt(111) (see figure 5.4) shows the lower energy shoulder disappearing from the spectrum, as already observed when adsorbed on Cu(111). Again, this is due to the interaction between the molecule and metal eliminating the BE differences of the individual carbon atoms. Looking at the naphthalene spectrum, not much change is seen between the spectrum when adsorbed on Pt(111) and the physisorbed state observed when adsorbed on Ag(111) and Cu(111). This does not necessarily mean that the BEs are not being affected. For azulene, the range of the BEs became much smaller and were much closer together, for naphthalene the BEs of the carbons were already close to begin with so if any change has occurred it is hard to identify.

The increased interaction strength has an extreme effect on the NEXAFS spectra. The overall shape of the NEXAFS spectra of the two molecules adsorbed on Pt(111) (bottom of figure 5.9) shows a weak dependence on the molecule involved. Both spectra are similar in shape and indeed almost indistinguishable from one another. The spectra have virtually lost all connection to the unoccupied molecular states previ-

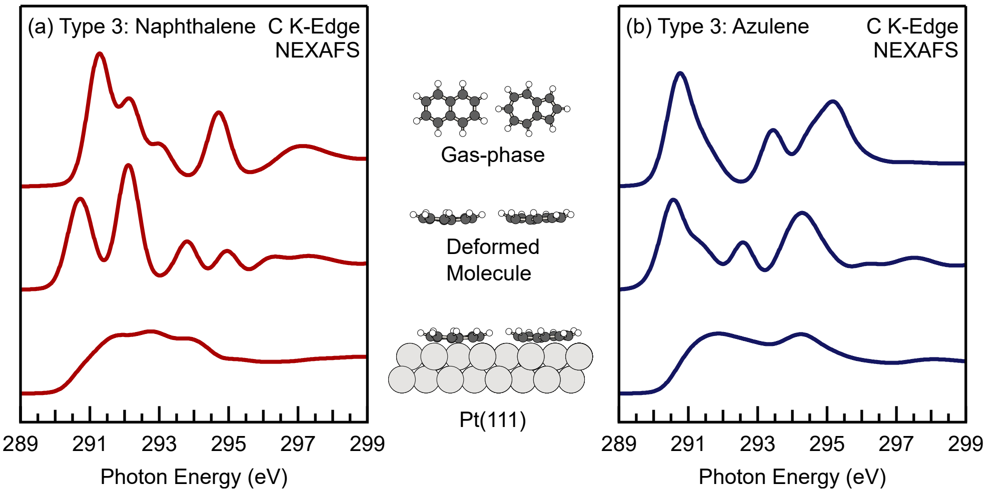

Figure 5.9: Simulated NEXAFS spectra, at 25° incidence angle, for naphthalene (a) and azulene (b) in different configurations. Top is the free gas-phase molecule, middle, the platinum FSO and bottom, the molecule adsorbed on the Pt(111) surface.

ously seen and any residual features are much broadened. Therefore, the identifiable features which arose from the difference in molecular topology between azulene and naphthalene (see figure 5.1) are severely diminished. This is a consequence of the strong hybridisation now present between the electronic states of molecule and metal, which completely dissolves the aromatic electronic structure of the molecules. The MO-projected NEXAFS show how the contribution of the molecular states to the NEXAFS have been reduced even further compared to the weak chemisorption regime and that a small contribution from the former HOMO is now present above due to its partial depopulation shown in figure 5.10 where the MOs have been scaled for ease of viewing. This also explains the observation of a net charge transfer close to zero, as LUMO and HOMO are partially populated and depopulated, respectively.

Furthermore, observed was a massive reduction in the dichroism of the NEXAFS signal (figure 5.11), suggesting an almost complete breakdown of the symmetry selection rules for the adsorbed molecule. This arises from the fact that the molecular electronic structure is now deeply embedded in the metallic band structure, and the molecular orbitals of the gas-phase molecule cease to be meaningful descriptors for the excitation process.

Given the significant adsorption induced deformation of the molecule, one could ask if the changes in the spectrum are not caused by the hybridisation of the electronic states, but instead by the structural change. Here an investigation into this possibility is carried out to provide additional insights. In figure 5.9 the NEXAFS spectra of the molecules adsorbed on Pt(111) (bottom) are compared to the spectra calculated for the deformed molecular geometry without the metal surface (middle) and the gas-phase spectra of the undeformed molecule (top). The spectra of the deformed molecules express noticeable changes from the spectra of the planar gas-phase molecules, in

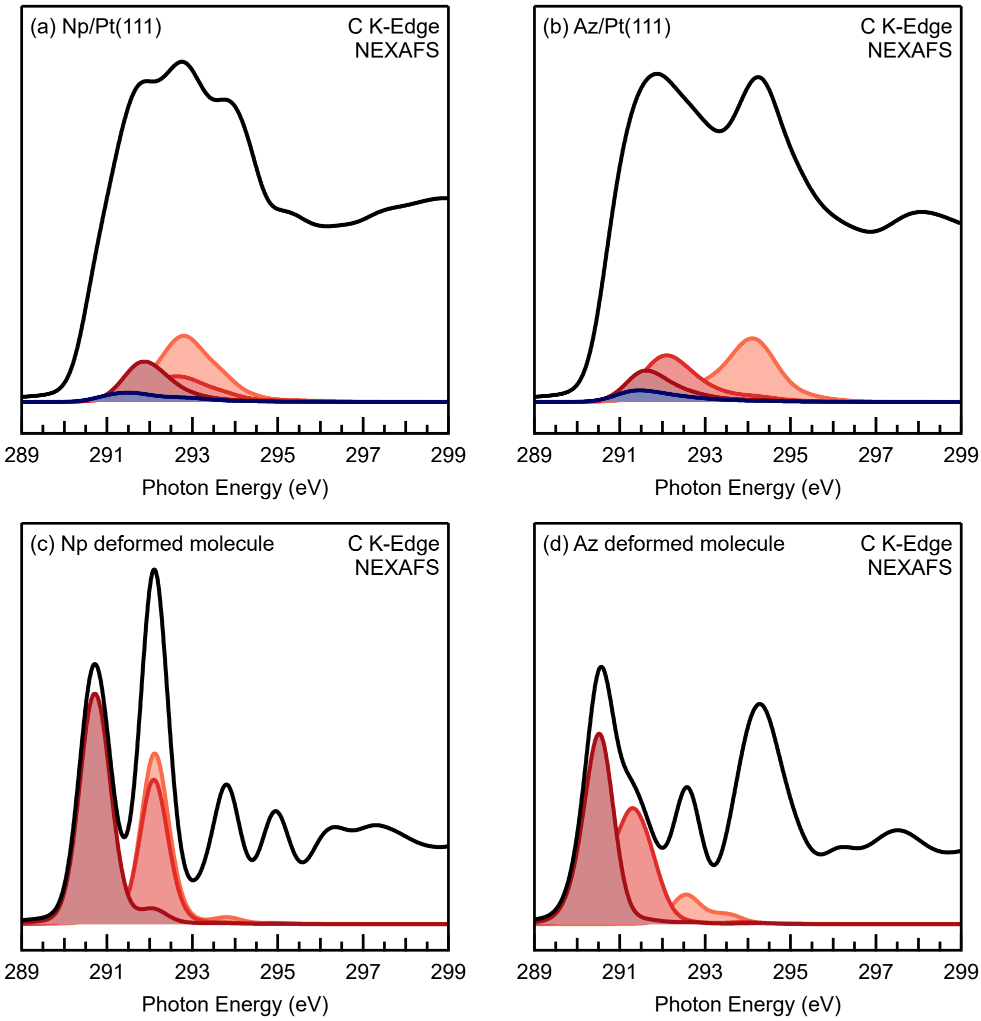

Figure 5.10: MO decomposition of 25° NEXAFS of the type III systems of naphthalene, (a), and azulene, (b), adsorbed on Pt(111). The MOs have been scaled in for the Pt structures to better view the orbitals. Similar projection for the deformed molecules of naphthalene and azulene present in (c) and (d) respectively.

particular for naphthalene. While the deformed molecules still present distinct peaks, it becomes apparent in the dichroism for the deformed molecules (figure 5.11) that the change in geometry already breaks the symmetry selection rules. In addition, the structural deformation shifts the energy of some transitions, leading to a clear gap between the first two transitions in the spectrum of naphthalene. However, the increased level of broadening in the spectra of the molecules adsorbed on Pt(111) and the overall reduction in intensity of the first peaks are indeed due to the hybridisation with the electronic states of the metal surface not due to the deformation.

The deformation of the molecule also shifts the energetic position of the leading edge. For naphthalene, the leading edge is shifted to lower energies compared with the gas-phase molecule and shifts back up and further when adsorbed on Pt(111). For azulene, on the other hand, the deformed molecule and gas-phase leading edges are

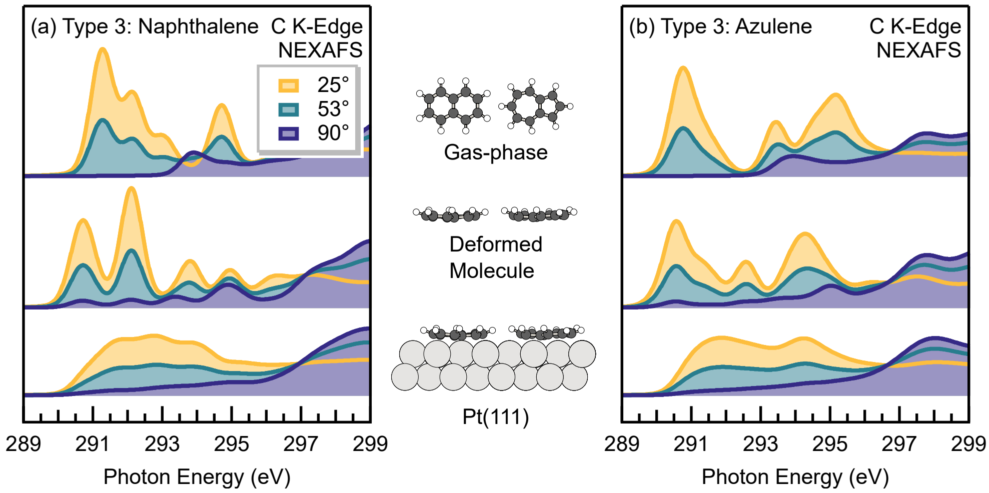

Figure 5.11: Simulated NEXAFS spectra of naphthalene (a) and azulene (b) at three different incidence angles, 25° (yellow), 53° (green), and 90° (blue), for the free gas-phase molecule (top), the Pt(111) surface deformed molecule without the metal (middle), and molecule adsorbed on a Pt(111) surface (bottom).

at similar energy but like naphthalene is also shifted to higher energy when adsorbed on Pt(111). This behaviour is a result of the complex reaction of the MOs to the deformation, which is linked to a general principle resulting in always the same shift direction.

5.4 Discussion

Through the simulated XP and NEXAFS spectra, it is possible to provide a level of insight into the mechanisms at work in the spectroscopy of molecules adsorbed on metal surfaces that experimental techniques alone can not accomplish. In the following, a summary to identify the interaction regime in the spectroscopic data of an adsorbate system is presented and a summary of the main features is presented in table 5.2.

The first regime of discussion is where the interaction between the molecule and the metal surface is minimal and can be classed as physisorption. Here, when compared to spectra of the gas-phase molecule, both the XPS and NEXAFS spectra show little change in the relative spectral features. Whilst change will be seen in the absolute shifts of the spectra due to the presence of the metal surface, when comparing the XPS (figure 5.4) no change is seen in the peak shape and for the NEXAFS (figure 5.5 and figure 5.6) only a slight broadening is present across the spectra with all features from the gas-phase still clear and identifiable. A similar behaviour in the dichroism of the NEXAFS spectra is also seen between the gas-phase and structures in this interaction regime. The π^* signals fall to having zero intensity when going from 25° to 90°. Looking at the MODOS, this can provide insight into any

Table 5.2: Summary of features to look out for and how they change depending on the interaction strength between molecule and metal.

Interaction Type	Key features
Type I: Physisorption	**NEXAFS features:** Overall spectra are fairly similar to the gas-phase spectra. All noticeable features are present with only slight broadening across the spectra. **Dichroism:** The dichroism is retained. **Molecular Orbitals:** A clear and present gap between the HOMO and LUMO of the molecule. **Net Charge:** Overall net charge of the system is negligible
Type II: Weak Chemisorption	**NEXAFS features:** The intensity of the leading peak is reduced when compared to the gas-phase and becomes more broadened. **Dichroism:** Becomes reduced, with finite intensity of the π^* states now showing when recorded at 90°. **Molecular Orbitals:** Orbitals around the Fermi level lose their clear sharp peaks and become smeared out with the LUMO now partially below the Fermi level and becoming slightly occupied. **Net Charge:** A negative net charge is seen from one-way charge transfer between the molecule and the metal surface.
Type III: Strong Chemisorption	**NEXAFS features:** The leading peak essentially disappears, along with any other visible features as spectra become significantly broadened and smeared out. **Dichroism:** Significant reduction of the dichroisim. **Molecular Orbitals:** Orbitals around the Fermi level are completely smeared out the LUMO is partially below the Fermi level and the HOMO is now partially above. **Net Charge:** The overall charge is again negligible due to charge donation/back-donation.

change in the molecular orbitals of the molecule and therefore the interaction strength between molecule and surface. For the physisorption case, as one would expect, a clear gap between the HOMO and LUMO is seen with well defined orbital features showing a lack of any charge which is confirmed by the negligible overall net charge in figure 5.3.

The next regime is where some noticeable features indicating an interaction between the molecule and metal are present, which has been labelled as “weak chemisorption”. In the XPS a change in the relative BEs of individual atoms is seen. In figure 5.7 (a), there is a loss of the shoulder for Az/Cu(111) that was present for the gas-phase and physisorption cases. This shows that the metal surface is having an influence on the relative BEs and more importantly one can pinpoint the cause of the change thanks to the initial-state deconvolution showing which atoms are affected and therefore gain additional insight into the interaction mechanism. In the simulated NEXAFS spectra, the most information is gained from the behaviour of the leading peak in the spectrum. Corresponding to the excitation into the LUMO, this peak is an important bellwether for the interaction strength. This is seen for the type II case of Az/Cu(111), where there is an increase in the interaction between the molecule and metal, the intensity of the first peak gets reduced as seen in figure 5.7 (b). This is a result of hybridisation of the both the LUMO and LUMO+1 leading to a reduction of the contribution of the leading peak by these molecular orbitals (figure 5.8). Further evidence for this hybridisation is seen in the MODOS, where orbitals around the Fermi level undergoing significant energetic broadening cause the LUMO to become partially occupied. The HOMO, even though broadened, remains below the Fermi level and does not lose any charge. This can also be seen by the negative net charge. Furthermore, the increased interaction leads to a loss in the dichroism seen in the NEXAFS spectra

The final regime coined “strong chemisorption” provides details on systems with significant interaction and covers the cases involving the Pt(111) surface in this work. Here again seen is how the interaction between the molecule and metal surface can change the relative BEs of the atoms in the XPS similar to the previous regime for azulene, where the shifts between atoms are reduced. However, for the naphthalene case, little change is seen in the XPS. This is not an indication that the interaction is having no effect on the BEs, more that in this case the shifts between the atoms were already close together so that any change cannot be seen at the simulated experimental resolution. The NEXAFS spectra show a further loss of intensity of the leading peak and significant broadening along the whole spectra resulting in a loss of visible features and both spectra for each molecule become indistinguishable. The cause of this is not simply due to charge transfer, looking at the overall net charge transfer, it is actually negligible again like in the case for a physisorption system. This does not mean that there is no charge transfer, more this is from the complicated donation back-donation mechanism between the molecule and metal. The loss of intensity of the leading peak can be attributed more to the broadening seen in the MOs due to hybridisation with the metal surface and also from the deformation from the molecule. These two factors of loss of the leading peak and minimal charge transfer paired together can be strong indication of strong interaction between the molecule and the metal surface. Looking at the MODOS (figure B.7) the molecular orbitals undergo significant energetic broadening but this time both the LUMO (below the Fermi level) and the HOMO is partially unoccupied (above the Fermi level). Also, a complete loss of the dichrosim (figure 5.11) as a result of the electronic hybridisation is seen.

5.5 Conclusion

The aromatic topological isomers naphthalene and azulene adsorbed on three different metal (111) surfaces (Ag, Cu and Pt) offer a wide reactivity range to study how the interaction strength at the metal organic interface influences core-level spectroscopy. Identified were three regimes of interaction: physisorption (type I: Np/Ag(111), Np/Cu(111), Az/Ag(111)), weak chemisorption (type II: Az/Cu(111)), and strong chemisorption (type III: Np/Pt(111), Az/Pt(111)). These spectra have been compared with experimental data and are in good agreement as shown in Chapter 4, allowing for confident analysis of the spectra.

These three regimes are expressed in the spectra in different ways and can be distinguished from each other through various markers. The gas-phase spectra were used as a reference to compare how the metal interaction alters various aspects. For the lowest interaction strength, physisorption, all gas-phase features stay unchanged with only a small amount of broadening. For weak chemisorption, increased broadening as well as a reduction in the first peak intensity is observed, attributed to a one-way charge transfer. The dichroism of the NEXAFS spectra is still appreciable, but a break-down of the selection rules is already happening. Strong chemisorption leads to the spectra losing almost all of their molecular character, due to both more pronounced deformation and stronger hybridisation of the molecular orbitals with the metallic states of the surface.

By analysis of the spectra in each of these interaction regimes, it is possible to identify specific features to look out for in both the XPS and NEXAFS spectra and calculated aspects such as net charge and the DOS that can be used in the future to help understand the level of interaction between a molecule and a metal surface. By understanding how the interaction between the molecule and metal surfaces and how certain aspects of the molecule (topology) affect this interaction, the information and insight gained could be applied to create and test systems with certain targeted properties.

Chapter 6

Simulation of X-ray Core-Level Spectroscopy of Two-Dimensional Self-Assembled Molecular Networks

Work presented in this chapter is part of a collaboration with the research group of Prof. Meike Stöhr of the Surface Science Group at the University of Groningen and planned to be published. Experimental STM, XPS, and NEXAFS spectra that are presented in section 6.1.1 were obtained by Leonid Solianyk.

6.1 Introduction

The self-assembly of two-dimensional porous molecular networks on metal surfaces [197–199] is an interesting process as it has many practical applications in e.g. host guest chemistry, [200–203] patterning of surfaces, [199, 204] and tuning surface electronic properties [205–207]. Systems based on metal-ligand interactions have also garnered interest due to their enhanced mechanical and thermal stability [198, 208, 209]. The structure of these networks can depend on various aspects such as certain functional groups present on the organic molecule and its coordination to the metal surface [210–212]. Self assembly at metal-organic interfaces depends on the competition of several fundamental interactions such as van der Waals forces, [213] dipolar coupling, [214] $\pi-\pi$ stacking, [215] hydrogen bonding, [216, 217] and metal-ligand interactions [218, 219].

Coordination between the molecule and metal occurs at specific sites where metal atoms have been supplied through deposition, through evaporation, or are extracted from the underlying metal surface or terraces of the crystalline structure [220–222]. In cases involving the Au(111) surface, coordination atoms can be provided through the herringbone reconstruction [223, 224]. Focusing on coordination with 2D molecular networks with Au surfaces, various levels of coordination between Au atoms and ligands have been identified, ranging from two, thee and fourfold coordination [197, 224–226].

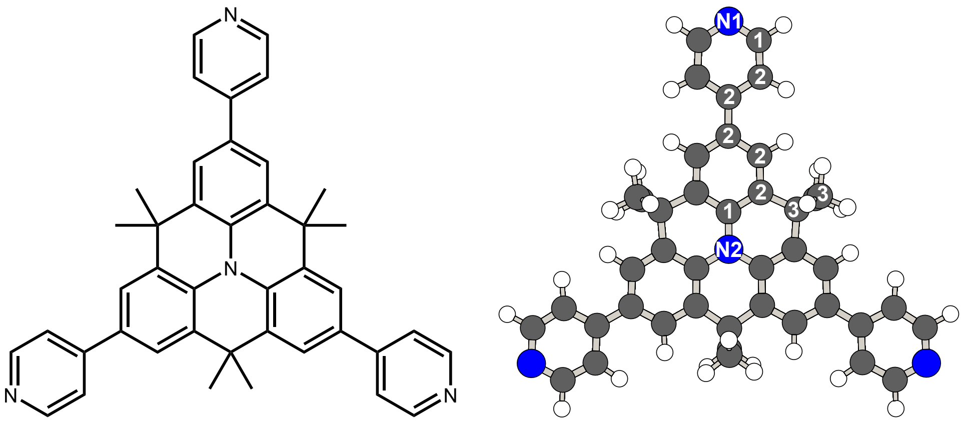

Figure 6.1: Skeletal structure of the HTA molecule (left), with molecular formula $C_{42}H_{36}N_4$ along with a ball-and-stick representation of HTA (right) with the chemically equivalent atoms labelled for carbon 1-3 and nitrogen N1 and N2.

An interesting aspect to investigate is how this coordination between a molecule and the Au substrate forms. Whether this type of coordination occurs for specific molecules or more as general rule and studying how these structures are formed as well as what makes them favourable on Au substrates.

Our collaboration partners at the University of Groningen looked into this via a combination of scanning tunneling microscopy (STM), XPS and NEXAFS experiments of a pyridyl-functionalised triarylamine molecule self-assembled onto a Au(111) surface. The molecule used is called 4,4,8,8,12,12-hexamethyl-2,6,10-tripyridin-4-yl-4H,8H,12H-benzo[1,9]quin-olizino [3,4,5,6,7-defg]acridine (abbreviated as HTA) with a chemical formula of $C_{42}H_{36}N_4$. The structure of HTA is shown in figure 6.1 through both a skeletal representation and a ball-and-stick representation. In the latter the carbon and nitrogen atoms have been labelled into chemically equivalent groups, based on the atom's hybridisation and bonded neighbours, which are discussed later. It was found to form different molecule phases after submonolayer deposition. Two of these phases are thought to be stabilised through coordination between native Au atoms and the ligand itself. Through computational core-level spectroscopy calculations, we aim to look into the presence of any metal adatom-ligand coordination. This chapter will provide a summary of the experimental results performed, along with the insights and conclusions brought forward from its analysis. DFT calculations performed to simulate core-level XPS and NEXAFS spectra have been provided to support and corroborate the experimental findings.

6.1.1 Experimental Data

Our collaboration partners at the University of Groningen performed a range of experiments with the results detailed in this section. Through their experiments a submonolayer of HTA molecule was deposited onto a Au(111) surface and characterised

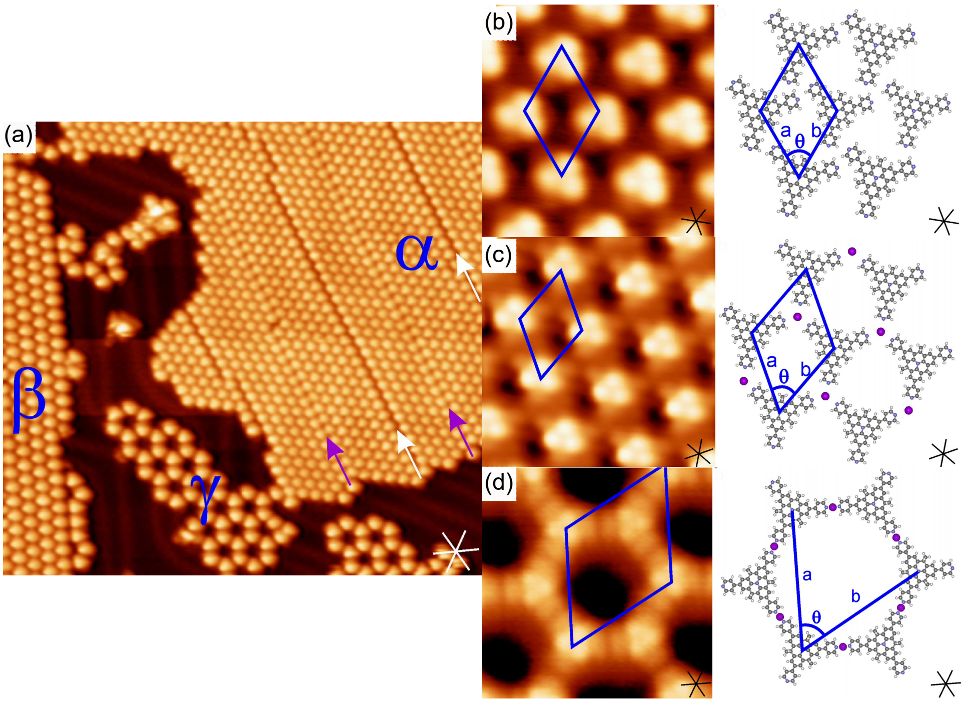

Figure 6.2: (a) STM of the three phases (α, β and γ) of HTA formed on an Au(111) surface. White and purple arrows represent two kinds of domain boundaries present in α. (b), (c) and (d) show detailed STM images of α, β and γ phases respectively with a visible unit cell drawn in blue, along with tentative structural models given besides from the experimental data and the three lines indicating the principle Au directions. Images are taken from Ref. [227]. The three lines shown in each picture indicate the principle Au directions, showing a rotation of 22°.

through the use of STM. Three distinct well-ordered 2D network phases were observed which were labelled as α-, β- and γ-phase. Figure 6.2, taken from Ref. [227], shows the three formed phases along with high resolution images of each phase along with tentative structural models constructed from STM and LEED measurements. These are shown alongside each for the α-phase in figure 6.2 (b), β-phase in 6.2 (c) and γ-phase in 6.2 (d).

The α- and β-phases both possess a densely packed structure compared to the γ-phase which shows an open porous structure. The unit cells depicted as blue lines in the structures correspond to the experimentally observed unit cells. Details of the three unit cells shown in figure 6.2 are summarised in table 6.1, showing the unit cell dimensions of a and b, the internal angle Θ and the rotation R of the unit cell with respect to the principle Au direction.

Looking at the structures of both the β- and γ-phases, the orientation of the molecule has the nitrogen atoms of the pyridyl rings on neighbouring molecules pointing at the same atoms on neighbouring molecules. This would mean lone pairs of the nitrogen atoms are pointing at each other which would introduce some electrostatic repulsion. This leads to the inclusion of a gold atom, suggested by our experimental

Table 6.1: Experimentally recorded values of the unit cells of the three phases of HTA on Au(111) surfaces from STM. *a* and *b* are the cell dimensions, Θ the internal angle of the cell and R is the rotation of the unit cell witch respect to the principle Au direction.

Phase	Experimental unit cell parameters		
α	$a = b = 1.56\,\mathrm{nm}$	$\Theta = 60°$	$R = \pm 9°$
β	$a = b = 1.94\,\mathrm{nm}$	$\Theta = 60°$	$R = \pm 30°$
γ	$a = b = 3.45\,\mathrm{nm}$	$\Theta = 60°$	$R = \pm 30°$

partners, between the molecules with the nitrogen atoms coordinating to the metal atom reducing this hindrance. This arrangement can not be confirmed through experimental analysis alone and poses a problem that can be addressed through computational calculations.

Experimental XPS and NEXAFS spectra were recorded for various structures of HTA on the Au(111) surface. Three different coverages of the system were recorded at 4.7 ML, 1.1 ML and 0.4 ML. The 4.7 ML and 1.1 ML coverages were achieved through deposition of the HTA molecule on a cooled Au(111) substrate at −70 °C and −54 °C respectively to achieve a first deposited layer of the α-phase. The 0.4 ML coverage was achieved through deposition at room temperature and subsequent annealing at 188 °C to obtain a purely γ-phase. The molecular coverages were calibrated using XPS. The 4.7 ML coverage is a multilayer structure that is used as a reference for both the 1.1 ML and 0.4 ML coverages, representing the HTA molecule in a more organic environment with the influence of the metal substrate reduced. A pure β-phase was never observed in the experiments performed.

The N1s and C1s XPS of these three phases were recorded to investigate the differences between the chemical environment of the molecule. In figure 6.1 the atoms in the molecule have been labelled into multiple nitrogen and carbon chemical environments. The atoms have been categorised into two nitrogen (N1, N2) and three carbon environments (C1, C2, C3). The two nitrogen environments consist of N1, the three pyridylic nitrogen atoms around the outside of the molecule and N2, the central aminic nitrogen. For the carbon atoms, the C1 environment are the sp^2 hybridised carbon atoms bonded directly to a nitrogen atom and C2, sp^2 hybridised carbon atoms not directly next to a nitrogen atom and C3 are the remaining sp^3 hybridised carbon atoms.

The experimentally recorded N1s and C1s XPS spectra are shown in figure 6.3 (a) and (b) respectively for the three previously mentioned ML coverages. The nitrogen XPS shows two clear main peaks in each spectrum. The top spectra in blue represents the 4.7 ML coverage and can be viewed as a reference of the system with limited interaction from the metal surface when compared to the α- and γ-phases, which are shown in orange and green respectively. The peak at lower BE labelled I is attributed to the pyridylic N1 nitrogen and the higher energy peak II corresponds to the aminic N2

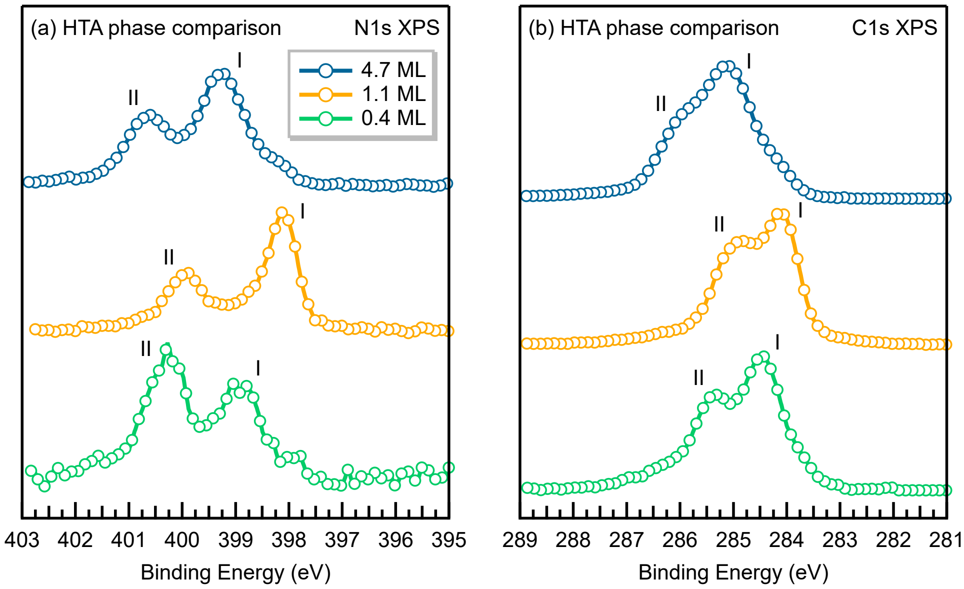

Figure 6.3: (a) N1s and (b) C1s experimentally recorded XPS spectra [227] for the 4.7 ML (top, blue), 1.1 ML (middle, orange) and 0.4 ML (bottom, green) coverage's of HTA on Au(111).

nitrogen. Comparing the absolute peak positions to the 4.7 ML coverage, both peaks in the 1.1 ML spectra shift towards lower energies which is attributed to core-hole screening due to the influence of the metal surface. In the 0.4 ML spectra, the shift of the peaks to lower energies is much less that the 1.1 ML. A cause for this shift is thought to be due to the coordination of the nitrogen to a gold adatom.

In the HTA molecule there are 3 N1 atoms and 1 N2 atom, the stoichiometric ratio between the two peaks (I : II) should therefore be 3 : 1. This ratio is not seen in the experimental spectra for all coverages. The area ratio of the peaks in the spectra for the 4.7 ML coverage is 1.62 : 1, whilst in the 1.1 ML case the ratio is 1.44 : 1. It is possible for these lower values to be within experimental error. However, for the spectra in the 0.4 ML phase the intensity ratio changes significantly with the N2 peak now greater in intensity with an area ratio of 0.67 : 1 between peaks I : II. This change is too significant a change to be in the realms of experimental error. It is therefore thought that this could be due to the pyridylic nitrogen atoms being much closer to the surface than the central aminic nitrogen. This would cause the signal of the pyridylic nitrogen to decrease due to an increase in interaction with the metal resulting in core-hole screening. However, this information on the heights of the nitrogen atoms on relation to the surface was not possible with the experimental data.

For the C1s spectra detailed in figure 6.3 (b), two main peaks are also identified. The lower BE peak I is assigned to the atoms labelled C2 in figure 6.1 and both the C1 and C3 environments correspond to the higher energy II peak. These assignments are based on reported BEs of similar sp^2 hybridised groups found in phthalocyanines [228] and the reports of sp^3 carbon groups possessing higher BEs than sp^2 groups [229, 230].

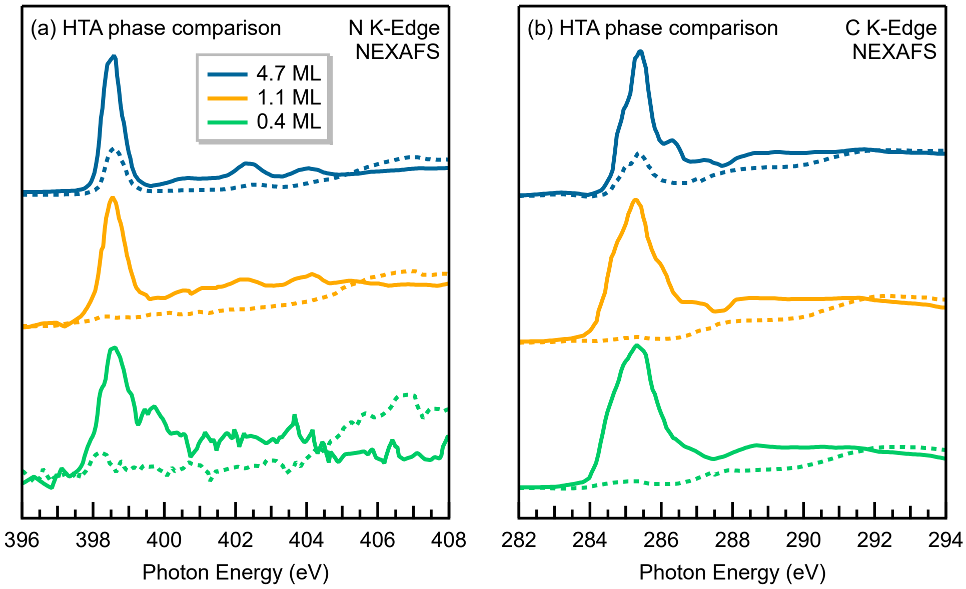

Figure 6.4: (a) N K-edge and (b) C K-edge experimentally recorded NEXAFS spectra [227] for the 4.7 ML (top, blue), 1.1 ML (middle, orange) and 0.4 ML (bottom, green) coverages of HTA on Au(111). Full lines are spectra acquired using p-polarised light and dashed lines are spectra recorded with s-polarised light.

The overall shifts between the top multilayer spectra and the two monolayer metal structures below are reported to be a consequence of the nitrogen-gold interactions drawing electron density away from the C1 atoms and shifting the peak to lower energies with the same effect seen for the C2 peak.

The stoichiometric ratio of the carbon atoms between peak I (24×C2) and peak II (9×C1, 9×C3) in the HTA molecule is 1.33 : 1 which shows good agreement with the experimental with the peak area ratios calculated from the spectra of 1.50 : 1 for the 4.7 ML coverage, 1.34 : 1 for 1.1 ML and 1.45 : 1 for 0.4 ML.

Experimentally recorded nitrogen and carbon K-edge NEXAFS spectra were provided for each of the previously discussed coverages and results are shown in figure 6.4 with experiments recorded using both p- (full lines) and s-polarised (dashed lines) light. For all spectra the first peak in the p-polarised light, the intense leading peak, was assigned to the N1s and C1s $\rightarrow \pi^*$ orbital transitions and compared to reported data for porphyrin derivatives in literature, which showed good agreement [231–234].

From analysis of the experimental data alone, a great deal of information about the system can be obtained but certain aspects are open to interpretation and some questions are left open. These include:

- Whether the structures laid out in figure 6.2 are correct? The models created from the experiment are only tentative and are assumed to be planar in all phases, can this be confirmed with DFT simulations of the structure and spectroscopic calculations?

- Can the presence of the gold adatoms be confirmed? Does their inclusion make sense in terms of the structure, and do they have any effect on the core-level spectroscopy?

Here is where through the use of theory we can look into gathering information to try and to answer these questions by use of DFT core-level spectroscopy simulations.

6.2 Computational Details

6.2.1 Geometry Optimisation

Computational structures of the three phases were optimised using DFT with FHI-aims code [105]. Initial periodic models were recreated from the unit cell values and tentative structures given in figure 6.2 for all three observed phases with a vacuum layer of 30 Å. An additional structure of the HTA molecule located in the middle of a large 30 Å vacuum cube was created as a gas-phase structure to act as a comparison to the multilayer structure.

For the α- and γ-phases, models with the inclusion of the metal surface were created. The α-phase was modelled with a $(\sqrt{31} \times \sqrt{31})$-R9° gold metal slab consisting of two metal layers (62 Au atoms), the γ-phase involved a $(7\sqrt{3} \times 7\sqrt{3})$-R30° metal slab also with two layers (297 Au atoms) and both with a 30 Å vacuum layer. As the interaction between the molecule and metal is expected to be minimal in a physisorbed system, two layers of metal were chosen as a balance between keeping the number of atoms in the system small enough to feasibly run multiple calculations needed and the inclusion of a metal surface to correctly model the chemistry between the molecule and substrate. During the optimisation of the structures with the metal surface, the bottom metal layer was fixed in the bulk geometry whilst only the top layer was allowed to relax.

Geometry optimisations of the structures were carried out in FHI-aims with the PBE XC-functional [53] and at the gamma point. A ‘tight-tier2’ basis set was used for all calculations except for the γ-phase structures with the 2-layer Au(111) surface where a ‘light-tier1’ basis set was used. These reduced parameters were needed for such a large system with two molecules (164 atoms) and the metal surface (297 atoms) included in the structure in order to run the calculations. For optimisations of the structures without a metal surface the z coordinate of each atom in the planar structure of the molecule was kept fixed to ensure planarity whilst the x and y coordinates were allowed to relax. This was so the molecule remained planar during optimisation as otherwise the molecule greatly deformed. However, the sp3 hybridised carbons above and below the plane of the molecule were allowed to fully relax in all 3 directions during optimisation. The unit cells were also allowed to relax with both the cell lengths and angles allowed to relax. Calculations were performed allowing the structure to relax until residual forces were below 1×10^{-3} eV/Å. The electronic convergence settings were set to $1 \times 10^{-4}\,\mathrm{e}/\text{Å}^3$ for the electron density, 1×10^{-2} eV for the KS-eigenvalues and 1×10^{-6} eV for the total energy.

6.2.2 XPS and NEXAFS Calculations

Core-hole simulations were carried out as described in section 3.3.1. CASTEP calculations were performed based on the FHI-aims optimised geometries with the PBE XC-functional [53] and a PW cut-off of 500 eV with a $1 \times 1 \times 1$ reciprocal k-point grid were used throughout. Spectra were broadened using the pseudo-Voigt broadening scheme [111, 112] as detailed in section 3.3.1.

6.3 Results

6.3.1 DFT Structure Optimisation

A variety of structures were created and have been labelled to succinctly explain what was involved. These two labels represent whether the structure contains either an adatom (+A) or whether the metal surface was included (+S) and can be combined if both were used (+AS), conversely if no additional label is included, this refers to a structure without any adatoms or metal surface. Two types of models have been optimised and included structures where the metal surface is absent in figure 6.5 for the α-phase, (a), β(+S), (b), and two γ-phases, γ and γ(+A), (c) and (d) respectively.

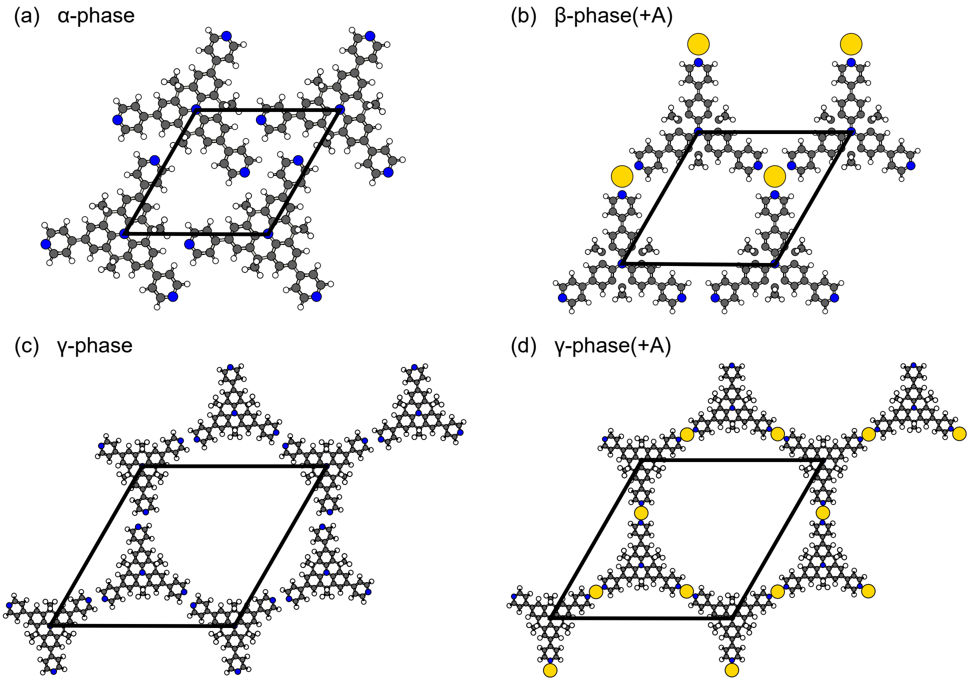

Figure 6.5: Relaxed unit cell geometries of HTA in the (a) α-phase, (b) β-phase, (c) and (d) in the γ-phase with and without the presence of a gold adatom respectively. Black lines represent the unit cell.

Models with the inclusion of a 2-layer metal surface are shown for α(+S) in figure 6.6, γ(+AS) in figure 6.7 and γ(+S) in figure B.8. Due to the incommensurate nature of the unit cells from the experiments, new commensurate structures were created and compared with corresponding experimental unit cells. A table of all the DFT optimised unit cells along with the experimentally observed values are shown in table 6.2 for comparison.

A comparison between the experimental and DFT unit cell lattice parameters for the various structures are shown in table 6.2. The experimental values for structures without a metal surface are from the STM structures shown in figure 6.2. The values labelled with a star, where a metal surface was modelled, are commensurate unit cells. The experimental value in these cases refer to where the unit cell has been created using an experimentally recorded gold lattice parameter.

For the α-phase structure the DFT optimised lattice value is in agreement with the experimental value and also between the values for the α(+S) structure, with a 0.5 Å difference between the commensurate and incommensurate values. Two separate α(+S) structures were created where the central aminic nitrogen occupied either a

a) α-phase(+S, top)

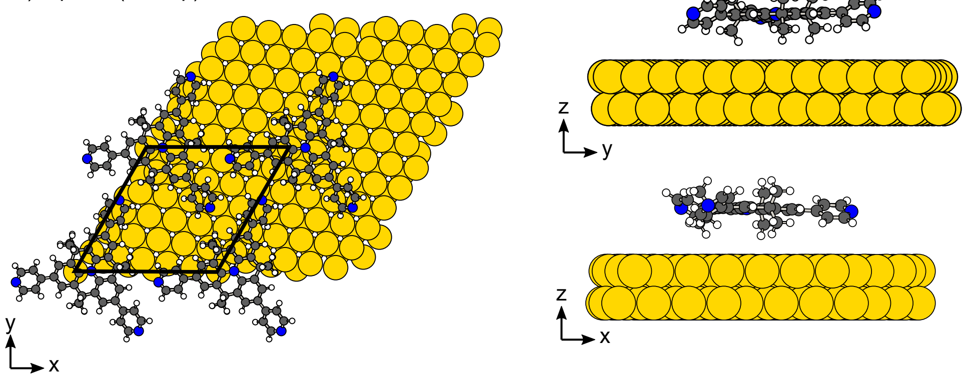

b) α-phase(+S, hollow)

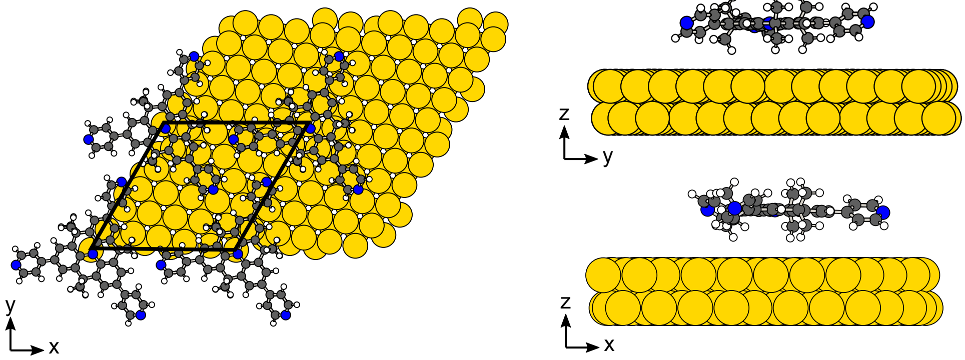

Figure 6.6: Unit cell geometries of optimised structures of HTA on a 2-layer Au(111) surface in the α-phase, with two molecule adsorption site where the central aminic nitrogen was in a (a) top site or (b) a hollow site. Three views along the x, y and z axis are provided. Black lines represent the unit cell.

top or a hollow metal site. In both models with and without the metal surface, the overall molecule is planar, however in the α(+S) structure the pyridine rings twist slightly out of the plane but no overall arching of the molecule is observed. For the β(+A) structure the DFT optimised unit cell lattice parameter of 18.8 Å is smaller than the experimental value of 19.4 Å due to a bond forming between the pyridylic nitrogen atoms and the gold adatom. For the γ-phase, three structures with different unit cell sizes were created. These include the γ-phase modelled without any adatoms or surface (γ), another with gold adatoms included (γ(+A)) and structures with a 2-layer metal slab ($\gamma(+S)$ & $(+AS)$). The planar γ structure, agreed well with the experimental STM unit cell values. The second unit cell for γ(+A), contained again a planar HTA molecule but this time with the presence of gold adatoms between neighbouring molecules. Here this structure could not fit into the experimental unit cell as it was too small to do so. To fit this structure, the unit cell had to increase by 2.4 Å to 36.9 Å.

Finally, a commensurate unit cell for the γ(+S) and γ(+AS) structures was created where the 2-layer metal surface was included. Two structures for each were created

(a) γ-phase(+AS, top)

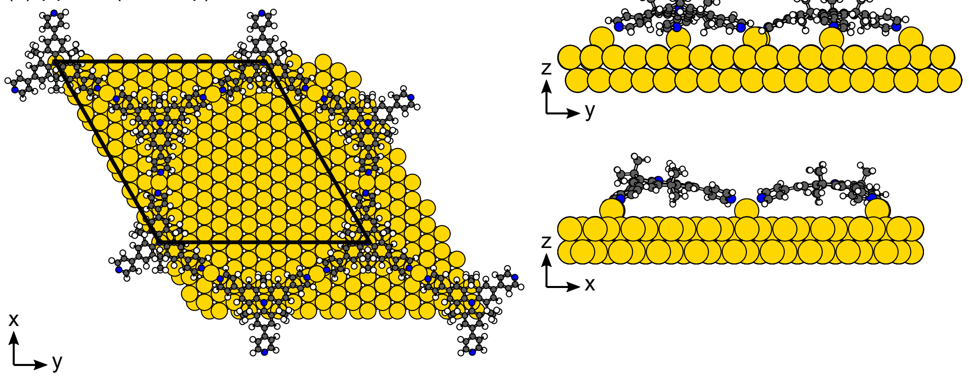

(b) γ-phase(+AS, hollow)

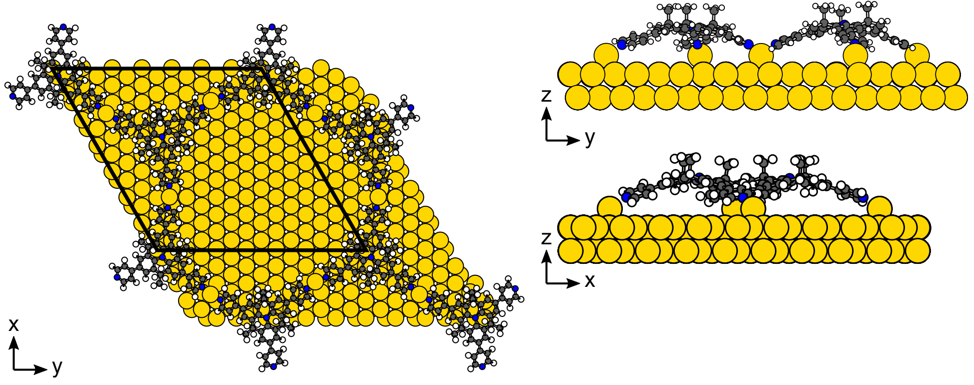

Figure 6.7: Unit cell geometries of optimised structures of HTA on a 2-layer Au(111) surface in the γ-phase with adatoms, with two molecule adsorption site where the central aminic nitrogen was in a (a) top site or (b) a hollow site. Three views along the x, y and z axis are provided. Black lines represent the unit cell.

Table 6.2: Unit cell values of both the experimentally observed unit cell and the DFT geometry optimised unit cell where cell angles were allowed to relax. Experimental values labelled with * are commensurate values. All values are given in angstrom.

Phase	Experimental	DFT Optimised
	Unit Cell (Å)	
α	15.6	15.6
α(+S)	16.2*	16.1
β(+A)	19.4	18.8
γ	34.5	34.5
γ(+A)	34.5	36.9
γ(+S)	34.9*	35.0
γ(+AS)	34.9*	35.0

with the aminic nitrogen placed on a top or hollow site. In both structures the HTA molecule becomes distorted and loses its planar shape with the pyridylic nitrogen groups pointing downwards towards the metal surface (forming a bond with the gold adatom in the γ(+AS) case) and the aminic nitrogen arching upwards away from the surface. This loss on planarity allowed for the γ(+AS) structure (figure 6.7) to fit into a smaller unit cell that was much closer to the experimental incommensurate unit cell. Without the presence of the gold adatoms in the γ(+S) structure (figure B.8), it can be seen that the HTA molecules rotate with the pyridylic nitrogen atoms twisting away from each other. This changes overall network structure and no longer agrees with the STM images and shows the need for the gold adatoms to achieve the structure seen in the STM.

6.3.2 XPS and NEXAFS Spectroscopy

The N1s and C1s XPS spectra were calculated for a selection of the previously mentioned structures. Due to the differences between the sizes of the unit cells and number of atoms, a direct comparison between the absolute BEs of each phase was not possible, however, the relative shifts of different atoms could be compared. For the N1s spectra the difference between the two nitrogen N1 and N2 shifts (ΔBE) were compared between the phases and with the experimental values, obtained from the spectra in figure 6.3, and are reported in table 6.3. The N1s shifts in the multilayer (4.7 ML) spectra were compared with the values from the HTA gas-phase structure (molecule in a vacuum box). A large disagreement between the two values is seen which suggest that this model is not an appropriate approximation for the experimental coverage.

Otherwise for the 1.1 ML (α-phase) and 0.4 ML (γ-phase) spectra a good agreement is possible with a DFT structure. In the case of the α-phase, the experimental difference of 1.81 eV is seen between the two peaks. Both the α and the α(+S)

Table 6.3: N1s XPS binding energy difference between aminic and pyridylic nitrogen atoms in HTA molecule for different experimental and DFT simulated phases. Shifts are reported in electronvolt.

Coverage (phase)	Experimental	DFT
	N1s ΔBE (eV)	
4.7 ML (multilayer)	1.40	2.07
1.1 ML (α-phase)	1.81	1.79 1.73 (+S)
0.4 ML (γ-phase)	1.39	2.20 1.26 (+A) 1.34 (+AS)

structures where the metal surface is either absent or included give similar results of 1.79 eV and 1.73 eV, respectively. This shows that the interaction between the molecule and metal does not significantly affect the XPS shifts. Between the three γ-phase structures the ΔBE varies. The γ structure has a shift of 2.20 eV which is far greater than the experimental value of 1.39 eV. When the adatom is included in the (+A) structure, this provides a more sensible value of 1.26 eV, but slightly lower than experimentally recorded. For the (+AS) structure, with the metal and adatom, the agreement with the experimental value is much closer (1.34 eV).

C1s XPS spectra were calculated for the α-phase which included the α and the two α(+S) structures. The XPS for the two α(+S) structures with the central aminic nitrogen placed on a top or hollow site, yield virtually identical spectra and little change was seen when compared with the α structure, with the spectra shown in figure B.9. This shows that the metal surface has little influence on the XPS. Moving forward, for the α-phase, the α structure without the metal surface will be discussed. The C1s spectrum for the α-structure is shown in figure 6.8. First, shown in figure 6.8 (a) is the breakdown of the HTA molecule into two groups based on symmetrically in-equivalent carbon atoms, labelled as different colours and the chemically in-equivalent carbon, labelled numerically. In figure 6.8 (b) and (c) are the C1s XPS spectra with the contributions from these two different labelling schemes.

In figure 6.8 (b) we can see the shift for each carbon in the HTA molecule and see exactly which atoms are contributing to each peak. It was assumed from the experiment that the two peaks consisted of contributions from carbon atoms labelled C2 for the lower energy peak and from C1 and C3 for the higher energy peak. We can sum up these carbon atoms and see the contributions to the simulated XPS from these groups in figure 6.8 (c). Here it can be seen that this assumption does not match the DFT simulated spectra. The C1 peak in red is consistent with carbon atoms of this group making up the higher energy peak but for the C2 and C3 carbon atoms there are some differences. Whilst the majority of the C2 carbon atoms make up the lower

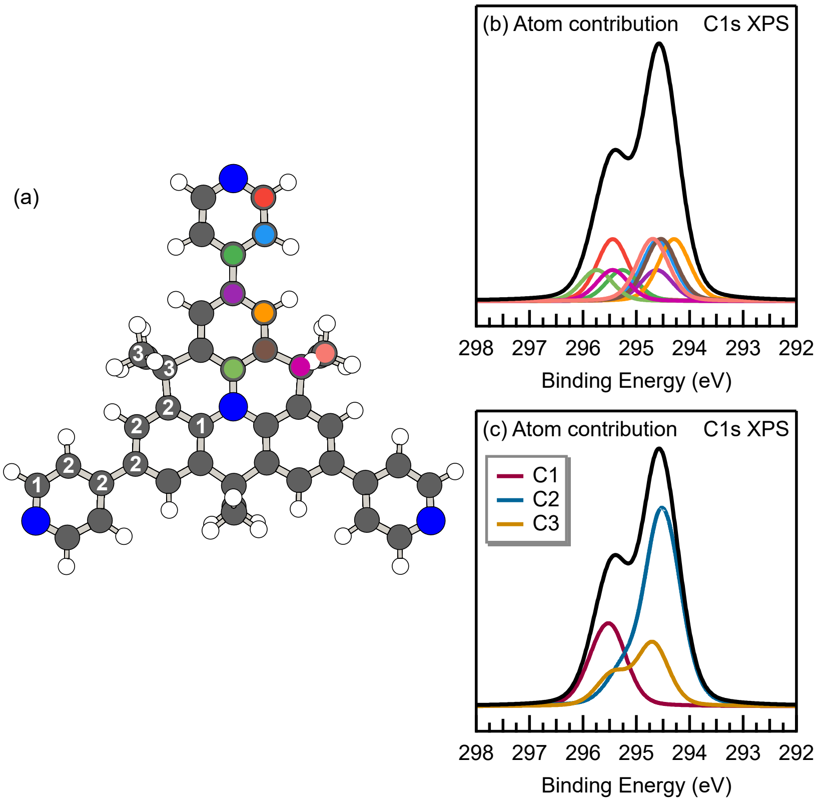

Figure 6.8: The structure of HTA shown in (a) along with two breakdowns of the atoms in terms of symmetry equivalent carbon atoms by colour and chemically in-equivalent carbon atoms by number. (b) DFT simulated C1s XP spectra of the α-phase with a breakdown of the spectra in terms of the coloured carbon atoms and (c) in terms of the numbered carbon atoms.

energy peak there is a small shoulder at higher energy which gives a contribution to the second peak. For the C3 carbon atoms there is a substantial contribution to both peaks.

Looking at the peak area ratio between the two peaks, the simulated spectra have a peak area ratio of 1.8 : 1. The experimental value of the α-phase was lower at 1.34 : 1 for the 1.1 ML coverage but this could be down due experimental uncertainty.

The N and C K-edge NEXAFS spectra were calculated for the α-phase structures. The spectra are shown in comparison with the experimental spectra in figure 6.9. Due to the prohibitive computational cost in simulating NEXAFS spectra only the α-phase without the metal surface was chosen to be calculated as other structures would not have been computationally viable. For both the carbon and nitrogen NEXAFS spectra, there is excellent agreement between the experimental and DFT simulations for both the p- and s-polarised light. The p-polarised light could be recreated by simply using the same incidence angle 6°, that the experiment used, in the simulation. To recreate the s-polarised light, also recorded with a 6° angle, the NEXAFS spectra were modelled with an incidence angle of 90°. The shape of the leading peaks in the

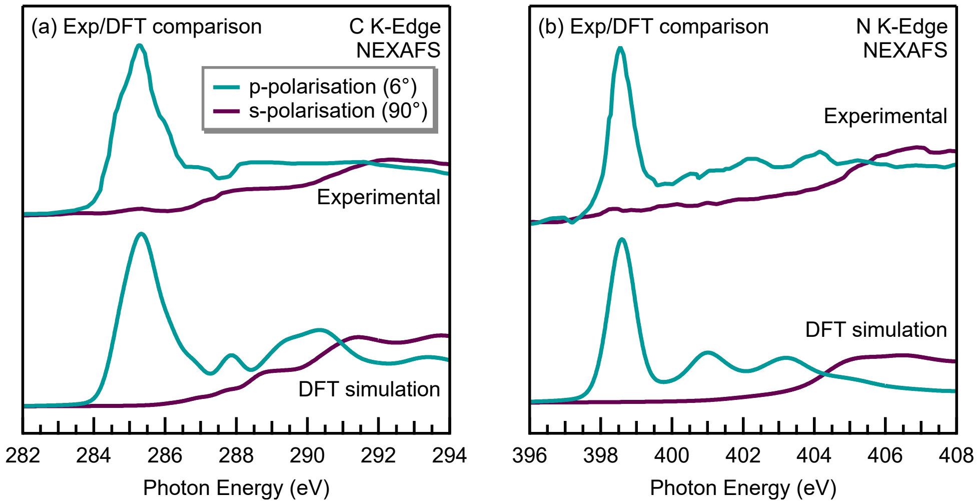

Figure 6.9: Comparison between the experimental carbon (a) and nitrogen (b) K-edge spectra and the DFT simulated spectra of the α-phase. Both experimental spectra were recorded at an incidence angle of 6° with the spectra in turquoise recorded with p-polarised light and spectra in purple with s-polarised light. In the simulations, the blue refers to spectra with a 6° incidence angle, and to achieve comparison to the s-polarised light a 90° incidence angle was used. Simulated spectra were shifted by 6.3 eV (carbon) and 7.5 eV (nitrogen) to match the experimental energy range.

carbon and nitrogen spectra have both been well reproduced.

6.4 Discussion

For both structures proposed for the α-phase (with and without the metal surface), a good agreement with the experimental unit cells was found. Two separate geometries for the α(+S) structure were found with the central aminic nitrogen atom either occupying a top site or a hollow site (shown in figure 6.6). In both adsorption sites the molecule stays overall planar, with a slight out-of-plane tilt of the pyridine ring. Both gold surface geometries of the α-phase yield the same N1s and C1s XPS spectra and when compared with the structure of α without a metal surface, again very little difference is seen between spectra. This shows that for the α-phase, the presence of the metal surface only weakly affects the resulting spectra. Further evidence to this is seen in the NEXAFS simulations of the α-phase shown in figure 6.9. These were performed on the α-phase without a metal surface and excellent agreement is seen between the experiment and DFT simulations. This gives more evidence that the effect of the metal surface on the molecule is minimal.

The unit cell for the β-phase is slightly smaller than the experimentally recorded unit cell values. This can be seen from the bond distance between the pyridylic nitrogen and the gold atom becoming smaller. Due to an absence of experimental data from obtaining a pure experimental β-phase structure no further study into this phase was carried out.

Three different structures of the γ-phase were modelled, when the HTA is modelled as a planar molecule, only the system without a gold adatom can fit into the experimentally measured unit cell parameters. To allow for the gold adatoms which are expected from the experimental analysis the unit cell required is 2.4 Å larger than observed. When modelling the surface with a metal surface, two key things can be seen. Geometries with and without gold adatoms on the structure of the metal were investigated as shown in figure 6.7 and figure B.8, respectively. In both cases the molecules showed significant distortion and loss of its planar shape. However, in the structure without any gold adatoms (γ(+S)) a significant rotation of the molecule was observed with the pyridine rings moving away from each other by a substantial amount. The structure no longer fits the STM images. For the structure of γ(+AS) the distortion of the molecule caused an arching in the molecule leading to the pyridine nitrogen groups pointing downwards towards the metal surface and bonding with the gold adatoms. This nitrogen-gold bond prevents the molecule from rotating as seen in the γ(+S) structure. The unit cell lattice parameters of this structure (35.0 Å) are much closer to the experimentally observed STM value of 34.5 Å. This shows that the inclusion of the metal adatoms is indeed necessary and present in the structure as they keep the molecule in the correct orientation. This confirms that the molecule is distorted and not planar otherwise it would not fit into the unit cell.

Along with needing the metal surface to be modelled to fit the structure into the unit cell values recorded by experiment, the N1s spectra allowed for a further confirmation of the requirement of the metal surface and adatoms. In table 6.3 the relative difference between the shifts of the two nitrogen groups only showed agreement in the structure where both were included. The γ(+AS) structure can also help to explain the change in ratio between the two peaks seen in figure 6.3 (a)). As the molecule is bent and the pyridine nitrogen atoms are pointing down towards the surface, this would suggest a significant screening of the core-hole is involved as due to the increased interaction between the molecule and the metal surface. This screening reduces the intensity of the pyridylic peak so much that it decreases below the central aminic nitrogen.

The experimental analysis from the C1s XPS in figure 6.3 (b) grouped the molecule into three different carbon environments (figure 6.8 (a)) and assigned the two peaks from contributions from C2 for the low energy peak and C1 and C3 for higher energy peak. In the DFT simulations, the spectra are calculated by summing up the peaks for all carbon atoms at their corresponding BEs. This allows us to present the total XPS as a breakdown of the symmetry in-equivalent carbon atoms as presented in figure 6.8 (b). In figure 6.8 (c), peaks belonging to the same chemical environment have been summed up. From these two breakdowns we can see that the assumption from the experimental analysis is not consistent with the DFT simulated results. It can be seen that the majority of the contribution of the low energy peak is indeed from the C2 group, it is also where the C3 carbon atoms are located. For the high energy peak, the C1 groups are correctly assigned to this peak but there are some contributions from C2 carbon atoms. This shows that for such a large molecule with many different symmetry environments, the XPS can not be so easily broken down and that assignment of peaks can be rather challenging from experiment alone.

6.5 Conclusions

In this chapter, it has been shown that DFT calculations can assist greatly in understanding and supporting experimental analysis. Provided were experimental results from a range of different experiments (STM, XPS and NEXFAS) along with conclusions obtained from its analysis. DFT optimised structures based on the experimental results were created and the XPS and NEXAFS were simulated. It was found that for the observed α-phase, the interaction between the molecule and metal are weak as the XPS and NEXAFS agree well when the metal surface is not included. This was also confirmed by the simulation of the XPS which shows little dependence on whether or not the metal surface was absent or included.

For the γ-phase, we have shown that adatoms must be present to understand the STM and XPS data. This is due to the pyridilic nitrogen atoms forming a bond with the adatom and keeping the molecule in the correct orientation observed by STM. This also affects the XPS BE of the nitrogen as from the XPS simulations, the relative shifts between the two nitrogens' agree more when a gold atom is present. It was also shown that the molecule in the γ-phase becomes greatly distorted and significant arching is observed. This was confirmed by the molecule only fitting into the experimentally recorded unit cell lattice parameters when arched, as when the molecule was planar this was not achievable.

DFT simulations can also provide additional insight into the breakdown of XPS spectra which can help with assignment of the XPS peaks. Here it was thought that the two peaks in the C1s spectra could be broken down into contributions from three different types of carbon environments, sp^2 hybridised carbon atoms bonded to only carbon and carbon atoms bonded directly to a nitrogen and sp^3 hybridised carbon atoms. The calculations performed have allowed an additional method into confirming this analysis and the simulations are not consistent. This shows that DFT simulations can be used to provide additional information to help in the assignment of XP spectra.

Chapter 7

Characterisation of Oxygen-Terminated Diamond via Measurements and Simulations of XPS

The following chapter presents work published in the paper referenced below and is a collaboration between experiment and theory. The detailed work presented in section 7.1 where calculations on the structure and stability were performed by Shayantan Chaudhuri and XPS experiments by Marc Walker and analysed by Dr. Benedikt P. Klein. Section 7.3 presents the work carried out for this thesis.

Coexistence of carbonyl and ether groups on oxygen-terminated (110)-oriented diamond surfaces
Shayantan Chaudhuri, Samuel J. Hall, Benedikt P. Klein, Marc Walker, Andrew J. Logsdail, Julie V. Macpherson and Reinhard J. Maurer
Communications Materials **3**, 6 (2022)
https://doi.org/10.1038/s43246-022-00228-4

7.1 Introduction

The practical uses of diamond are wide ranging and have found uses in many fields due its hardness [235], thermal conductivity [236] and a high Debye temperature [237]. For many of these uses diamond is grown via chemical vapour deposition (CVD) [238]. Typically, after growth, diamond surfaces posses hydrogen termination [239], subsequent treatments such as mechanical polishing or chemical cleaning render the surface oxygen terminated, or if left untreated and exposed to air, the surface can oxidise over time [240, 241]. These oxygen terminations can affect various properties by reducing the surface electrical conductivity [240], increasing capacitance [242], and by changing the electron-transfer kinetics in electrochemical reactions on boron-doped diamond (BDD) electrodes [243].

The oxygen-termination states of diamond have been studied previously in literature, with studies on the (111) and (100) surfaces [244] receiving the most attention while less is known of the (110) surface. This can be attributed to the difficulties in obtaining a single crystal (110) diamond surface with desirable quality [245]. Carbonyl and ether functional groups have been found to be present on (111) and (100) surfaces through various theoretical studies [246–259]. The presence of these same groups has also been proposed in experimental studies of (111) and (100) surfaces through the use of infra-red and x-ray spectroscopy [260–264]. Studies on the (110) surface are not as prevalent in literature but also suggest the presence of carbonyl and ether groups [244, 265–267].

A CVD grown (110)-oriented single-crystal boron-doped diamond sample was characterised with XPS by Dr. Marc Walker. Spectra were recorded both before and after annealing at a temperature of 500 °C to remove any surface contaminants from the sample. XPS results for the annealed surface of both the C1s and O1s are shown in figure 7.1 where both spectra have been fitted with two sub-peaks [268]. In figure 7.1 (a) the spectra exhibit a main peak with a small shoulder at higher energies. This can be fitted as one large main peak (gold) and a smaller overlapping peak (blue) with a difference between the two peaks of 0.7 eV. For the O1s spectra in figure 7.1 (b), the broad spectrum can also be fitted to two peaks with a ratio of 2:1 between the low BE peak and the high BE peak. The relative shift between the two is 1.5 eV. By comparing to the values seen in the literature [265, 266] the low energy peak can be attributed to the carbonyl oxygen whilst the higher energy peak can be attributed to the ether oxygen group. The results found from these experiments are reported in table 7.2 and 7.3. As these peaks are close together and the experimental resolution is not good enough to identify these peaks, XPS simulations are performed to further corroborate this analysis.

Following a characterisation of various oxygen-terminations on a (110) diamond surface through the use of *ab initio* atomistic thermodynamics [269–271] based on DFT by Shayantan Chaudhuri, a phase diagram was created for a large number of surface structures and used to identify the most stable oxygenation state of the (110) surface. This phase diagram presented how the termination of the diamond surface changes with temperature and pressure from a clean diamond surface to oxygenated surfaces. Various terminations based on different surface coverages and terminations of carbonyl/ketone, ether, peroxide and hydroxyl groups were investigated. The phase with the largest adsorption energy was found to be the $p(2\times1)$Keto-Ether$_5$ phase (figure 7.2 (b)) with both values as a function of surface area ($E_{\mathrm{ads}}A$) and per atomic adsorbate (E_{ads}) of $0.34\,\mathrm{eV}/\mathrm{\AA}^2$ and $3.03\,\mathrm{eV}/\mathrm{atom}$ respectively. As the name suggests this phase consists of two types of oxygen groups in the form of a ketone (C=O) and ether (C–O–C) with Ether$_5$ indicated a 5-ring ether. This combination of carbonyl and ether groups also provided the most stable structure across lower coverage phases, $p(2\times2)$Keto-Ether$_5$ (figure 7.2 (c)).

Looking at a range of temperatures and pressures, the $p(2\times1)$Keto-Ether$_5$ was found to be the most prevalent phases at a temperature range of 0 K to 1000 K and at standard pressure. At higher temperatures (>1000 K) and lower pressures ($<1 \times 10^{-6}$ atmosphere) the hydrogen-terminated surface became more stable whilst at lower temperatures, below 100 K the p(1×1)Peroxide (figure 7.2 (a)) was most stable.

XPS simulations on the stable oxygen-terminated structures of a (110) diamond surface determined by DFT calculations were performed and compared to the experiments detailed previously by collaborators to help corroborate the structures and to provide helpful insight into the analysis of XPS spectra. This also helped to test the validity of the core-level simulations using an insulating system and to further study the role of finite-size effects [143] on the periodic unit cell used, through comparison with an aperiodic method.

7.2 Computational Details

XPS calculations were performed using both the FHI-aims and CASTEP approaches described in section 3.3.1. Both C1s and O1s BEs were calculated using the PBE XC functional [53]. Periodic calculation with CASTEP used a PW cut-off of 650 eV and an electronic energy tolerance of 1×10^{-6} eV/atom. Supercells of various sizes were constructed to systematically assess the BE convergence and the role of finite size effects along with models with increased carbon layers. As the supercell size increased the reciprocal grid size was gradually decreased to perform calculations with constant k-grid density.

Aperiodic or cluster calculations were performed in FHI-aims and used the FOB keyword to constrain the core-hole. A ‘tight-tier2’ basis set was implemen-

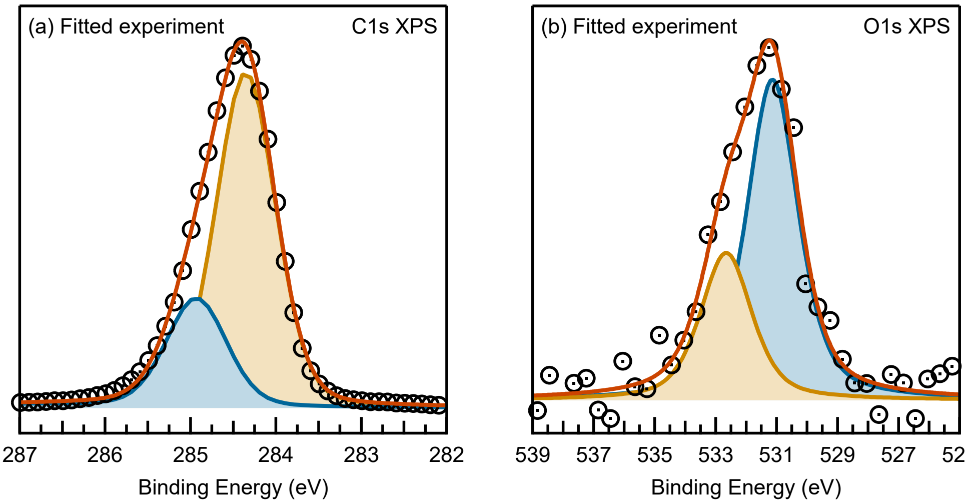

Figure 7.1: Experimental x-ray photoelectron (a) carbon 1s and (b) oxygen 1s spectra of diamond sample taken at normal emission after annealing to 500 °C [268]. Blue peaks represent signals originating from an carbonyl moiety whilst gold are from an ether. Open circles: data, red line: fit function, shaded areas: fitted peaks.

ted and calculations performed to convergence thresholds of 1×10^{-4} e/Å for the electron density, 1×10^{-2} eV for the sum of eigenvalues and 1×10^{-6} eV for the total energy with a variation of the MOM [65] utilised to keep the constraint in place. All calculations performed, placed the constrained atom in the centre of the surface cluster model. The raw input and output files for the calculations in this chapter can be found in the NOMAD repository and are freely available (DOI: https://dx.doi.org/10.17172/NOMAD/2021.03.01-1).

7.3 Results

7.3.1 Convergence

The XPS BEs of the p(1×1)Peroxide and $p(2 \times 1)$Keto-Ether$_5$ structures were calculated using both periodic and aperiodic (cluster) models. Whilst cluster calculations allow for absolute BEs to be calculated and compared to experiment, periodic calculation suffer from inherent problems that prevent direct comparison to experiment, however relative shifts within the structure can be calculated (see Chapter 3). An investigation of these two models looking at the convergence of the BEs with respect to the size of the unit cell, through increasing supercells, and cluster radius was conducted. The initial primitive unit cells for the two structures of p(1×1)Peroxide

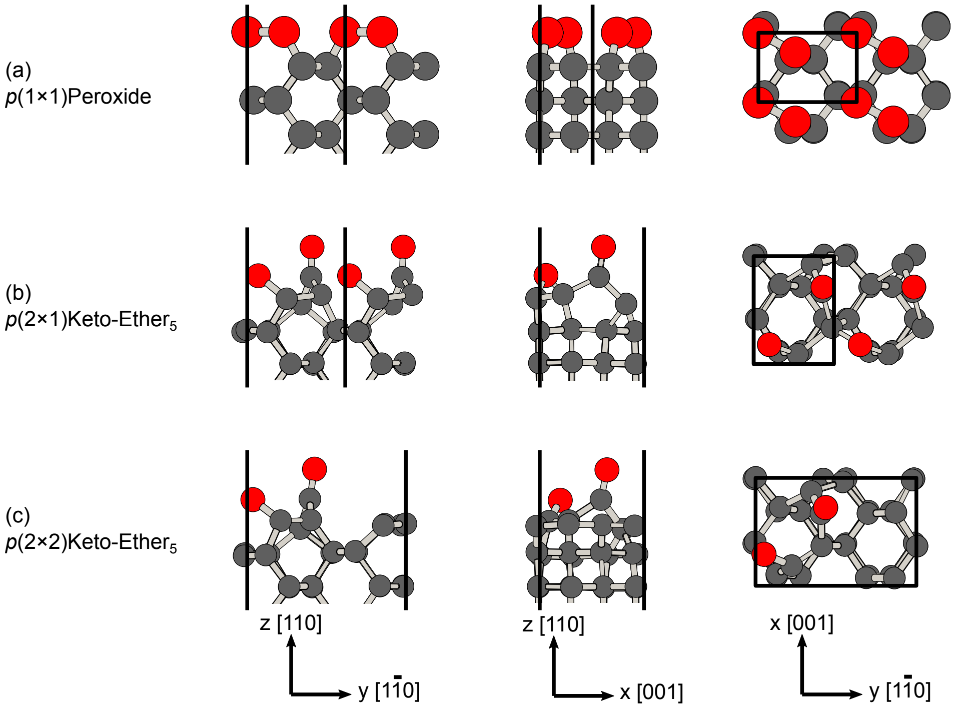

Figure 7.2: Structure visualisation of the $p(1 \times 1)$Peroxide and $p(2 \times 1)$Keto-Ether$_5$ and $p(2 \times 2)$Keto-Ether$_5$ structures shown from three different perspectives. Unit cell outlines are shown as black lines.

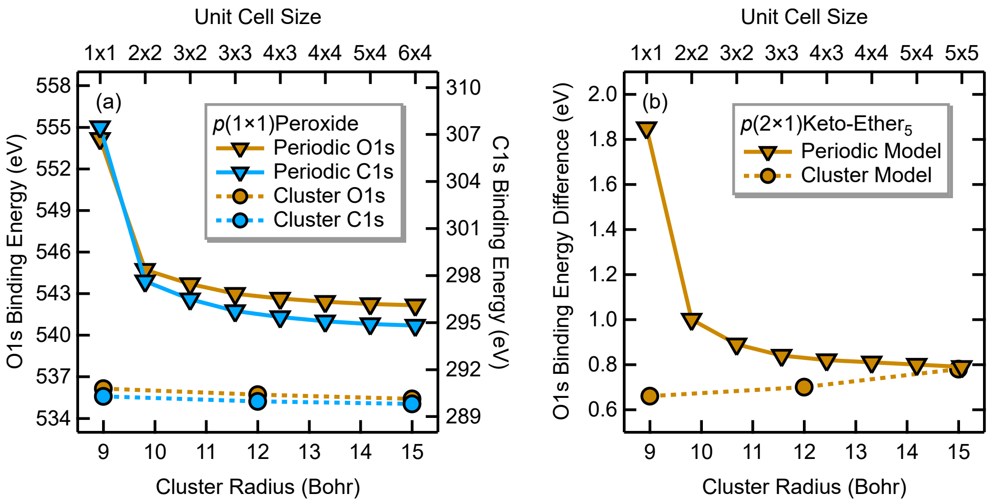

Figure 7.3: Graphs showing the convergence behaviour of XPS BEs calculations of (a) the $p(1 \times 1)$Peroxide phase and (b) the $p(2 \times 1)$Keto–Ether$_5$ phase for with respect to either unit cell and cluster size for CASTEP and FHI-aims respectively. (a) shows the absolute values of the C1s and O1s BEs whilst (b) shows the relative difference in shifts between the O1s shifts of the carbonyl and ether.

and $p(2 \times 1)$Keto-Ether$_5$ are shown in figure 7.2 (a) and (b) respectively, whilst three cluster sizes of each structure are shown in the appendix in figure B.11 and B.10. The convergence behaviour of these two models with respect to increasing size are shown in figure 7.3. Figure 7.3 (a) shows the absolute BEs of both the O1s and C1s XPS in the p(1×1)Peroxide structure as the supercell size and cluster radius are increased. Here the absolute BE value between the periodic and cluster models are not comparable due to the inherent problem of PBCs, the need for a homogeneous background charge and the use of pseudopotentials.

For the $p(2 \times 1)$Keto-Ether$_5$ in figure 7.3 (b), the relative shift between the O1s BEs of the carbonyl and ether were compared to system size. This comparison allows for both model types (periodic and cluster) to be directly compared and as the system sizes for each increase both converge onto the same value of 0.8 eV. Using this knowledge, all calculations and results obtained were performed using a periodic model at converged unit cell sizes due the greater computational efficiency of periodic models. Full convergence behaviour and absolute values of the convergence study are shown in the appendix in table B.8 and B.9.

Both structures of peroxide and keto-ether are modelled with 7 carbon layers. This was found to provide enough layers to provide a converged carbon bulk value. The difference between the C1s BEs of a surface carbon and the lower layers for a 7- and 9-layer clean diamond surface were compared. The results are given in table 7.1, showing that the bulk BE value converged by the 4th layer indicating that the structures used have adequate layers when taking the BE of the centre layer for the bulk value.

Looking into the behaviour of the O1s and C1s XPS simulations with respect to

Table 7.1: C1s XPS BE each layer in two systems of bulk diamond consisting of either 7- or 9-layers.

Structure	Surface	2nd	3rd	4th	5th
7-layer	291.25	293.11	293.27	293.53	-
9-layer	290.07	291.96	292.16	292.45	292.45

the size of the model used. It is found that whilst the absolute BEs obtained through use of the periodic model are not consistent with the cluster model and experiments, (figure 7.3 (a) the relative shifts seen in the structure as in the case of the two oxygen groups in $p(2\times1)$Keto-Ether$_5$ (figure 7.3 (b)) converge onto the same value, giving considerable confidence in the obtained value.

7.3.2 XPS results

The O1s and C1s BEs were calculated for the two keto-ether phases at different coverages shown in figure 7.2. Due to different sizes of the primitive cell for both the converged supercells used in the simulations are different. Converged values for the high coverage $p(2\times1)$Keto-Ether$_5$ phase were found at the 5×5 cell with a unit cell size of 17.9 Å×25.3 Å. The converged size for the lower coverage $p(2\times2)$Keto-Ether$_5$ phase was for the 4×4 supercell with unit cell dimensions of 20.2 Å×28.6 Å. The results presented use the XPS values from these supercells and are shown in table 7.2 and table 7.3 and compared to experimental and literature results.

The centre most atom in the cell was constrained with the core-hole for each coverage phase. For the C1s results, the BEs for the carbonyl carbon and both carbon atoms were calculated. Table 7.2 shows the calculated carbon BEs of the surface groups compared with the bulk carbon BE from the central layer. For the more stable higher coverage $p(2\times1)$Keto-Ether$_5$ phase the carbonyl C=O value does not match well with any of the experimental or literature results. The ether carbon

Table 7.2: Comparison of C1s BE shifts for the Keto-Ether$_5$ phases with respect to the diamond bulk signal (ΔBE). For the simulation of the ether group, two carbon BEs are given, one for each oxygen-bonded carbon atom. The experiments by Warwick only showed two peaks, the bulk carbon and one carbon-oxygen peak, whereas in the literature, two peaks were given in relation to the bulk carbon.

	C1s ΔBE (eV)				
	Simulation		Experiment		
Species	$p(2\times1)$	$p(2\times2)$	Warwick [268]	Baldwin [265]	Makau [266]
$\underline{\mathrm{C}}\mathrm{=O}$	1.16	0.74	0.7	2.2	4.5
$\underline{\mathrm{C}}\mathrm{-O-C}$	1.46	0.80	0.7	1.1	1.9
$\mathrm{C-O-}\underline{\mathrm{C}}$	1.23	0.30	0.7	1.1	1.9

Table 7.3: Comparison of the O1s BE difference (ΔBE) for the Keto-Ether$_5$ phases. The O1s ΔBE is calculated as the difference between the BEs of the oxygen atoms involved in the carbonyl ($\underline{C}=O$) and ether ($\underline{C}-O-C$) functional groups. The experimental data reports the ΔBE between the two peaks in the corresponding O1s spectra.

O1s ΔBE (eV)				
Simulation		Experiment		
$p(2\times1)$	$p(2\times2)$	Warwick [268]	Baldwin [265]	Makau [266]
1.0	1.3	1.5	1.7	2.1

atoms C−O−C, again disagree with the experiments performed for this work but lie in-between the two values from Baldwin [265] and Makau [266]. For the lower coverage $p(2\times2)$Keto-Ether$_5$ phase, the values for the carbonyl and ether are in close agreement with the experiments but also show one ether BE much lower than the other.

The absolute BEs of the carbonyl and ether agree with the experimental fitting with the carbonyl having a lower BE and the higher BE peak belonging to the ether group. For comparison of the O1s BEs, the relative difference between the BEs of the two oxygen groups was compared, these are shown in figure 7.3. For the $p(2\times1)$Keto-Ether$_5$ phase, the shift between the two BEs was 1.00 eV, this value is much smaller that the experimental value at 1.50 eV and both the literature values which are higher still. The $p(2\times2)$Keto-Ether$_5$ phase exhibits a slightly larger shift (1.3 eV) than the higher coverage, which is much closer to the fitted shifts from experiment shown in figure 7.1.

7.4 Discussion

By using two different modelling approaches, a periodic and cluster models a comparison between the two can be carried out. For both models the size of the structure needs to be taken into consideration to achieve a converged result, with rather large models with a significant total number of atoms needed. It has further shown that the CASTEP code with its PW PP basis can still provide reliable result for relative shifts when compared to all-electron codes such as FHI-aims, given that finite-size effects and cell charging are dealt with using a large enough unit cell. The agreement can be seen in figure 7.3 (b) where for the $p(2\times1)$Keto-Ether$_5$ phase both the periodic and cluster models converge to the same result of 0.8 eV for the relative shift between the two O1s BEs. On the other hand, for the cluster method, where the diamond structure is not a repeating model and requires terminating hydrogen species at the edges of the structure, the agreement with the periodic method also points to the fact that these effects have no great influence on the XPS.

As seen in table 7.2, the simulated results show a smaller difference between the two literature values reported [265, 266]. Out of the two keto-ether coverages, the values of the carbonyl and ether carbon BEs with respect to the bulk carbon value is much lower and closer to the value for experiments performed by Dr. Marc Walker. In table 7.3, showing the relative O1s shifts the same trends with the experimental results are seen with the lower coverage system providing more agreeable results with the Warwick experiments. Out of the XPS simulations of the two coverages, both the C1s and O1s results provide a closer result to experiment for the lower $p(2\times2)$Keto-Ether$_5$ phase rather than the $p(2\times1)$Keto-Ether$_5$ phase, which was found to be the most stable and most prevalent. A reasoning behind this is thought to be that even though the higher coverage structure is computationally suggested to be the most stable and likely phase, this structure might be difficult to realise in a realistic experimental setting.

The discrepancy seen in the two literature results as reported by Baldwin [265] and Makau [266] are believed to be a consequence of the quality of the sample used in these studies. In the procedural details provided on the experiments, no mention of any annealing was given before recording the XPS spectra. The peaks that are reported at much higher values than anything seen in the simulations and experiments could therefore be originating from various surface contaminants. As previously mentioned, XPS experiments carried out by Marc Walker were performed both before and after annealing the surface at 500 °C. In the C1s spectra obtained before annealing, additional peaks at 1.5 eV and 4.1 eV above the bulk diamond peak are present which align much closer the the values reported in these studies, suggested that these could be the origin of the high BE values found in the literature.

7.5 Conclusion

A joint experiment and theory study combining *ab initio* atomistic thermodynamics based on DFT with both experimental and simulated (with DFT) XPS spectra to investigate oxygen-terminated diamond (110) surfaces was conducted. Shayantan Chaudhuri used DFT to establish a phase diagram of the most stable oxygen terminations of the diamond (110) surface. The results from this found the $p(2\times1)$Keto-Ether$_5$ phase to be the most stable phase at standard pressure and between 0-1000 K. C1s and O1s XPS experiments were performed by Dr. Marc Walker and analysed by Dr. Benedikt P. Klein and found a disagreement between the BEs recorded when compared to literature data. XPS simulations of the theoretical $p(2\times1)$Keto-Ether$_5$ phase were performed and were found to neither adequately match both the experiment and the literature results. Therefore, a lower coverage structure of the same phase was investigated. The simulated XPS BEs agreed much more favourably with the experimental results. The reason for this could be the most stable phase found is experimentally difficult to achieve and that the lower covergae phase is the most prevalent phase found in an experimental setting, which gave way to the lower coverage system being a better representation of the experimental results.

In the case for the disagreement between the literature results, it was report that no annealing of the diamond surfaces was performed. This would lead to contaminants still possibly being present on the surface. Peaks reported in the literature were found in before the surface and annealed but disappeared after annealing which points to the surfaces in the literature contained contaminants.

Chapter 8

Conclusion

Core-level spectroscopy represents an important and effective tool to reveal various properties of materials from chemical state, structural geometry, chemical bonding and electronic structure. It is particularly useful for molecular adsorbate systems due to the surface sensitive nature of the technique. First principles simulations of XPS and NEXAFS can be used to provide additional insight into the analysis of organic molecules adsorbed onto metal surfaces that are not possible through experiment alone. These simulations can help with peak assignment and to disentangle overlapping features that are widely seen in systems with similar chemical environments such as conjugated structures. The simulations can allow for further investigation into the structure, stability and chemistry at surfaces by understanding and identifying the features seen in spectra.

This thesis has in detail presented the methodology to simulate 1s XPS and K-Edge NEXAFS spectra in the PW code CASTEP [102]. For performing the ΔSCF and ΔIP-TP simulations, several tools have been created, which simplify and automate the process as much as possible to result in fully broadened spectra. The numerical and technical details of these simulations have been widely tested on various systems ranging from organic molecules, molecular crystals to metal-organic interfaces. Technical and numerical issues originating from PBCs and the need for a homogeneous background charge, which affects absolute energies, were investigated. Results were compared with the all-electron DFT code FHI-aims [105] where these problems are not a factor of consideration and performance was found to agree well on the relative shifts seen within the spectra. This highlighted that, when the proper measures are taken into account, comparable results are possible.

After benchmarking the performance of the core-level simulations, the simulated spectra were compared against experimental data, [79–81, 157] first for azulene and naphthalene in a multilayer structure and adsorbed on three metal surfaces Ag(111), Cu(111) and Pt(111) and then against the two larger molecules of pyrene and azupyrene (multilayer and on Cu(111)). Excellent agreement was seen for both XPS and NEXAFS spectra of azulene and naphthalene with the exception of the XPS for Az/Ag(111). Here a peak shoulder present in the experiment was not modelled in the calculations.

This was found to be caused by spurious charge transfer arising from erroneous Fermi level pinning of the LUMO of the molecule. The cause of the problem was a self-interaction error and could be reduced by shifting chosen reference orbitals with a penalty functional. This resulted in more agreeable spectra with the experiment. In the ΔIP-TP method where the XPS BEs are used as onset for the NEXAFS spectra, any error in the XPS BEs can be carried over into the NEXAFS simulations. By using the the corrected BEs for Az/Ag(111) the resulting NEXAFS lead to a better comparison to the experiment. The core-level simulations were then tested further by comparing the simulated results to the larger conjugated molecules of pyrene and azupyrene and agreement between experiment and DFT simulation was found.

After establishing that the simulations are in agreement with experiments, focus was put on the interaction between the molecule and metal surface. Looking into the systems of azulene and naphthalene on the three metal surfaces, three different interaction regimes were identified: physisorption for Np/Ag(111), Np/Cu(111) and Az/Ag(111); weak chemisorption for Az/Cu(111) and strong chemisorption for Np/Pt(111) and Az/Pt(111). From the simulations a list a key features that can be used to help identify the strength and nature of interaction was put forward. In particular, large changes can be seen in spectral features in both the XPS and NEXAFS. Metal adsorbed structures can be compared to systems with little or no metal influence as a reference to see how the interaction changes the spectra. Any changes the in spectra is an indication of interaction between the metal surface. In XPS these can be a loss of noticeable features and a change in peak shape. Changes in NEXAFS can be used to further quantify the strength of interaction. Only slight broadening but still clear and present features can indicate physisorption of the molecule. The reduction in intensity of the first peak can show greater interaction strength and loss of all distinct peak features indicate a strong chemisorption interaction. By recording spectra at different angles, the dichroism of the spectra can also be used to help identify the orientation of the molecule, as the dichroism decreases, the interaction strength increases. Other analysis methods such as the net charge transfer and changes in the DOS can be used to help highlight and describe the bonding between a molecule and metal surface.

Not only can core-level spectra help to describe the molecule-metal interaction, but they can also be used to help understand the structures adsorption, with the case of the self-assembled molecule HTA highlighting this. Experiments found three different phases (α, β, and γ) and core-level spectra were recorded. By creating various models representing the different phases and simulating XPS a better understanding of the experimental structure was able to be obtained and experimental misinterpretations were corrected. This included the distortion of the molecule that was present by the molecule arching upwards and away from the metal surface in the centre of the molecule. When arched, the molecule could fit into the experimentally recorded unit cell. This arching also helped to describe the intensity ratio seen in the XPS experiment as change in height of the nitrogen atoms affected the screening of the atom. Also, the presence of gold adatoms on the surface was confirmed due to the chemical shifts in the simulated spectra matching the shift seen in experiment when they were included.

Finally, the stability of oxygen-terminated diamond (110) surfaces was investigated. XPS was used to compare stable phases found from a structure search against experiment and literature results. It was found that the most stable phase of $p(2\times1)$Keto-Ether$_5$ did not represent the best agreement with the experimental data but that a lower coverage phase $p(2\times2)$Keto-Ether$_5$ provided the best agreement. It is possible, that this lower coverage phase is more likely to be found in real world experiments than the most stable $p(2\times1)$Keto-Ether$_5$ as the theoretical investigation works on idealised surface conditions not attainable in a real system.

The work presented in this thesis has shown an effective and reliable method to calculate core-level spectroscopy. The method has proved to provide great efficiency in computational resources when compared to other methods and the development of tools to help automate the process, allows for a simple and fast set up and execution of all necessary post processing. These core-level simulations allow for XP and NEXAFS spectroscopic features to be identified and pinpointed to various aspects of the system, including initial-state atom contributions and final-state MO contributions. Changes in features seen in spectra have been detailed and linked to the level of interaction between the molecule and metal surface and provide valuable information for experiment in the future to help analyse and understand similar spectra.

Further work should explore the applicability of this methodology for higher core-shell spectral simulations. Moving on from the C1s and C K-edge NEXAFS spectra, the method can be used to look into higher shell excitations such as 2s and 2p XPS and L-edge NEXAFS of transition metals, like Mn, Fe, Co and Ni etc. To implement this, more factors would need to be taken into consideration such as spin-orbit coupling. Whilst mainly focusing on carbon spectra, a few examples of simulating nitrogen and oxygen spectra have been simulated. This work could be expanded to look at the performance of these elements along with other heteroatoms in molecules could be investigates to further expand the practicable uses this method.

Whilst CASTEP can provide a reliable and accurate method, allowing for exact localisation of the core-hole on the required atom and calculation of relative energies, absolute energies are unattainable due to the ‘frozen’ core-electron and homogeneous background charge. This is not as much of a problem for FHI-aims with its all-electron approach, and possibility to calculate aperiodic models and allowing for absolute BEs. The localisation of the core-hole onto the chosen atom can provide a stumbling block especially for conjugated aromatic molecules. Various problems in calculating the XPS BEs can occur, with either the core-hole localising across multiple atoms, the core-hole localising on the wrong atom or the calculation not converging at all due to localising problems. Further work can be carried out to look into this problem and address the localisation issues. This would open this method to reliably calculate XPS and NEXAFS spectra opening the door to assess the results on an absolute scale with experiment.

Appendix A

Code

```python
#!/usr/bin/python

import os
import shutil
from ase.calculators.castep import Castep
from ase.io import read
from core_excitation import CoreExcitation
from core_excitation import NEXAFS, XPS

#Full name of the geometry input file for script to read and create files for
input_name = 'hta.cell'
#Seedname of the CASTEP files that the script will output
output_name = 'azulene_Ag'

#Add all atom pseudopotentials you want
Cpseudo = 'C 2|1.4|10|12|13|20:21(qc=7)'
Hpseudo = 'H 1|0.6|13|15|17|10(qc=8)'
#Npseudo = 'N 2|1.1|14|16|18|20:21(qc=7)'
Agpseudo = 'Ag 3|1.5|1.5|0.8|15|17|19|40U:50:41:42(qc=7)'

#If a MO analysis is needed as the list of MOs to be projected and
#checkfile name to be used as the reference for the MODOS calculation
MO = list(map(str, range(17,29)))
check = 'azulene_free.check'

##############################################################
#CASTEP calculators: if one set of keywords is needed for both XPS and NEXAFS put all
#keywords you want in QM1 and leave QM2 blank of castep keywords.
#If different set of keywords needed put XPS keywords in QM1 and anything you want to
#overide and change in NEXAFS put into QM2

QM1 = Castep(
            castep_command='/storage/molases/mstrdw/MARBURG_bins/castep20.1/castep.mpi', #Directory path to location of castep binary
            label=output_name,
            _rename_existing_dir=False,
            _export_settings=False,
            _pedantic=False,
            _find_pspots=False,
#List the paramters and what setting you want to be included in the .param file
            xc_functional='PBE',
            cut_off_energy=450,
            spin_polarized=False,
            data_distribution='default',
            elec_energy_tol='1e-06',
            grid_scale=2.0,
            iprint=1.0,
            max_scf_cycles=300,
            metals_method='dm',
            mixing_scheme='Pulay',
            nextra_bands=100,
            smearing_scheme='Gaussian',
            smearing_width=0.1,
            fix_occupancy=False,
            num_backup_iter=5,
            num_dump_cycles=0,
            opt_strategy_bias=3,
            pdos_calculate_weights=True,
            fix_com=False,
            fix_all_cell=True,
            kpoints_mp_grid='6 6 1',
            kpoints_mp_offset='0. 0. 0.')

QM2 = Castep(
            castep_command='/storage/molases/mstrdw/MARBURG_bins/castep20.1/castep.mpi',
            label=output_name,
            _rename_existing_dir=False,
            _export_settings=False,
            _pedantic=False,
            _find_pspots=False,
#List of parameters to change for NEXAFS files go here
            nextra_bands=1000,
            elnes_nextra_bands=1000)

###############################################################
#Change to the required element and pseudopotential string to correct selection
#and add the required core holes for XPS(full) and NEXAFS(half) in the electron
```

```
#configuration

#Using core_excition.py read the input file and run XPS and NEXAFS to generate the folder
#and files
cell = read(input_name);
xce = XPS(atoms=cell, element=’C’, pspots=’2|1.4|10|12|13|20:21{1s1,2s2,2p3}(qc=7)’, calc=QM1)
xce.move_hole()

QM1.merge_param(QM2.param) #Merge QM2 with QM1 to overwrite any changes needed in the NEXAFS files
cell = read(input_name);
nce = NEXAFS(atoms=cell, element=’C’, pspots=’2|1.4|10|12|13|20:21{1s1.5,2s2,2p2.5}(qc=7)’, calc=QM1)
nce.move_hole()

############################################################
#Add all the ground state pseudopotentials stated above to the XPS and NEXAFS .cell files
#Add and change the lines to the same variables stated above for each pseudpopotential
#and add it to the writeout line

xps = ’XPS/’
nexafs = ’NEXAFS/’

xdirecs = os.listdir(xps)
ndirecs = os.listdir(nexafs)

#Loop over all the directories in the XPS folder
for x in xdirecs:
    xifile = open(xps+x+’/’+output_name+’.cell’, ’r’).readlines() #Read each .cell file to memory
    xofile = open(xps+x+’/’+output_name+’.cell’, ’w’) #Open .cell file to write into
#Search the xi file and if string is present then write out each line below in the xo file
    for line in xifile:
        xofile.write(line)
        if ’%BLOCK SPECIES_POT’ in line:
            line1 = ’%s’ %(Cpseudo)
            line2 = ’%s’ %(Hpseudo)
            #line3 = ’%s’ %(Npseudo)
            line3 = ’%s’ %(Agpseudo)
            xofile.write(line1 + ’\n’ + line2 + ’\n’ + line3 + ’\n’)# + line4 + ’\n’)
    xofile.close()

#Do the same for NEXAFS files
```

```
for n in ndirecs:
    nifile = open(nexafs+n+'/'+output_name+'.cell', 'r').readlines()
    nofile = open(nexafs+n+'/'+output_name+'.cell', 'w')
    for line in nifile:
        nofile.write(line)
        if '%BLOCK SPECIES_POT' in line:
            line1 = '%s' %(Cpseudo)
            line2 = '%s' %(Hpseudo)
            #line3 = '%s' %(Npseudo)
            line3 = '%s' %(Agpseudo)
            nofile.write(line1 + '\n' + line2 + '\n' + line3 + '\n')# + line4 + '\n')
    nofile.close()

###########################################################
#To add the neccesary keywords to run a MolPDOS calculation comment out assert
#quit()

#For CASTEP 20.1 and higher
#In all of the NEXAFS atom directories open the .param file and write out the
#required keyords for MODOS calculation
for n in ndirecs:
    file = open(nexafs+n+'/'+output_name+'.param', 'a+')
    file.write('\nCALCULATE_MODOS: TRUE\n')
    file.write('MODOS_CHECKPOINT: '+check)
    file.write('\n%BLOCK MODOS_STATES\n')
    for m in MO:
        file.write(m+' 1\n')
    file.write('%ENDBLOCK MODOS_STATES')
    file.close()

#For CASTEP 19 and lower (a seperate .deltacsf file will need ot be created)
#Add devel_code block for MolPDOS calculation to .param file in all NEXAFS directories
#A seperate .deltascf file will be needed to created and added to all of the atom
#directories to define the settings wanted
#for i in ndirecs:
#     file = open(nexafs+i+'/'+output_name+'.param', 'a+')
#     file.write('\n%BLOCK DEVEL_CODE\n')
#     file.write('MolPDOS\n')
#     file.write('%ENDBLOCK DEVEL_CODE')
#     file.close()
```

Listing A.1: autoscript.py

```python
#!/usr/bin/python

import os

class CoreExcitation(object):

    prefix = './'

    def __init__(self, atoms, element, calc=None, directory='./'):
        self.atoms = atoms
        self.element = element
        self.calc = calc
        self.directory = directory

    def _find_all_elements(self):
        self.idx = [] #Define idx as a string
        i = 0
        for elem in self.atoms.symbols: #Look through the elements in the atoms object
            if elem == self.element: #If stated element found
                self.idx.append(i) #Add element position to the idx string
            i += 1

    def _create_subdirectories(self):
        self._find_all_elements()
        for idx in self.idx: #For all element in the idx string
            os.makedirs(self.prefix + self.element + str(idx)) #Make a directory for all elements found

    def move_hole(self):
        self._create_subdirectories()
        for idx in self.idx: #For each element in string
            if self.atoms.symbols[idx - 1] == 'X': #If previous element in string is X
                self.atoms.symbols[idx - 1] = self.element #Change it back to stated element
            self.atoms.symbols[idx] = 'X' #And change new element to X
            self._create_input(idx)

    def _create_input(self, idx):
        directory = self.prefix + self.element + str(idx) #Defining the diretory path
        self.calc._directory = directory #Changing the path of the castep calculator
        self.atoms.set_calculator(self.calc) #Run the cstep calculator for cell
        self.calc.prepare_input_files(elnes_species=self.element)
        #Prepare the input files for that folder

class NEXAFS(CoreExcitation):

    prefix = 'NEXAFS/'

    def __init__(self, atoms, element, pspots, calc=None,
directory='./'):
        super(NEXAFS, self).__init__(atoms, element, calc)
        self.calc.param.task = 'ELNES'
        self.calc.param.charge = 0.5
        self.calc.set_pspot(pspot=pspots, elems='{}:exc'.format(
element), manual=True)

class XPS(CoreExcitation):

    prefix = 'XPS/'

    def __init__(self, atoms, element, pspots, calc=None,
directory='./'):
        super(XPS, self).__init__(atoms, element, calc)
        self.calc.param.task = 'SINGLEPOINT'
        self.calc.param.charge = 1.0
        self.calc.set_pspot(pspot=pspots, elems='{}:exc'.format(
element), manual=True)
```

Listing A.2: core_excitation.py

```
import re
import ase
from ase.io import read

def get_energy_level(line):
    for word in line.split():
        try:
            return float(word)
        except ValueError:
            pass

#This script searches through the ground state and excited state .castep files
#and calculates the XPS binding energies for a pseudopotential calculation
#based on the method in J. Phys.: Condens. Matter 21 (2009) 104204

#Set the element, the numbers of the XPS directories and the seedname of
#the castep calculations
element = ’C’
num_start = 48
num_end = 57
filename = ’azulene_Ag.castep’
#Set the range of the atom numbers
numbers = list(range(num_start,num_end+1))
################################################################

#Open the ground state .castep file
out = open(’../’+filename, ’r’)
content = out.read()
#Find lines with the atomic and pesudoatomic energies for the ground state
#element
atoC = re.findall(r’for ’+element+’: 1(.*?)V’, content, re.DOTALL)
atoC = "".join(atoC)
atoC = re.findall(r’energy(.*?)e’, atoC, re.DOTALL)
pseC = re.findall(r’for ’+element+’ 2(.*?)V’, content, re.DOTALL)
pseC = "".join(pseC)
pseC = re.findall(r’energy(.*?)e’, pseC, re.DOTALL)
out.close()
#Open the first excited atom .castep file and do the same as before for
#excited element
outx = open(element + str(numbers[0]) + ’/’ + filename, ’r’)
contentx = outx.read()
atoCx = re.findall(r’for ’+element+’:exc: 1(.*?)V’, contentx, re.DOTALL)
atoCx = "".join(atoCx)
atoCx = re.findall(r'energy(.*?)e', atoCx, re.DOTALL)
pseCx = re.findall(r'for '+element+':exc 2(.*?)V', contentx, re.
    DOTALL)
pseCx = "".join(pseCx)
pseCx = re.findall(r'energy(.*?)e', pseCx, re.DOTALL)
outx.close()

#Get the energy values from each of the previously acquired line
for line in atoC:
    if 'of' in line:
        aC_enrgy = get_energy_level(line)
print('Atomic '+element+' energy:', aC_enrgy)

for line in atoCx:
    if 'of' in line:
        aCx_enrgy = get_energy_level(line)
print('Atomic '+element+':exc energy:', aCx_enrgy)

for line in pseC:
    if 'of' in line:
        pC_enrgy = get_energy_level(line)
print('Pseudo '+element+' energy:', pC_enrgy)

for line in pseCx:
    if 'of' in line:
        pCx_enrgy = get_energy_level(line)
print('Pseudo '+element+':exc', pCx_enrgy)

#Get the difference between the atomic energies of the element (
    DeltaE_all orbitals(atom) in paper
#and the pseudoatomic energies (DeltaE_valence(atom) in paper
#Then the correction term DeltaE_core(atom)
D_Eall_orb = aCx_enrgy - aC_enrgy
print('Delta E_all_orb:', D_Eall_orb)
D_Eval_at = pCx_enrgy - pC_enrgy
print('Delta E_val:', D_Eval_at)
D_Ecore_at = D_Eall_orb - D_Eval_at
print('Delta E_core_at:', D_Ecore_at)

F_enrgy = 'Final energy'

#Open ground state .castep file and get the total final energy
with open('../'+filename, 'r') as ground:
    for line in ground:
        if F_enrgy in line:
            ground_enrgy = get_energy_level(line)
print('Ground-state energy:', ground_enrgy)

#Get all of the individual final excited state energies for all
```

```
    atoms
energies = []
for i in numbers:
    with open(element + str(i) + ’/’ + filename, ’r’) as exc:
        for line in exc:
            if F_enrgy in line:
                energies.append(get_energy_level(line))

#Calculate the energy difference between ground state and excired
     states
#then apply the pseudopotential correction term
D_Eval = [x - ground_enrgy for x in energies]
E_BE = [x + D_Ecore_at for x in D_Eval]

#Print out energies into file
with open(element+’_XPS_peaks.txt’, ’w’) as f:
    for item in E_BE:
        f.write(’%s\n’ % item)
```

Listing A.3: castep_get_XPS_energies.py

```
import numpy as np

def gaussian(x, x_mean, broadening):

    gaussian_val = np.sqrt((4*np.log(2))/(np.pi*(broadening**2)))
    * np.exp(-((4*np.log(2))/(broadening**2))*(x-x_mean)**2);
    return gaussian_val

def lorentzian(x, x_mean, broadening):

    lorentzian_val = (1/(2*np.pi))* (broadening)/(((broadening/2)
    **2)+(x-x_mean)**2);
    return lorentzian_val

def PseudoVoigt(x, x_mean, broadening, mixing):
    """
    Combines gaussian and lorentzian schemes together
    """
    return (1-mixing)*gaussian(x, x_mean, broadening)+mixing*
    lorentzian(x, x_mean, broadening)

def dos_binning(eigenvalues,broadening=0.75, bin_width=0.01, mix1
    =0., mix2 = None,
        coeffs=None,start=0.0, stop=10.0, broadening2 = None,
    ewid1 = 10.0, ewid2 = 20.0):
    """
    performs binning for a given set of eigenvalues and
    optionally weight coeffs.
    """
    if broadening2 is None:
        broadening2 = broadening
    if coeffs is None:
        coeffs = np.ones(len(eigenvalues))
    lowest_e = start
    highest_e = stop
    num_bins = int((highest_e-lowest_e)/bin_width)
    x_axis = np.zeros([num_bins])
    data = np.zeros([num_bins])
    #setting up x-axis
    for i in range(num_bins):
        x_axis[i] = lowest_e + i * bin_width
    #get DOS
    sigma=np.zeros((len(eigenvalues)))
    mixing=np.zeros((len(eigenvalues)))

    for ei,e in enumerate(eigenvalues):
        if e<=(ewid1):
            sigma[ei]=broadening
            mixing[ei]=mix1
        elif e>(ewid2):
            sigma[ei]=broadening2
            mixing[ei]=mix2
        else:
            sigma[ei]=broadening + ((broadening2-broadening)/(
    ewid2-ewid1))*(e-ewid1)
            mixing[ei]=(mix1 + ((mix2-mix1)/(ewid2-ewid1))*(e-
    ewid1))
    for i in range(num_bins):
        pseudovoigt_vec = np.zeros((len(eigenvalues)))
        pseudovoigt_vec=PseudoVoigt(x_axis[i],eigenvalues,sigma,
    mixing)*coeffs
        data[i]= np.sum(pseudovoigt_vec)
    return x_axis, data

###################################
xstart = 285.
xstop = 305.
broad1 = 0.7
broad2 = 0.7
firstpeak = 285.0
ewid1 = firstpeak+1.0
ewid2 = firstpeak+2.0
mix1 = 0.3
mix2 = 0.3
########################################

#Set what element you have calculated XPS for
element = 'C'
#Read in the XPS peaks in generated with python script
data = np.loadtxt(element+'_XPS_peaks.txt')
print(data)

#Apply the broadening
x, y = dos_binning(data, broadening=broad1, mix1=mix1, mix2=mix2,
     start=xstart, stop=xstop,
                   coeffs = None, broadening2=broad2, ewid1=ewid1,
    ewid2=ewid2)

#Write out the spectrum to a text file
fileout = open(element+'_XPS_spectrum.txt', 'w')
for (xi, yi) in zip(x,y):
    dat = str(xi) + ' ' + str(yi) + '\n'
    fileout.write(dat)
fileout.close()

#To get the indivdual atom peaks uncomment the quit() command
quit()

xs = []
ys = []
```

```python

for z in range(len(data)):
    peak = []
    peak.append(data[z])
    x_tmp, y_tmp = dos_binning(peak, broadening=broad1, mix1=mix1, mix2=mix2, start=xstart, stop=xstop,
                coeffs = None, broadening2=broad2, ewid1=ewid1, ewid2=ewid2)
    xs.append(x_tmp)
    ys.append(y_tmp)

    txtfile = open(element+'_XPS_spectrum_'+element+str(z)+'.txt','w')
    for (xsz, ysz) in zip(x_tmp, y_tmp):
        txt = str(xsz) + ' ' + str(ysz) + '\n'
        txtfile.write(txt)
    txtfile.close()
```

Listing A.4: plot_xps.py

```
#!/bin/bash

#Set the range of of numbers of the element directories
#seq(first step last) so seq 0 1 9) is 0, 1, 2... 9
#Set the angles wanted to run MolPDOS for
declare -a Array=($(seq 48 1 57))
#Theta values
declare -a AngleArray=("00" "25" "53" "90")

#Change to the molecule and metal of the system for filename
molecule="azulene"
metal="Ag"
element="C"

system="${molecule}_${metal}"

#Read the XPS binding energies and store in an array
readarray -t ArrayX < ../XPS/${element}_XPS_peaks.txt

#Search through all the directories and add the XPS energy to each of the .molpdos file
for index in ${!Array[@]}; do
    cd ${element}${Array[$index]}/
    sed -i "s/nexafs_xshift         :  [0-9]*.[0-9]*/nexafs_xshift     :  ${ArrayX[$index]}/g" ${system}.molpdos >> ${system}.molpdos
    cd ../
done

#Enter all of the directories and run MolPDOS for each angle stated and printing out the progress
for number in ${Array[@]}; do
  echo $number
  for angle in ${AngleTArray[@]}; do
      cd ${element}$number/
      echo $number $angle
      mkdir t$angle
      sed -i "s/nexafs_theta          :   [0-9]*/nexafs_theta   :   $angleT/g" ${system}.molpdos >> ${system}.molpdos
      MolPDOS $system
      mv *.dat t$angle/
      echo $number $angle "done"
      cd ../
  done
  echo $number "done"
done
```

Listing A.5: execute_molpdos.sh

```python
import numpy as np

def gaussian(x, x_mean, broadening):

    gaussian_val = np.sqrt((4*np.log(2))/(np.pi*(broadening**2))) * np.exp(-((4*np.log(2))/(broadening**2))*(x-x_mean)**2);
    return gaussian_val

def lorentzian(x, x_mean, broadening):

    lorentzian_val = (1/(2*np.pi))* (broadening)/(((broadening/2)**2)+(x-x_mean)**2);
    return lorentzian_val

def PseudoVoigt(x, x_mean, broadening, mixing):
    """
    Combines gaussian and lorentzian schemes together
    """
    return (1-mixing)*gaussian(x, x_mean, broadening)+mixing*lorentzian(x, x_mean, broadening)

def dos_binning(eigenvalues,broadening=0.75, bin_width=0.01, mix1=0., mix2 = None,
        coeffs=None,start=0.0, stop=10.0, broadening2 = None, ewid1 = 10.0, ewid2 = 20.0):
    """
    performs binning for a given set of eigenvalues and
    optionally weight coeffs.
    """
    if broadening2 is None:
        broadening2 = broadening
    if coeffs is None:
        coeffs = np.ones(len(eigenvalues))
    lowest_e = start
    highest_e = stop
    num_bins = int((highest_e-lowest_e)/bin_width)
    x_axis = np.zeros([num_bins])
    data = np.zeros([num_bins])
    #setting up x-axis
    for i in range(num_bins):
        x_axis[i] = lowest_e + i * bin_width
    #get DOS
    sigma=np.zeros((len(eigenvalues)))
    mixing=np.zeros((len(eigenvalues)))

    for ei,e in enumerate(eigenvalues):
        if e<=(ewid1):
            sigma[ei]=broadening
            mixing[ei]=mix1
        elif e>(ewid2):
            sigma[ei]=broadening2
            mixing[ei]=mix2
        else:
            sigma[ei]=broadening + ((broadening2-broadening)/(ewid2-ewid1))*(e-ewid1)
            mixing[ei]=(mix1 + ((mix2-mix1)/(ewid2-ewid1))*(e-ewid1))
    for i in range(num_bins):
        pseudovoigt_vec = np.zeros((len(eigenvalues)))
        pseudovoigt_vec=PseudoVoigt(x_axis[i],eigenvalues,sigma,mixing)*coeffs
        data[i]= np.sum(pseudovoigt_vec)
    return x_axis, data

######BROADENING PARAMETERS###################################

xstart = 275. #Start Value
xstop = 330. #End Value
broad1 = 0.75 #Broadening value for first section
broad2 = 2.0 #Broadening value for last section
firstpeak = 290.0
ewid1 = firstpeak+5.0 #Set the range to linearly move from broad1 to broad2
ewid2 = firstpeak+15.0
mix1 = 0.2 #First G/L mix raitio
mix2 = 0.8 #Last G/L mix ratio

######SYSTEM PARAMETERS########################################

n_type = 4 #1 for Total NEXAFS, 2 for angular, 3 for polarised, 4 for average polarised
angle = ['t25','t53','t90'] #Incidence angles
molecule = 'azulene' #Name of molecule
metal = 'Ag' #Surface in system
elem = 'C'
num_start = 48 # Set the num_start and num_end to values corresponding the the first and last numbers of your directories C48, C49... C57
num_end = 57
atom = '4' #The number of the excited atom in the list of elements in the system, always last do if systems contains H, C, Ag, C:exc, it will be 4
atom_contribute = False
numbers - list(range(num_start,num_end)) #Creates a range of numbers corresponding to the atom directory numbers

#####SETUP ALL LIST AND VARIABLES NEEDED#######################

#Set up a list of all the folders all the data is in C48/, C49/... C57/
```

```python
folders = []
for n in numbers:
    folders.append(elem+str(n)+'/')

#Create variable with a string for the delta file which will be read
filename = '/'+molecule+'_'+metal+'_'+atom+'_1_1_1_deltas.dat'

#Get the length of the deltas file
bands = np.loadtxt(elem+str(numbers[0])+'/'+angle[0]+'/'+filename)
bands_num = len(bands)

#Create arrays with sizes of the system to use
peaks = np.zeros([len(numbers),bands_num])
I = np.zeros([len(numbers),bands_num])

##########################################################
#Loop over all the angles and the individual directories
for a in angle:
    for i,direc in enumerate(folders):
#Load the data from the MolPDOS calculation
        data = np.loadtxt(direc+a+filename)
        x, y = data[:,0], data[:,n_type]
        peaks[i,:] = x
        I[i,:] = y
#Write out all of the data for all atoms into a delta peaks file
    fileout = open(molecule+'_'+metal+'_deltas_'+a+'.txt','w')
    fileout.write('#    <x in eV>      Intensity\n')
    for p,i in zip(peaks.flatten(), I.flatten()):
        fileout.write('{0:16.8f}    {1:16.8f}\n'.format(p,i))
    fileout.close()
#Apply the broadening to the data
    x, y = dos_binning(peaks.flatten(), broadening=broad1, mix1=mix1, mix2=mix2, start=xstart, stop=xstop,
        coeffs = I.flatten(), broadening2=broad2, ewid1=ewid1, ewid2=ewid2)
#Write out spectrum into a text file
    datafile = open(molecule+'_'+metal+'_spectrum_'+a+'.txt', 'w')
    for (xi, yi) in zip(x,y):
        asd = str(xi) + ' ' + str(yi) + '\n'
        datafile.write(asd)
    datafile.close()

if atom_contribute = True:

#Run this part to output the individual atom contribution spectra, only for one incidince angle at a time
    xs = []
    ys = []

    for z in range(len(numbers)):
        x_tmp, y_tmp = dos_binning(peaks[z,:], broadening=broad1, mix1=mix1, mix2=mix2, start=xstart, stop=xstop,
                coeffs = I[z,:], broadening2=broad2, ewid1=ewid1, ewid2=ewid2)
        xs.append(x_tmp)
        ys.append(y_tmp)

        txtfile = open(molecule+'_'+metal+'_'+elem+str(z)+'.txt', 'w')
        for (xsz, ysz) in zip(x_tmp, y_tmp):
            txt = str(xsz) + ' ' + str(ysz) + '\n'
            txtfile.write(txt)
        txtfile.close()
else:
    quit()
```

Listing A.6: plot_nexafs.py

```
import numpy as np

def gaussian(x, x_mean, broadening):

    gaussian_val = np.sqrt((4*np.log(2))/(np.pi*(broadening**2)))
    * np.exp(-((4*np.log(2))/(broadening**2))*(x-x_mean)**2);
    return gaussian_val

def lorentzian(x, x_mean, broadening):

    lorentzian_val = (1/(2*np.pi))* (broadening)/(((broadening/2)
    **2)+(x-x_mean)**2);
    return lorentzian_val

def PseudoVoigt(x, x_mean, broadening, mixing):
    """
    Combines gaussian and lorentzian schemes together
    """
    return (1-mixing)*gaussian(x, x_mean, broadening)+mixing*
    lorentzian(x, x_mean, broadening)

def dos_binning(eigenvalues,broadening=0.75, bin_width=0.01, mix1
    =0., mix2 = None,
        coeffs=None,start=0.0, stop=10.0, broadening2 = None,
    ewid1 = 10.0, ewid2 = 20.0):
    """
    performs binning for a given set of eigenvalues and
    optionally weight coeffs.
    """
    if broadening2 is None:
        broadening2 = broadening
    if coeffs is None:
        coeffs = np.ones(len(eigenvalues))
    lowest_e = start
    highest_e = stop
    num_bins = int((highest_e-lowest_e)/bin_width)
    x_axis = np.zeros([num_bins])
    data = np.zeros([num_bins])
    #setting up x-axis
    for i in range(num_bins):
        x_axis[i] = lowest_e + i * bin_width
    #get DOS
    sigma=np.zeros((len(eigenvalues)))
    mixing=np.zeros((len(eigenvalues)))

    for ei,e in enumerate(eigenvalues):
        if e<=(ewid1):
            sigma[ei]=broadening
            mixing[ei]=mix1
        elif e>(ewid2):
            sigma[ei]=broadening2
            mixing[ei]=mix2
        else:
            sigma[ei]=broadening + ((broadening2-broadening)/(ewid2-ewid1))*(e-ewid1)
            mixing[ei]=(mix1 + ((mix2-mix1)/(ewid2-ewid1))*(e-ewid1))
    for i in range(num_bins):
        pseudovoigt_vec = np.zeros((len(eigenvalues)))
        pseudovoigt_vec=PseudoVoigt(x_axis[i],eigenvalues,sigma,mixing)*coeffs
        data[i]= np.sum(pseudovoigt_vec)
    return x_axis, data

######BROADENING PARAMETERS################################

xstart = 275. #Start Value
xstop = 330. #End Value
broad1 = 0.75 #Broadening value for first section
broad2 = 2.0 #Broadening value for last section
firstpeak = 290.0
ewid1 = firstpeak+5.0 #Set range to linearly move from braod1 to broad2
ewid2 = firstpeak+15.0
mix1 = 0.2 #First G/L mix ratio
mix2 = 0.8 #Last G/L mix ratio

######SYSTEM_PARAMTERS######################################

n_type = 4 #1 for Total NEXAFS, 2 for angular, 3 for polarised, 4 for average polarised
MO_start = 17 #Give the first and last numbers of the range of MO numbers
MO_end = 28
MO = list(map(str, range(MO_start,MO_end+1))) #Creat a list of MO numbers you want
angle = ['t25','t53','t90'] #Incidence angles
molecule = 'azulene' #Name of molecule
metal = 'Ag' #Surface in system
elem = 'C'
num_start = 48 # Set the num_start and num_end to values corresponding the the first and last numbers of your directories C48, C49... C57
num_end = 57
numbers = list(range(num_start,num_end)) #Creates a range of numbers corresponding to the directory numbers
atom = '4' #The number of the exicted atom in the list of elements in the system, always the last, if system contains H, C, Ag, C:exc, it will be 4

```

```
######SETUP ALL LIST AND VARIABLES############################

#Create list of all the folders all the data is in C48/, C49/... C57/
folders = []
for n in numbers:
    folders.append(elem+str(n)+’/’)

#Create variable with a string og the delta file which will be read
filename = ’/’+molecule+’_’+metal+’_’+atom+’_1_1_1_deltas.dat’

#Get the number of kpoints used in calculation in order to correct the MO projected state
kpts = []
with open(elem+str(numbers[0])+’/’+molecule+’_’+metal+’.bands’, ’r’) as bands:
    for line in bands:
        if ’Number of k-points’ in line:
            for word in line.split():
                try:
                    kpts.append(float(word))
                except ValueError:
                    pass

#Get the length of the deltas file
bands = np.loadtxt(elem+str(numbers[0])+’/’+angle[0]+’/’+filename)
bands_num = len(bands)

#Read .param file to see if calculation is spin_polarised and set up required settings
with open (elem+str(numbers[0])+’/’+molecule+’_’+metal+’.param’) as param:
    if ’SPIN_POLARIZED: TRUE’ in param.read():
        spin = True
        spin_val = list(map(str,range(1,3)))
        spin_num - bands_num/2
    else:
        spin = False
        spin_val = list(map(str, range(1,2)))
        spin_num = bands_num

#Create arrays with sized of the system to use
peaks = np.zeros([len(numbers),int(spin_num)])
I = np.zeros([len(numbers), int(spin_num)])


###############################################
#Loop over spin, MOs and angles in the indivdual directories
```

```
for s in spin_val:
    for m in MO:
        for a in angle:
            for i,direc in enumerate(folders):
#Load the data from the MolPDOS calculation
                data = np.loadtxt(direc+a+filename)
                x, y = data[:,0], data[:,n_type]
#If spin polarized is on then split the data in half for each spin, x1, y1 and x2, y2
                if spin == True:
                    x1, y1 = x[:int(spin_num)], y[:int(spin_num)]
                    x2, y2 = x[int(spin_num):], y[int(spin_num):]
                    spindict = {
                            'spin1x' : x1,
                            'spin2y' : y1,
                            'spin2x' : x2,
                            'spin2y' : y2
                            }
#If not spin polarized load all data as x, y
                else:
                    spindict = {
                            'spin1x' : x,
                            'spin1y' : y,
                            }
#Load the indivdual MO data from the MolPDOS calculation and add the k-point scaling and add
#multiply the intesity of the MO with the overall spectrum
                data2 = np.loadtxt(direc+a+'/'+molecule+'_'+metal+'_'+m+'_spin'+s+'_deltas.dat')
                data2*= kpts
                peaks[i,:] = spindict['spin'+s+'x']
                I[i,:] = spindict['spin'+s+'y']*data2[:,1]
#Write out all of the MO data into a delta file
            fileout = open(molecule+'_'+metal+'_MO'+m+'_deltas_'+a+'_spin'+s+'.txt','w')
            fileout.write('#   <x in eV>     Intensity\n')
            for p,i in zip(peaks.flatten(), I.flatten()):
                fileout.write('{0:16.8f}    {1:16.8f}\n'.format(p,i))
            fileout.close()
#Apply the broadening
            x, y = dos_binning(peaks.flatten(), broadening=broad1, mix1=mix1, mix2=mix2, start=xstart, stop=xstop,
                    coeffs = I.flatten(), broadening2=broad2, ewid1=ewid1, ewid2=ewid2)
#Write out MO peak into a text file
            datafile = open(molecule+'_'+metal+'_MO'+m+'_'+a+'_spin'+s+'.txt', 'w')
            for (xi, yi) in zip(x,y):
                asd = str(xi) + ' ' + str(yi) + '\n'
                datafile.write(asd)
            datafile.close()
```

Listing A.7: plot_mo.py

Appendix B

Additional Results

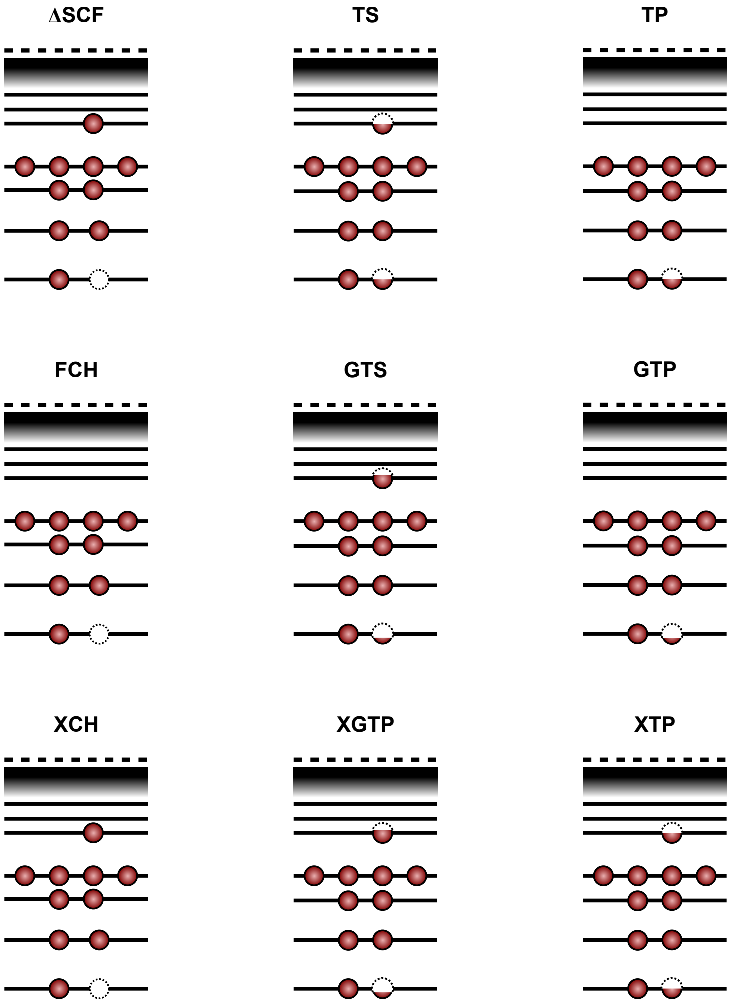
ΔSCF
TS
TP
FCH
GTS
GTP
XCH
XGTP
XTP

Figure B.1: Overview of the various core-hole constraining approaches in a schematic diagram to visualise each approach utilises its core hole. From left to righ, top to bottom they are ΔSCF, [60, 61, 113] TS, [60] TP [76] FCH, [272–274] GTS, [67] GTP, [69] XCH [72–75] XGTP, [69] and XTP [69]

Table B.1: Comparison of the absolute carbon 1s binding energies of ETFA calculated with various XC functional with the experimental values. All theoretical values were calculated using the ΔSCF approach in the all-electron code FHI-aims with a core-augmented “tight-tier2” basis set. All energies are in eV.

Carbon	Exp.	PBE	PW91	TPSS	SCAN	PBE0	B3LYP	HSE06	xDH-PBE0
C1	298.93	297.52	297.88	298.35	298.78	298.39	299.00	298.44	298.39
C2	295.80	294.52	294.88	295.32	295.72	295.38	295.99	295.43	295.38
C3	293.19	292.32	292.64	293.09	293.24	292.79	293.38	292.85	292.79
C4	291.47	290.79	291.11	291.58	291.76	291.15	291.76	291.21	291.15

Table B.2: Comparison of the relative shifts in the carbon 1s binding energies of ETFA calculated with various XC functional with the experimental values. All theoretical values were calculated using the ΔSCF approach in the all-electron code FHI-aims with a core-augmented “tight-tier2” basis set. All energies are in eV and were calculated with repsect to C4 using values from table B.1.

Carbon	Exp	PBE	PW91	TPSS	SCAN	PBE0	B3LYP	HSE06	xDH-PBE0
C1	7.46	6.73	6.77	6.77	7.14	7.24	7.24	7.23	7.24
C2	4.33	3.73	3.77	3.74	4.08	4.23	4.23	4.22	4.23
C3	1.72	1.52	1.53	1.51	1.60	1.64	1.62	1.64	1.64
C4	0.00	0.00	0.00	0.00	0.00	0.00	0.00	0.00	0.00

Table B.3: Comparison of the absolute carbon 1s binding energies of azupyrene calculated with various XC functionals. All theoretical values were calculated using the ΔSCF approach in the all-electron code FHI-aims with a core-augmented “tight-tier2” basis set. All energies are in eV.

Carbon	PBE	PW91	TPSS	SCAN	PBE0	B3LYP	HSE06	xDH-PBE0
C1	288.90	289.20	289.56	289.61	289.26	289.78	289.31	289.26
C2	289.14	289.45	289.81	289.87	289.62	290.08	289.62	289.58
C3	289.15	289.45	289.75	289.84	289.57	290.00	289.57	289.52
C4	288.71	289.02	289.37	289.42	289.13	289.58	289.13	289.08
C5	289.72	290.02	290.32	290.47	290.22	290.62	290.22	290.17

Table B.4: Comparison of the relative shifts of the carbon 1s binding energies of azupyrene calculated with various XC functionals. All theoretical values were calculated according to the Koopmans’ theorem as $E_{\mathrm{B}}(i) = -\varepsilon_{i,\mathrm{KS}}$h in the all-electron code FHI-aims with a core-augmented “tight-tier2” basis set. All energies are in eV and w.r.t the binding energy of C1.

Carbon	PBE	PW91	TPSS	SCAN	PBE0	B3LYP	HSE06	xDH-PBE0
C1	0.00	0.00	0.00	0.00	0.00	0.00	0.00	0.00
C2	0.30	0.30	0.31	0.36	0.38	0.36	0.37	0.38
C3	0.24	0.24	0.19	0.22	0.25	0.22	0.25	0.25
C4	−0.14	−0.14	−0.14	−0.16	−0.15	−0.16	−0.15	−0.15
C5	0.81	0.81	0.77	0.84	0.88	0.84	0.88	0.88

Ultrasoft

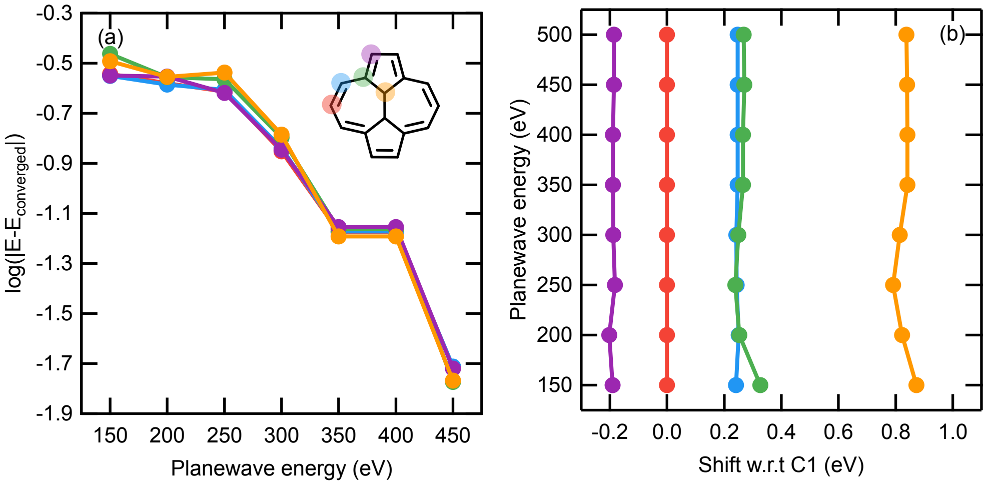

Two Ultrasoft

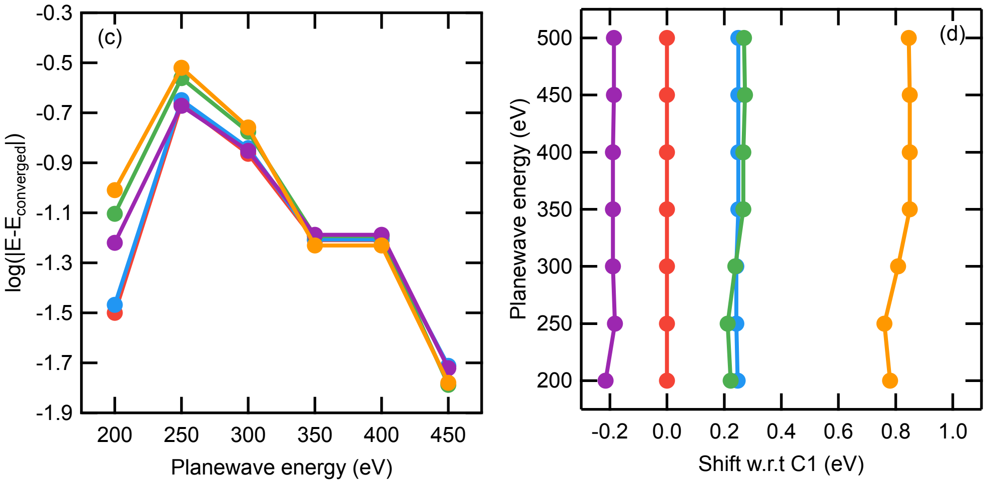

Norm conserving

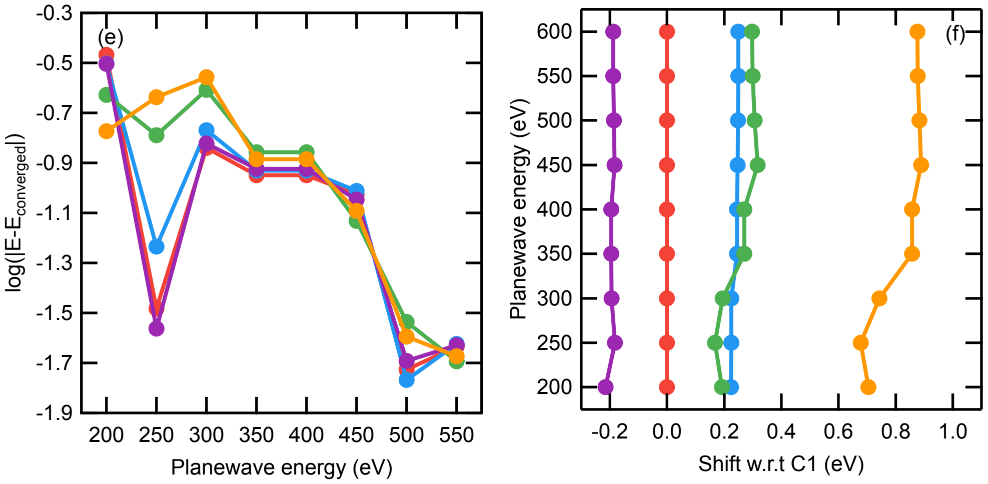

Figure B.2: Graphs showing the convergence of the XPS BEs of azupyrene with respect to the planewave cut-off energy for different types of PP (a) and (b) for ultrasoft, (c) and (d) for two ultrasoft and (e) and (f) for norm conserving PPs. Graphs on the left shows a semi-log plot of difference between the converged BE which is taken as one step higher than shown and right the relative energy with respect to C1 (red outline). Coloured lines represent the coloured carbon in panel (a).

Table B.5: Mulliken and Hirshfeld charges and dipole moments calculated for gas-phase azulene using FHI-aims. Shown are the joint partial charges of the carbon and hydrogen atoms for each symmetry inequivalent CH group. All charges are in units of e, with the dipole moments in Debye.

Carbon		1	2	3	4	5	6	Sum	Dipole Moment
Mulliken	Neutral	0.00	−0.12	0.10	0.01	−0.02	0.02	0.00	1.03
	Anion	−0.15	−0.31	0.07	−0.28	−0.18	−0.14	−0.01	0.82
Hirshfeld	Neutral	0.00	−0.07	0.00	0.06	−0.02	−0.02	−1.00	0.85
	Anion	−0.14	−0.23	−0.10	−0.18	−0.18	−0.13	−0.96	0.67

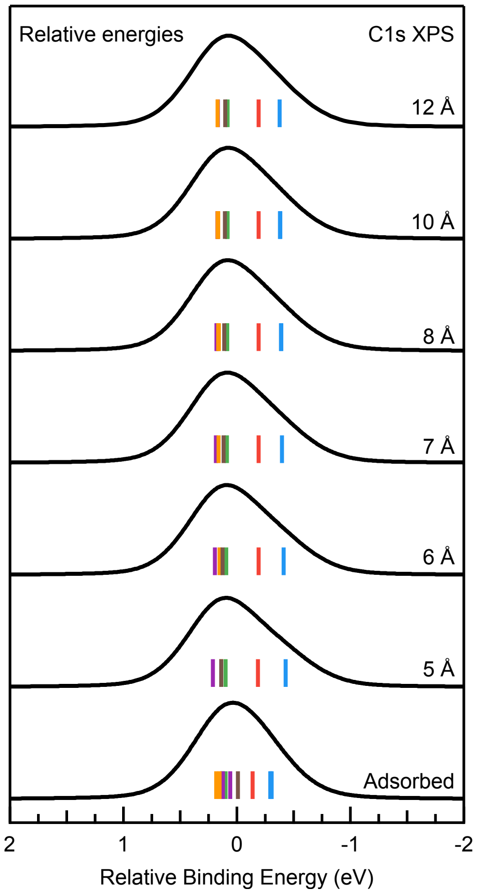

Figure B.3: DFT simulated XPS spectra of azulene on Ag(111) recorded with the molecule move upwards at different distances away from the metal surface, starting at the equilibrium adsorbed structure (bottom) to 12 Å away (top). All spectra have been shifted to the respective centres of gravity and a breakdown of the spectra of each carbon atom are shown in various colours.

Table B.6: Molecular orbital energy levels of the HOMO, LUMO and LUMO+1 for different functionals including the differences between the HOMO-LUMO and LUMO-LUMO+1 on azulene. Followed by all tested values when applying the +U(MO) shifts for the PBE case. All values given in eV.

XC Functional	HOMO	LUMO	LUMO+1	HOMO-LUMO Gap	LUMO-LUMO+1 Gap
PBE	−1.51	0.56	1.43	2.07	0.88
PBE0	−8.74	−5.17	−4.25	3.60	0.89
HSE06	−8.27	−5.42	−4.53	2.84	0.89

+U(MO) Shifts			HOMO	LUMO	LUMO+1	HOMO-LUMO Gap	LUMO-LUMO+1 Gap
HOMO	LUMO	LUMO+1					
0.00	2.50	0.00	−2.39	0.86	0.56	3.25	−0.31
0.00	3.00	0.00	−2.39	1.10	0.56	3.49	−0.54
0.00	3.25	0.00	−2.39	1.22	0.56	3.61	−0.66
0.00	3.40	0.00	−2.39	1.29	0.56	3.68	−0.73
−0.50	2.75	0.00	−2.63	0.98	0.56	3.61	−0.42
−0.50	3.00	0.00	−2.63	1.10	0.56	3.73	−0.54
−1.00	1.00	0.00	−2.46	0.56	1.04	3.02	0.48
−1.00	−1.50	0.00	−2.70	0.56	1.04	3.26	0.48
0.00	3.40	1.70	−3.12	0.56	0.63	3.68	0.07
0.00	3.40	3.40	−3.12	0.56	1.43	3.68	0.87
1.00	4.40	4.40	−3.12	0.56	1.43	3.68	0.87
1.50	4.80	4.90	−3.07	0.56	1.48	3.63	0.92
1.50	4.90	4.90	−3.07	0.60	1.47	3.67	0.87
2.00	5.25	5.25	−2.84	0.77	1.64	3.60	0.87
2.00	5.25	5.30	−2.83	0.77	1.66	3.60	0.90
2.00	5.40	5.40	−2.83	0.84	1.71	3.67	0.87
2.50	5.90	5.90	−2.60	1.07	1.95	3.67	0.87

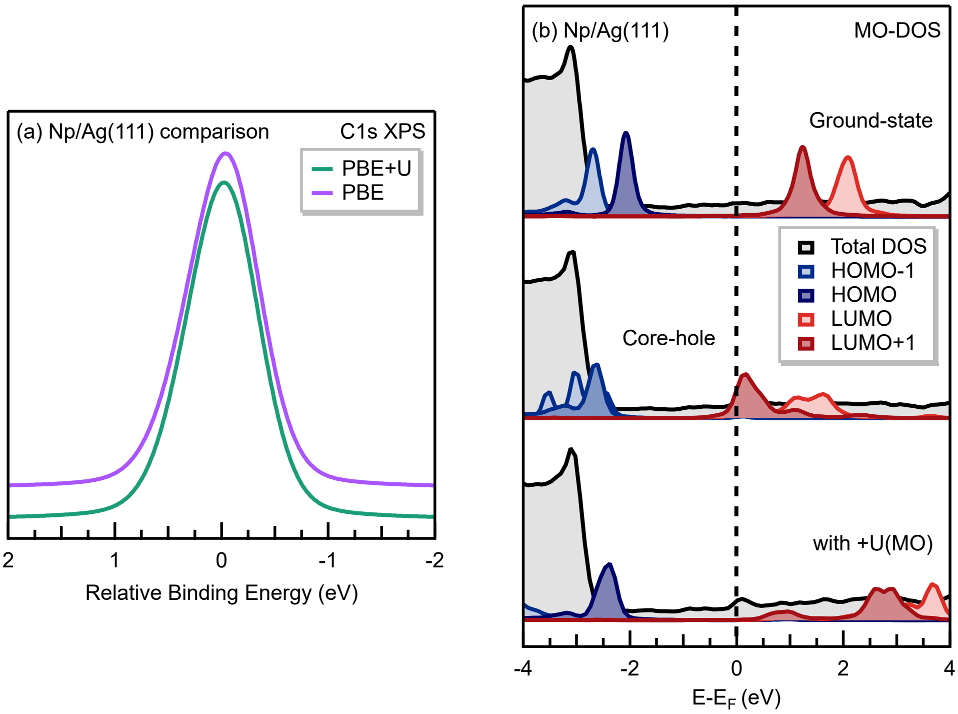

Figure B.4: DFT Simulated XP spectra of Np/Ag(111) performed in periodic boundary conditions using the CASTEP code using the ΔSCF method (purple) and with the PBE+U(MO) (green) to shift specific orbitals. Spectra are aligned to the average shift of the individual atoms. (b) Total density of states (DOS) and MO-DOS for Np/Ag(111). From top to bottom, the DOS for the ground-state system, core-hole excited state and the core-hole excited state with +U(MO). For the core-hole excited state DOS, all possible core-hole excited carbons species have been calculated and summed up. Total DOS is shown by the black line with grey shading. MO contributions have been scaled for ease of viewing.

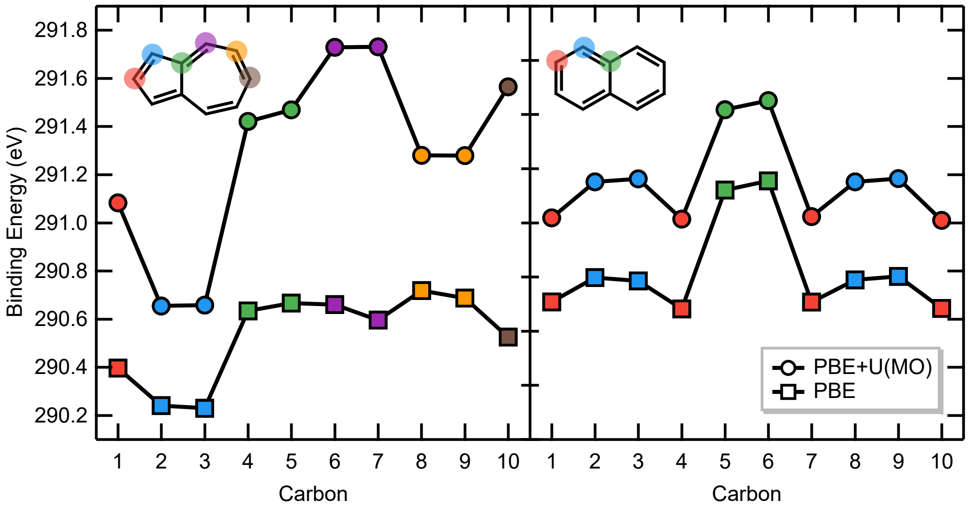

Figure B.5: Absolute carbon shifts for each individual carbon atom in azulene (left) and naphthalene (right) adsorbed onto an Ag(111) surface. Squares represent results from a ΔSCF calculation with CASTEP using the PBE functional and circles are results where the PBE+U(MO) correction has been applied.

Table B.7: Calculated net charge transfer of all metal adsorbed systems investigated using various charge analysis methods and electronic structure codes.

Method	Np/Ag	Az/Ag	Np/Cu	Az/Cu	Nt/Pt	Az/Pt
DOS (CASTEP)	−0.05	−0.21	−0.13	−1.39	−1.70	−1.60
Hirshfeld (CASTEP)	−0.07	−0.11	−0.05	−0.35	−0.32	−0.31
Hirshfeld (VASP)	−0.04	−0.07	−0.01	−0.25	−0.20	−0.21
It-Hirshfeld (VASP)	−0.14	−0.19	−0.12	−0.60	−0.86	−0.84

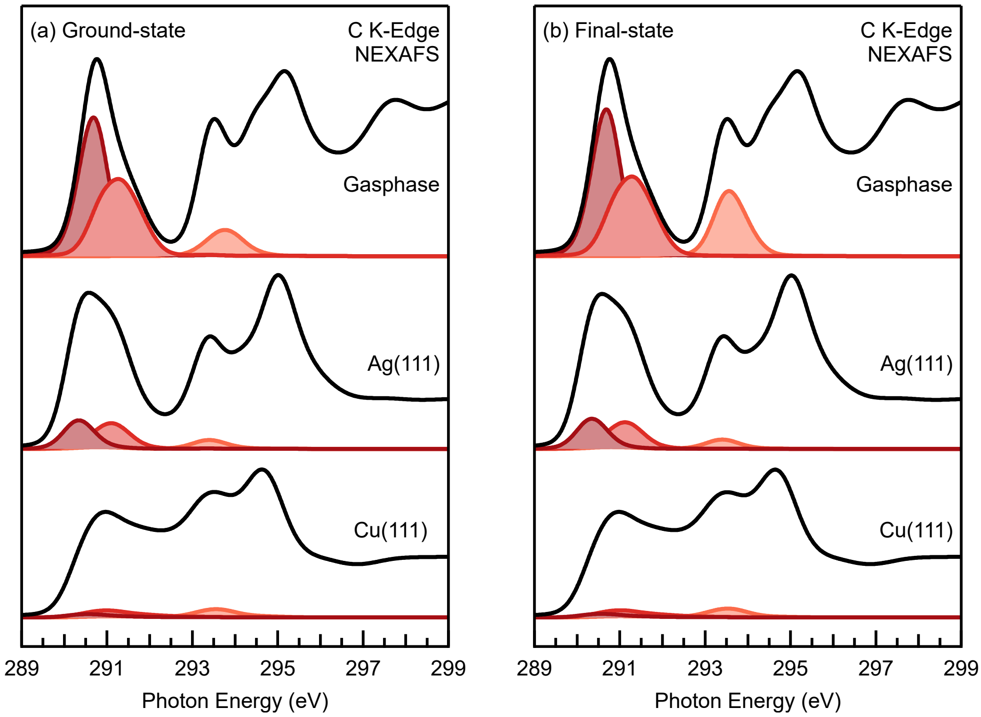

Figure B.6: MO-projected NEXAFS using the calculated 25° spectra for azulene in the gas-phase (top) and adsorbed on a Ag(111) (middle) and Cu(111) (bottom) surface, either with the ground-state (a) as the reference or the final-state (b).

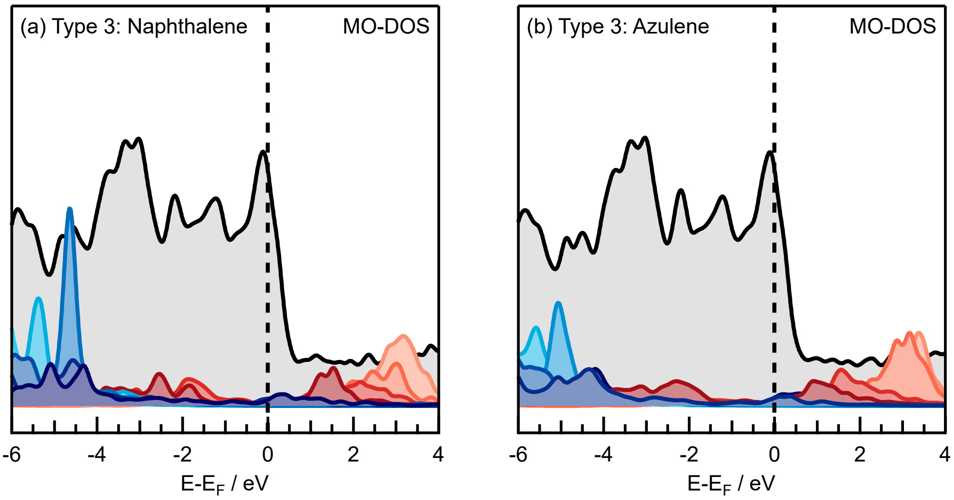

Figure B.7: DFT density of states (DOS) for naphthalene (a) and azulene (b) on a Pt(111) surface. Total DOS is shown in black and Fermi level shown with dashed line, contributions from orbitals scaled for ease of viewing. Orbitals labelled in blue represent the HOMOs and red the LUMOs with the lighter shade moving lower or higher in energy respectively.

(a) γ-phase(+S, top)

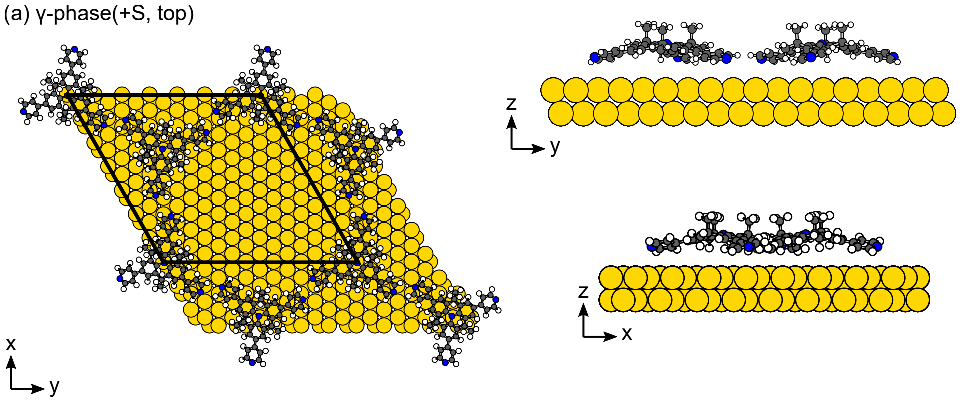

(b) γ-phase(+S, hollow)

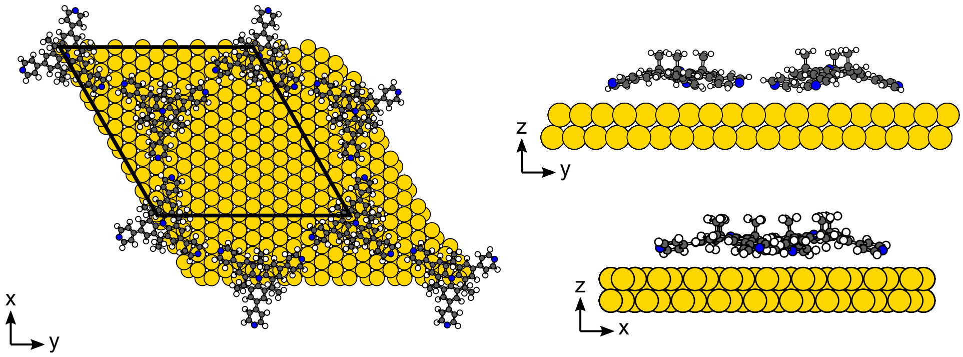

Figure B.8: Unit cell geometries of optimised structures of HTA on a 2-layer Au(111) surface in the γ-phase, with two molecule adsorption site where the central aminic nitrogen was in a (a) top site or (b) a hollow site. Three views along the x, y and z axis are provided.

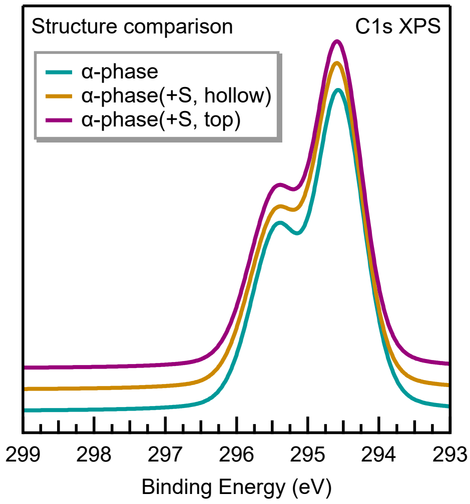

Figure B.9: DFT simulation of C1s XPS for structures of the α-phase. Turqouise shows result from the α structure without a metal surface modelled whilst the gold and purple lines represent the α(+S) structure with the central aminic nitrogen occupying a hollow or top site respectively. The α(+S) spectra have been shifted by 1.2 eV to align all spectra together.

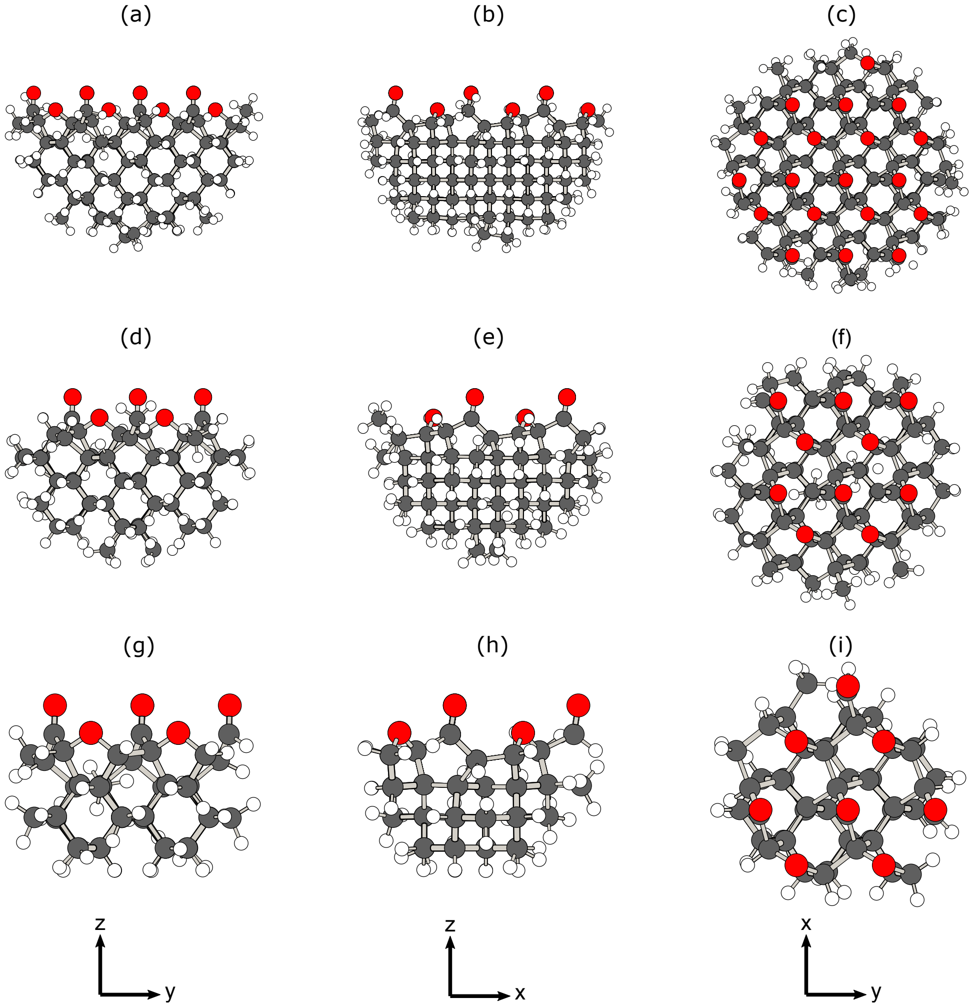

Figure B.10: Visualisations of the cluster models of $p(2\times 1)$Keto-Ether$_5$ with different cluster radii (a)-(c) 9 Bohr, (d)-(f) 12 Bohr, and (g)-(i) 15 Bohr. Three views along the x, y, and z axis are provided.

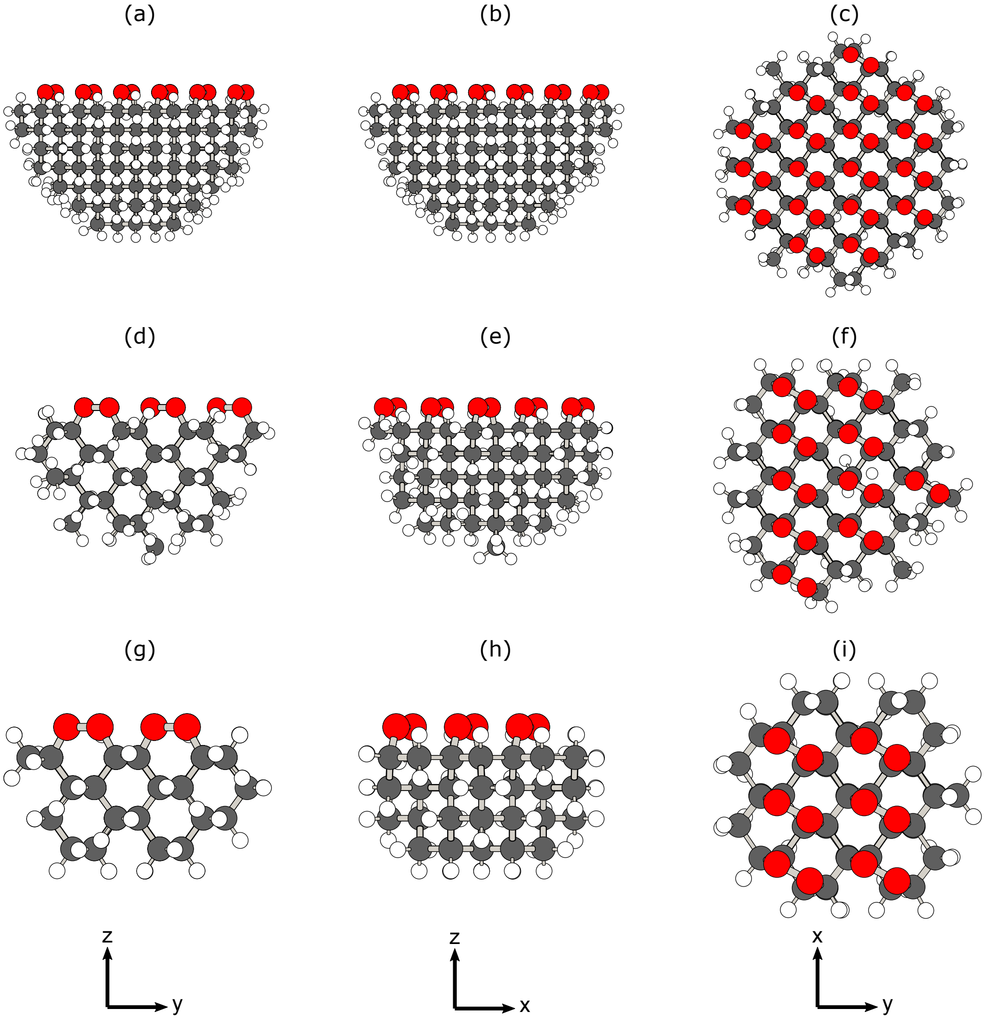

Figure B.11: Visualisations of the cluster models of $p(1 \times 1)$Peroxide with different cluster radii (a)-(c) 9 Bohr, (d)-(f) 12 Bohr, and (g)-(i) 15 Bohr. Three views along the x, y, and z axis are provided.

Table B.8: Table showing the convergence data of the C1s and O1s absolute BEs for supercells and clusters of various sizes of the $p(1 \times 1)$Peroxide phase.

Unit Cell	Reciprocal Space	Binding Energy (eV)	
Size	Grid Size	C1s	O1s
1×1	$16 \times 16 \times 1$	307.47	554.17
2×2	$16 \times 16 \times 1$	297.63	544.71
3×2	$12 \times 12 \times 1$	296.48	543.68
3×3	$12 \times 12 \times 1$	295.73	542.99
4×3	$8 \times 8 \times 1$	295.34	542.65
4×4	$8 \times 8 \times 1$	295.07	542.40
5×4	$4 \times 4 \times 1$	294.90	542.25
6×4	$4 \times 4 \times 1$	294.81	542.16
Cluster Radius (Bohr)		C1s	O1s
9.0		290.28	536.14
12.0		289.97	535.70
15.0		289.81	535.40

Table B.9: Table showing the convergence data of the C1s BEs with respect to the diamond bulk and O1s absolute BEs for supercells and clusters of various sizes of the $p(2 \times 1)$Keto-Ether$_5$ and $p(2 \times 2)$Keto-Ether$_5$ phases. For cluster models, where a diamond bulk value was not calculated, the absolute BE is shown. Entry marked '/' is a result of the calculation failing to converge.

		$p(2 \times 1)$Keto-Ether$_5$					
Unit Cell	Reciprocal Space	ΔC1s Binding Energy (eV)			O1s Binding Energy (eV)		
Size	Grid Size	$\underline{\mathrm{C}}{=}\mathrm{O}$	$\underline{\mathrm{C}}{-}\mathrm{O}{-}\mathrm{C}$	$\mathrm{C}{-}\mathrm{O}{-}\underline{\mathrm{C}}$	$\mathrm{C}{=}\underline{\mathrm{O}}$	$\mathrm{C}{-}\underline{\mathrm{O}}{-}\mathrm{C}$	Difference
1×1	$16 \times 16 \times 1$	6.59	7.52	7.15	547.33	549.18	1.85
2×2	$16 \times 16 \times 1$	2.33	2.41	2.16	543.24	544.24	1.00
3×2	$12 \times 12 \times 1$	1.88	1.85	1.61	542.80	543.69	0.89
3×3	$8 \times 8 \times 1$	1.59	1.52	1.29	542.53	543.37	0.84
4×3	$8 \times 8 \times 1$	1.44	1.35	1.12	542.39	543.21	0.82
4×4	$6 \times 6 \times 1$	1.34	1.25	1.02	542.30	543.11	0.81
5×4	$4 \times 4 \times 1$	1.28	1.18	0.96	542.25	543.05	0.80
5×5	$2 \times 2 \times 1$	1.24	1.15	0.92	542.22	543.01	0.79
Cluster Radius (Bohr)		$\underline{\mathrm{C}}{=}\mathrm{O}$	$\underline{\mathrm{C}}{-}\mathrm{O}{-}\mathrm{C}$	$\mathrm{C}{-}\mathrm{O}{-}\underline{\mathrm{C}}$	$\mathrm{C}{=}\underline{\mathrm{O}}$	$\mathrm{C}{-}\underline{\mathrm{O}}{-}\mathrm{C}$	Difference
9.0		291.16	290.75	290.70	535.72	536.38	0.66
12.0		291.06	290.71	290.78	535.37	536.07	0.70
15.0		/	290.64	290.41	535.18	535.96	0.78
		$p(2 \times 2)$Keto-Ether$_5$					
Unit Cell	Reciprocal Space	ΔC1s Binding Energy (eV)			O1s Binding Energy (eV)		
Size	Grid Size	$\underline{\mathrm{C}}{=}\mathrm{O}$	$\underline{\mathrm{C}}{-}\mathrm{O}{-}\mathrm{C}$	$\mathrm{C}{-}\mathrm{O}{-}\underline{\mathrm{C}}$	$\mathrm{C}{=}\underline{\mathrm{O}}$	$\mathrm{C}{-}\underline{\mathrm{O}}{-}\mathrm{C}$	Difference
3×2	$8 \times 8 \times 1$	0.74	0.27	0.81	541.35	542.27	0.92
3×3	$4 \times 4 \times 1$	0.57	0.10	0.63	541.12	542.51	1.39
4×3	$2 \times 2 \times 1$	0.48	−0.03	0.53	541.12	542.42	1.30
4×4	$2 \times 2 \times 1$	0.42	−0.08	0.44	541.04	542.33	1.30

Bibliography

[1] J. E. Anthony, "The larger acenes: versatile organic semiconductors", Angewandte Chemie International Edition **47**, 452–483 (2008) (cit. on p. 1).

[2] A. Mishra and P. Bäuerle, "Small molecule organic semiconductors on the move: promises for future solar energy technology", Angewandte Chemie International Edition **51**, 2020–2067 (2012) (cit. on p. 1).

[3] J. H. Burroughes, D. D. C. Bradley, A. R. Brown, R. N. Marks, K Mackay, R. H. Friend, P. L. Burns and A. B. Holmes, "Light-emitting diodes based on conjugated polymers", Nature **347**, 539–541 (1990) (cit. on pp. 1, 79).

[4] A. Pron and P. Rannou, "Processible conjugated polymers: from organic semiconductors to organic metals and superconductors", Progress in Polymer Science **27**, 135–190 (2002) (cit. on p. 1).

[5] J. Wu, W. Pisula and K. Müllen, "Graphenes as potential material for electronics", Chemical Reviews **107**, 718–747 (2007) (cit. on p. 1).

[6] S. R. Forrest, "The path to ubiquitous and low-cost organic electronic appliances on plastic", Nature **428**, 911–918 (2004) (cit. on pp. 1, 79).

[7] J. C. Scott, "Metal–organic interface and charge injection in organic electronic devices", Journal of Vacuum Science & Technology A **21**, 521–531 (2003) (cit. on p. 1).

[8] I. Tanaka and T. Mizoguchi, "First-principles calculations of x-ray absorption near edge structure and energy loss near edge structure: present and future", Journal of Physics: Condensed Matter **21**, 104201 (2009) (cit. on pp. 2, 7).

[9] N. A. Besley, "Density functional theory based methods for the calculation of x-ray spectroscopy", Accounts of Chemical Research **53**, 1306–1315 (2020) (cit. on p. 2).

[10] B. N. C. Tenorio, R. R. Oliveira, M. A. C. Nascimento and A. B. Rocha, "Coupled cluster and time-dependent density functional theory description of inner shell photoabsorption cross sections of molecules", Journal of Chemical Theory and Computation **14**, 5324–5338 (2018) (cit. on p. 2).

[11] D. Golze, J. Wilhelm, M. J. van Setten and P. Rinke, “Core-level binding energies from GW: an efficient full-frequency approach within a localized basis”, Journal of Chemical Theory and Computation **14**, 4856–4869 (2018) (cit. on pp. 2, 16).

[12] D. Golze, M. Dvorak and P. Rinke, “The GW compendium: a practical guide to theoretical photoemission spectroscopy”, Frontiers in Chemistry **7**, 377 (2019) (cit. on pp. 2, 16).

[13] B. Helmich-Paris, “Simulating x-ray absorption spectra with CASSCF linear response methods”, arXiv:2004.05845 [physics] (2020) (cit. on p. 2).

[14] J. Liu, D. Matthews, S. Coriani and L. Cheng, “Benchmark calculations of k-edge ionization energies for first-row elements using scalar-relativistic core–valence-separated equation-of-motion coupled-cluster methods”, Journal of Chemical Theory and Computation **15**, 1642–1651 (2019) (cit. on p. 2).

[15] M. Nooijen and R. J. Bartlett, “Description of core-excitation spectra by the open-shell electron-attachment equation-of-motion coupled cluster method”, The Journal of Chemical Physics **102**, 6735–6756 (1995) (cit. on p. 2).

[16] A. Nilsson, “Applications of core level spectroscopy to adsorbates”, Journal of Electron Spectroscopy and Related Phenomena **126**, 3–42 (2002) (cit. on p. 4).

[17] J. Stöhr, *NEXAFS spectroscopy*, edited by R. Gomer, 1st ed. (Springer, Berlin, 1992), 403 pp. (cit. on pp. 4, 6, 7, 15, 50, 74, 79).

[18] F. d. Groot and A. Kotani, *Core level spectroscopy of solids* (CRC Press, Boca Raton, 10th Mar. 2008), 512 pp. (cit. on p. 4).

[19] F. Frati, M. O. J. Y. Hunault and F. M. F. de Groot, “Oxygen k-edge x-ray absorption spectra”, Chemical Reviews **120**, 4056–4110 (2020) (cit. on p. 4).

[20] P. S. Bagus, C. J. Nelin, X. Zhao, S. V. Levchenko, E. Davis, X. Weng, F. Späth, C. Papp, H. Kuhlenbeck and H.-J. Freund, “Revisiting surface core-level shifts for ionic compounds”, Physical Review B **100**, 115419 (2019) (cit. on p. 4).

[21] F. P. Netzer and M. G. Ramsey, “Structure and orientation of organic molecules on metal surfaces”, Critical Reviews in Solid State and Materials Sciences **17**, 397–475 (1992) (cit. on p. 4).

[22] Y. Gao, “Surface analytical studies of interface formation in organic light-emitting devices”, Accounts of Chemical Research **32**, 247–255 (1999) (cit. on p. 4).

[23] C. Papp and H.-P. Steinrück, “In situ high-resolution x-ray photoelectron spectroscopy – fundamental insights in surface reactions”, Surface Science Reports **68**, 446–487 (2013) (cit. on p. 4).

[24] T. Breuer, M. Klues and G. Witte, “Characterization of orientational order in -conjugated molecular thin films by NEXAFS”, Journal of Electron Spectroscopy and Related Phenomena, Organic Electronics **204**, 102–115 (2015) (cit. on pp. 5, 15, 50, 74).

[25] J. Haase, “NEXAFS and SEXAFS studies of chemisorbed molecules”, Applied Physics A **38**, 181–190 (1985) (cit. on p. 5).

[26] J. Niskanen, C. J. Sahle, K. Gilmore, F. Uhlig, J. Smiatek and A. Föhlisch, “Disentangling structural information from core-level excitation spectra”, Physical Review E **96**, 013319 (2017) (cit. on p. 5).

[27] H. R. Hertz, “Uber einen einfluß des ultravioletten lichtes auf die electrische entladung”, Annalen der Physik und Chemie **31**, 983–1000 (1887) (cit. on p. 5).

[28] W. Hallwachs, “Uber den einfluß des lichtes auf electrostatisch geladene körper”, Annalen der Physik und Chemie **33**, 301–312 (1888) (cit. on p. 5).

[29] A. Einstein, “Über einen die erzeugung und verwandlung des lichtes betreffenden heuristischen gesichtspunkt”, Annalen der Physik **322**, 132–148 (1905) (cit. on p. 5).

[30] R. Steinhardt and E. Serfass, “X-ray photoelectron spectrometer for chemical analysis”, Analytical Chemistry **23**, 1585–1590 (1951) (cit. on p. 5).

[31] C. Nordling, E. Sokolowski and K. Siegbahn, “Precision method for obtaining absolute values of atomic binding energies”, Physical Review **105**, 1676–1677 (1957) (cit. on p. 5).

[32] K. Siegbahn, *ESCA; atomic, molecular and solid state structure studied by means of electron spectroscopy* (Almqvist & Wiksells, 1967), 292 pp. (cit. on p. 5).

[33] F. Reinert and S. Hüfner, “Photoemission spectroscopy—from early days to recent applications”, New Journal of Physics **7**, 97 (2005) (cit. on p. 5).

[34] C. J. Powell and A. Jablonski, “Surface sensitivity of x-ray photoelectron spectroscopy”, Nuclear Instruments and Methods in Physics Research Section A: Accelerators, Spectrometers, Detectors and Associated Equipment, Special issue in honour of Prof. Kai Siegbahn **601**, 54–65 (2009) (cit. on p. 5).

[35] J. Osterwalder, “Electron based methods: 3.2.2 photoelectron spectroscopy and diffraction”, in *Surface and interface science* (John Wiley & Sons, Ltd, 2013), pp. 151–214 (cit. on pp. 5, 6).

[36] K. Diller, F. Klappenberger, F. Allegretti, A. C. Papageorgiou, S. Fischer, D. A. Duncan, R. J. Maurer, J. A. Lloyd, S. C. Oh, K. Reuter and J. V. Barth, "Temperature-dependent templated growth of porphine thin films on the (111) facets of copper and silver", The Journal of Chemical Physics **141**, 144703 (2014) (cit. on p. 6).

[37] T. C. Taucher, I. Hehn, O. T. Hofmann, M. Zharnikov and E. Zojer, "Understanding chemical versus electrostatic shifts in x-ray photoelectron spectra of organic self-assembled monolayers", The Journal of Physical Chemistry C **120**, 3428–3437 (2016) (cit. on p. 6).

[38] W. Kossel, "Zum Bau der Röntgenspektren", Zeitschrift für Physik **1**, 119–134 (1920) (cit. on p. 7).

[39] W. Kossel, "Über die Ausbildung der Röntgenserien mit wachsender Ordnungszahl", Zeitschrift für Physik **2**, 470–478 (1920) (cit. on p. 7).

[40] R. d. L. Kronig, "Zur Theorie der Feinstruktur in den Röntgenabsorptionsspektren", Zeitschrift für Physik **70**, 317–323 (1931) (cit. on p. 7).

[41] R. d. L. Kronig, "Zur Theorie der Feinstruktur in den Röntgenabsorptionsspektren. II", Zeitschrift für Physik **75**, 191–210 (1932) (cit. on p. 7).

[42] R. d. L. Kronig, "Zur Theorie der Feinstruktur in den Röntgenabsorptionsspektren. III", Zeitschrift für Physik **75**, 468–475 (1932) (cit. on p. 7).

[43] G. Hähner, "Near edge x-ray absorption fine structure spectroscopy as a tool to probe electronic and structural properties of thin organic films and liquids", Chemical Society Reviews **35**, 1244–1255 (2006) (cit. on pp. 7, 8).

[44] G. Bunker, *Introduction to XAFS: a practical guide to x-ray absorption fine structure spectroscopy* (Cambridge University Press, Cambridge, 2010), 260 pp. (cit. on pp. 7, 79).

[45] W. Koch and M. C. Holthausen, *A chemist's guide to density functional theory*, 2nd ed. (John Wiley & Sons, Ltd, 12th July 2001) (cit. on p. 8).

[46] E. Engel and R. M. Dreizler, *Density functional theory: an advanced course*, Theoretical and Mathematical Physics (Springer Berlin Heidelberg, Berlin, Heidelberg, 2011) (cit. on p. 9).

[47] R. G. Parr and Y. Yang Weitao, *Density-functional theory of atoms and molecules* (Oxford University Press, Incorporated, Oxford, UNITED STATES, 1994) (cit. on p. 9).

[48] E. Schrödinger, "Quantisierung als eigenwertproblem", Annalen der Physik **384**, 361–376 (1926) (cit. on p. 9).

[49] M. Born and R. Oppenheimer, "Zur quantentheorie der molekeln", Annalen der Physik **389**, 457–484 (1927) (cit. on p. 9).

[50] P. Hohenberg and W. Kohn, “Inhomogeneous electron gas”, Physical Review **136**, B864–B871 (1964) (cit. on p. 9).

[51] W. Kohn and L. J. Sham, “Self-consistent equations including exchange and correlation effects”, Physical Review **140**, A1133–A1138 (1965) (cit. on p. 10).

[52] J. P. Perdew and K. Schmidt, “Jacob’s ladder of density functional approximations for the exchange-correlation energy”, AIP Conference Proceedings **577**, 1 (2001) (cit. on p. 11).

[53] J. P. Perdew, K. Burke and M. Ernzerhof, “Generalized gradient approximation made simple”, Physical Review Letters **77**, 3865–3868 (1996) (cit. on pp. 11, 33, 41, 42, 44, 61, 62, 67, 105, 106, 117).

[54] T Koopmans, “Über die Zuordnung von Wellenfunktionen und Eigenwerten zu den Einzelnen Elektronen Eines Atoms”, Physica **1**, 104–113 (1934) (cit. on p. 11).

[55] J. F. Janak, “Proof that $\frac{\partial E}{\partial n_i} = \varepsilon$ in density-functional theory”, Physical Review B **18**, 7165–7168 (1978) (cit. on pp. 11, 13).

[56] N. P. Bellafont, F. Illas and P. S. Bagus, “Validation of koopmans’ theorem for density functional theory binding energies”, Physical Chemistry Chemical Physics **17**, 4015–4019 (2015) (cit. on p. 11).

[57] A. R. Williams and N. D. Lang, “Core-level binding-energy shifts in metals”, Physical Review Letters **40**, 954–957 (1978) (cit. on p. 11).

[58] N. Pueyo Bellafont, P. S. Bagus and F. Illas, “Prediction of core level binding energies in density functional theory: rigorous definition of initial and final state contributions and implications on the physical meaning of kohn-sham energies”, The Journal of Chemical Physics **142**, 214102 (2015) (cit. on pp. 11, 12).

[59] D. P. Chong, O. V. Gritsenko and E. J. Baerends, “Interpretation of the kohn–sham orbital energies as approximate vertical ionization potentials”, The Journal of Chemical Physics **116**, 1760–1772 (2002) (cit. on pp. 11, 35).

[60] J. C. Slater, “Statistical exchange-correlation in the self-consistent field”, Advances in Quantum Chemistry **6**, 1–92 (1972) (cit. on pp. 12, 13, 29, 74, 80, 150).

[61] O Gunnarsson and B. I. Lundqvist, “Exchange and correlation in atoms, molecules, and solids by the spin-density-functional formalism”, Physical Review B **13**, 4274–4298 (1976) (cit. on pp. 12, 29, 80, 150).

[62] U. von Barth, “Local-density theory of multiplet structure”, Physical Review A **20**, 1693–1703 (1979) (cit. on pp. 12, 29).

[63] P. S. Bagus, “Self-consistent-field wave functions for hole states of some ne-like and ar-like ions”, Physical Review **139**, A619–A634 (1965) (cit. on p. 12).

[64] Johansson and S. Stafström, “A -self-consistent-field study of the nitrogen 1s binding energies in carbon nitrides”, The Journal of Chemical Physics **111**, 3203–3208 (1999) (cit. on p. 12).

[65] N. A. Besley, A. T. B. Gilbert and P. M. W. Gill, “Self-consistent-field calculations of core excited states”, The Journal of Chemical Physics **130**, 124308 (2009) (cit. on pp. 12, 31, 39, 74, 118).

[66] F. Viñes, C. Sousa and F. Illas, “On the prediction of core level binding energies in molecules, surfaces and solids”, Physical Chemistry Chemical Physics **20**, 8403–8410 (2018) (cit. on p. 12).

[67] A. R. Williams, R. A. deGroot and C. B. Sommers, “Generalization of slater’s transition state concept”, The Journal of Chemical Physics **63**, 628–631 (1975) (cit. on pp. 12, 150).

[68] G. S. Michelitsch, “Ab initio simulation of core-level spectroscopies and correlated materials”, PhD thesis (Technische Universität München, 2019) (cit. on p. 13).

[69] G. S. Michelitsch and K. Reuter, “Efficient simulation of near-edge x-ray absorption fine structure (NEXAFS) in density-functional theory: comparison of core-level constraining approaches”, The Journal of Chemical Physics **150**, 074104 (2019) (cit. on pp. 13, 14, 35, 51, 53, 150).

[70] M. Stener, A. Lisini and P. Decleva, “Density functional calculations of excitation energies and oscillator strengths for c1s → and o1s → excitations and ionization potentials in carbonyl containing molecules”, Chemical Physics **191**, 141–154 (1995) (cit. on pp. 13, 80).

[71] C.-H. Hu and D. P. Chong, “Density functional computations for inner-shell excitation spectroscopy”, Chemical Physics Letters **262**, 729–732 (1996) (cit. on pp. 13, 80).

[72] R. Ahuja, P. A. Brühwiler, J. M. Wills, B. Johansson, N. Mårtensson and O. Eriksson, “Theoretical and experimental study of the graphite 1s x-ray absorption edges”, Physical Review B **54**, 14396–14404 (1996) (cit. on pp. 13, 150).

[73] R. Buczko, G. Duscher, S. J. Pennycook and S. T. Pantelides, “Excitonic effects in core-excitation spectra of semiconductors”, Physical Review Letters **85**, 2168–2171 (2000) (cit. on pp. 13, 150).

[74] K. Lie, R. Høier and R. Brydson, “Theoretical site- and symmetry-resolved density of states and experimental EELS near-edge spectra of AlB_2 and TiB_2”, Physical Review B **61**, 1786–1794 (2000) (cit. on pp. 13, 150).

[75] D. Prendergast and G. Galli, “X-ray absorption spectra of water from first principles calculations”, Physical Review Letters **96**, 215502 (2006) (cit. on pp. 13, 150).

[76] L Triguero, L. G. M. Pettersson and H Ågren, “Calculations of near-edge x-ray-absorption spectra of gas-phase and chemisorbed molecules by means of density-functional and transition-potential theory”, Physical Review B **58**, 8097–8110 (1998) (cit. on pp. 14, 29, 38, 74, 80, 150).

[77] B. Klein, S. Hall and R. Maurer, “The nuts and bolts of core-hole constrained ab-initio simulation for k-shell x-ray photoemission and adsorption spectra”, Journal of Physics: Condensed Matter **33**, 154005 (2021) (cit. on pp. 14, 29, 68, 74, 80, 81).

[78] K. Diller, R. J. Maurer, M. Müller and K. Reuter, “Interpretation of x-ray absorption spectroscopy in the presence of surface hybridization”, Journal of Chemical Physics **146**, 214701 (2017) (cit. on pp. 14, 51, 80).

[79] B. P. Klein, N. J. van der Heijden, S. R. Kachel, M. Franke, C. K. Krug, K. K. Greulich, L. Ruppenthal, P. Müller, P. Rosenow, S. Parhizkar, F. C. Bocquet, M. Schmid, W. Hieringer, R. J. Maurer, R. Tonner, C. Kumpf, I. Swart and J. M. Gottfried, “Molecular topology and the surface chemical bond: alternant versus nonalternant aromatic systems as functional structural elements”, Physical Review X **9**, 11030 (2019) (cit. on pp. 14, 33, 38, 50, 52, 56, 57, 60–62, 64, 65, 67, 69, 77, 80, 83–86, 124).

[80] B. P. Klein, J. M. Morbec, M. Franke, K. K. Greulich, M. Sachs, S. Parhizkar, F. C. Bocquet, M. Schmid, S. J. Hall, R. J. Maurer, B. Meyer, R. Tonner, C. Kumpf, P. Kratzer and J. M. Gottfried, “The molecule-metal bond of alternant versus nonalternant aromatic systems on coinage metal surfaces: naphthalene versus azulene on ag(111) and cu(111)”, The Journal of Physical Chemistry C **128**, 29219–29230 (2019) (cit. on pp. 14, 50, 56–62, 64, 65, 67, 69, 73–75, 77, 80, 84–86, 90, 124).

[81] B. P. Klein, S. E. Harman, L. Ruppenthal, G. M. Ruehl, S. J. Hall, S. J. Carey, J. Herritsch, M. Schmid, R. J. Maurer, R. Tonner, C. T. Campbell and J. M. Gottfried, “Enhanced bonding of pentagon–heptagon defects in graphene to metal surfaces: insights from the adsorption of azulene and naphthalene to pt(111)”, Chemistry of Materials **32**, 1041–1053 (2020) (cit. on pp. 14, 53, 56–58, 60, 61, 63–65, 77, 80, 83–86, 124).

[82] C. Hébert-Souche, P. H. Louf, P. Blaha, M. Nelhiebel, J. Luitz, P. Schattschneider, K. Schwarz and B. Jouffrey, “The orientation-dependent simulation of ELNES”, Ultramicroscopy **83**, 9–16 (2000) (cit. on p. 14).

[83] D. A. Duncan, J. H. K. Pfisterer, P. S. Deimel, R. G. Acres, M. Fritton, P. Feulner, J. V. Barth and F. Allegretti, “Formation of a thermally stable bilayer of coadsorbed intact and deprotonated thymine exploiting the surface corrugation of rutile TiO2(110)”, Physical Chemistry Chemical Physics **18**, 20433–20442 (2016) (cit. on p. 15).

[84] T. H. Dunning, W. J. Hunt and W. A. Goddard, “The theoretical description of the (*) excited states of ethylene”, Chemical Physics Letters **4**, 147–150 (1969) (cit. on p. 16).

[85] H. Ågren, V. Carravetta, O. Vahtras and L. G. M. Pettersson, “Direct, atomic orbital, static exchange calculations of photoabsorption spectra of large molecules and clusters”, Chemical Physics Letters **222**, 75–81 (1994) (cit. on p. 16).

[86] H. Ågren, V. Carravetta, O. Vahtras and L. G. M. Pettersson, “Direct SCF direct static-exchange calculations of electronic spectra”, Theoretical Chemistry Accounts **97**, 14–40 (1997) (cit. on p. 16).

[87] D. Hait and M. Head-Gordon, “Excited state orbital optimization via minimizing the square of the gradient: general approach and application to singly and doubly excited states via density functional theory”, Journal of Chemical Theory and Computation **16**, 1699–1710 (2020) (cit. on p. 16).

[88] D. Hait, E. A. Haugen, Z. Yang, K. J. Oosterbaan, S. R. Leone and M. Head-Gordon, “Accurate prediction of core-level spectra of radicals at density functional theory cost via square gradient minimization and recoupling of mixed configurations”, The Journal of Chemical Physics **153**, 134108 (2020) (cit. on p. 16).

[89] A. Dreuw and M. Head-Gordon, “Single-reference ab initio methods for the calculation of excited states of large molecules”, Chemical Reviews **105**, 4009–4037 (2005) (cit. on p. 16).

[90] N. A. Besley and F. A. Asmuruf, “Time-dependent density functional theory calculations of the spectroscopy of core electrons”, Physical Chemistry Chemical Physics **12**, 12024–12039 (2010) (cit. on p. 16).

[91] J. J. Kas, F. D. Vila, J. J. Rehr and S. A. Chambers, “Real-time cumulant approach for charge-transfer satellites in x-ray photoemission spectra”, Physical Review B **91**, 121112 (2015) (cit. on p. 16).

[92] S. DeBeer George, T. Petrenko and F. Neese, “Prediction of iron k-edge absorption spectra using time-dependent density functional theory”, The Journal of Physical Chemistry A **112**, 12936–12943 (2008) (cit. on p. 16).

[93] K. Lopata, B. E. Van Kuiken, M. Khalil and N. Govind, "Linear-response and real-time time-dependent density functional theory studies of core-level near-edge x-ray absorption", Journal of Chemical Theory and Computation **8**, 3284–3292 (2012) (cit. on p. 16).

[94] S. Coriani, O. Christiansen, T. Fransson and P. Norman, "Coupled-cluster response theory for near-edge x-ray-absorption fine structure of atoms and molecules", Physical Review A **85**, 022507 (2012) (cit. on p. 16).

[95] X. Zheng and L. Cheng, "Performance of delta-coupled-cluster methods for calculations of core-ionization energies of first-row elements", Journal of Chemical Theory and Computation **15**, 4945–4955 (2019) (cit. on p. 16).

[96] B. Peng, P. J. Lestrange, J. J. Goings, M. Caricato and X. Li, "Energy-specific equation-of-motion coupled-cluster methods for high-energy excited states: application to k-edge x-ray absorption spectroscopy", Journal of Chemical Theory and Computation **11**, 4146–4153 (2015) (cit. on p. 16).

[97] M. L. Vidal, P. Pokhilko, A. I. Krylov and S. Coriani, "Equation-of-motion coupled-cluster theory to model l-edge x-ray absorption and photoelectron spectra", The Journal of Physical Chemistry Letters **11**, 8314–8321 (2020) (cit. on p. 16).

[98] D. R. Nascimento and A. E. DePrince, "Simulation of near-edge x-ray absorption fine structure with time-dependent equation-of-motion coupled-cluster theory", The Journal of Physical Chemistry Letters **8**, 2951–2957 (2017) (cit. on p. 16).

[99] J. Vinson, J. J. Rehr, J. J. Kas and E. L. Shirley, "Bethe-salpeter equation calculations of core excitation spectra", Physical Review B **83**, 115106 (2011) (cit. on p. 16).

[100] J. Vinson and J. J. Rehr, "Ab initio bethe-salpeter calculations of the x-ray absorption spectra of transition metals at the l-shell edges", Physical Review B **86**, 195135 (2012) (cit. on p. 16).

[101] L. Hedin, "New method for calculating the one-particle green's function with application to the electron-gas problem", Physical Review **139**, A796–A823 (1965) (cit. on p. 16).

[102] S. Clark, M. Segall, C. Pickard, P. Hasnip, M. Probert, K. Refson and M. Payne, "First principles methods using CASTEP", Zeitschrift für Kristallographie **220**, 567–570 (2005) (cit. on pp. 17, 29, 124).

[103] D. D. Koelling and B. N. Harmon, "A technique for relativistic spin-polarised calculations", Journal of Physics C: Solid State Physics **10**, 3107–3114 (1977) (cit. on pp. 18, 19).

[104] R. J. Maurer and K. Reuter, “Excited-state potential-energy surfaces of metal-adsorbed organic molecules from linear expansion -self-consistent field density-functional theory (SCF-DFT)”, The Journal of Chemical Physics **139**, 14708 (2013) (cit. on pp. 18, 35, 81).

[105] V. Blum, R. Gehrke, F. Hanke, P. Havu, V. Havu, X. Ren, K. Reuter and M. Scheffler, “Ab initio molecular simulations with numeric atom-centered orbitals”, Computer Physics Communications **180**, 2175–2196 (2009) (cit. on pp. 18, 29, 33, 62, 105, 124).

[106] C. Chang, M. Pelissier and P. Durand, “Regular two-component pauli-like effective hamiltonians in dirac theory”, Physica Scripta **34**, 394–404 (1986) (cit. on p. 19).

[107] J.-L. Heully, I. Lindgren, E. Lindroth, S. Lundqvist and A.-M. Martensson-Pendrill, “Diagonalisation of the dirac hamiltonian as a basis for a relativistic many-body procedure”, Journal of Physics B: Atomic and Molecular Physics **19**, 2799–2815 (1986) (cit. on p. 19).

[108] E. v. Lenthe, E. J. Baerends and J. G. Snijders, “Relativistic regular two-component hamiltonians”, The Journal of Chemical Physics **99**, 4597–4610 (1993) (cit. on p. 19).

[109] A. H. Larsen, J. J. Mortensen, J. Blomqvist, I. E. Castelli, R. Christensen, M. Dułak, J. Friis, M. N. Groves, B. Hammer, C. Hargus, E. D. Hermes, P. C. Jennings, P. B. Jensen, J. Kermode, J. R. Kitchin, E. L. Kolsbjerg, J. Kubal, K. Kaasbjerg, S. Lysgaard, J. B. Maronsson, T. Maxson, T. Olsen, L. Pastewka, A. Peterson, C. Rostgaard, J. Schiøtz, O. Schütt, M. Strange, K. S. Thygesen, T. Vegge, L. Vilhelmsen, M. Walter, Z. Zeng and K. W. Jacobsen, “The atomic simulation environment—a python library for working with atoms”, Journal of Physics: Condensed Matter **29**, 273002 (2017) (cit. on pp. 19, 21).

[110] T. Mizoguchi, I. Tanaka, S.-P. Gao and C. J. Pickard, “First-principles calculation of spectral features, chemical shift and absolute threshold of ELNES and XANES using a plane wave pseudopotential method.”, Journal of Physics: Condensed Matter **21**, 104204 (2009) (cit. on pp. 25, 31, 74).

[111] M. Schmid, H.-P. Steinrück and J. M. Gottfried, “A new asymmetric pseudo-voigt function for more efficient fitting of XPS lines”, Surface and Interface Analysis **46**, 505–511 (2014) (cit. on pp. 26, 32, 62, 106).

[112] M. Schmid, H.-P. Steinrück and J. M. Gottfried, “A new asymmetric pseudo-voigt function for more efficient fitting of XPS lines”, Surface and Interface Analysis **47**, 1080 (2015) (cit. on pp. 26, 32, 62, 106).

[113] U. von Barth and G. Grossmann, “Dynamical calculations of x-ray absorption and emission spectra”, Physica Scripta **21**, 580–584 (1980) (cit. on pp. 29, 80, 150).

[114] J. M. Kahk and J. Lischner, “Accurate absolute core-electron binding energies of molecules, solids, and surfaces from first-principles calculations”, Physical Review Materials **3**, 100801 (2019) (cit. on pp. 31, 35, 39, 49).

[115] S.-P. Gao, C. J. Pickard, A. Perlov and V. Milman, “Core-level spectroscopy calculation and the plane wave pseudopotential method”, Journal of Physics: Condensed Matter **21**, 104203 (2009) (cit. on pp. 31, 35, 39).

[116] C. J. Pickard, “Ab initio electron energy loss spectroscopy”, PhD thesis (University of Cambridge, 1997) (cit. on p. 31).

[117] S.-P. Gao, C. J. Pickard, M. C. Payne, J. Zhu and J. Yuan, “Theory of core-hole effects in 1s core-level spectroscopy of the first-row elements”, Physical Review B **77**, 115122 (2008) (cit. on p. 32).

[118] J. P. Perdew, J. A. Chevary, S. H. Vosko, K. A. Jackson, M. R. Pederson, D. J. Singh and C. Fiolhais, “Atoms, molecules, solids, and surfaces: applications of the generalized gradient approximation for exchange and correlation”, Physical Review B **46**, 6671–6687 (1992) (cit. on pp. 33, 44).

[119] J. Tao, J. P. Perdew, V. N. Staroverov and G. E. Scuseria, “Climbing the density functional ladder: nonempirical meta–generalized gradient approximation designed for molecules and solids”, Physical Review Letters **91**, 146401 (2003) (cit. on pp. 33, 62, 67).

[120] J. Sun, A. Ruzsinszky and J. P. Perdew, “Strongly constrained and appropriately normed semilocal density functional”, Physical Review Letters **115**, 036402 (2015) (cit. on pp. 33, 62, 67).

[121] C. Adamo and V. Barone, “Toward reliable density functional methods without adjustable parameters: the PBE0 model”, The Journal of Chemical Physics **110**, 6158–6170 (1999) (cit. on pp. 33, 72, 74).

[122] P. J. Stephens, F. J. Devlin, C. F. Chabalowski and M. J. Frisch, “Ab initio calculation of vibrational absorption and circular dichroism spectra using density functional force fields”, The Journal of Physical Chemistry **98**, 11623–11627 (1994) (cit. on p. 33).

[123] J. Heyd, G. E. Scuseria and M. Ernzerhof, “Hybrid functionals based on a screened coulomb potential”, The Journal of Chemical Physics **118**, 8207–8215 (2003) (cit. on pp. 33, 62, 67, 74).

[124] I. Y. Zhang, N. Q. Su, A. G. Brémond, C. Adamo and X. Xu, “Doubly hybrid density functional xDH-PBE0 from a parameter-free global hybrid model PBE0”, The Journal of Chemical Physics **136**, 174103 (2012) (cit. on p. 33).

[125] A. D. Becke, “Density-functional exchange-energy approximation with correct asymptotic behavior”, Physical Review A **38**, 3098–3100 (1988) (cit. on pp. 33, 44).

[126] C. Lee, W. Yang and R. G. Parr, “Development of the colle-salvetti correlation-energy formula into a functional of the electron density”, Physical Review B **37**, 785–789 (1988) (cit. on pp. 33, 44).

[127] K. Siegbahn, “Electron spectroscopy for chemical analysis”, in Atomic physics 3, edited by S. J. Smith and G. K. Walters (1973), pp. 493–522 (cit. on pp. 33, 36).

[128] U. Gelius, E. Basilier, S. Svensson, T. Bergmark and K. Siegbahn, “A high resolution ESCA instrument with x-ray monochromator for gases and solids”, Journal of Electron Spectroscopy and Related Phenomena **2**, 405–434 (1973) (cit. on pp. 33, 36).

[129] O. Travnikova, K. J. Børve, M. Patanen, J. Söderström, C. Miron, L. J. Sæthre, N. Mårtensson and S. Svensson, “The ESCA molecule—historical remarks and new results”, Journal of Electron Spectroscopy and Related Phenomena, Special Issue in honor of Prof. T. Darrah Thomas: High-Resolution Spectroscopy of Isolated Species **185**, 191–197 (2012) (cit. on pp. 33, 36, 37).

[130] M. J. Kahk and J. Lischner, “Core electron binding energies of adsorbates on cu(111) from first-principles calculations”, Physical Chemistry Chemical Physics **20**, 30403–30411 (2018) (cit. on p. 35).

[131] J. M. Foster and S. F. Boys, “Canonical configurational interaction procedure”, Reviews of Modern Physics **32**, 300–302 (1960) (cit. on p. 35).

[132] N. Ferré and X. Assfeld, “Application of the local self-consistent-field method to core-ionized and core-excited molecules, polymers, and proteins: true orthogonality between ground and excited states”, The Journal of Chemical Physics **117**, 4119–4125 (2002) (cit. on p. 35).

[133] P.-F. Loos and X. Assfeld, “Core-ionized and core-excited states of macromolecules”, International Journal of Quantum Chemistry **107**, 2243–2252 (2007) (cit. on p. 35).

[134] D. Mejía-Rodríguez and S. B. Trickey, “Analysis of over-magnetization of elemental transition metal solids from the SCAN density functional”, Physical Review B **100**, 41113 (2019) (cit. on p. 36).

[135] J. M. Pi, M. Stella, N. K. Fernando, A. Y. Lam, A. Regoutz and L. E. Ratcliff, “Predicting core level photoelectron spectra of amino acids using density functional theory”, The Journal of Physical Chemistry Letters **11**, 2256–2262 (2020) (cit. on p. 38).

[136] I. Tolbatov and D. M. Chipman, “Performance of density functionals for computation of core electron binding energies in first-row hydrides and glycine”, in *Isaiah shavitt: a memorial festschrift from theoretical chemistry accounts*, edited by R. Shepard, R. M. Pitzer and T. Dunning, Highlights in Theoretical Chemistry (Springer, Berlin, Heidelberg, 2016), pp. 187–193 (cit. on p. 38).

[137] D. P. Chong, “Localized and delocalized 1s core-holes in DFT calculations”, Journal of Electron Spectroscopy and Related Phenomena **159**, 94–96 (2007) (cit. on p. 38).

[138] M. A. Ambroise and F. Jensen, “Probing basis set requirements for calculating core ionization and core excitation spectroscopy by the self-consistent-field approach”, Journal of Chemical Theory and Computation **15**, 325–337 (2019) (cit. on p. 39).

[139] R. Sarangi, M. L. Vidal, S. Coriani and A. I. Krylov, “On the basis set selection for calculations of core-level states: different strategies to balance cost and accuracy”, Molecular Physics **118**, e1769872 (2020) (cit. on p. 39).

[140] M. C. Payne, M. P. Teter, D. C. Allan, T. A. Arias and J. D. Joannopoulos, “Iterative minimization techniques for ab initio total-energy calculations: molecular dynamics and conjugate gradients”, Reviews of Modern Physics **64**, 1045–1097 (1992) (cit. on p. 39).

[141] L. Kleinman and D. M. Bylander, “Efficacious form for model pseudopotentials”, Physical Review Letters **48**, 1425–1428 (1982) (cit. on p. 39).

[142] D. Vanderbilt, “Soft self-consistent pseudopotentials in a generalized eigenvalue formalism”, Physical Review B **41**, 7892–7895 (1990) (cit. on p. 39).

[143] T. C. Taucher, O. T. Hofmann and E. Zojer, “Final-state simulations of core-level binding energies at metal-organic hybrid interfaces: artifacts caused by spurious collective electrostatic effects”, ACS Omega **5**, 25868–25881 (2020) (cit. on pp. 41, 51, 68, 117).

[144] H. J. Monkhorst and J. D. Pack, “Special points for brillouin-zone integrations”, Physical Review B **13**, 5188–5192 (1976) (cit. on p. 48).

[145] C Mainka, P. S. Bagus, A Schertel, T Strunskus, M Grunze and C. Wöll, “Linear dichroism in x-ray absorption spectroscopy of strongly chemisorbed planar molecules: role of adsorption induced rehybridisations”, Surface Science **341**, L1055–L1060 (1995) (cit. on p. 51).

[146] Y. Ito, Y. Shen, D. Hojo, Y. Itagaki, T. Fujita, L. Chen, T. Aida, Z. Tang, T. Adschiri and M. Chen, “Correlation between chemical dopants and topological defects in catalytically active nanoporous graphene”, Advanced Materials **28**, 10644–10651 (2016) (cit. on p. 56).

[147] S. Malola, H. Häkkinen and P. Koskinen, “Structural, chemical, and dynamical trends in graphene grain boundaries”, Physical Review B **81**, 165447 (2010) (cit. on p. 56).

[148] R. Grantab, V. B. Shenoy and R. S. Ruoff, “Anomalous strength characteristics of tilt grain boundaries in graphene”, Science **330**, 946–948 (2010) (cit. on p. 56).

[149] H. I. Rasool, C. Ophus, W. S. Klug, A. Zettl and J. K. Gimzewski, “Measurement of the intrinsic strength of crystalline and polycrystalline graphene”, Nature Communications **4**, 2811 (2013) (cit. on p. 56).

[150] Y. Wei, J. Wu, H. Yin, X. Shi, R. Yang and M. Dresselhaus, “The nature of strength enhancement and weakening by pentagon–heptagon defects in graphene”, Nature Materials **11**, 759–763 (2012) (cit. on p. 56).

[151] A. Shekhawat and R. O. Ritchie, “Toughness and strength of nanocrystalline graphene”, Nature Communications **7**, 10546 (2016) (cit. on p. 56).

[152] A. W. Tsen, L. Brown, M. P. Levendorf, F. Ghahari, P. Y. Huang, R. W. Havener, C. S. Ruiz-Vargas, D. A. Muller, P. Kim and J. Park, “Tailoring electrical transport across grain boundaries in polycrystalline graphene”, Science **336**, 1143–1146 (2012) (cit. on p. 56).

[153] O. V. Yazyev and S. G. Louie, “Electronic transport in polycrystalline graphene”, Nature Materials **9**, 806–809 (2010) (cit. on p. 56).

[154] J. Červenka, M. I. Katsnelson and C. F. J. Flipse, “Room-temperature ferromagnetism in graphite driven by two-dimensional networks of point defects”, Nature Physics **5**, 840–844 (2009) (cit. on p. 56).

[155] B. Ni, T. Zhang, J. Li, X. Li and H. Gao, “Topological design of graphene”, in *Handbook of graphene set*, edited by E. Celasco, A. N. Chaika, T. Stauber, M. Zhang, C. Ozkan, C. Ozkan, U. Ozkan, B. Palys and S. W. Harun (John Wiley & Sons, Ltd, 2019), pp. 1–44 (cit. on p. 56).

[156] S. R. Kachel, B. P. Klein, J. M. Morbec, M. Schöniger, M. Hutter, M. Schmid, P. Kratzer, B. Meyer, R. Tonner and J. M. Gottfried, “Chemisorption and physisorption at the metal/organic interface: bond energies of naphthalene and azulene on coinage metal surfaces”, The Journal of Physical Chemistry C **124**, 8257–8268 (2020) (cit. on pp. 56–59, 80, 84).

[157] B. P. Klein, L. Ruppenthal, S. J. Hall, L. E. Sattler, S. M. Weber, J. Herritsch, A. Jaegermann, R. J. Maurer, G. Hilt and J. M. Gottfried, “Topology effects in molecular organic electronic materials: pyrene and azupyrene”, ChemPhysChem **22**, 1065–1073 (2021) (cit. on pp. 56, 61, 75–77, 80, 81, 124).

[158] C. A. Coulson and G. S. Rushbrooke, “Note on the method of molecular orbitals”, Mathematical Proceedings of the Cambridge Philosophical Society **36**, 193–200 (1940) (cit. on p. 56).

[159] D. P. Woodruff, “Normal incidence x-ray standing wave determination of adsorbate structures”, Progress in Surface Science **57**, 1–60 (1998) (cit. on pp. 57, 58).

[160] D. P. Woodruff, “Surface structure determination using x-ray standing waves”, Reports on Progress in Physics **68**, 743–798 (2005) (cit. on pp. 57, 58).

[161] K. Christmann, *Introduction to surface physical chemistry*, edited by K. Christmann, Topics in Physical Chemistry (Steinkopff, Heidelberg, 1991), 283 pp. (cit. on pp. 57, 58).

[162] F. C. Bocquet, G. Mercurio, M. Franke, G. van Straaten, S. Weiß, S. Soubatch, C. Kumpf and F. S. Tautz, “Torricelli: a software to determine atomic spatial distributions from normal incidence x-ray standing wave data”, Computer Physics Communications **235**, 502–513 (2019) (cit. on p. 58).

[163] G. van Straaten, M. Franke, F. C. Bocquet, F. S. Tautz and C. Kumpf, “Non-dipolar effects in photoelectron-based normal incidence x-ray standing wave experiments”, Journal of Electron Spectroscopy and Related Phenomena **222**, 106–116 (2018) (cit. on p. 58).

[164] J. Zegenhagen, “Surface structure determination with x-ray standing waves”, Surface Science Reports **18**, 202–271 (1993) (cit. on p. 58).

[165] B. Stadtmüller, S. Schröder and C. Kumpf, “Heteromolecular metal–organic interfaces: electronic and structural fingerprints of chemical bonding”, Journal of Electron Spectroscopy and Related Phenomena, Organic Electronics **204**, 80–91 (2015) (cit. on p. 58).

[166] A. Bondi, “Van der waals volumes and radii”, The Journal of Physical Chemistry **68**, 441–451 (1964) (cit. on p. 58).

[167] W. Liu, F. Maaß, M. Willenbockel, C. Bronner, M. Schulze, S. Soubatch, F. S. Tautz, P. Tegeder and A. Tkatchenko, “Quantitative prediction of molecular adsorption: structure and binding of benzene on coinage metals”, Physical Review Letters **115**, 036104 (2015) (cit. on p. 58).

[168] I. Kröger, P. Bayersdorfer, B. Stadtmüller, C. Kleimann, G. Mercurio, F. Reinert and C. Kumpf, “Submonolayer growth of h${}_{2}$-phthalocyanine on ag(111)”, Physical Review B **86**, 195412 (2012) (cit. on p. 58).

[169] D. R. Lide, ed., *CRC handbook of chemistry and physics*, 90th ed (CRC Press, Boca Raton, FL, 2010) (cit. on pp. 58, 80).

[170] A. M. de Jong and J. W. Niemantsverdriet, “Thermal desorption analysis: comparative test of ten commonly applied procedures”, Surface Science **233**, 355–365 (1990) (cit. on p. 58).

[171] D. L. S. Nieskens, A. P. van Bavel and J. W. Niemantsverdriet, “The analysis of temperature programmed desorption experiments of systems with lateral interactions; implications of the compensation effect”, Surface Science **546**, 159–169 (2003) (cit. on p. 58).

[172] J. M. Gottfried, E. K. Vestergaard, P. Bera and C. T. Campbell, “Heat of adsorption of naphthalene on pt(111) measured by adsorption calorimetry”, The Journal of Physical Chemistry B **110**, 17539–17545 (2006) (cit. on p. 58).

[173] S. Grimme, J. Antony, S. Ehrlich and H. Krieg, “A consistent and accurate ab initio parametrization of density functional dispersion correction (DFT-d) for the 94 elements h-pu”, The Journal of Chemical Physics **132**, 154104 (2010) (cit. on p. 61).

[174] A. D. Becke and E. R. Johnson, “A density-functional model of the dispersion interaction”, The Journal of Chemical Physics **123**, 154101 (2005) (cit. on p. 61).

[175] E. Zojer, T. C. Taucher and O. T. Hofmann, “The impact of dipolar layers on the electronic properties of organic/inorganic hybrid interfaces”, Advanced Materials Interfaces **6**, 1900581 (2019) (cit. on p. 68).

[176] J. M. Kahk, G. S. Michelitsch, R. J. Maurer, K. Reuter and J. Lischner, “Core electron binding energies in solids from periodic all-electron -self-consistent-field calculations”, The Journal of Physical Chemistry Letters **12**, 9353–9359 (2021) (cit. on p. 68).

[177] V. I. Anisimov, J. Zaanen and O. K. Andersen, “Band theory and mott insulators: hubbard u instead of stoner i”, Physical Review B **44**, 943–954 (1991) (cit. on p. 71).

[178] S. L. Dudarev, G. A. Botton, S. Y. Savrasov, C. J. Humphreys and A. P. Sutton, “Electron-energy-loss spectra and the structural stability of nickel oxide: an LSDA+u study”, Physical Review B **57**, 1505–1509 (1998) (cit. on p. 71).

[179] W. E. Pickett, S. C. Erwin and E. C. Ethridge, “Reformulation of the LDA $+U$ method for a local-orbital basis”, Physical Review B **58**, 1201–1209 (1998) (cit. on p. 71).

[180] A. G. Petukhov, I. I. Mazin, L. Chioncel and A. I. Lichtenstein, “Correlated metals and the LDA $+U$ method”, Physical Review B **67**, 153106 (2003) (cit. on p. 71).

[181] R. J. Maurer, “First-principles description of the isomerization dynamics of surface-adsorbed molecular switches”, PhD thesis (Technische Universität München, 2014) (cit. on p. 71).

[182] M. Müller, K. Diller, R. J. Maurer and K. Reuter, “Interfacial charge rearrangement and intermolecular interactions: density-functional theory study of free-base porphine adsorbed on ag(111) and cu(111)”, The Journal of Chemical Physics **144**, 024701 (2016) (cit. on p. 71).

[183] D. A. Egger, Z.-F. Liu, J. B. Neaton and L. Kronik, “Reliable energy level alignment at physisorbed molecule–metal interfaces from density functional theory”, Nano Letters **15**, 2448–2455 (2015) (cit. on p. 74).

[184] E. Wruss, E. Zojer and O. T. Hofmann, “Distinguishing between charge-transfer mechanisms at organic/inorganic interfaces employing hybrid functionals”, The Journal of Physical Chemistry C **122**, 14640–14653 (2018) (cit. on p. 74).

[185] B. P. Klein, A. Ihle, S. R. Kachel, L. Ruppenthal, S. J. Hall, L. E. Sattler, S. M. Weber, J. Herritsch, A. Jaegermann, D. Ebeling, R. J. Maurer, G. Hilt, R. Tonner-Zech, A. Schirmeisen and J. M. Gottfried, “Topological stone-wales defects enhance bonding and electronic coupling at the graphene/metal interface”, ACS Nano, ’in review’ (cit. on p. 77).

[186] Y. Yamaguchi, M. Takubo, K. Ogawa, K.-i. Nakayama, T. Koganezawa and H. Katagiri, “Terazulene isomers: polarity change of OFETs through molecular orbital distribution contrast”, Journal of the American Chemical Society **138**, 11335–11343 (2016) (cit. on p. 79).

[187] H. Xin and X. Gao, “Application of azulene in constructing organic optoelectronic materials: new tricks for an old dog”, ChemPlusChem **82**, 945–956 (2017) (cit. on p. 79).

[188] J. M. Gottfried, “Quantitative model studies for interfaces in organic electronic devices”, New Journal of Physics **18**, 111002 (2016) (cit. on p. 79).

[189] A Nilsson, J Hasselström, A Föhlisch, O Karis, L. G. M. Pettersson, M Nyberg and L Triguero, “Probing chemical bonding in adsorbates using x-ray emission spectroscopy”, Journal of Electron Spectroscopy and Related Phenomena **110-111**, 15–39 (2000) (cit. on p. 80).

[190] C Morin, D Simon and P Sautet, “Chemisorption of benzene on pt(111), pd(111), and rh(111) metal surfaces: a structural and vibrational comparison from first principles”, The Journal of Physical Chemistry B **108**, 5653–5665 (2004) (cit. on p. 80).

[191] G Fronzoni, G Balducci, R De Francesco, M Romeo and M Stener, “Density functional theory simulation of NEXAFS spectra of molecules adsorbed on surfaces: c2h4 on si(100) case study”, The Journal of Physical Chemistry C **116**, 18910–18919 (2012) (cit. on p. 80).

[192] B Hammer and J. K. Norskov, “Why gold is the noblest of all the metals”, Nature **376**, 238–240 (1995) (cit. on p. 80).

[193] L. G. M. Pettersson and A. Nilsson, “A molecular perspective on the d-band model: synergy between experiment and theory”, Topics in Catalysis **57**, 2–13 (2014) (cit. on p. 80).

[194] R. B. Mallion and D. H. Rouvray, “The golden jubilee of the coulson-rushbrooke pairing theorem”, Journal of Mathematical Chemistry **5**, 1–21 (1990) (cit. on p. 80).

[195] M. J. S. Dewar, Bulletin de la Société Chimique de France **18** (1951) (cit. on p. 85).

[196] J Chatt and L. A. Duncanson, "586. olefin co-ordination compounds. part III. infra-red spectra and structure: attempted preparation of acetylene complexes", Journal of the Chemical Society, 2939–2947 (1953) (cit. on p. 85).

[197] A. Bétard and R. A. Fischer, "Metal–organic framework thin films: from fundamentals to applications.", Chemical Reviews **112**, 1055–1083 (2012) (cit. on p. 99).

[198] L. Dong, Z. Gao and N. Lin, "Self-assembly of metal–organic coordination structures on surfaces", Progress in Surface Science **91**, 101–135 (2016) (cit. on p. 99).

[199] J. V. Barth, "Molecular architectonic on metal surfaces", Annual Review of Physical Chemistry **58**, 375–407 (2007) (cit. on p. 99).

[200] S. Stepanow, M. Lingenfelder, A. Dmitriev, H. Spillmann, E. Delvigne, N. Lin, X. Deng, C. Cai, J. V. Barth and K. Kern, "Steering molecular organization and host–guest interactions using two-dimensional nanoporous coordination systems", Nature Materials **3**, 229–233 (2004) (cit. on p. 99).

[201] A. Kiebele, D. Bonifazi, F. Cheng, M. Stöhr, F. Diederich, T. Jung and H. Spillmann, "Adsorption and dynamics of long-range interacting fullerenes in a flexible, two-dimensional, nanoporous porphyrin network", ChemPhysChem **7**, 1462–1470 (2006) (cit. on p. 99).

[202] M. Stöhr, M. Wahl, H. Spillmann, L. H. Gade and T. A. Jung, "Lateral manipulation for the positioning of molecular guests within the confinements of a highly stable self-assembled organic surface network", Small **3**, 1336–1340 (2007) (cit. on p. 99).

[203] K. Cui, F. Schluetter, O. Ivasenko, M. Kivala, M. G. Schwab, S.-L. Lee, S. F. Mertens, K. Tahara, Y. Tobe, K. Muellen, K. Mali and S. De Feyter, "Multicomponent self-assembly with a shape-persistent n-heterotriangulene macrocycle on au(111)", Chemistry - a European Journal **21**, 1652–1659 (2015) (cit. on p. 99).

[204] J. V. Barth, G. Costantini and K. Kern, "Engineering atomic and molecular nanostructures at surfaces", Nature **437**, 671–679 (2005) (cit. on p. 99).

[205] J. Lobo-Checa, M. Matena, K. Müller, J. H. Dil, F. Meier, L. H. Gade, T. A. Jung and M. Stöhr, "Band formation from coupled quantum dots formed by a nanoporous network on a copper surface", Science **325**, 300–303 (2009) (cit. on p. 99).

[206] F. Klappenberger, D. Kühne, W. Krenner, I. Silanes, A. Arnau, F. J. García de Abajo, S. Klyatskaya, M. Ruben and J. V. Barth, “Tunable quantum dot arrays formed from self-assembled metal-organic networks”, Physical Review Letters **106**, 026802 (2011) (cit. on p. 99).

[207] K. Müller, M. Enache and M. Stöhr, “Confinement properties of 2d porous molecular networks on metal surfaces”, Journal of Physics: Condensed Matter **28**, 153003 (2016) (cit. on p. 99).

[208] J. A. A. W. Elemans, S. Lei and S. De Feyter, “Molecular and supramolecular networks on surfaces: from two-dimensional crystal engineering to reactivity”, Angewandte Chemie International Edition **48**, 7298–7332 (2009) (cit. on p. 99).

[209] J. V. Barth, “Fresh perspectives for surface coordination chemistry”, Surface Science, Special Issue of Surface Science dedicated to Prof. Dr. Dr. h.c. mult. Gerhard Ertl, Nobel-Laureate in Chemistry 2007 **603**, 1533–1541 (2009) (cit. on p. 99).

[210] B. D. Baker Cortés, N. Schmidt, M. Enache and M. Stöhr, “Coverage-dependent structural transformation of cyano-functionalized porphyrin networks on au(111) via addition of cobalt atoms”, The Journal of Physical Chemistry C **123**, 19681–19687 (2019) (cit. on p. 99).

[211] M. Matena, J. Björk, M. Wahl, T.-L. Lee, J. Zegenhagen, L. H. Gade, T. A. Jung, M. Persson and M. Stöhr, “On-surface synthesis of a two-dimensional porous coordination network: unraveling adsorbate interactions”, Physical Review B **90**, 125408 (2014) (cit. on p. 99).

[212] J. Björk, M. Matena, M. S. Dyer, M. Enache, J. Lobo-Checa, L. H. Gade, T. A. Jung, M. Stöhr and M. Persson, “STM fingerprint of molecule–adatom interactions in a self-assembled metal–organic surface coordination network on cu(111)”, Physical Chemistry Chemical Physics **12**, 8815–8821 (2010) (cit. on p. 99).

[213] M. Böhringer, K. Morgenstern, W.-D. Schneider and R. Berndt, “Separation of a racemic mixture of two-dimensional molecular clusters by scanning tunneling microscopy”, Angewandte Chemie International Edition **38**, 821–823 (1999) (cit. on p. 99).

[214] T. Yokoyama, S. Yokoyama, T. Kamikado, Y. Okuno and S. Mashiko, “Selective assembly on a surface of supramolecular aggregates with controlled size and shape”, Nature **413**, 619–621 (2001) (cit. on p. 99).

[215] S. Beniwal, S. Chen, D. A. Kunkel, J. Hooper, S. Simpson, E. Zurek, X. C. Zeng and A. Enders, “Kagome-like lattice of – stacked 3-hydroxyphenalenone on cu(111)”, Chemical Communications **50**, 8659–8662 (2014) (cit. on p. 99).

[216] J. V. Barth, J. Weckesser, C. Cai, P. Günter, L. Bürgi, O. Jeandupeux and K. Kern, “Building supramolecular nanostructures at surfaces by hydrogen bonding”, Angewandte Chemie International Edition **39**, 1230–1234 (2000) (cit. on p. 99).

[217] J. A. Theobald, N. S. Oxtoby, M. A. Phillips, N. R. Champness and P. H. Beton, “Controlling molecular deposition and layer structure with supramolecular surface assemblies”, Nature **424**, 1029–1031 (2003) (cit. on p. 99).

[218] A. Dmitriev, H. Spillmann, N. Lin, J. V. Barth and K. Kern, “Modular assembly of two-dimensional metal–organic coordination networks at a metal surface”, Angewandte Chemie **115**, 2774–2777 (2003) (cit. on p. 99).

[219] U. Schlickum, R. Decker, F. Klappenberger, G. Zoppellaro, S. Klyatskaya, M. Ruben, I. Silanes, A. Arnau, K. Kern, H. Brune and J. V. Barth, “Metalorganic honeycomb nanomeshes with tunable cavity size”, Nano Letters **7**, 3813–3817 (2007) (cit. on p. 99).

[220] N. Lin, D. Payer, A. Dmitriev, T. Strunskus, C. Wöll, J. V. Barth and K. Kern, “Two-dimensional adatom gas bestowing dynamic heterogeneity on surfaces”, Angewandte Chemie **117**, 1512–1515 (2005) (cit. on p. 99).

[221] H. Walch, R. Gutzler, T. Sirtl, G. Eder and M. Lackinger, “Material- and orientation-dependent reactivity for heterogeneously catalyzed carbonbromine bond homolysis”, The Journal of Physical Chemistry C **114**, 12604–12609 (2010) (cit. on p. 99).

[222] J. Park, K. Y. Kim, K.-H. Chung, J. K. Yoon, H. Kim, S. Han and S.-J. Kahng, “Interchain interactions mediated by br adsorbates in arrays of metal–organic hybrid chains on ag(111)”, The Journal of Physical Chemistry C **115**, 14834–14838 (2011) (cit. on p. 99).

[223] P. Maksymovych, D. C. Sorescu and J. T. Yates, “Gold-adatom-mediated bonding in self-assembled short-chain alkanethiolate species on the au(111) surface”, Physical Review Letters **97**, 146103 (2006) (cit. on p. 99).

[224] P. Maksymovych and J. T. Yates, “Au adatoms in self-assembly of benzenethiol on the au(111) surface”, Journal of the American Chemical Society **130**, 7518–7519 (2008) (cit. on p. 99).

[225] J. Meyer, A. Nickel, R. Ohmann, Lokamani, C. Toher, D. A. Ryndyk, Y. Garmshausen, S. Hecht, F. Moresco and G. Cuniberti, “Tuning the formation of discrete coordination nanostructures”, Chemical Communications **51**, 12621–12624 (2015) (cit. on p. 99).

[226] T. Anh Pham, F. Song, M. N. Alberti, M.-T. Nguyen, N. Trapp, C. Thilgen, F. Diederich and M. Stöhr, “Heat-induced formation of one-dimensional coordination polymers on au(111): an STM study”, Chemical Communications **51**, 14473–14476 (2015) (cit. on p. 99).

[227] L. Solianyk, “Tailoring molecular nano-architectures on metallic surfaces”, Thesis fully internal (DIV) (University of Groningen, [Groningen], 2019) (cit. on pp. 101, 103, 104).

[228] Y. Niwa, H. Kobayashi and T. Tsuchiya, “X-ray photoelectron spectroscopy of tetraphenylporphin and phthalocyanine”, The Journal of Chemical Physics **60**, 799–807 (1974) (cit. on p. 103).

[229] C. Zhang, L. Fu, N. Liu, M. Liu, Y. Wang and Z. Liu, “Synthesis of nitrogen-doped graphene using embedded carbon and nitrogen sources”, Advanced Materials **23**, 1020–1024 (2011) (cit. on p. 103).

[230] Z.-S. Wu, A. Winter, L. Chen, Y. Sun, A. Turchanin, X. Feng and K. Müllen, “Three-dimensional nitrogen and boron co-doped graphene for high-performance all-solid-state supercapacitors”, Advanced Materials **24**, 5130–5135 (2012) (cit. on p. 103).

[231] W. Auwärter, F. Klappenberger, A. Weber-Bargioni, A. Schiffrin, T. Strunskus, C. Wöll, Y. Pennec, A. Riemann and J. V. Barth, “Conformational adaptation and selective adatom capturing of tetrapyridyl-porphyrin molecules on a copper (111) surface”, Journal of the American Chemical Society **129**, 11279–11285 (2007) (cit. on p. 104).

[232] F. Klappenberger, A. Weber-Bargioni, W. Auwärter, M. Marschall, A. Schiffrin and J. V. Barth, “Temperature dependence of conformation, chemical state, and metal-directed assembly of tetrapyridyl-porphyrin on cu(111)”, The Journal of Chemical Physics **129**, 214702 (2008) (cit. on p. 104).

[233] G. Di Santo, C. Castellarin-Cudia, M. Fanetti, B. Taleatu, P. Borghetti, L. Sangaletti, L. Floreano, E. Magnano, F. Bondino and A. Goldoni, “Conformational adaptation and electronic structure of 2h-tetraphenylporphyrin on ag(111) during fe metalation”, The Journal of Physical Chemistry C **115**, 4155–4162 (2011) (cit. on p. 104).

[234] K. Diller, F. Klappenberger, M. Marschall, K. Hermann, A. Nefedov, C. Wöll and J. V. Barth, “Self-metalation of 2h-tetraphenylporphyrin on cu(111): an x-ray spectroscopy study”, The Journal of Chemical Physics **136**, 014705 (2012) (cit. on p. 104).

[235] C. E. Wooddell, “Method of comparing the hardness of electric furnace products and natural abrasives”, Transactions of the Electrochemical Society **68**, 111 (1935) (cit. on p. 115).

[236] L. Wei, P. K. Kuo, R. L. Thomas, T. R. Anthony and W. F. Banholzer, “Thermal conductivity of isotopically modified single crystal diamond”, Physical Review Letters **70**, 3764–3767 (1993) (cit. on p. 115).

[237] T. Tohei, A. Kuwabara, F. Oba and I. Tanaka, “Debye temperature and stiffness of carbon and boron nitride polymorphs from first principles calculations”, Physical Review B **73**, 64304 (2006) (cit. on p. 115).

[238] M Werner and R Locher, “Growth and application of undoped and doped diamond films”, Reports on Progress in Physics **61**, 1665–1710 (1998) (cit. on p. 115).

[239] R. S. Balmer, J. R. Brandon, S. L. Clewes, H. K. Dhillon, J. M. Dodson, I Friel, P. N. Inglis, T. D. Madgwick, M. L. Markham, T. P. Mollart, N Perkins, G. A. Scarsbrook, D. J. Twitchen, A. J. Whitehead, J. J. Wilman and S. M. Woollard, “Chemical vapour deposition synthetic diamond: materials, technology and applications”, Journal of Physics: Condensed Matter **21**, 364221 (2009) (cit. on p. 115).

[240] L. A. Hutton, J. G. Iacobini, E. Bitziou, R. B. Channon, M. E. Newton and J. V. Macpherson, “Examination of the factors affecting the electrochemical performance of oxygen-terminated polycrystalline boron-doped diamond electrodes”, Analytical Chemistry **85**, 7230–7240 (2013) (cit. on p. 115).

[241] A. E. Fischer, Y. Show and G. M. Swain, “Electrochemical performance of diamond thin-film electrodes from different commercial sources”, Analytical Chemistry **76**, 2553–2560 (2004) (cit. on p. 115).

[242] F. B. Liu, J. D. Wang, B Liu, X. M. Li and D. R. Chen, “Effect of electronic structures on electrochemical behaviors of surface-terminated boron-doped diamond film electrodes”, Diamond and Related Materials **16**, 454–460 (2007) (cit. on p. 115).

[243] J. V. Macpherson, “A practical guide to using boron doped diamond in electrochemical research”, Physical Chemistry Chemical Physics **17**, 2935–2949 (2015) (cit. on p. 115).

[244] B. L. Mackey, Russell John N., J. E. Crowell, P. E. Pehrsson, B. D. Thoms and J. E. Butler, “Oxygen adsorption on the (110)-oriented diamond surface”, The Journal of Physical Chemistry B **105**, 3803–3812 (2001) (cit. on p. 116).

[245] J Achard, F Silva, A Tallaire, X Bonnin, G Lombardi, K Hassouni and A Gicquel, “High quality MPACVD diamond single crystal growth: high microwave power density regime”, Journal of Physics D: Applied Physics **40**, 6175–6188 (2007) (cit. on p. 116).

[246] K. P. Loh, X. N. Xie, S. W. Yang and J. C. Zheng, “Oxygen adsorption on (111)-oriented diamond: a study with ultraviolet photoelectron spectroscopy, temperature-programmed desorption, and periodic density functional theory”, The Journal of Physical Chemistry B **106**, 5230–5240 (2002) (cit. on p. 116).

[247] J. C. Zheng, X. N. Xie, A. T. S. Wee and K. P. Loh, “Oxygen-induced surface state on diamond (100)”, Diamond and Related Materials **10**, 500–505 (2001) (cit. on p. 116).

[248] J. L. Whitten, P. Cremaschi, R. E. Thomas, R. A. Rudder and R. J. Markunas, “Effects of oxygen on surface reconstruction of carbon”, Applied Surface Science **75**, 45–50 (1994) (cit. on p. 116).

[249] X. M. Zheng and P. V. Smith, “The stable configurations for oxygen chemisorption on the diamond (100) and (111) surfaces”, Surface Science **262**, 219–234 (1992) (cit. on p. 116).

[250] H. Tamura, H. Zhou, K. Sugisako, Y. Yokoi, S. Takami, M. Kubo, K. Teraishi, A. Miyamoto, A. Imamura, M. N.-Gamo and T. Ando, “Periodic density-functional study on oxidation of diamond (100) surfaces”, Physical Review B **61**, 11025–11033 (2000) (cit. on p. 116).

[251] F. Liu, J. Wang, B. Liu, X. Li and D. Chen, “Electronic structures of the oxygenated diamond (100) surfaces”, Chinese Science Bulletin **51**, 2437–2443 (2006) (cit. on p. 116).

[252] S. Skokov, B. Weiner and M. Frenklach, “Molecular-dynamics study of oxygenated (100) diamond surfaces”, Physical Review B **49**, 11374–11382 (1994) (cit. on p. 116).

[253] M Frenklach, D Huang, R. E. Thomas, R. A. Rudder and R. J. Markunas, “Activation energy and mechanism of CO desorption from (100) diamond surface”, Applied Physics Letters **63**, 3090–3092 (1993) (cit. on p. 116).

[254] D Petrini and K Larsson, “A theoretical study of the energetic stability and geometry of hydrogen- and oxygen-terminated diamond (100) surfaces”, The Journal of Physical Chemistry C **111**, 795–801 (2007) (cit. on p. 116).

[255] T. E. Derry, N. W. Makau and C Stampfl, “Oxygen adsorption on the (1 × 1) and (2 × 1) reconstructed c(111) surfaces: a density functional theory study”, Journal of Physics: Condensed Matter **22**, 265007 (2010) (cit. on p. 116).

[256] K Larsson and Y Tian, “Effect of surface termination on the reactivity of nano-sized diamond particle surfaces for bio applications”, Carbon **134**, 244–254 (2018) (cit. on p. 116).

[257] K. Larsson, “The combined influence of dopant species and surface termination on the electronic properties of diamond surfaces”, C - Journal of Carbon Research **6**, 10.3390/c6020022 (2020) (cit. on p. 116).

[258] M. M. Hassan and K. Larsson, “Effect of surface termination on diamond (100) surface electrochemistry”, The Journal of Physical Chemistry C **118**, 22995–23002 (2014) (cit. on p. 116).

[259] G. Wan, M. Cattelan and N. A. Fox, “Electronic structure tunability of diamonds by surface functionalization”, The Journal of Physical Chemistry C **123**, 4168–4177 (2019) (cit. on p. 116).

[260] M. Z. Hossain, T. Kubo, T. Aruga, N. Takagi, T. Tsuno, N. Fujimori and M. Nishijima, “Surface phonons, electronic structure and chemical reactivity of diamond (100)(2 ×1) surface”, Japanese Journal of Applied Physics **38**, 6659–6666 (1999) (cit. on p. 116).

[261] L. M. Struck and M. P. D’Evelyn, “Interaction of hydrogen and water with diamond (100): infrared spectroscopy”, Journal of Vacuum Science & Technology A **11**, 1992–1997 (1993) (cit. on p. 116).

[262] P. E. Pehrsson and T. W. Mercer, “Oxidation of the hydrogenated diamond (100) surface”, Surface Science **460**, 49–66 (2000) (cit. on p. 116).

[263] P. E. Pehrsson and T. W. Mercer, “Oxidation of heated diamond c(100):h surfaces”, Surface Science **460**, 74–90 (2000) (cit. on p. 116).

[264] D Takeuchi, S.-G. Ri, N Tokuda and S Yamasaki, “Recovery of negative electron affinity by annealing on (111) oxidized diamond surfaces”, Diamond and Related Materials **18**, 206–209 (2009) (cit. on p. 116).

[265] C. G. Baldwin, J. E. Downes, C. J. McMahon, C Bradac and R. P. Mildren, “Nanostructuring and oxidation of diamond by two-photon ultraviolet surface excitation: an XPS and NEXAFS study”, Physical Review B **89**, 195422 (2014) (cit. on pp. 116, 120–122).

[266] N. W. Makau and T. E. Derry, “Study of oxygen on the three low index diamond surfaces by XPS”, Surface Review and Letters **10**, 295–301 (2003) (cit. on pp. 116, 120–122).

[267] K Bobrov, H Shechter, A Hoffman and M Folman, “Molecular oxygen adsorption and desorption from single crystal diamond (1 1 1) and (1 1 0) surfaces”, Applied Surface Science **196**, 173–180 (2002) (cit. on p. 116).

[268] S. Chaudhuri, S. J. Hall, B. P. Klein, M. Walker, A. J. Logsdail, J. V. Macpherson and R. J. Maurer, “Coexistence of carbonyl and ether groups on oxygen-terminated (110)-oriented diamond surfaces”, Communications Materials **3**, 6 (2022) (cit. on pp. 116, 117, 120, 121).

[269] K. Reuter and M. Scheffler, “Composition, structure, and stability of $RuO_2(110)$ as a function of oxygen pressure”, Physical Review B **65**, 35406 (2001) (cit. on p. 116).

[270] K. Reuter and M. Scheffler, “Composition and structure of the $RuO_2(110)$ surface in an O_2 and CO environment: implications for the catalytic formation of CO_2”, Physical Review B **68**, 45407 (2003) (cit. on p. 116).

[271] K. Reuter, C. Stampf and M. Scheffler, "Ab initio atomistic thermodynamics and statistical mechanics of surface properties and functions BT - handbook of materials modeling: methods", in , edited by S. Yip (Springer Netherlands, Dordrecht, 2005), pp. 149–194 (cit. on p. 116).

[272] I. Tanaka, H. Araki, M. Yoshiya, T. Mizoguchi, K. Ogasawara and H. Adachi, "First-principles calculations of electron-energy-loss near-edge structure and near-edge x-ray-absorption fine structure of BN polytypes using model clusters", Physical Review B **60**, 4944–4951 (1999) (cit. on p. 150).

[273] C. Elsässer and S. Köstlmeier, "Density-functional modelling of core-hole effects in electron energy-loss near-edge spectra", Ultramicroscopy, International Symposium on Spectroscopy of Materials **86**, 325–337 (2001) (cit. on p. 150).

[274] B. Hetényi, F. De Angelis, P. Giannozzi and R. Car, "Calculation of near-edge x-ray-absorption fine structure at finite temperatures: spectral signatures of hydrogen bond breaking in liquid water", The Journal of Chemical Physics **120**, 8632–8637 (2004) (cit. on p. 150).